Integrity Assessment of Augmented GNSS for Reliable Navigation

Boubeker Belabbas

Thesis to get the degree of a doctor of philosophy

Integrity Assessment of Augmented GNSS for Reliable Navigation

Boubeker Belabbas

xx.yy.2016

Replace this box e. g. by the coat of arms of the university.

Université Paris Est
École Doctorale MSTIC
Laboratoire ESYCOM

Directeur de Thèse:
Prof. Dr. Geneviève Baudoin

Rapporteurs:
Prof. Dr. Gérard Scemama
Dr. Christophe Macabiau

Examinateurs:
Prof. Dr. Bernard Lapeyre
Prof. Dr. xxx yyy

Date of the graduation (optional)
xx.yy.2016

This thesis is dedicated to my parents

Contents

Summary

This thesis tackles one of the main challenge for satellite based navigation to be used in safety critical applications: the integrity level of trust one can put in the navigation solution provided by Global Navigation Satellite System (GNSS) as stand alone or with augmentations including inertial sensors.

The level of trust is well characterized as standard requirements in every safety of life applications and is usually defined in terms of probability to have a position error larger than an alarm limit without an alert. This metric is then compared to an acceptable integrity risk.

A first step in this challenge is to characterize a position error. For that we brake down the global error into individual errors so that each can be explained in a physical way. This is what has been developed in Chapter 2. In this chapter, a statistical analysis was conducted to characterize not only the magnitude of the individual errors but also the level of correlations. The correlation considered are the correlations between individual errors and the correlations of individual errors with respect to the user location (correlation between stations). Then the impact of individual errors at the position level is investigated and some important results are that the satellite orbit and clock errors are correlated and that in the case of standalone single frequency positioning, the ionosphere delay after correction is the dominant effect in the vertical direction. As we investigated the impact in the position domain, we also considered the combination of the American Global Positioning System (GPS) with Galileo satellites and evaluated the performance.

This first step provides a very sophisticated covariance model of satellite pseudo range errors which is location dependent (a regional covariance matrix of pseudo range errors) and we decided to apply this regional matrix to a residual based Receiver Autonomous Integrity Monitoring (RAIM) algorithm. The result is a better integrity performance (better trust in the position accuracy) than with the legacy RAIM approach without increasing the risk of errors larger than the protection levels. The price to pay would be to broadcast the regional covariance matrix to users which will induce additional operational costs to the infrastructure.

Then in a third part we investigated the integrity performance of GNSS when augmented with either a Space Based Augmentation System (SBAS) or a Ground Based Augmentation System (GBAS). The dual constellation dual frequency GBAS was particularly investigated and the performances using different smoothing techniques were assessed. One of the major source of threat is the strong ionosphere gradients

that were already observed in the past. Therefore its impact in GBAS was one of the focus of this thesis. GBAS single frequency and single constellation is vulnerable to large gradient and therefore we investigated special ionosphere gradient monitor based on double difference carrier phase observations from the ground reference receiver. An exhaustive analysis shows the performance that can be achieved using such a monitor and an optimal architecture that can increase the detectability performance to a very high value without inducing additional costs. A sensitivity analysis to design parameters have been conducted and shows the parameter space that have a high stability with respect to errors in the parameters.

In a fourth part we define and analyze an integrity concept for GNSS with inertial hybridization tackling also the complex problem of integrity for positioning while using non linear filtering. Different sensitivity analysis are conducted and the approach considered in this part can easily be generalized for any filtering techniques.

Most of the sequential approaches investigated in this thesis make use of stochastic processes. The most important assumption is tho have Gaussian processes. When considering more general process distribution, we still considered that this process is overbounded by a Gaussian distributed one. This approach fits very well the nominal behavior of errors as they usually can be modeled using Gaussian distributed process. Therefore the integrity concepts is adapted to nominal behavior of errors and therefore the approach using diffusion processes is sufficient to develop a formalism for an integrity concept.

Another approach is to consider more sophisticated processes like those with jump. This would perfectly model the non detected fault modes that cannot be covered by a nominal Gaussian distributed process. This approach will necessitate to understand the distribution of occurrences of jumps and the distribution of their magnitude. The integrity concept would therefore have a very general form and will better suit the real world.

This thesis investigates the different integrity aspects that need to be considered from the characterization of the physical effects at pseudo range level to their propagation to the position domain. This work was concentrated in integrity measure for a nominal operation of GNSS with augmentation, but some fault modes considerations were also investigated and for the special case of non linear filters provides a novel approach of integrity.

1. Introduction

The Global Positioning System (GPS) originally designed for restricted military applications is now in almost all mobile communication devices. Knowing ones position is a prerequisite for starting a journey. This elementary service is the basis of all GPS receivers. The first receivers where just giving a rough approximation of the position in latitude, longitude and height. Now every hand-held GPS receiver is able to locate the user in a map and using additional information, the GPS is able to guide the user from a location to another one minimizing the fuel consumption or minimizing the travel time. Additional information like traffic situation in real time enable the GPS receiver to select the fastest itinerary avoiding traffic jams. Additional sensors information can support the localization and navigation functions.

Along with the development of this traditional navigation service, another possible use of GPS is the support to the so called Location Based Services (LBS). And this is an exploding market. The general principle of LBS is to propose services fitting the best the user needs. In its journey, the user may be interested in having the weather predictions in the targeted location or simply want to know where he can find the closest restaurant or the closest hotel. As the user is overwhelmed by too much information, location based information is an intelligent way to fit it to his real needs.

Knowing were we are and knowing in which direction we want to go have been always the prerequisite for starting a journey. This ancient principle is still relevant today.

From the sextant to the most recent Global Navigation Satellite Systems (GNSS), the primary information a navigator needs is to determine his or her localization in order to plan the direction he or she has to follow.

The first idea of using satellites as mean of navigation started at the beginning of the space adventure with the localization of Sputnik using the Doppler frequency and the knowledge of the position of 2 antennas on the ground. It appeared that the inverse problem i.e. positioning the ground antenna using satellites is a much easier problem and also a much accurate one. The first satellite navigation system called TRANSIT composed of two satellites was using 2 frequencies and the Doppler shift to determine the position of a user. This system developed in 1958 stayed operational until 1996.

In 1973, GPS a new satellite based navigation system program is started based not only on Doppler but also on direct pseudo-range estimation. The performance

in terms of accuracy are very high. The system was performing so well that the US Department of Defense (US DoD) decided to worsen the accuracy by adding a Selective Availability (SA) consisting of intentionally adding noise in the on-board satellite clocks to avoid enemies to use the open service for military purposes.

The first augmentation system consisting of differential GPS were developed in order to bypass the selective availability problem. In fact it offered the opportunity to develop carrier phase based solutions by providing double difference carrier phase positioning. This work was mainly supported by geodetic research institutions for which a cm or even millimeter accuracy was required to study for example tectonic plates displacements or simply to provide a precise topographic maps with precise survey points.

This level of accuracy was beyond the expectations for a global navigation system. Finally The US DoD decided to switch the SA off the 1^{st} of May 2000. One of the motivations was to enable the use of GPS for civil aviation which expressed its interest from the early stage of the GPS deployment. An example of motivating the use of GPS for civil aviation was the incident of Korean Air Lines Flight #902 flying by mistake in the USSR air space on the 20th of April 1978 and intercepted and shot down by the Soviet Air Defense. The violation of the air space could have been avoided using GPS.

What was thought being an easy task to enable GPS for civil aviation, looking at the level of accuracy that could be reached using carrier phase positioning, was in fact a tremendous challenge when dealing with positioning integrity and confidence with low level of risk. It appears to be a fruitful research area and is the principal motivation for this thesis.

The problems can be summarized in the following way: For static applications like geodetic survey for example for which the position could be averaged during a very long period, outliers have only a very limited impact in the expected position. But for aviation applications, the user is interested in an instantaneous position and not in an averaged position. In that case an outlier in the position estimate can potentially drive to a catastrophic behavior of the aircraft especially during critical phases of flight under low visibility conditions. The required performance for different phases of flight are summarized in Figure Tab. 1.1. This table is extracted from [ICA06] and shows the metrics used to qualify navigation systems for different phases of flight from the less stringent (En-route) to the most stringent ones (Category I precision approach with a decision height of 200 ft.).

Integrity, Continuity and Availability are the key parameters for safety of life applications. NAVSTAR GPS cannot guaranty the performance of the positioning system and just provide a commitment to raise the unhealthy flag for a given GPS satellite being in a fault mode within 6 hours. This is for any phase of flight unacceptable. The avionic system must be informed about an integrity issue of a satellite within 6 seconds for non critical phases of flight and down to CAT I[1]. For a CAT II to

[1]Category I, II, III is a level of precision approach for aircraft corresponding to a low visibility

Typical operation	Accuracy horizontal 95%	Accuracy vertical 95%	Integrity	Time to alert	Continuity	Availability (%)
En-route	3.7 km	N/A	$1-1\times 10^{-7}/h$	5 min	$1-1\times 10^{-4}/h$ to $1-1\times 10^{-8}/h$	99 to 99.999
En-route, Terminal	0.74 km	N/A	$1-1\times 10^{-7}/h$	15 s	$1-1\times 10^{-4}/h$ to $1-1\times 10^{-8}/h$	99 to 99.999
Initial approach, intermediate approach, non-precision approach, departure	220 m	N/A	$1-1\times 10^{-7}/h$	10 s	$1-1\times 10^{-4}/h$ to $1-1\times 10^{-8}/h$	99 to 99.999
Approach operation with vertical guidance (APV-I)	16.0 m	20 m	$1-2\times 10^{-7}$ in any approach	10 s	$1-8\times 10^{-6}$ per 15 s	99 to 99.999
Approach operation with vertical guidance (APV-II)	16.0 m	8 m	$1-2\times 10^{-7}$ in any approach	6 s	$1-8\times 10^{-6}$ per 15 s	99 to 99.999
Category I precision approach	16.0 m	6 to 4 m	$1-2\times 10^{-7}$ in any approach	6 s	$1-8\times 10^{-6}$ per 15 s	99 to 99.999

Table 1.1.: Navigation requirements for the civil aviation [ICA06]

CAT III precision approach it is of 1 or 2 seconds (see [AIR01] for a definition and explanation of the approach categories).

Stand-alone GPS cannot provide enough reliability to be used for safety of life applications. Based on this statement, augmentation systems to mitigate navigation threats were unavoidable.

Historically, the Large Area Differential GPS able to cover the US Airspace was first envisaged beginning of the 90s. The resulting Wide Area Augmentation System (WAAS) program was implemented and put in service in 2003. This system provides additionally to satellite outage monitoring also differential corrections and resulting

condition (CAT 1 corresponds to a decision height of 200 ft. which is the altitude at which the pilot should see the runway, 100 ft for CAT II and 0 ft. for CAT III) For CAT III the pilot should activate the automatic landing system.

ranging error bounds enabling the user to calculate its protection levels, key concept that will be discussed later.

Additionally to WAAS, a Receiver Autonomous Integrity Monitoring (RAIM) has been suggested in the case WAAS is not available. In the multi-constellation configuration, RAIM provide a very cheap and efficient integrity monitoring especially when associated with an Integrity Support Message (ISM) providing a priori statistical parameters of the constellations in use. This ISM concept associated to an Advanced RAIM algorithm is an actual research focus. It seduces by the high level of performance potentially achieved by using multiple constellation based consistency check and only a very light ground infrastructure for the generation of the ISM message.

In order to serve other air spaces, a compatible system was developed in Europe and is called EGNOS (European Geostationary Navigation Overlay Service) and cover the ECAC (European Civil Aviation Conference) region and is extending towards the south to cover in a near future Africa and towards the east to ensure an overlap with Asian wide area augmentation system. A generic name defines each of these systems which is SBAS (Space Based Augmentation System).

This system provides an acceptable navigation service for all phases of flight except for precision approach under low visibility conditions.

For CAT II-III, it is necessary to provide a navigation solution with low vertical alert limit (10 m) with an integrity risk of 10^{-7} and a time to alarm of 1 to 2 seconds. This level of requirements requires a local augmentation system able to correct or monitor all possible errors that can drive to an unacceptable position error and to flag faulty ranges instantaneously. The first certified GBAS (Ground Based Augmentation System) has been installed in Bremen airport and provides CAT I performance also known as GAST-C (GBAS Approach Service Type C).

The challenge is to provide CAT III performance using a single frequency based GBAS also called GAST D (GBAS Approach Service Type D). This system based on dual smoothing method [NSP10] has been deeply investigated [BDLK10b, BDF$^+$10, BRMP11, RTC08, NSP10, HM07, HM09, SK12] and is in some areas (of a relatively quiet ionosphere) almost ready to be deployed and certified.

GAST-D operations are intended to be conducted using an automatic landing system. In this case, the whole GBAS Auto-land system need to fulfill the CS-AWO (Certifications Specifications for All Weather Operations) of a CAT III Auto-land System which have been derived from the specifications for the use of a CAT III ILS (Instrument Landing System)[JAA03].

In comparison with ILS, GBAS proposes a service volume and therefore more flexibility in the definition of the approach trajectory. The drawback of GBAS is that the error model depends on many different effects that are for most of them random in nature and not directly observable (ionosphere gradients, multipaths, interference). Furthermore the availability of the data communication link may be lost due

to signal interference or blocked by an other aircraft especially during the last phase of landing. All these effects may result in the loss of service continuity during the very last phase before landing. Therefore it is necessary to couple GBAS with an Inertial Navigation System (INS) in order to fill in the possible GBAS gaps with inertial navigation solution. To simplify the GNSS/INS fusion problem, the train application have been selected in this thesis.

The purpose of this thesis is to characterize the error sources of GNSS, that can have an hazardous impact in the positioning solution, to support and complement the research conducted by the navigation community for the use of satellite navigation for safety of life applications.

The thesis is organized as follows:

In the rest of this chapter we will set the problem tackled in this thesis and the most important definitions and notations

Chapter 2 and 3 provide the GNSS error characterization and a receiver based integrity monitoring without augmentations

Chapter 4 describes the work done in the augmentation scheme case with respect to error characterization and integrity monitoring.

Chapter 5 describes the integrity concept when using in addition to GNSS, inertial sensors. This Chapter includes not only the error propagation theory but also the inertial sensor error monitoring and a curvature change detector for trains.

A conclusion and future work recalling the main achievements of the thesis and the problems remaining and those new problems/opportunities generated by this work will close this thesis.

1.1. Safety Critical Applications and Challenges for Satellite Navigation

This thesis focuses on the safety critical applications for which navigation or positioning plays an important role.

We will focus mostly on aviation and for the last part of the thesis on rail application.

Aviation didn't wait for satellite navigation to enable aviation navigation. For all phases of flight, traditional navigation systems are already existing using navigation aids like DME (Distance Measuring Equipment), VOR (VHF Omnidirectional Range), NDB (Non Directional Beacon) and using airborne based navigation as for example barometric altimeter or a radar altimeter and for commercial aircraft use of INS. The previous equipment are foreseen for en route down to non precision approach. For precision approach, ILS is the technology enabler since already 40 years and provide safe approach and landing under low visibility conditions.

Why search for another solution if the aviation community has already all means of navigation that are needed?

Two main drawbacks of the traditional navigation aids limits its attractiveness: its expensive maintenance and operating costs and its incapacity of handling doubling air traffic without substantial increase of investment costs.

Satellite navigation not only provides solutions to the main drawbacks of the traditional navigation aids but it also serves unlimited users and provides with a unique receiver a navigation service from en route down to CAT III precision approach and landing.

What is the challenge then, if satellite based navigation is already established and integrated in almost all hand-held smart phones?

The challenge is to ensure integrity of the position solution. Global Navigation Satellite Systems are facing various types of ranging errors and each of these errors may introduce if not monitored unacceptable biases in the position. The problem is to bound these errors with a very low probability of missed detection (10^{-7}). Another problem concerns the weakness of the signal power, that makes them vulnerable to all kinds of radio frequency interference. This effect though is not an integrity issue as most of the time when the signal is experiencing radio frequency interference, the receiver loose the lock and makes the ranging source unavailable. But it affects the continuity of the service and therefore also its availability for a given phase of flight.

1.2. Problems Addressed in this Thesis

The first problem tackled by the thesis is the characterization of GNSS ranging errors which consists of setting up an inventory of possible errors that can impact position accuracy and the analysis of their magnitudes based on data collection from ground reference stations.

This thesis introduces the notion of instantaneous pseudo range error (IPRE) which is a statistical value obtained by comparing the pseudo range error after corrections with a reference post processed data including the accurate position of the receiver.

A statistical analysis is conducted to characterize different error sources and to study their impact in the positioning error. The analysis includes also the correlations between individual errors for fixed locations and their spatial correlations.

The IPRE is then applied to a receiver autonomous integrity monitoring algorithm for which a generalized test statistic is suggested that considers also correlations between pseudo ranges.

The second problem tackled in this thesis is the design of an ionosphere gradient monitor for GBAS based on a double difference carrier phase monitor architecture. Based on first investigations by Khanafseh ([KYP+10]), a further investigation and generalization has been conducted in this thesis.

The third problem tackled in this thesis is the hybridization of GNSS solutions with Inertial measurement unit to overcome the lack of continuity. In this part a stochastic error model of inertial sensors has been intensively investigated and a fault free error bound have been suggested. Furthermore a curvature detector based on 3 different combinations of inertial sensor information has been submitted to the European Patent Office.

1.3. Definitions and Notations

1.3.1. Definitions

The notions of Integrity, Continuity, Availability of the GNSS system are defined in [RTC06] and in [ICA06] and are recalled hereafter:

Integrity "A measure of the trust that can be placed in the correctness of the information supplied by the total system. Integrity includes the ability of a system to provide timely and valid warnings to the user (alerts)." extracted from [ICA06] page 3.59

Continuity "The continuity of a system is the ability of the total system (comprising all elements necessary to maintain aircraft position within the defined airspace) to perform its function without interruption during the intended operation. More specifically, continuity is the probability that the specified system performance will be maintained for the duration of a phase of operation, presuming that the system was available at the beginning of that phase of operation and was predicted to operate throughout the operation." extracted from [RTC06] page 13.

Availability "The availability of a navigation system is the ability of the system to provide the required function and performance at the initiation of the intended operation. Availability is an indication of the ability of the system to provide usable service within the specified coverage area. Signal availability is the percentage of time that navigational signals transmitted from external sources are available for use. Availability is a function of both the physical characteristics of the environment and the technical capabilities of the transmitter facilities." extracted from [RTC06] page 13.

Additionally to these 3 performance indicators are the following derived terms:

Horizontal Alert Limit "The Horizontal Alert Limit (HAL) is the radius of a circle in the horizontal plane (the local plane tangent to the WGS-84 ellipsoid), with its center being at the true position, that describes the region that is required to contain the indicated horizontal position with the required probability for a particular navigation mode (e.g. 10^{-7} per flight hour

for en route), assuming the probability of a GPS satellite integrity failure being included in the position solution is less than or equal to 10^{-4} per hour" extracted from [RTC06] page 14.

Vertical Alert Limit "The Vertical Alert Limit (VAL) is the half the length of a segment on the vertical axis (perpendicular to the horizontal plane of WGS-84 ellipsoid, with its center being at the true position, that describes the region that is required to contain the indicated vertical position with a probability of $1 - 2 \times 10^{-7}$ per approach, for a particular navigation mode, assuming the probability of a GPS satellite integrity failure being included in the position solution is less than or equal to 10^{-4} per hour." extracted from [RTC06] page 14.

Horizontal Protection Level$_{\text{Fault Detection}}$ "The Horizontal Protection Level$_{\text{Fault Detection}}$ (HPL_{FD}) is the radius of a circle in the horizontal plane (the local plane tangent to the WGS-84 ellipsoid), with its center being at the true position, that describes the region assured to contain the indicated horizontal position. It is a horizontal region where the missed alert and false alert requirements are met for the chosen set of satellites when autonomous fault detection is used. It is a function of the satellite and user geometry and the expected error characteristics: it is not affected by actual measurements. Its value is predictable given reasonable assumptions regarding the expected error characteristics." extracted from [RTC06] page 14.

Vertical Protection Level$_{\text{Fault Detection}}$ "The Vertical Protection Level$_{\text{Fault Detection}}$ (VPL_{FD}) is half the length of a segment on the vertical axis (perpendicular to the horizontal plane of WGS-84 ellipsoid), with its center being at the true position, that describes the region assured to contain the indicated vertical position when autonomous fault detection is used. It defines the vertical region where the missed alert and false alert requirements are met for the chosen set of satellites when autonomous fault detection is used." extracted from [RTC06] page 14.

Time-To-Alert "The maximum allowable time elapsed from the onset of the navigation system being out of tolerance until the equipment enunciates the alert." extracted from [ICA06] page 3.59

Attempts to provide mathematical definitions have been conducted and some of them are still in use today: Protection level concepts , Integrity Monitoring [ICA06, NSP10, RTC08, RTC06]. Taking into account that the threats are non stationary, an attempt to characterize these threats based on historical observations have been investigated [LPD+03, LPE+04, LPWE04, DB04, DBRP10, MBD09, MBJ+09, MJB08a, MJB+08b], evil wave forms [Phe01, PAE00, PMP+01] . Usually the characterization ends with the behavior of a threat taken independently from each other. A statistical approach of the problem has been conducted only to provide simple threat space, based on a worst case scenario for the ionosphere or in form of UERE

(User Equivalent Range Error) budgets [Kov00, Zap02, Bou98, WBH06].

1.3.2. Notations

We adopt the following notations: Matrices and vectors are represented in bold fonts. Matrices are represented using capital letters and vectors small letters. Upper scripts are related to satellites, lower scripts to user.

$\rho_u^{(s)}$ is the pseudo range observation relative to satellite s and user u. When using multiple frequencies, we distinguish the pseudo range observations between frequencies by adding the frequency in the index $\rho_{L1,u}^{(s)}$ for example for $L1$. We use the frequencies $L1$, $L2$ and $L5$ for GPS and $E1$, $E5a$ and $E5b$ for Galileo. When indexed by time, we use k and as discrete time variable, and t as continuous time variables. For example the pseudo range observation relative to Galileo satellite s and receiver u for the frequency $E1$ at epoch k is written $\rho_{E1,u,k}^{(s)}$. These notations can be simplified if there is no ambiguity (to avoid long expressions).

$\phi_u^{(s)}$ is the carrier phase observation and we use the same conventions as for the pseudo range observation.

λ_f is the carrier wave length related to the frequency f. When not specified it is related to the L1 frequency

$N_k^{(s)}$ is the integer number of phase cycles between receiver u and satellite s

$r_u^{(s)}$ is the geometric range between satellite s and receiver u

$\mathbf{r}^{(s)}$ is the position vector of the satellite s in ECEF (Earth Centered Earth Fixed) coordinate system

n is the number of visible satellites

n_C is the number of visible satellites from constellation C

$\mathbf{G}$ is the geometry matrix composed of the components of the unit line of sight vector in ENU (East North Up) coordinate system.

$\mathbf{W}$ is the weighting matrix of the pseudo range vector. Unless differently specified it is the inverse of the covariance matrix of the pseudo range vector.

$\Delta^2\phi_{ij}^{(kl)}$ is the double difference phase observation: $\Delta^2\phi_{ij}^{(kl)} = \left(\phi_i^{(k)} - \phi_i^{(l)}\right) - \left(\phi_j^{(k)} - \phi_j^{(l)}\right)$

$N_{ij}^{(kl)}$ is the double difference integer number of phase cycles between receiver i and satellite k. When needed to be specified, the frequency indicator of the carrier is associated to N

$\mathbf{b}_{ij}$ is the baseline vector between receiver i and receiver j

$\hat{X}$ is an estimate of the random variable X (after all possible corrections)

$\mathring{X}$ is the true value of X (usually not accessible but can be estimated thanks to post processed data)

ΔX is the error (or deviation to a reference) of the random variable X ($\Delta X = \hat{X} - \mathring{X}$)

We use the following mathematical notations:

$E[X]$ is the expectation of the random variable X with respect to the law of X

$V[X]$ is the variance of the random variable X with respect to the law of X.

$P[A]$ is the probability that an event A happens

$P[A|B]$ is the conditional probability that an event A happens under the condition that the event B happened.

$E[\Delta X|X]$ is the conditional expectation of the random variable ΔX conditioned by the occurrence of the event $X = x$

$\check{X} = X - E[X]$ for a random variable X

2. Characterization of Effects that Impact Position Accuracy

Position accuracy using multi-lateration can be improved in two ways: To improve the geometry of the ranging sources with respect to the user (geometry based improvement) and to improve the ranging performance by reducing the ranging errors thanks to a better modeling of residual errors (pseudo range based improvement).

An extensive analysis of pseudo range error impacting GPS has been done in [Kov00]. In this paper a very complete ranging error list with the estimated magnitude (table 4, in [Kov00]) have been proposed. But this budget is an averaged one. As we will see in the present chapter, the ranging errors are user location dependent for some of them and elevation dependent.

2.1. Introduction to GNSS (Example of GPS)[KLMP06]

The positioning problem using GNSS consists of determining the distance between multiple ranging sources (from visible satellites) and a receiver. The distance is based on the estimated signal propagation time (see Fig. 2.1). Prior to combining the ranging sources to form the system of n equations with 4 unknowns, it is necessary first to synchronize the ranging sources. Therefore each satellite is broadcasting together with its navigation message, an estimation of the satellite clock offset to the GNSS system time in form of a second order polynomial coefficients. The user clock offset to the GNSS system time is considered as the fourth unknown of the problem. The GNSS system time is an averaged time taking into account atomic clocks on satellites and on ground. The ground processing facility of GNSS determines simultaneously both the navigation message and the satellite clock correction parameters.

We call the pseudo range observation, the estimated code delay which is the cumulative output of the DLL (Delay Lock Loop) of the receiver. This is the elementary information to be used in the calculation of the position of the receiver.

Additionally to the pseudo range observation, the carrier phase observation is the cumulative output of the PLL (Phase Lock Loop) of the receiver. The phase observation is ambiguous due to the unknown number of full cycles from satellite to receiver.

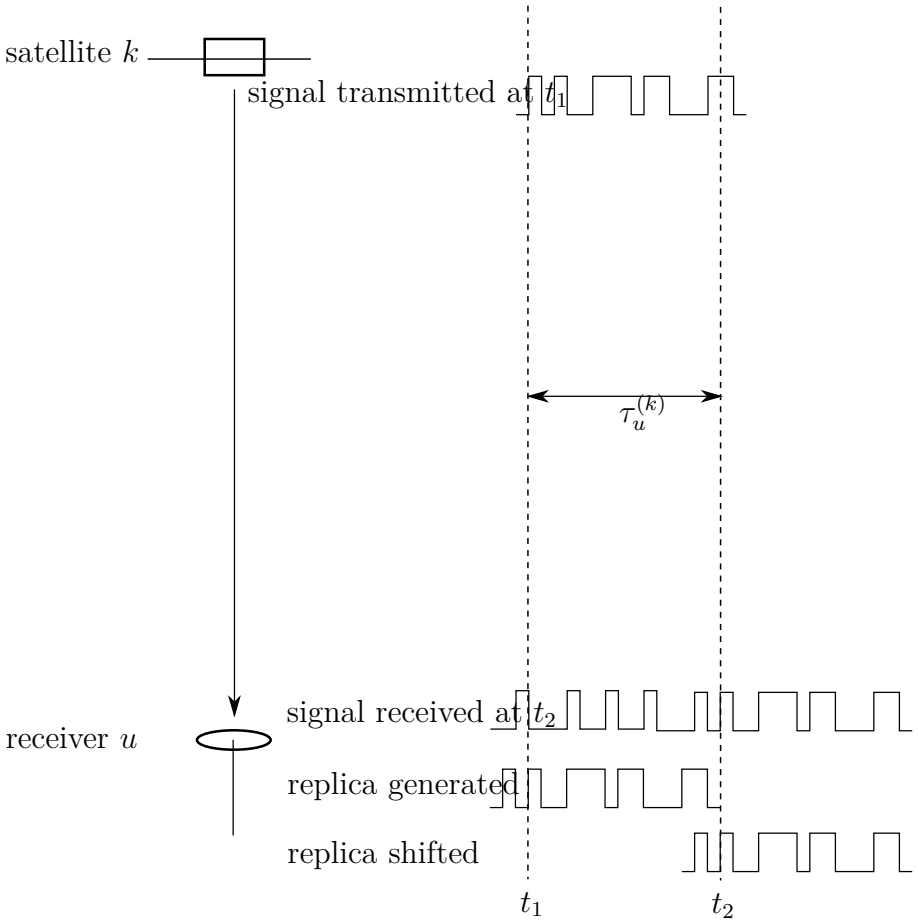

Figure 2.1.: GNSS ranging principle: The satellite is generating a signal that is transmitted at time t_1 and a receiver receives the signal at time t_2. The receiver generate a replica of the signal including the known PRN code and this replica is correlated with the received signal in order to determine $\tau_u^{(k)}$. At this stage, the time of transmission and the time of reception are calculated using 2 different non synchronized clocks, therefore the corresponding range is a "pseudorange" and not a "range". Therefore also it is necessary to have at least 4 satellites and not 3 as the receiver clock delay to GNSS system time is considered as the fourth unknown of the navigation and timing problem.

The geometry matrix is a linearized transfer matrix from the position of the user to the set of pseudo ranges. Each row represents the unit vector component from the user to a satellite. The last value of the row being set to 1 to map the user clock bias (to system time) in the pseudo range domain, considering that the estimated pseudo ranges are simultaneously calculated by the receiver.

2.2. Single Frequency Single Constellation Stand Alone Positioning Service

2.2.1. Pseudo Range Estimation

The observation equation is based on the propagation time of the signal from satellite k to receiver u.

Let's call τ_u^k this time, and let's consider the pseudo range calculation at received time t:

$$\rho_u^{(k)} = c\left(t_u\left(t\right) - t^{(k)}\left(t - \tau_u^k\right)\right) \tag{2.1}$$

where c is the speed of light, $t_i\left(t\right)$ is the reception time of the signal given by the receiver clock and $t^k\left(t - \tau_u^k\right)$ is the transmission time of the signal given by the satellite clock.

The times of transmission and the time of receptions are erroneous and are provided by different clocks that are not synchronized with each other.

We use the convention adopted in ([ME06], page 148-149):

$$t_u\left(t\right) = t + \delta t_u\left(t\right) \tag{2.2}$$

$$t^{(k)}\left(t\right) = t + \delta t^{(k)}\left(t\right) \tag{2.3}$$

where δt_u is the receiver clock off set to the GNSS time and $\delta t^{(k)}$ is the satellite clock offset to the GNSS time.

We rewrite equation 2.1:

$$\rho_u^{(k)} = c\left(\tau_u^{(k)} + \delta t_u\left(t\right) - \delta t^{(k)}\left(t - \tau_u^{(k)}\right)\right) \tag{2.4}$$

In this equation $\delta t^{(k)}$ is modeled as a second order polynomial whose coefficients are estimated by the GNSS ground processing facility and are broadcast in the navigation message. during $\tau_u^{(k)}$, the variations of $\delta t^{(k)}$ is negligible. Therefore we can write: $\delta t^{(k)}\left(t-\tau_u^{(k)}\right) \approx \delta t^{(k)}(t)$. We consider $\delta t^{(k)}$ to be a random variable, thus the approximation should be revisited. We consider that during a short period of time $\tau_u^{(k)}$, the process $\delta t^{(k)}$ is a continuous stationary process. Let's suggest a suitable model for $\tau_u^{(k)}$:

$$c\tau_u^{(k)} = \left(\mathbf{u}_u^{(k)}\right)^T \cdot \left(\mathbf{r}^{(k)}\left(t-\tau_u^{(k)}\right) - \mathbf{r}_u(t)\right) + I_u^{(k)} + T_u^{(k)} + \mathcal{E}_u^{(k)} \tag{2.5}$$

with

$\mathbf{u}_u^{(k)}$ being the unit vector from receiver u to satellite k

$\mathbf{r}^{(k)}\left(t-\tau_u^{(k)}\right)$being the position vector of satellite k at epoch $t-\tau_u^{(k)}$

$\mathbf{r}_u(t)$being the position vector of the receiver u at epoch t (three dimensional unknown of the problem)

$I_u^{(k)}$ the ionospheric delay in meter

$T_u^{(k)}$ the tropospheric delay in meter

$\mathcal{E}_u^{(k)}$ the residual pseudo ranging errors.

The complete model of the pseudo range observation can be written as follows:

$$\rho_u^{(k)} = \left(\mathbf{u}_u^{(k)}\right)^T \cdot \left(\mathbf{r}^{(k)}\left(t-\tau_u^{(k)}\right) - \mathbf{r}_u(t)\right) + c\left(\delta t_u - \delta t^{(k)}\right) + I_u^{(k)} + T_u^{(k)} + \mathcal{E}_u^{(k)} \tag{2.6}$$

For simplicity, we discard the time variable of the individual components.

Let assume that the position of the static user is well known thanks to a long time precise geodetic survey, $\tau_u^{(k)}$ represents the duration for the signal to travel from the satellite to the user antenna phase center. If the signal would propagate in the vacuum without any reflection, this duration would be exactly the geometric distance divided by the speed of light.

The user wants to have access to the geometric range (the first term of the right hand side of equation 2.6). For that the ionosphere delay, the troposphere delay and the ephemeris and satellite clock errors must be corrected.

The navigation message consists of all information the user need to get for improving the pseudo range performance and that are independent from the user location (each satellite sends the same message regardless where the user is located). The user calculates an estimation of the ionosphere delay using the Klobuchar model [Klo85, Klo96] whose parameters are broadcast in the navigation message. The satellite orbit estimation and the time corrections are the main part of the navigation message.

The troposphere delay is estimated using a model. No additional parameter is broadcast in the navigation message due to a strong variability of the troposphere conditions with time and space. Broadcasting a worldwide troposphere map with a high update rate would be bandwidth consuming. The performance benefit of such a processing facility is economically not justified.

The troposphere delay is compensated using a tropospheric model implemented in the receiver like for example the one defined in the MOPS (Minimum Operational Performance Standard) model [RTC06].

The position of the satellite at $t - \tau_u^{(k)}$ is estimated using the ephemeris information contained in the navigation message.

The receiver corrects as best as he can each error contribution, the remaining errors is called the instantaneous pseudo range error.

2.2.2. Determination of the Position Using the Pseudo Range Estimation

The user calculates its 3D position and the receiver clock bias using 4 satellites solving the following system of equations in $x_u, y_u, z_u, \delta t_u$:

$$\begin{aligned}
\rho_u^{(1)} &= \sqrt{\left(x^{(1)} - x_u\right)^2 + \left(y^{(1)} - y_u\right)^2 + \left(z^{(1)} - z_u\right)^2} + c\delta t_u \\
\rho_u^{(2)} &= \sqrt{\left(x^{(2)} - x_u\right)^2 + \left(y^{(2)} - y_u\right)^2 + \left(z^{(2)} - z_u\right)^2} + c\delta t_u \\
\rho_u^{(3)} &= \sqrt{\left(x^{(3)} - x_u\right)^2 + \left(y^{(3)} - y_u\right)^2 + \left(z^{(3)} - z_u\right)^2} + c\delta t_u \\
\rho_u^{(4)} &= \sqrt{\left(x^{(4)} - x_u\right)^2 + \left(y^{(4)} - y_u\right)^2 + \left(z^{(4)} - z_u\right)^2} + c\delta t_u
\end{aligned} \tag{2.7}$$

let's call $\mathbf{x}_u = \left(\mathbf{r}_u^T \; \delta t_u\right)^T$ the 4 dimensional unknown vector whose components are the user position (in 3 dimensions) and the receiver clock bias. This system of equations is non linear. Direct methods of solving such a system exists but for simplification we choose to linearize this system around an initial approximate of the user position and solve this system in an iterative way considering a first order development of the non linear equations. This iterative method is named Newton-Raphson method and is broadly used in practice. It appears that even when the initial estimate is chosen as the center of the earth, the method converge to an accurate solution after only 4 iterations.

Let's take an initial estimate of the user position called $\tilde{\mathbf{x}}_u$, then we express the unknown vector $\mathbf{x}_u = \tilde{\mathbf{x}}_u + D\mathbf{x}_u$ which is the estimate plus an increment to this estimate. Let's define $f_k\left(x_u, y_u, z_u, \delta t_u\right) = f_k\left(\mathbf{x}_u\right) = \sqrt{\left(x^{(k)} - x_u\right)^2 + \left(y^{(k)} - y_u\right)^2 + \left(z^{(k)} - z_u\right)^2} + c\delta t_u$.

We have $f_k(\mathbf{x}_u) = f_k(\tilde{\mathbf{x}}_u + D\mathbf{x}_u)$. As f_k is derivable and considering $D\mathbf{x}_u \ll \tilde{\mathbf{x}}_u$ we can write a first order development of f_k as follows:

$$f_k(\tilde{\mathbf{x}}_u + D\mathbf{x}_u) \approx f_k(\tilde{\mathbf{x}}_u) + \frac{\partial f_k(\tilde{\mathbf{x}}_u)}{\partial x_u} Dx_u + \frac{\partial f_k(\tilde{\mathbf{x}}_u)}{\partial y_u} Dy_u + \frac{\partial f_k(\tilde{\mathbf{x}}_u)}{\partial z_u} Dz_u + \frac{\partial f_k(\tilde{\mathbf{x}}_u)}{\partial \delta t_u} D\delta t_u \tag{2.8}$$

The estimated pseudo ranges are calculated based on the initial estimate $\tilde{\mathbf{x}}_u$:

$$\tilde{\rho}_u^{(k)} = f_k(\tilde{\mathbf{x}}_u) \tag{2.9}$$

So we have:

$$\rho_u^{(k)} = \tilde{\rho}_u^{(k)} - \frac{x^{(k)} - \hat{x}_u}{\|\mathbf{x}^{(k)} - \tilde{\mathbf{x}}_u\|} Dx_u - \frac{x^{(k)} - \hat{x}_u}{\|\mathbf{x}^{(k)} - \tilde{\mathbf{x}}_u\|} Dy_u - \frac{x^{(k)} - \hat{x}_u}{\|\mathbf{x}^{(k)} - \tilde{\mathbf{x}}_u\|} Dz_u + cD\delta t_u \tag{2.10}$$

Let's define $D\rho_u^{(k)} = \tilde{\rho}_u^{(k)} - \rho_u^{(k)}$, the above equation can be written as follows:

$$D\rho_u^{(k)} = \frac{x^{(k)} - \hat{x}_u}{\|\mathbf{x}^{(k)} - \tilde{\mathbf{x}}_u\|} Dx_u + \frac{y^{(k)} - \hat{y}_u}{\|\mathbf{x}^{(k)} - \tilde{\mathbf{x}}_u\|} Dy_u + \frac{z^{(k)} - \hat{z}_u}{\|\mathbf{x}^{(k)} - \tilde{\mathbf{x}}_u\|} Dz_u - cD\delta t_u \tag{2.11}$$

This equation is the linearized positioning equation. In the practice the linearization approximation works quite well whenever the user-satellite distance is much larger than the position increments after each iterations. Even taking the center of the earth as initialization point, we have observed that the linearization approximation enables the convergence to the user position solution.

If we take the example of 4 observations we have the following system of equations:

$$\underbrace{\begin{pmatrix} D\rho_u^{(1)} \\ D\rho_u^{(2)} \\ D\rho_u^{(3)} \\ D\rho_u^{(4)} \end{pmatrix}}_{D\rho} = \underbrace{\begin{pmatrix} \frac{x^{(1)}-\hat{x}_u}{\|\mathbf{x}^{(1)}-\tilde{\mathbf{x}}_u\|} & \frac{y^{(1)}-\hat{y}_u}{\|\mathbf{x}^{(1)}-\tilde{\mathbf{x}}_u\|} & \frac{z^{(1)}-\hat{z}_u}{\|\mathbf{x}^{(1)}-\tilde{\mathbf{x}}_u\|} & -1 \\ \frac{x^{(2)}-\hat{x}_u}{\|\mathbf{x}^{(2)}-\tilde{\mathbf{x}}_u\|} & \frac{y^{(2)}-\hat{y}_u}{\|\mathbf{x}^{(2)}-\tilde{\mathbf{x}}_u\|} & \frac{z^{(2)}-\hat{z}_u}{\|\mathbf{x}^{(2)}-\tilde{\mathbf{x}}_u\|} & -1 \\ \frac{x^{(3)}-\hat{x}_u}{\|\mathbf{x}^{(3)}-\tilde{\mathbf{x}}_u\|} & \frac{y^{(3)}-\hat{y}_u}{\|\mathbf{x}^{(3)}-\tilde{\mathbf{x}}_u\|} & \frac{z^{(3)}-\hat{z}_u}{\|\mathbf{x}^{(3)}-\tilde{\mathbf{x}}_u\|} & -1 \\ \frac{x^{(4)}-\hat{x}_u}{\|\mathbf{x}^{(4)}-\tilde{\mathbf{x}}_u\|} & \frac{y^{(4)}-\hat{y}_u}{\|\mathbf{x}^{(4)}-\tilde{\mathbf{x}}_u\|} & \frac{z^{(4)}-\hat{z}_u}{\|\mathbf{x}^{(4)}-\tilde{\mathbf{x}}_u\|} & -1 \end{pmatrix}}_{\mathbf{G}_{4\times 4}} \underbrace{\begin{pmatrix} Dx_u \\ Dx_u \\ Dx_u \\ cD\delta t_u \end{pmatrix}}_{D\mathbf{x}} \tag{2.12}$$

The new position increment is obtained by inverting this equation. This operation is allowed because $\mathbf{G}_{4\times 4}$ is invertible. The reason for that is because the unit vectors

to the four satellites are not colinear (the user is pointing to different directions to different satellites). We can therefore write:

$$D\mathbf{x} = \mathbf{G}_{4\times4}^{-1} D\rho \tag{2.13}$$

Equation 2.13 can be generalized for $n \geq 4$ observations by taking rather than $\mathbf{G}_{4\times4}^{-1}$ the pseudo inverse matrix defined by $\left(\mathbf{G}_{4\times n}^{T}\mathbf{G}_{n\times4}\right)^{-1}\mathbf{G}_{4\times n}^{T}$ and we obtain the following generalized linear position equation:

$$D\mathbf{x} = \left(\mathbf{G}_{4\times n}^{T}\mathbf{G}_{n\times4}\right)^{-1}\mathbf{G}_{4\times n}^{T} D\rho \tag{2.14}$$

In this equation, all observations have the same weight. It is often considered see for example [SC101]that the observations coming from satellites with low elevation angles are experiencing larger ranging errors than the observations coming from satellites with high elevation angle (due for example to larger multipath, receiver noise, tropospheric and ionospheric errors). This statement is validated in section sec. 2.2.10. In [SC101], an elevation model of error standard deviation function of the elevation angle is provided and for each observation (and each corresponding elevation angle), a measurement co-variance matrix is generated $\mathbf{C}_{n\times n}$. In order to improve the accuracy of 2.14, we introduce a weighting matrix to the measurements $D\rho$ taking into account the expected errors for each pseudo range, giving more weight to the measurements with high elevation than the measurements with low elevations. One possible weighting matrix can be defined as the inverse of the error co-variance of the measurements: $\mathbf{W}_{n\times n} = \mathbf{C}_{n\times n}^{-1}$. Equation 2.14 is transformed in its weighted form:

$$D\mathbf{x} = \left(\mathbf{G}_{4\times n}^{T}\mathbf{W}_{n\times n}\mathbf{G}_{n\times4}\right)^{-1}\mathbf{G}_{4\times n}^{T}\mathbf{W}_{n\times n} D\rho \tag{2.15}$$

2.2.2.1. From pseudo range error to position error

In the section above, the linearization applies to iteration increments, using the properties that the pseudo range increments $\|D\rho\|$ are very small compared to the full ranges $\|\rho\|$. If we replace the range increments with the deviations to the truth $\|\Delta\rho\|$, we have the same property. The magnitude in this case is defined with respect to the L_2 norm as we consider this time the deviations to the truth as being random variables. The relationship between the pseudo range deviations (error relative to a reference pseudo range) and the position deviations (error relative to a reference position) follows the same law described by Equation 2.15:

$$\Delta\mathbf{x} = \left(\mathbf{G}_{4\times n}^{T}\mathbf{W}_{n\times n}\mathbf{G}_{n\times4}\right)^{-1}\mathbf{G}_{4\times n}^{T}\mathbf{W}_{n\times n}\Delta\rho \tag{2.16}$$

This equation provides the error propagation rule from the pseudo range to the position domain.

2.2.2.2. The Dilution of Precision

Let us consider pseudo range and position errors as random vectors following a normal distribution. The variance of the position error can be expressed from 2.16 and considering $\mathbf{G}$ and $\mathbf{W}$ being deterministic matrices.

By definition the variance of $\Delta\mathbf{x}$ noted $V[\Delta\mathbf{x}]$is:

$$V[\Delta\mathbf{x}] = E\left[\Delta\mathbf{x}\Delta\mathbf{x}^T\right]$$

in this formulation we consider $\Delta\mathbf{x}$ as being a centered normal distributed vector. If not , we replace $\Delta\mathbf{x}$ by $\Delta\mathbf{x} - b$ with b being the mean vector of $\Delta\mathbf{x}$.

$$V[\Delta\mathbf{x}] = E\left[\left(\mathbf{G}^T\mathbf{W}\mathbf{G}\right)^{-1}\mathbf{G}^T\mathbf{W}\Delta\rho\left(\left(\mathbf{G}^T\mathbf{W}\mathbf{G}\right)^{-1}\mathbf{G}^T\mathbf{W}\Delta\rho\right)^T\right]$$

$$V[\Delta\mathbf{x}] = E\left[\left(\mathbf{G}^T\mathbf{W}\mathbf{G}\right)^{-1}\mathbf{G}^T\mathbf{W}\Delta\rho\Delta\rho^T\mathbf{W}\mathbf{G}\left(\mathbf{G}^T\mathbf{W}\mathbf{G}\right)^{-1}\right]$$

$\mathbf{G}$ and $\mathbf{W}$ being deterministic matrices we have:

$$V[\Delta\mathbf{x}] = \left(\mathbf{G}^T\mathbf{W}\mathbf{G}\right)^{-1}\mathbf{G}^T\mathbf{W}E\left[\Delta\rho\Delta\rho^T\right]\mathbf{W}\mathbf{G}\left(\mathbf{G}^T\mathbf{W}\mathbf{G}\right)^{-1}$$

We have $E\left[\Delta\rho\Delta\rho^T\right] = \mathbf{C} = \mathbf{W}^{-1}$, thus $V[\Delta\mathbf{x}]$ simplifies to:

$$V[\Delta\mathbf{x}] = \left(\mathbf{G}^T\mathbf{W}\mathbf{G}\right)^{-1} \tag{2.17}$$

We see that the variance of the position error vector (also the variance of the position vector) is defined as a geometric term and a term depending on the ranging performance.

We define the dilution of precision matrix by setting the weighting matrix $\mathbf{W}$ to the identity matrix:

$$\mathbf{Q} = \left(\mathbf{G}^T\mathbf{G}\right)^{-1}$$

Q depends only on the relative directions of the satellites with respect to a given user location and gives the information about the geometry of the satellites-user configuration.

We therefore can define the following dilution of precision terms. If we set $(q_{ij})_{i,j\in\{1,\ldots,4\}}$ the elements of **Q**, we have:

- Horizontal DOP or HDOP = $\sqrt{q_{11}+q_{22}}$
- Vertical DOP or VDOP = $\sqrt{q_{33}}$
- Position DOP or PDOP = $\sqrt{q_{11}+q_{22}+q_{33}}$
- Time DOP or TDOP = $\sqrt{q_{44}}$
- Geometric DOP or GDOP = $\sqrt{q_{11}+q_{22}+q_{33}+q_{44}}$

THE REST OF THIS CHAPTER REPRESENTS A PERSONAL CONTRIBUTION

2.2.3. The Concept of Instantaneous Pseudo Range Error (IPRE)

Let us represent a component x after receiver corrections by $\hat{x}$ (can be interpreted as the receiver estimate of x) and the "true" (unknown) value of x by $\mathring{x}$. Equation 2.6 can be written as follows:

$$\mathring{\rho}_u^{(k)} = \left(\mathring{\mathbf{u}}_u^{(k)}\right)^T \cdot \left(\mathring{\mathbf{r}}\left(t-\mathring{\tau}_u^{(k)}\right) - \mathring{\mathbf{r}}_u(t)\right) + c\left(\delta\mathring{t}_u - \delta\mathring{t}^{(k)}\right) + \mathring{I}_u^{(k)} + \mathring{T}_u^{(k)} \tag{2.18}$$

In the same way we have:

$$\hat{\rho}_u^{(k)} = \left(\hat{\mathbf{u}}_u^{(k)}\right)^T \cdot \left(\hat{\mathbf{r}}^{(k)}\left(t-\tau_u^{(k)}\right) - \hat{\mathbf{r}}_u(t)\right) + c\left(\delta\hat{t}_u - \delta\hat{t}^{(k)}\right) + \hat{I}_u^{(k)} + \hat{T}_u^{(k)} + \hat{\mathcal{E}}_u^{(k)} \tag{2.19}$$

In this equation we assume $\mathring{\mathcal{E}}_u^{(k)} = 0$.

We also assume that $\mathring{\mathbf{u}}_u^{(k)} \approx \hat{\mathbf{u}}_u^{(k)}$. By differentiating 2.19−2.18, and by setting for each component x, $\Delta x = \hat{x} - \mathring{x}$ we obtain:

$$\Delta\rho_u^{(k)} = \left(\mathbf{u}_u^{(k)}\right)^T \cdot \left(\Delta\mathbf{r}^{(k)}\left(t-\tau_u^{(k)}\right) - \Delta\mathbf{r}_u(t)\right) + c\left(\Delta\delta t_u - \Delta\delta t^{(k)}\right) + \Delta I_u^{(k)} + \Delta T_u^{(k)} + \Delta\mathcal{E}_u^{(k)} \tag{2.20}$$

We will call this equation the fundamental error equation. It has to be mentioned that $\Delta\mathbf{r}_u(t)$ and $\Delta\delta t_u$ are considered in the same way as the user position and user

clock offset to be the unknown of the positioning error problem (by linearity of the multi-lateration equations).

In this section, the convention used to define the error is as follows: $\Delta X = \widehat{X} - X =$ estimate-reference
The IPRE (instantaneous pseudo range error) $\Delta\rho_u^{(k)}(t)$ can be expressed in terms of individual errors based on the equation 2.19:

$$\mathrm{IPRE}(t) = -\mathrm{Clk}(t) + \mathrm{Eph}(t) + \mathrm{Iono}(t) + \mathrm{Trop}(t) + \mathrm{MN}(t) \tag{2.21}$$

with the following notations:

$\mathrm{Clk}(t) \triangleq c\Delta\delta t^{(k)}$ is the vector of instantaneous satellite clock error,

$\mathrm{Eph}(t) \triangleq \left(\mathbf{u}_u^{(k)}\right)^T \cdot \left(\Delta\mathbf{r}^{(k)}\left(t - \tau_u^{(k)}\right)\right)$ is the vector of instantaneous ephemeris error,

$\mathrm{Iono}(t) \triangleq \Delta I_u^{(k)}$ is the vector of instantaneous ionospheric error,

$\mathrm{Trop}(t) \triangleq \Delta T_u^{(k)}$ is the the vector of instantaneous tropospheric error,

$\mathrm{MN}(t) \triangleq \Delta\mathcal{E}_u^{(k)}$ is the vector of instantaneous receiver noise and multipath error

$\mathrm{IPRE}(t)$ is by definition the contribution of all these individual vector errors.

If necessary we can also group $\mathrm{Clk}(t)$ and $\mathrm{Eph}(t)$ into the ODTS (Orbit Determination and Time Synchronization Error). We set $\mathrm{ODTS}(t) \triangleq \mathrm{Eph}(t) - \mathrm{Clk}(t)$

$$UERE = \sqrt{\frac{1}{N}\sum_{k=1}^{N} IPRE_k^2} \tag{2.22}$$

The Root Mean Squared (RMS) over time of the IPRE is defined in this thesis as the User Equivalent Range Error (UERE). However, the exploration of the time varying IPRE rather than its RMS, as we will see later in this chapter gives a much deeper insight into the error behavior. This is made possible thanks to the temporal pseudo range observations of the satellites.

2.2.4. Methodology

The main problem is to determine the true quantities to be used as reference. This is a difficult problem to be solved in real time as usually GNSS is the most accurate navigation system. But if we replace true values by precise reference values, then one can just use a sort of reference measurement system and define the error as a deviation of estimated values from this reference:

Error(t)= Estimate(t) – Reference(t).

The idea here is to use as estimates the correction models implemented in the receiver or broadcasted by the satellites and as reference, the post processed IGS files[1]. Tab. 2.1 resumes the configuration used for our scenario:

Identifier	Full name	Estimation/ Correction	Reference	Sampling period of reference
Clk	Satellite clock delay	Navigation message	SP3 files	15 min
Eph	Ephemeris error	Navigation message	SP3 files	15 min
Iono	Residual ionosphere delay	Navigation message + Klobuchar model	IONEX files	2 hours
Trop	Residual troposphere delay	MOPS model [5] + Niell's mapping function [6]	SINEX files	2 hours
MN	Multipath and receiver noise error	No estimation	Results of the use of TEQC program [4]	Period of Observation files (30 sec)

Table 2.1.: Practical error component definition

Some explanation of Tab. 2.1 are necessary:

To determine the reference of each individual effect, post processed IGS products have been used: SP3 for precise orbit and clocks of GNSS satellites, IONEX for precise ionospheric maps, SINEX for precise tropospheric maps.

The receiver does not correct the multipath error using models. The multipath and receiver noise error are estimated using a linear combination of code and phase observations in L1 and L2.

Post-processed files except for MN are standard IGS-files taking into account a given time sampling period. We decided to take 15 minutes as the overall sampling period for our study. Thus for Iono and Trop we had to interpolate data to 15 minutes interval. We used for both linear interpolations, which means that short period effects (under 2 hours) for Iono and Trop are not representative because the ionospheric and tropospheric maps are provided with a sampling period of 2 hours (see Tab. 2.1).

[1]The International GNSS Service (IGS) is a network of worldwide distributed GNSS stations hosted by different institutions and agreeing to provide raw measurements to dedicated central processing facilities to produce different products in form of files as enumerated in this chapter.

2.2.5. Database

The work described in this section is my personal contribution.

One year observation files (2003) of 7 different IGS stations (see Tab. 2.2) have been used.

Code	City	Latitude in [°]	Longitude in [°]	Altitude in [m]
albh	Victoria (Canada)	48.390	236.51	32
lhas	Lhassa (China)	29.657	91.104	3622
mcm4	Ross Island (Antarctica)	-77.838	166.67	98
ntus	Singapore	1.3458	103.68	79
nya1	NY-Alesund (Norway)	78.930	11.865	84
obe2	Wessling (Germany)	48.1	11.3	651
pots	Potsdam (Germany)	52.38	13.07	174

Table 2.2.: Selected IGS station locations

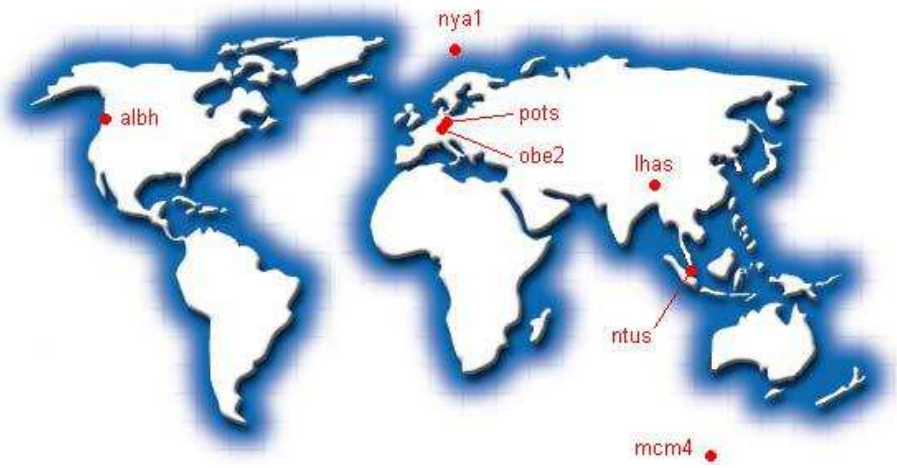

Figure 2.2.: Geographic locations of studied IGS stations

2.2.6. UERE Calculus

This graphic has been obtained by calculating for each station the RMS value of the IPRE series:

$$UERE = \sqrt{\frac{1}{N}\sum_{k=1}^{N} IPRE_k^2} \tag{2.23}$$

With N being the number of samples for which a valid $IPRE$ could be estimated.

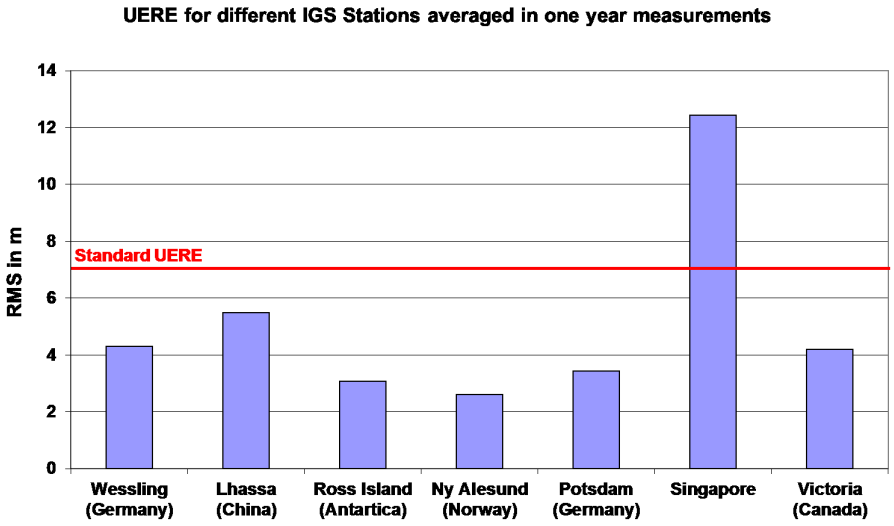

Figure 2.3.: UERE (RMS) for studied IGS stations and comparison with a standard UERE from [CCH+06] page 322.

From these first results (Fig. 2.3), we can see the high dependency of UERE with the location of the user. The UERE is four times bigger at Singapore than at NY-Alesund for a single frequency absolute positioning receiver. We will see in the next results that the magnitude of the UERE follows the dominant error here the Iono.

2.2.7. Temporal Analysis of Individual Range Errors

Based on measurements gathered from the seven IGS stations mentioned earlier, each individual error is estimated for each epoch.

Fig. 2.4, Fig. 2.5 and Fig. 2.6 represent the evolution in time of the individual and total error using measurements of a GNSS receiver located at Oberpfaffenhofen (near Munich) (station Obe2). Each satellite is represented using one color. If we look at the individual errors (Fig. 2.5 and Fig. 2.6) we can subdivide them in three categories:

1. The satellite dependent errors: Clk and Eph belong to this category. We can distinguish colors which emphasize a common behavior of these errors with respect to the corresponding satellite.
2. The environment dependent errors: Iono and Trop belong to this category: We can't distinguish colors but we can see a general behavior very well represented for Trop error with a sinusoidal effect of one year period.
3. The Gaussian like errors: NM belongs to that category: we can't distinguish colors, the distribution of data follow the same law. Only standard deviation seems to vary.

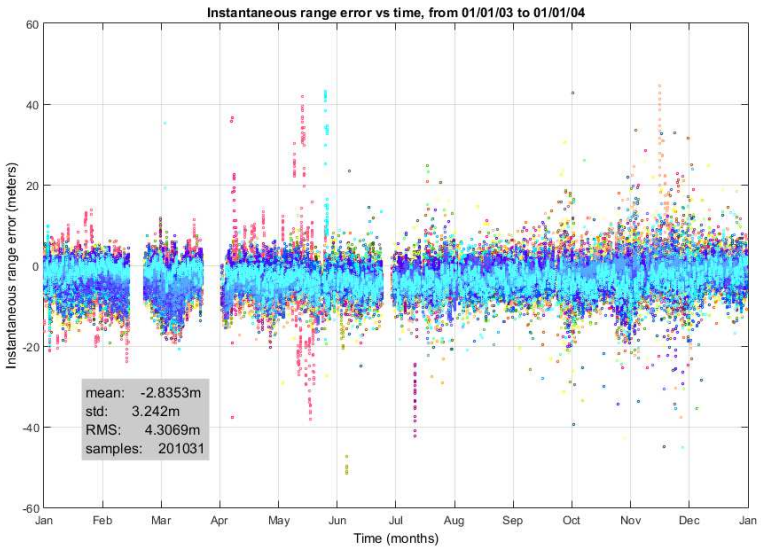

Figure 2.4.: IPRE (t) at Obe2 (Oberpfaffenhofen) based on one year measurements in 2003. "Mean" and "std" mean respectively the mean and the standard deviation of the considered data (IPRE), "RMS" means the root mean squared and "samples" means the number of samples considered to calculate the different statistical values.

Gaps in the data corresponds to a lack of observations for the corresponding epochs.

2.2.8. Correlations Between Individual Errors

From Instantaneous errors, we use the following formulas to calculated the correlation factors and we used for a good visual representation a gradual color scale.

The covariance between two random variables x and y is calculated as follows:

$$c_{xy} = \frac{1}{N} \sum_{i=1}^{N} (x_i - \bar{x})(y_i - \bar{y}) \tag{2.24}$$

with $\bar{x} = \frac{1}{N} \sum_{i=1}^{N} x_i$.

The correlation is calculated as follows:

$$r_{xy} = \frac{c_{xy}}{\sqrt{c_{xx}}\sqrt{c_{yy}}} \tag{2.25}$$

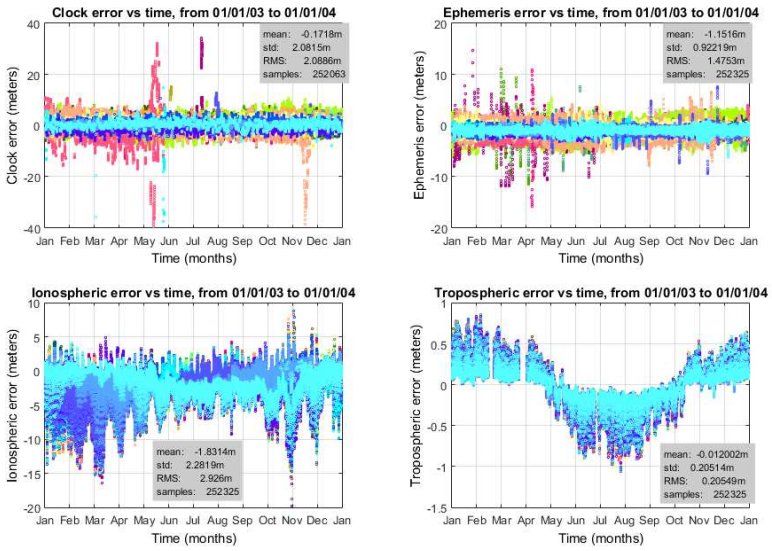

Figure 2.5.: $Clk\,(t)$,$Eph\,(t)$,$Iono\,(t)$ and $Trop\,(t)$ at Obe2 based on one year measurements in 2003

Fig. 2.7 shows a weak correlations between errors except for satellite clock and ephemeris errors for which a correlation of 30% can be observed. A physical correlation has to be excluded since satellite clock bias and orbital deviations of satellites are totally independent effects. If independent instruments could measure these two effects, we would certainly find no correlation. But this is unfortunately not the case, clock bias and perturbation factors of the satellite orbit are determined together and are in a relation through a system of equations. It is better to talk about a correlation generated by the processing facility on the ground.

2.2.9. Individual Error Correlations Between Stations

In the following, we consider instantaneous results calculated for each station. As for correlations between errors, we represent correlation factors using color scales. The correlation factor is calculated using data coming from the same satellite. This imposes that a satellite should be seen during a certain time by both considered stations. No results are available for (mcm4, nya1), (mcm4, pots), (mcm4, albh) and (mcm4, obe2) for which no satellites have been seen at the same time by these stations (which is understandable because of the location of mcm4 (Antarctica) compared to the locations of the other ones.

From these results, space correlations of errors are characterized. For Iono and Trop, regional effects can be seen. For Iono, albh shows negative correlations with other stations which can be explained simply by the diurnal effect of the ionosphere (see Tab. 2.3 and Fig. 2.2 for comparison of geographic situation of stations). For Trop,

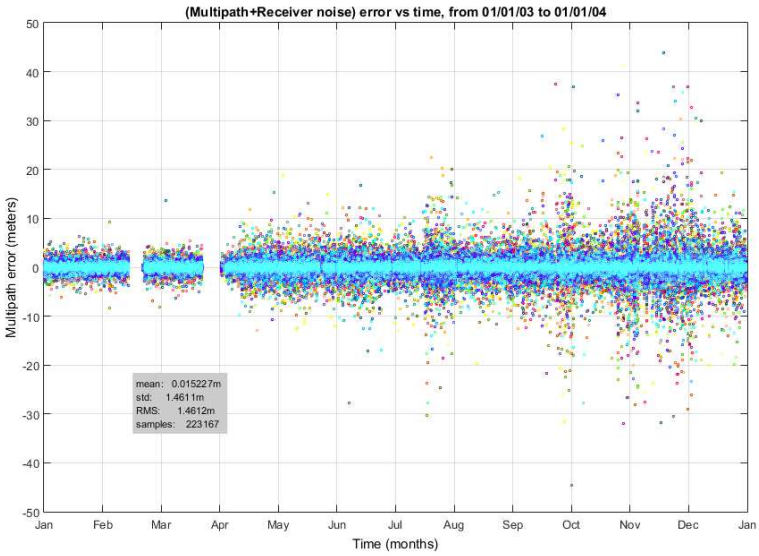

Figure 2.6.: $MN\,(t)$ at Obe2 based on one year measurements in 2003

the seasonal effect plays the main role here. North hemisphere and south hemisphere have inverted seasons and if we look at ntus, (south hemisphere), the correlations seem to be inverted with the stations situated in the northern hemisphere. As expected no correlations have been found for MN error. Clk error is totally correlated which is obvious because this error is a property of the considered satellite. We could expect the same for Eph error and it is surprisingly not so. In fact what we call ephemeris error is not the absolute orbit error of the satellite but it's projection to the line of sight which is the only component that plays a role in the pseudo-range error. Thus Eph will vary with the relative position of the station in comparison with the considered satellite and this will generate decorrelations.

2.2.10. Individual Errors Function of the Elevation Angle

The method used is always considering instantaneous errors. The elevation is obviously a characteristic parameter of the error. Intuitively, the propagation errors are going to be larger when the elevation angle is lower, due to the width of the atmosphere crossed by the signal. But to be able to make a statistical analysis, i.e. to calculate the bias (mean), the random (standard deviation) and the total (RMS), we need to use classes of elevation angles (El). Thus for each class (of 5°) it is possible to collect enough data to produce sufficient representativity.

Negative biases can be obtained because errors are in this work defined as deviation from a reference. A measurement can be below or above this reference and thus will influence the sign of the instantaneous error.

A mask angle of 10° has been used.

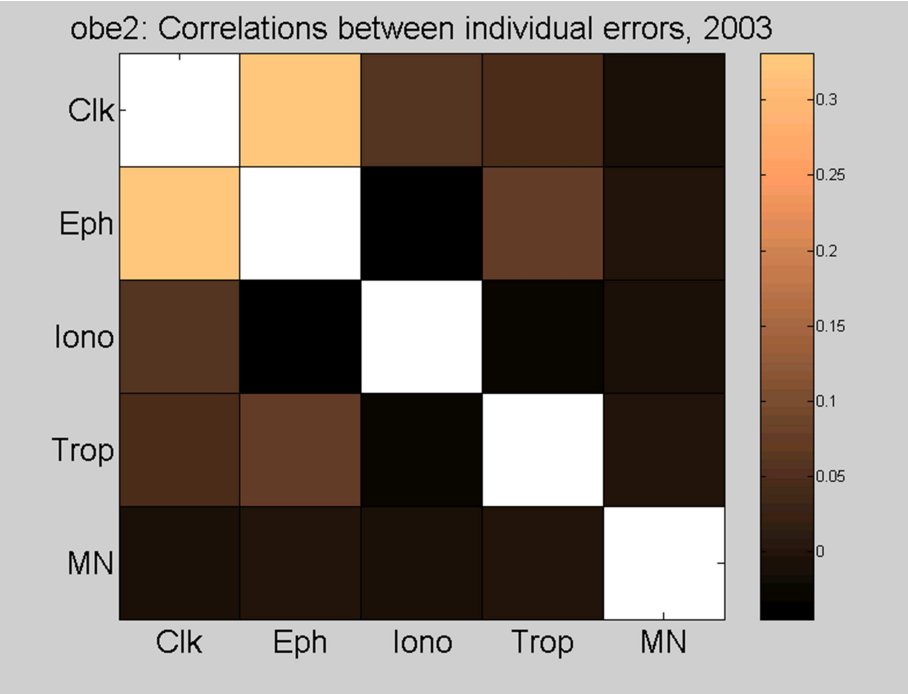

Figure 2.7.: Correlations between individual errors at Obe2

These evolutions are well known and do not differ from what has been generally accepted in the literature [Zap02, Kov00]. Nevertheless, if we focus on the behavior of the bias and the standard deviation part, we can see that these evolutions are not always the same: for Trop and MN, the bias is negligible which means that the dispersion constitutes the major part of the error. If we consider that biases correspond to deterministic errors, this means that Trop is well corrected using MOPS model at Obe2 when averaging one year measurements, and MN error can be considered almost totally random at Obe2 as the bias seems not to depend on the elevation angle. The random part shows a strong dependency with the elevation angle. As expected, variance of MN is higher for small elevation angle. The separation in noise and multipath errors as function of elevation angle will be interesting to analyze. Iono diagram shows that in single frequency receivers not using differential measurements, this error is the largest one. The deterministic part of the ionosphere delay (characterized by systematic errors or bias) is relatively high for any elevation angle and this characterizes the limitation of the Klobuchar model to correct the total ionospheric delay. Clk and Eph function of elevation angle have not been represented here because they obviously don't depend on the elevation angle.

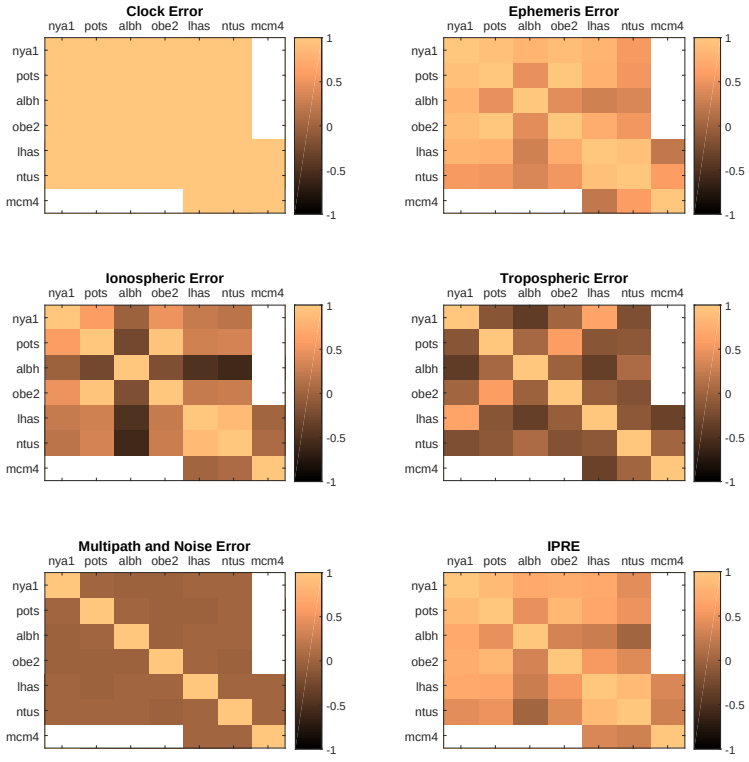

Figure 2.8.: Geographical correlations of errors based on one year measurement in 2003

2.2.11. Individual Error Contributions to Position Error

From the single user-satellite range error equation 2.20, that we recall hereafter, we have for each r:

we build up its vector form considering all pseudo range observations:

$$\mathbf{IPRE}_{\mathrm{u}} = \Delta\boldsymbol{\rho}_u = (\mathbf{u}_u)^T \cdot (\Delta\mathbf{r}\,(t - \boldsymbol{\tau}_u) - \Delta\mathbf{r}_u\,(t)) + c\,(\Delta\delta t_u - \Delta\boldsymbol{\delta t}) + \Delta\boldsymbol{I}_u + \Delta\boldsymbol{T}_u + \Delta\boldsymbol{\mathcal{E}}_u \tag{2.26}$$

where each row represents the pseudo range related to one satellite in view.

This is the multi-lateration error equation where the unknowns are the user position error $\Delta\mathbf{r}_u\,(t)$ and the user clock error $\Delta\delta t_u$.

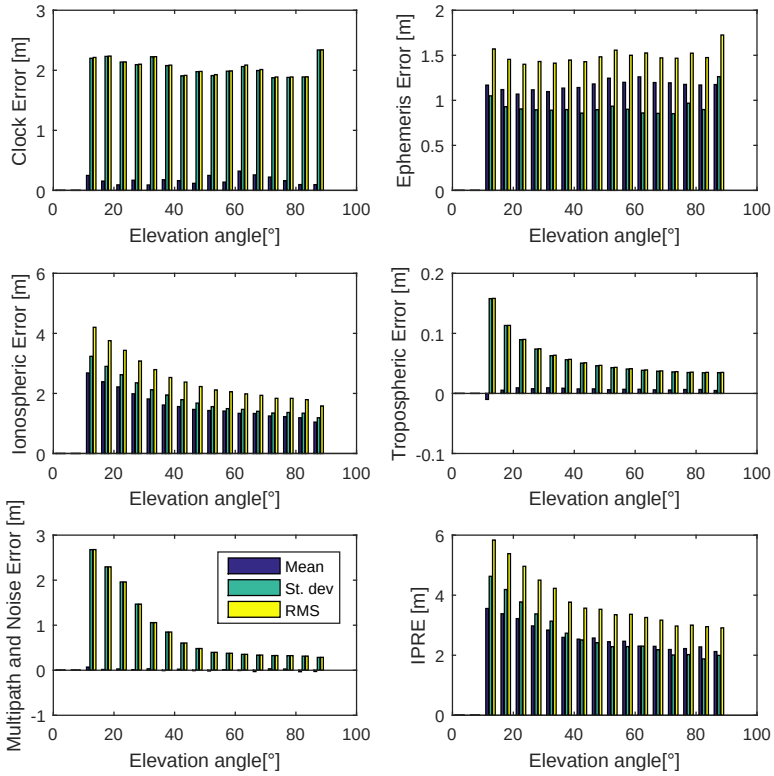

Figure 2.9.: Error sources vs. elevation angle at Obe2 station from 1.1.2003 to 31.12.2003

This linearized equation can also be written as follows:

$$\mathbf{IPRE}_{\mathrm{u}} = \Delta\boldsymbol{\rho}_u = \mathbf{G}\Delta\boldsymbol{x}_u \tag{2.27}$$

Where the vector $\Delta\boldsymbol{x}_u = \left(\Delta\mathbf{r}_u^T \; \Delta\delta t_u\right)^T$ is the error in the user position and in the user clock.

By taking the individual errors per satellite we can analyze their contribution to the position error.

The pseudo inverse equation is derived from Equation 2.16 and can be written as follows:

$$\Delta\boldsymbol{x}_u = \left(\mathbf{G}^T\mathbf{W}\mathbf{G}\right)^{-1}\mathbf{G}^T\mathbf{W}\cdot\mathbf{IPRE}_{\mathrm{u}} \tag{2.28}$$

Let's define $\mathbf{S} = \left(\mathbf{G}^T\mathbf{W}\mathbf{G}\right)^{-1}\mathbf{G}^T\mathbf{W}$, and let's decompose the $\mathbf{IPRE}_{\mathrm{u}}$ vector into its individual elements:

$$\Delta\boldsymbol{x}_u(t) = -\mathbf{S}\mathrm{Clk}(t) + \mathbf{S}\mathrm{Eph}(t) + \mathbf{S}\mathrm{Iono}(t) + \mathbf{S}\mathrm{Trop}(t) + \mathbf{S}\mathrm{MN}(t) \tag{2.29}$$

Each element represents its contribution to the user position error. For simplicity, we decided to work with raw data (without filtering the measurements) and all observations have been used. In parallel, we determined the 2σ ellipsoid envelops for each individual error and the IPRE as if the distribution would be Gaussian centered on corresponding biases. One of the objectives is to determine the deviation from normal distributions of real error distributions; another one is to determine qualitatively the dominant error.

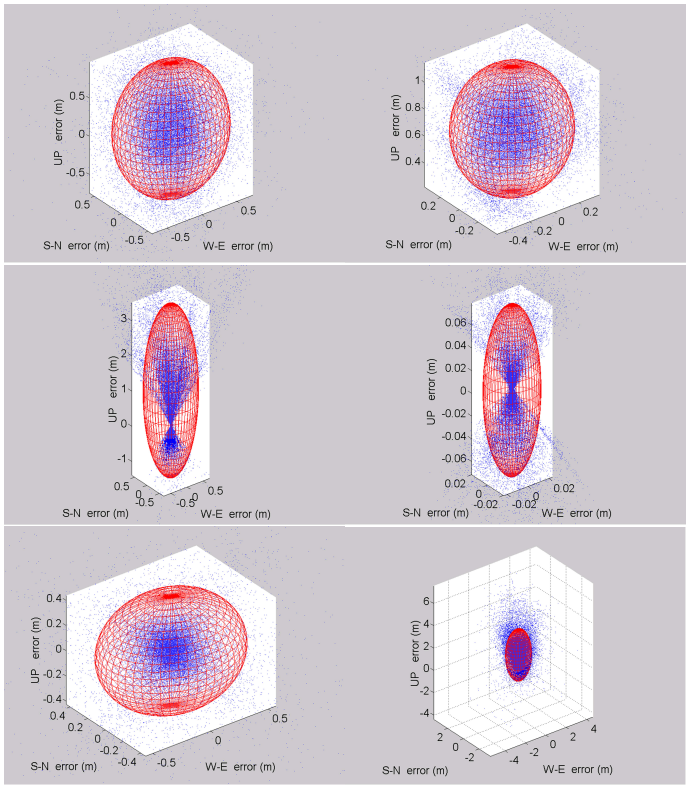

Figure 2.10.: Individual errors contribution to position error at Obe2 using one year of measurements in 2003 including a 2σ error envelope. From top left to bottom right we have the Clk, Eph, Iono, Trop, MN and IPRE projections to the position domain

Fig. 2.10 represents the position error a user of a single frequency receiver would experience if he stays at the location of the considered IGS station (here Obe2) during one year. In this figure, we can see the contribution of individual errors to the user position. For each error, we have determined statistically the standard deviation in

3 directions and the bias also in three directions. Then we set the ellipsoid centered at the bias and as semi major axes in 3 directions the corresponding standard deviation multiplied by 2 (2σ error envelope). We can see that some errors correspond very well to a 3D Gaussian distribution (Clk, Eph, and MN). For Trop and Iono, we can see another type of distribution and the ellipsoid can hardly represent such a distribution. To explain this phenomenon, we can say that considering satellites on visibility, the horizontal component of propagation error will be compensated because satellites are almost equivalently distributed in the horizontal plan. The vertical component cannot be compensated because the elevation angle of satellites is always positive (satellites are up in the sky not down on earth!). This is different to pseudo range level for which propagation errors are bigger for low elevation angle.

Now let's keep only the 2σ ellipsoid envelop for each error and let's analyze the results for each seven stations considered in our study.

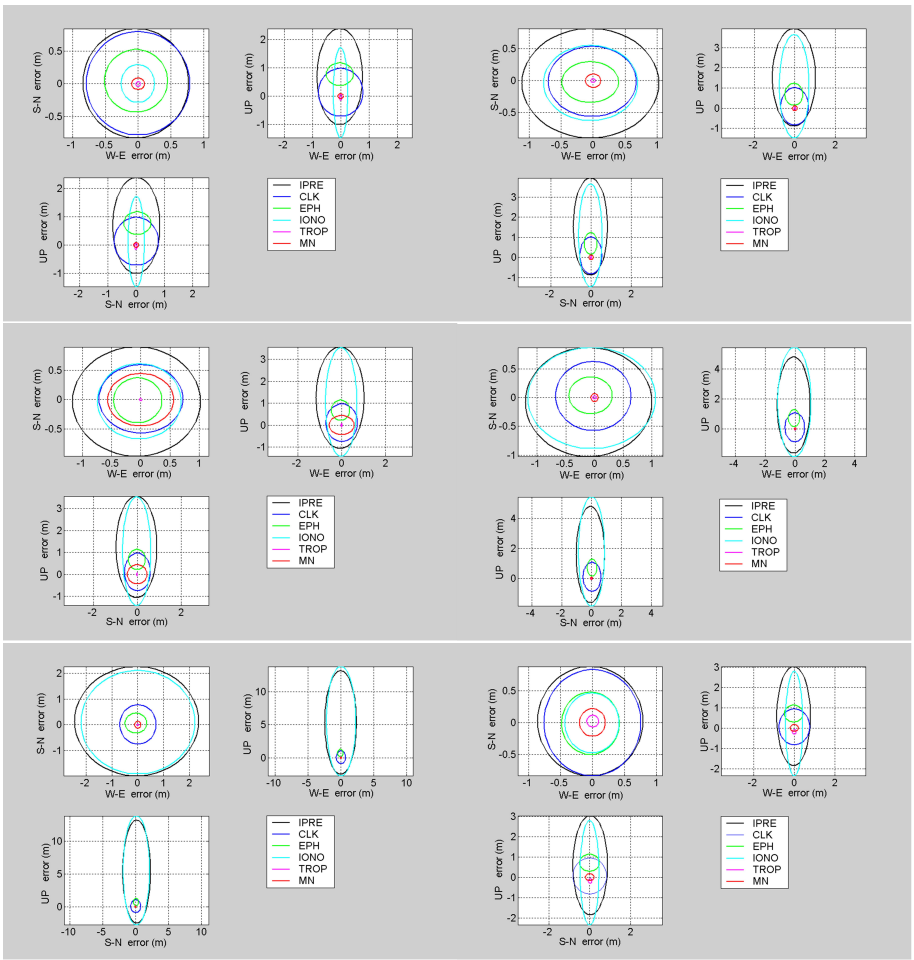

Figure 2.11.: Repartition of the 2σ error envelop using one year of measurements in 2003 for the selected IGS stations. From top left to bottom: Nya1, Albh, Obe2, Lhas, Ntus and Mcm4

Here we can see how the dominant error plays a role in the horizontal and vertical position error. In black we can see the IPRE contribution to position error which is simply the overall position error. The horizontal position error is mostly influenced by the Clk or the Iono error in regions where ionosphere activity is important. We don't see horizontally a privileged error direction (envelops are almost circular) but the vertical error, as expected, is larger than the horizontal one. The main conclusion of Fig. 2.11 is that the Iono error drives the vertical position error and the ephemeris error seems to experience a systematic bias in the vertical direction. This effect is investigated in the next section.

2.3. Single Frequency Dual Constellation Stand Alone Positioning Service

In this chapter we are going to investigate the accuracy of GPS, Galileo and the combination GPS+ Galileo. For GPS, we consider the estimation of errors (orbit determination and time synchronization error, ionospheric error, tropospheric error and multipath+noise error) by using real navigation messages and observations from IGS stations and taking post processing data as our reference . For that, we considered 3 IGS station locations: one in the equatorial region (ntus in Singapore) another one in a mid latitude region (obe2 in Germany) and a third one inside the polar circle (nya1 in Norway). The period of measurements used is the year 2003. The Galileo constellation has been simulated using foreseen UERE budget projected into the directions user to satellites and the foreseen almanacs. For both constellations, we used the same multipath scenario.
In a first part, we will define the field of our study and the scenario used for both GPS and Galileo constellations. In a second part, we recall the mathematical background providing the general formula to be applied and in a third part, we analyze the results obtained for GPS and Galileo separately and for the combined GPS + Galileo scenario. We conclude this section by recalling the important results we obtained.

2.3.1. Field of study

The year 2003 has been taken as our period of measurement for GPS. As written in the introduction, this concerns 3 IGS stations presented in Tab. 2.3. A single frequency absolute positioning receiver has been simulated. For GPS we used BPSK(1) in L1 and for Galileo the binary offset carrier BOC(1,1) modulation [BG02] for the same center frequency.

These locations have been used for both GPS and Galileo constellations.

Tab. 2.4 represents the assumptions used to produce the individual errors for GPS. By defining the error as a reference value minus the computed one with help of a

Country	Latitude	Longitude	Altitude	
[0.5ex] Germany	48.1^o	11.3^o	651m	
Norway	78.9^o	11.9^o	84m	
ntus	Singapore	1.35^o	104^o	79m
[1ex]				

Table 2.3.: IGS locations

Estimation	Reference	Sampling period
[0.5ex] RINEX NAV	SP3	15 min
Klobuchar	IONEX model	2 hours
MOPS model	SINEX	2 hours
–	Synthetic	15 min scenario

Table 2.4.: Measurement assumptions for GPS

correction model or using the parameters broadcasted by the satellites.
In Tab. 2.4 the notations are as defined in section sec. 2.2 where we set the combined Eph and Clk error as the Orbit Determination and Time Synchronization (ODTS) error.

Estimation	Reference	Sampling period
[0.5ex] –	Random Generator [Zap02]	15 min
Klobuchar	IONEX model	2 hours
MOPS	SINEX model	2 hours
–	Synthetic scenario	15 min

Table 2.5.: Simulation assumptions for Galileo

Tab. 2.5 represents the assumptions used to estimate the individual errors for Galileo. The main difference from the previous table is the ODTS random generation of errors using the UERE budget of [Zap02]. The synthetic scenario used for multipath is defined as follow. The reference propagation delay are those used for GPS but applied with the Galileo satellite positions. For better comparison we used the same

correction models in both GPS and Galileo. The synthetic scenario is common for GPS and Galileo and is defined in the next subsection.

The Galileo case

For that case we used the foreseen UERE Budget for Galileo [BPH05a] which considered an ODTS error standard deviation of 0.67 m. Because the bias level was not specified, we took a centered Gaussian distribution with 0.67 m of standard deviation as input for our random generator. This means that no regional effect of the user location has been taken into account in the ephemeris error.

Practically, for each satellite in view, we took a sample every 15 min; the time series is given in the Fig. 2.14. The blanks in the figures are intentionally put in order to fit with the lack of data for GPS. This is done in order to combine easily both sets of data for the combined GPS+Galileo scenario.

The use of a centered Gaussian noise model for ODTS is an approximation available for a relatively low sampling frequency. This is done in order to consider the ODTS error decorrelated from two consecutive time steps for a given satellite

		obe2	nya1	ntus
Bias (m)	GPS	-1.014	-1.040	-1.033
	GAL(*)	0.003	-0.002	-0.001
	COM(*)	-0.422	-0.455	-0.454
σ (m)	GPS	1.636	1.656	1.610
	GAL	0.671	0.671	0.670
	COM	1.278	1.310	1.285
RMS (m)	GPS	1.924	1.956	1.913
	GAL	0.671	0.671	0.670
	COM	1.346	1.387	1.363

(*) GAL for Galileo and COM for combined GPS+Galileo

Table 2.6.: Statistical results for ODTS error at pseudo range level

Tab. 2.6 shows small differences in bias and standard deviation for GPS due to the ephemeris error because of a short regional dependency due to the geometry of the constellation. The ephemeris error is the satellite orbit error projected into the direction of user to satellite. It has not been taken into account for Galileo because we did not want to decompose the ODTS error into more fundamental errors. But for that some questions have still to be solved like the level of the deterministic part of the error and the stochastic part. The low level of ODTS error for Galileo is of course

one point that should be verified. To be fair in our comparison, one should take into account the foreseen UERE budget for GPS when Galileo will be available that means one should consider a comparison with the modernized GPS performances. The aim of our study is to introduce the concept of IPRE in both measurements and simulation, as Galileo measurements are not available yet, we chose to use the GPS measurements to prove the efficiency of this approach. In Fig. 2.12 we can see the probability density function of the ODTS error with respect to the level of accuracy of GPS based on measurements and Galileo based on simulations.

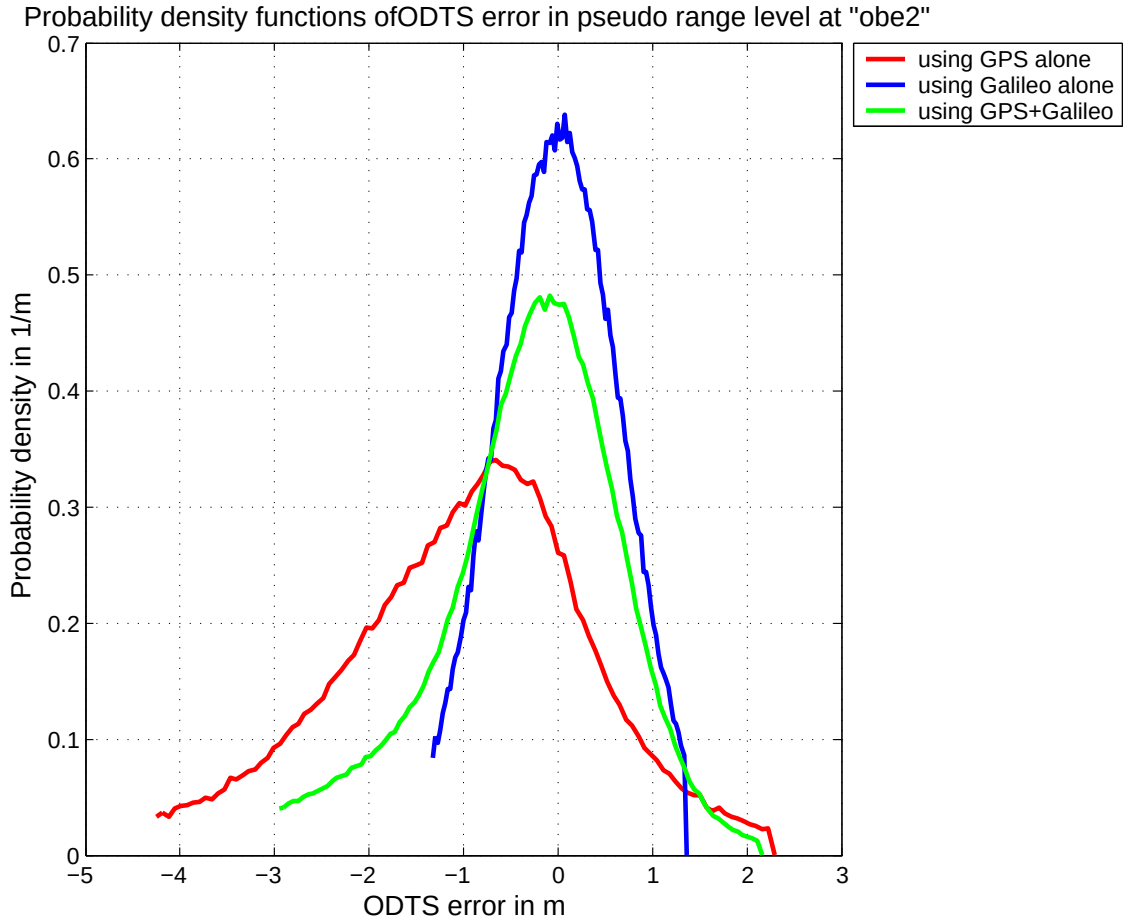

Figure 2.12.: Probability densities of ODTS error

2.3.2. The multipath synthetic scenario

We chose to simulate the multipath and receiver noise error for both GPS and Galileo constellation in order to compare both constellations using the same base of comparison. As the multipath environment of IGS stations is difficult to model, we used a synthetic environment as follow. The multipath scenario chosen is a single

ground reflection echo with an attenuation of -3 dB with respect to the line of sight signal.

A choke ring antenna [Fuh01] has been used with different right and left hand circular polarization gain, assuming that the reflected signal is 100% left hand polarized. In Fig. 2.13 is represented schematically the multipath scenario. In this figure LOS is the line of sight signal, El is the elevation angle and h is the height of the receiver antenna with respect to the ground (h=2 m in our scenario). The echo delay is given by $2h\sin(El)$.

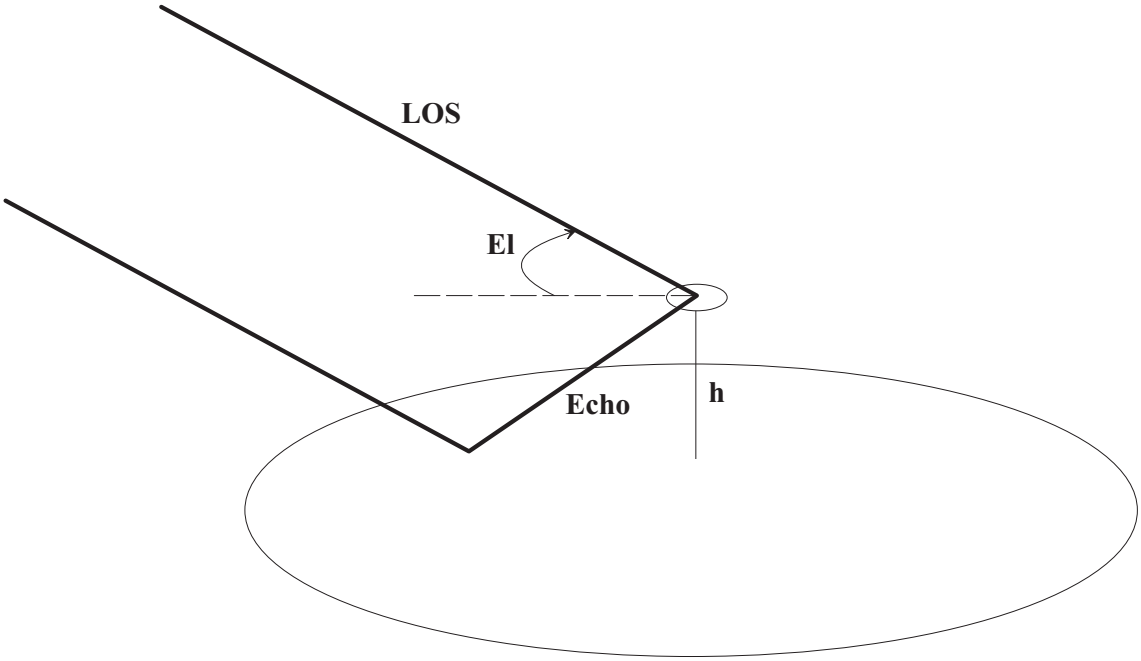

Figure 2.13.: Multipath scenario for GPS and Galileo

Given the level of C/N0 for both GPS [PSJ96] and Galileo [CZ02] [HGI+02] it is possible to provide the input for a multipath and receiver noise generator assuming the use of an example of receiver parameters (receiver bandwidth of 20 MHz and a correlator spacing of 0.1 chip) (see Tab. 2.7).

2.3.3. Mathematical model

In this section we use the same method and the same notations as described in sec. 2.2.

The IPRE(t)vector is based on the pseudo range errors from GPS observations, Galileo observation and the concatenation of GPS and Galileo observations in the combined scenario.

G is in the case of the combined scenario a 5×5 matrix. The fifth column corresponds to the receiver clock bias with respect to the Galileo system time whose values are

Elevation angle [°]	Relative power of Echo [dB]	Delay of echo [ns]	GPS BPSK(1) C/N0 [dBHz]	Galileo BOC(1,1) C/N0 [dBHz]
90^o	-32.57	13.34	48.20	53.20
85^o	-32.57	13.29	48.20	53.20
80^o	-32.28	13.14	47.91	52.91
75^o	-31.31	12.89	47.80	52.80
70^o	-31.82	12.54	47.45	52.45
65^o	-29.42	12.09	47.05	52.05
60^o	-28.27	11.55	46.48	51.48
55^o	-29.24	10.93	45.91	50.91
50^o	-28.27	10.22	44.93	49.93
45^o	-24.54	9.43	43.73	48.73
40^o	-24.60	8.58	43.10	48.10
35^o	-22.82	7.65	41.43	46.43
30^o	-22.99	6.67	40.46	45.46
25^o	-22.65	5.64	39.14	44.14
20^o	-19.04	4.56	37.94	42.94
15^o	-18.69	3.45	36.27	41.27
10^o	-16.28	2.32	35.07	40.07
5^o	-13.59	1.16	33.52	38.52

Table 2.7.: Parameters of the multipath scenario

set to 0 for GPS related rows and to 1 for Galileo related rows. The fourth column is as previously defined with 0 for the Galileo related rows and 1 for the GPS related raws. Therefore we consider for the combined scenario a 5D unknown vector (3 for the spatial localization, the receiver clock bias with respect to GPS system time and the receiver clock bias with respect to Galileo system time). We could keep the unknown to 4 if we use the GPS Galileo Time Offset (GGTO).

In this chapter we don't weight the measurements so we consider $\mathbf{W}$ as the identity matrix and therefore will drop out of the position equations.

We consider the minimized GDOP method to select the 4 or 5 observations among all satellites and then to perform the propagation of pseudo range error to the position domain. The definition of GDOP is given in sec. 2.2.

The selection method is such that we test all combinations of 4 or 5 observations among all satellites in view that minimize the trace of the matrix $\mathbf{Q}$. Let us call

$\mathbf{G}^*$ the 4×4 or the 5×5 optimal geometry matrix, we have:

$$\mathbf{G}^* = \underset{\mathbf{G}}{\operatorname{argmin}} \left\{ \operatorname{tr} \left(\left(\mathbf{G}^T \mathbf{G} \right)^{-1} \right) \right\} \tag{2.30}$$

The position error equation is then

$$\Delta \boldsymbol{x}_u (t) = \mathbf{G}^{*-1} \mathrm{IPRE} (t) = \mathbf{G}^{*-1} \mathrm{ODTS} (t) + \mathbf{G}^{*-1} \mathrm{Iono} (t) + \mathbf{G}^{*-1} \mathrm{Trop} (t) + \mathbf{G}^{*-1} \mathrm{MN} (t) \tag{2.31}$$

2.3.4. The errors at pseudo range level

In this section we present the results obtained for GPS and Galileo for each type of error. The statistical results give also the results for the combined GPS+Galileo which is obtained by fusion of both sets of data. All these procedures have been implemented in NAVSIM, the End to End navigation simulator of DLR [FES+00]. The possibilities given by this new functionality to proceed to an error calculation by using "reference - correction" from both measurements or from simulations using models or by using a random generator of noise, offers the possibility to simulate the performances of a given application or a navigation system using the concept of IPRE as presented in sec. 2.2. Thanks to the generation of time series of individual errors, it is possible for a given constellation to proceed to an error calculation at the pseudo range level and as will be developed in the next section at the position level.

2.3.4.1. The ODTS error

Except for multipath and receiver noise error, the methodology used is the same as in [BPH05b]. we chose to present the ODTS error at Oberpfaffenhoffen near Munich (obe2), the results obtained from the other stations are similar and differs only by the direction of projection to the line of sight from satellite to user location.

In Fig. 2.14 we plot the ODTS error for each satellite for GPS and Galileo. Each satellite is represented by a specific color. Taken independently, these satellites experience independent ODTS errors. Some of the GPS satellites are experiencing biases of more than 1 meter which has been observed also for the 2 other stations. These biases due to the fact that the navigation message is using the phase center of the sending antenna as the origin of the Keplarian parameters and the precise orbits for some of the satellites are using the center of gravity of the satellite.

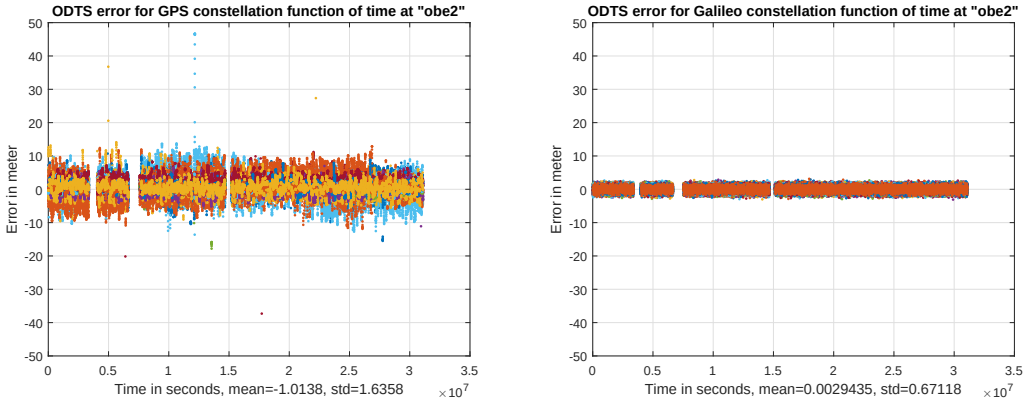

Figure 2.14.: ODTS error vs. time for GPS and Galileo

2.3.4.2. The ionospheric error

In this subsection, we represented the ionospheric error for the station near the equator (ntus in Singapore). This choice is motivated by the high level of ionospheric activity in that region. This causes the ionospheric error to be the dominant effect affecting the pseudo range performance. As observed in sec. 2.2, the IPRE distribution is driven by the ionospheric error.

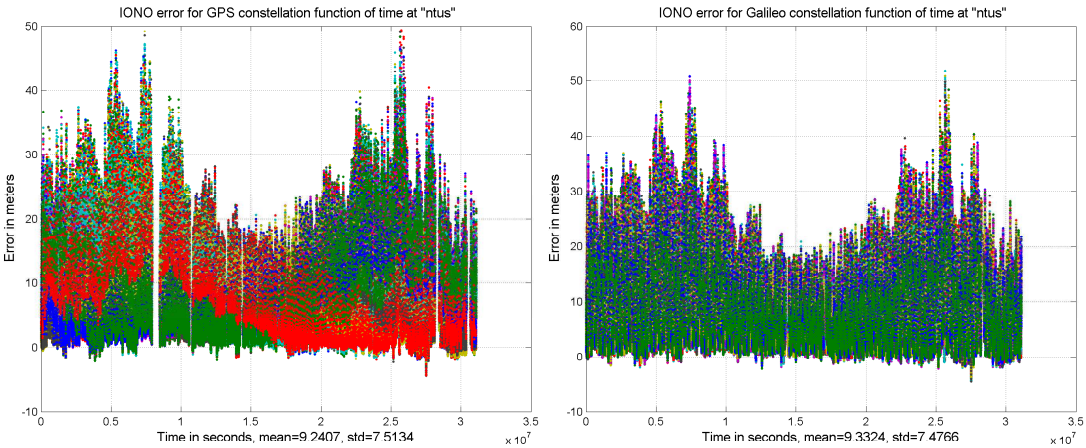

Figure 2.15.: Ionospheric error vs. time for GPS and Galileo

Fig. 2.15 represents the ionospheric error after correction with the Klobuchar model. The magnitude of error is here very large and for both the bias and the standard deviation.

As the same conditions have been taken for GPS and Galileo satellites, the same type of results should be obtained. The difference comes from the different number of satellites in the constellations (30 for Galileo and 24 for GPS) and for the different

line of sight projections (the distribution of satellites in the sky is not the same for GPS and for Galileo).

The ionospheric error for Galileo satellites is the error that the pseudo ranges would have experienced if the constellation would have been available in 2003 at ntus (Singapore). We recall that the ionospheric error could have been corrected using another correction model (NeQuick) but the Klobuchar model has been chosen for comparison purposes. The results are quite similar with what has been obtained for GPS. This is as expected because this effect impacts the GPS signals in the same way as it impacts the Galileo signals. The only difference is due to the geometry of the constellation i.e. the distribution of elevation angles (the model does not take into account the impact of the azimuth angle).

		obe2	nya1	ntus
Bias (m)	GPS	1.752	0.310	9.241
	GAL	1.760	0.233	9.332
	COM	1.756	0.267	9.292
σ (m)	GPS	2.403	1.184	7.513
	GAL	2.413	1.233	7.477
	COM	2.409	1.212	7.493
RMS (m)	GPS	2.974	1.224	11.910
	GAL	2.987	1.254	11.958
	COM	2.981	1.241	11.937

Table 2.8.: Statistical results for ionospheric error at pseudo range level

An important disparity of results can be observed in Tab. 2.8. The main remark concerning this error source is that it is not a constellation dependent error. Only a slight difference can be observed in high latitude. For that a possible explanation is the relatively low elevation angle of the observed satellite. The consequence is the higher sensitivity of the error to the elevation angle due to the mapping function used. The consequence is that the slightest difference in the mean elevation angle can produce a higher deviation of the magnitude of the error both at bias and at standard deviation level. Fig. 2.16 shows a superimposition of probability density functions

2.3.4.3. The tropospheric error

For both constellations, we used the SINEX files from IGS stations and as correction model the MOPS model associated with the Niell's mapping function [Nie96]

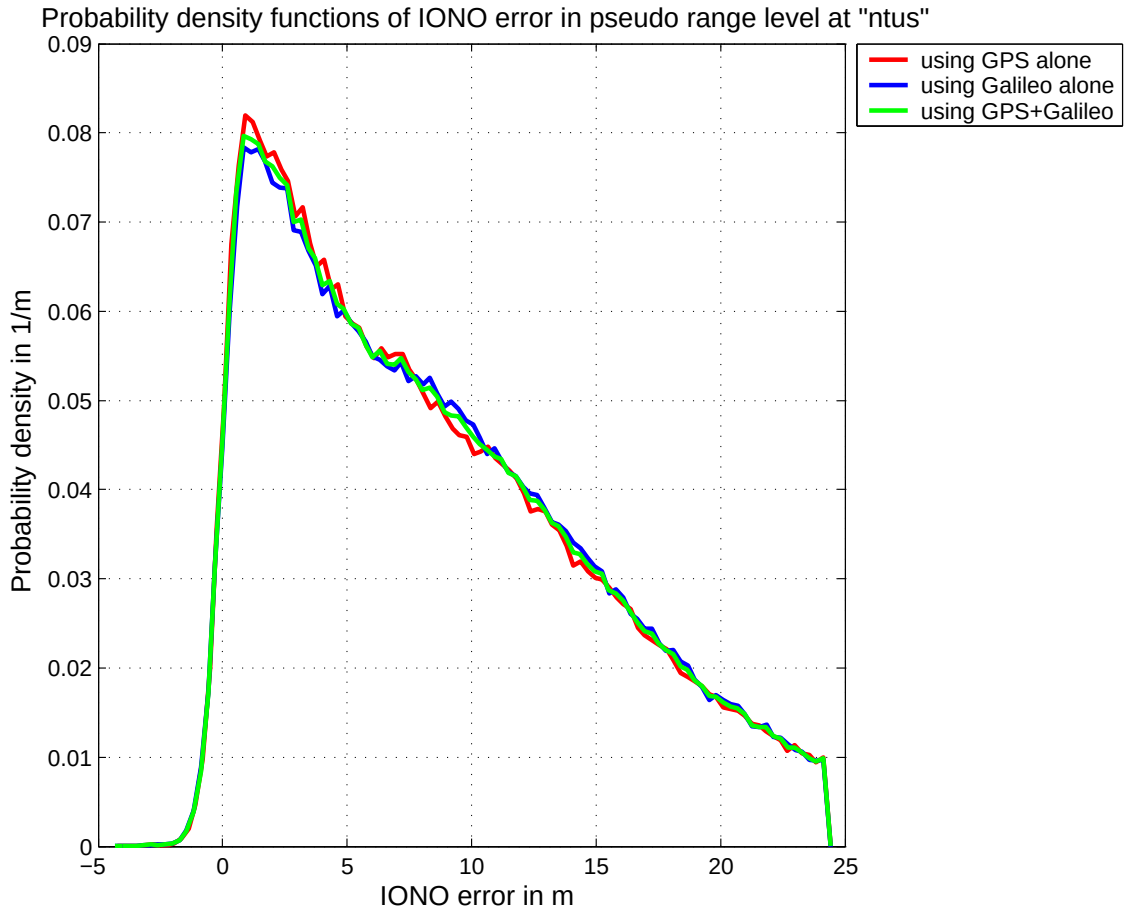

Figure 2.16.: Probability densities of ionospheric error

to transform the azimuth tropospheric delay to the slant delay. In this subsection, we use the results of nya1 for the graphical representation. The same comment as for the ionospheric delay can be made.

Fig. 2.17 represents the tropospheric error for the GPS and Galileo constellations. One can easily see the impact of the elevation angle in the magnitude of the error. The upper bound corresponds to the envelop of tropospheric error for maximal elevation of satellites. This is for nya1 not necessary the zenith because of the inclination of orbits of satellites (56^o for Galileo).

The tropospheric environment is taken the same for both constellations and only the differences in geometry plays a role.

Tab. 2.9 gives the statistical results for the tropospheric error for each configuration and each IGS station. The level of this error seems to be quite low in comparison with the ionospheric error. The correction model associated with the Neill's mapping function is fitting the real tropospheric delay well. Even for ntus (Singapore) where

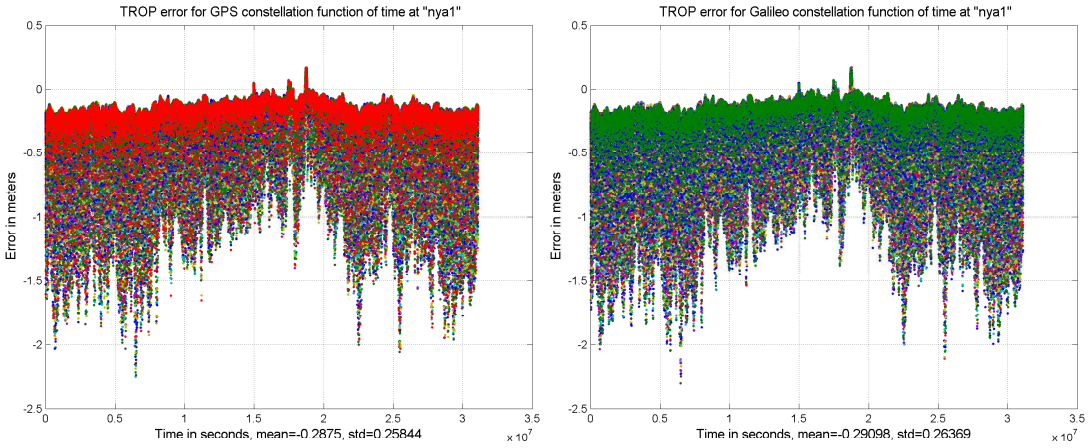

Figure 2.17.: Tropospheric error vs. time for GPS and Galileo

		obe2	nya1	ntus
Bias (m)	GPS	-0.314	-0.288	-0.633
	GAL	-0.336	-0.291	-0.640
	COM	-0.327	-0.289	-0.637
σ (m)	GPS	0.333	0.258	0.512
	GAL	0.354	0.264	0.517
	COM	0.345	0.261	0.514
RMS (m)	GPS	0.458	0.387	0.814
	GAL	0.488	0.393	0.822
	COM	0.475	0.390	0.819

Table 2.9.: Statistical results for tropospheric error at pseudo range level

the partial water vapor pressure can reach high levels and thus can generate a wet tropospheric delay difficult to model, the level of bias and standard deviation of the errors stay in an acceptable range in comparison with the ionospheric error.

It is interesting to see from Fig. 2.18 the perfect superimposition of the probability density functions. The elevation angle distributions for the 3 configurations has even less influence than for the ionospheric error. To resume, the propagation middle impacts the constellations in the same way. Unless using different correction models, the ionospheric and the tropospheric errors have for both constellations and thus for the combined GPS+ Galileo the same magnitude.

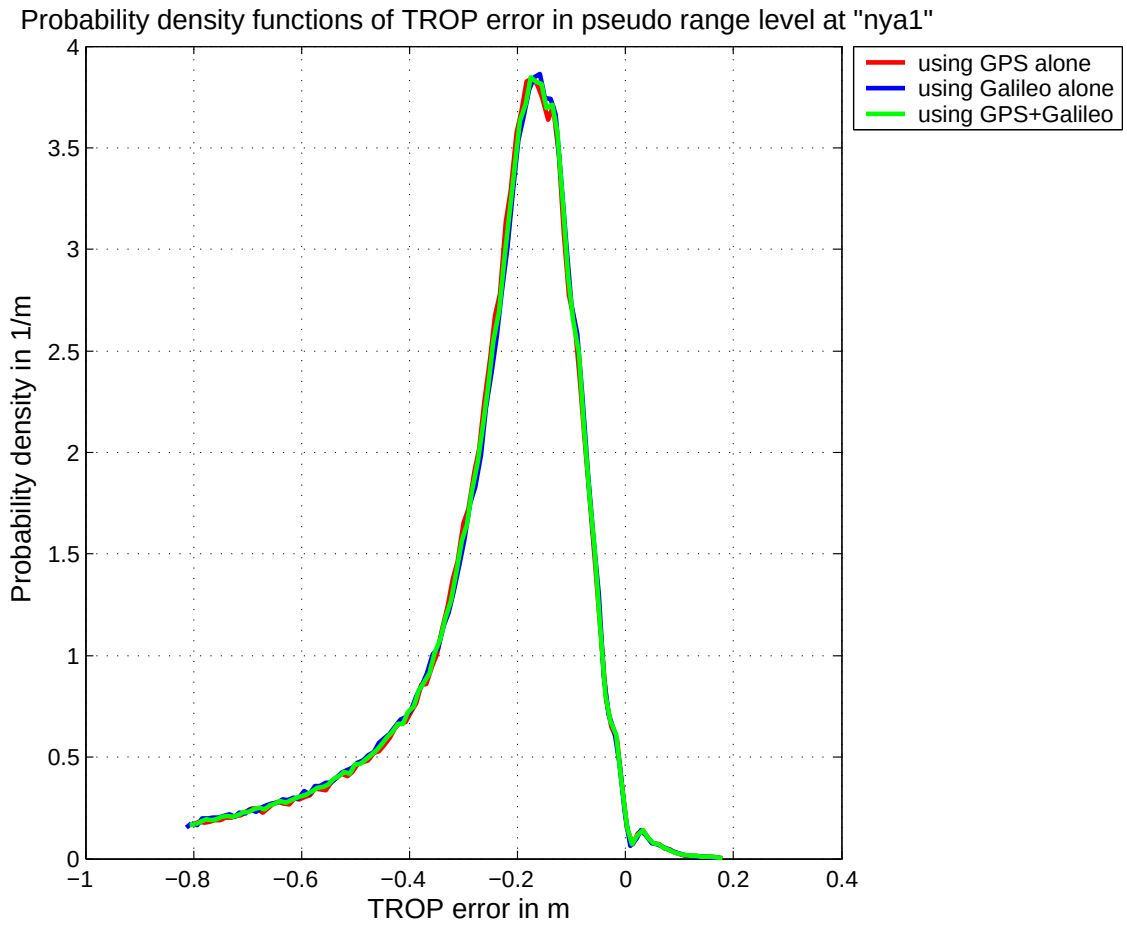

Figure 2.18.: Probability densities of tropospheric error

2.3.4.4. The multipath and receiver noise error

For both constellations, we used the synthetic environment defined above. It was possible using the random multipath generator of NAVSIM to provide the following results for both bias and standard deviation function of the elevation angle for GPS and Galileo. This model respects for both GPS and Galileo the dependency with the elevation angle.

We used a third order polynomial regression to fit the bias function of the elevation angle (see Fig. 2.19) and a fourth order polynomial regression to fit the standard deviation function of the elevation angle (see Fig. 2.20). We proceed then to a random generation of multipath and receiver noise error for each satellite using its elevation angle and the Gaussian distribution corresponding. The results obtained are presented for both constellations in Fig. 2.21.

Fig. 2.21 represents the multipath and receiver noise error for GPS and Galileo satellites. By using the synthetic model, considering a single ground reflection, no

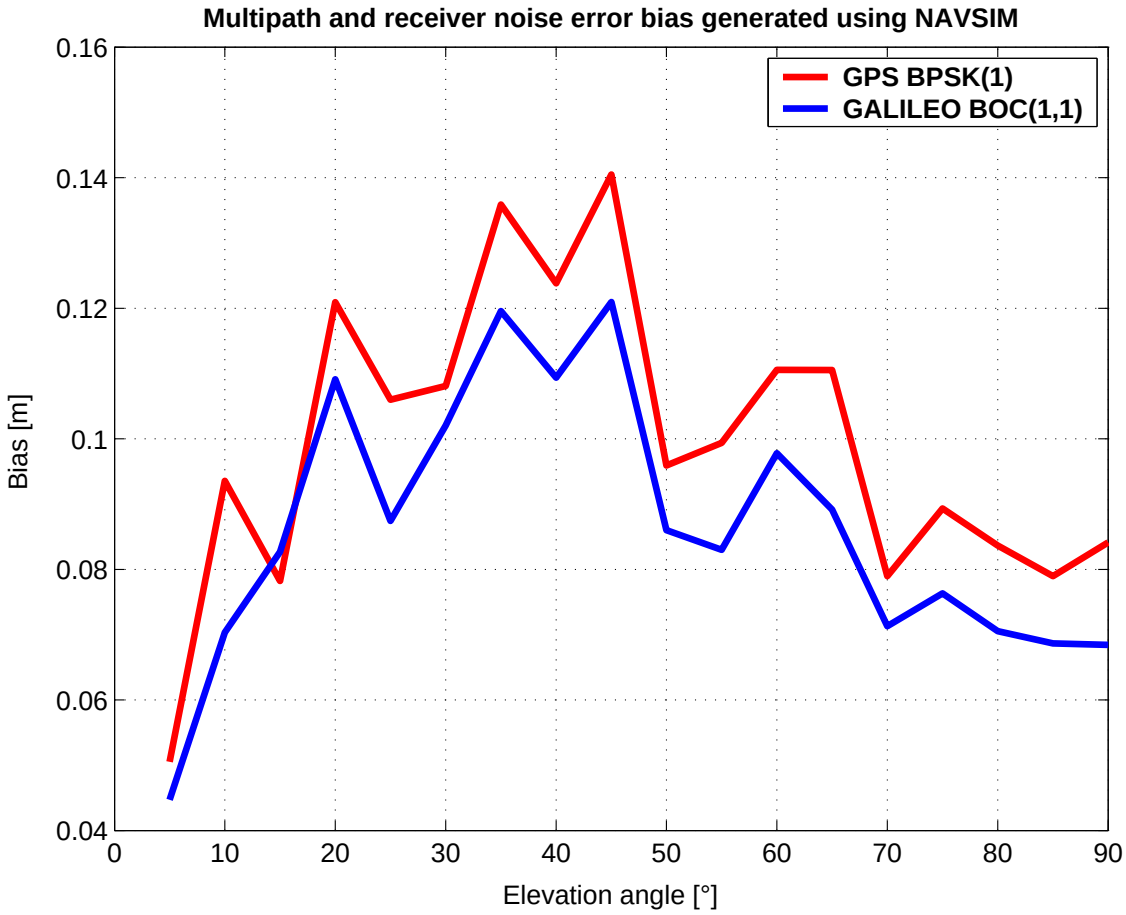

Figure 2.19.: Bias of multipath and receiver noise error function of the elevation angle

dependency with the azimuth angle has been taken into account.

The multipath and receiver noise error is lower for Galileo than for GPS. This is mainly due to the characteristics of the BOC signal and its ability to mitigate multipath error. In fact, the use of a narrow correlator and the characteristics of the BOC signal itself provide a multipath error envelop function of the multipath delay lower than for the GPS C/A code which has a BPSK modulation at 1.023×10^6 chips per seconds. The Receiver noise error plays also an important role assuming that the Galileo system should provide a higher power of signal and thus a higher C/N0 than GPS. Here again, this should be updated with the specifications of the modernized GPS. And a new simulation should take into account the modernized GPS constellation to take advantage of the future satellite blocks.

From Tab. 2.10, we can see that the results correspond to what was expected. These results obtained for GPS have been compared with those obtained from real measurements (see[EM99]for a detailed method used to estimate multipath and receiver

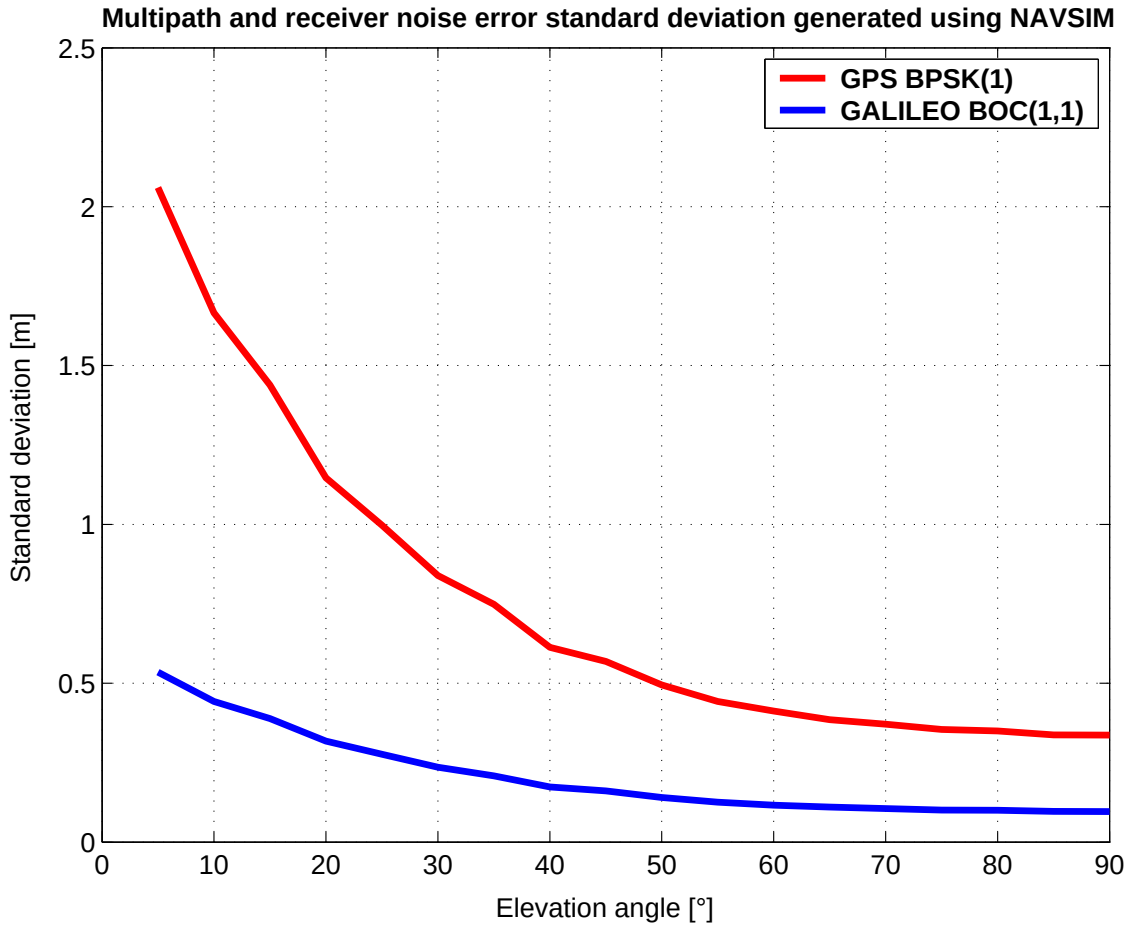

Figure 2.20.: σ of multipath and receiver noise error function of the elevation angle

noise error based on observation files of the considered IGS station) and the level of multipath and receiver noise error fit the results obtained with our simulation. Also the errors function of the elevation angle shows a similar profile as for the measurements. This model is of course available only when considering a sampling period not less than 15 minutes. For shorter periods, one has to take into account an auto-correlation effect due to the non changing configuration for successive measurements.

As expected from our multipath and receiver noise error generator, the probability density functions of Fig. 2.22 are Gaussian like distributions. The Galileo constellation has a sharper distribution and here again as in all other cases, the combined GPS+Galileo is between the two other curves.

2.3.4.5. The Global IPRE

By using Eq. 2.21 we obtain easily the results for the global Instantaneous Pseudo Range Error.

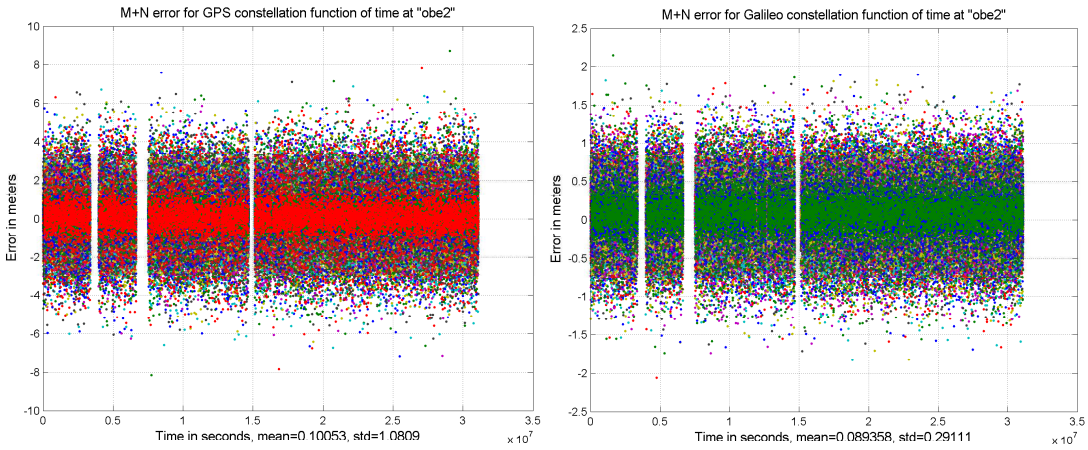

Figure 2.21.: Multipath and receiver noise error vs. time for GPS and Galileo

Tab. 2.11 resumes the results obtained for the global pseudo range error. These results are coherent with respect to the results of [BPH05a] and [BHS05a]. The high level of IPRE at ntus Singapore is due to the ionospheric error which drive both the Galileo and the GPS pseudo range errors. Another remark concerns the level of IPRE for the combined GPS and Galileo constellations. It seems to be always a compromise between the errors found for GPS and the errors found for Galileo. The results obtained are coherent with this averaging effect. But because the ionospheric error level is almost the same for both constellations, the IPRE for the combined constellation shows also a similar level of relative magnitude.

In Fig. 2.23 we can see that the curves have the same shape but present different shifts in the right part of the probability density functions. The consequence is the augmentation of both the bias and the standard deviation from the best to the worst case: we find respectively the Galileo constellation, the combined GPS+ Galileo and the GPS constellation.

2.3.5. The impact of IPRE at position level

In this section, we are going to present the impact of the IPRE at the position level at obe2. The results obtained for the other IGS stations does not give new results and thus we restrain our study to that station. The method used to determine the position error is the "all in view" algorithm. No significant differences have been observed by using the minimum GDOP method. At least the results does not justify the immense additional processing time to select and to calculate the GDOP for all possible combinations of 4 satellites among n satellites in view where n can reach 18 for the combined GPS+ Galileo constellation. Our study is focused on the impact of IPRE at position level. For the study of the impact of individual errors see [BPH05a].

		obe2	nya1	ntus
Bias (m)	GPS	0.101	0.106	0.106
	GAL	0.089	0.096	0.093
	COM	0.095	0.101	0.099
σ (m)	GPS	1.081	1.069	1.078
	GAL	0.291	0.290	0.294
	COM	0.782	0.772	0.777
RMS (m)	GPS	1.086	1.074	1.083
	GAL	0.305	0.306	0.309
	COM	0.787	0.779	0.784

Table 2.10.: Statistical results for multipath and receiver noise error at pseudo range level

2.3.6. The 3D IPRE error at the position level

Fig. 2.24 gives a good overview of the performances reached for each configuration by observing the delimitation of the axis. In fact we used a $\pm 4\sigma$ delimitation along the three axis around the mean values of the results. One should pay attention to the different scales used for horizontal and vertical axis. For all cases, the distribution of points is more scattered in the vertical direction.

2.3.7. Probability density functions of position errors along each axis

The aim of this section is to study the probability density functions of the position error with respect to each axis. This gives us a better overview of the relative performances of constellations. Similar results have been obtained for the two other IGS stations used.

In Fig. 2.25 (bottom), the PDF curve of the combined GPS+Galileo in the vertical direction tends to be closer to the PDF of Galileo than in the horizontal directions see Fig. 2.25 (top left and right). This is an interesting result since the vertical error is often the limiting factor to fulfill the requirements of a given application. Is it enough to say that a combined GPS+ Galileo constellation tends to better correct the vertical error? This point should be investigated further taking into account a decomposition of the position error into individual error contribution to the positioning error and to compare their PDF along each axis. What is also interesting from these results is that the accuracy order is preserved from the pseudo

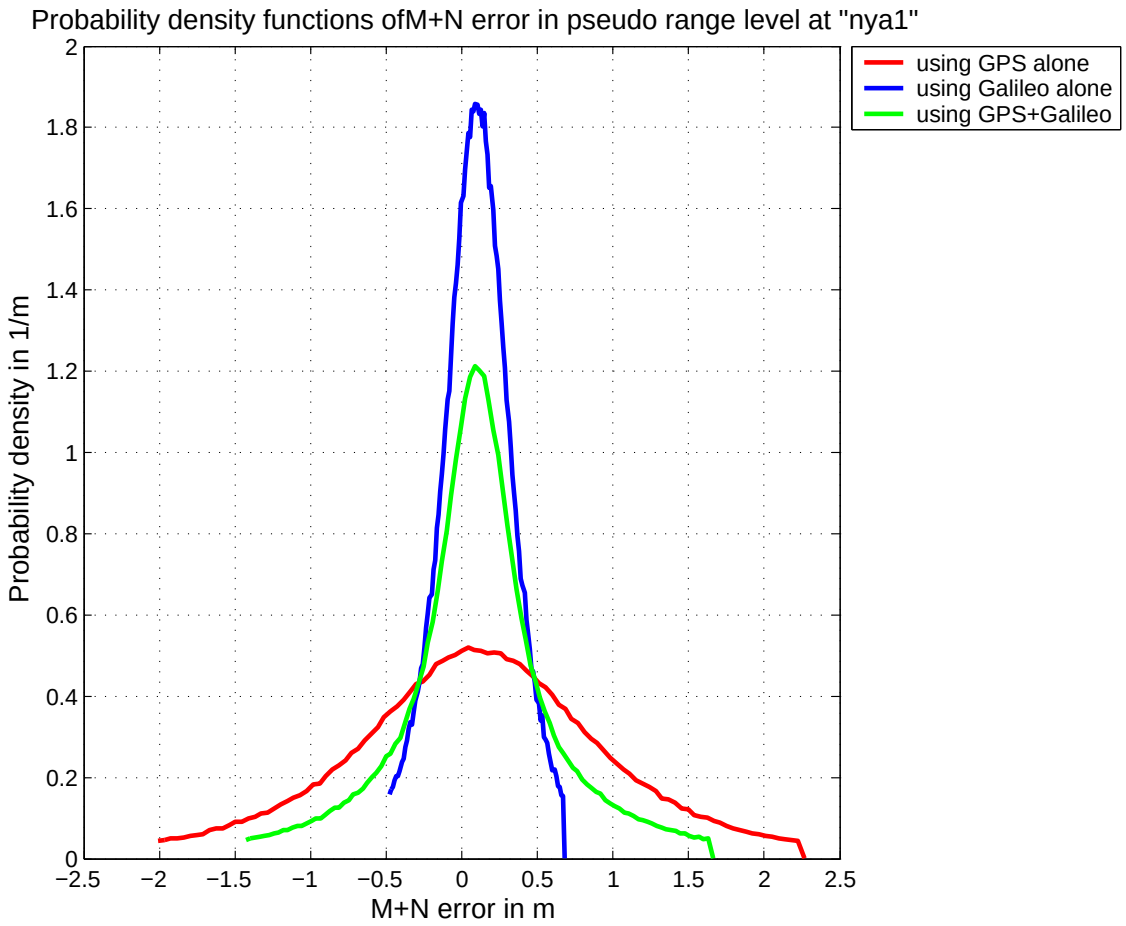

Figure 2.22.: Probability densities of multipath and receiver noise error

range level to the position level. This indicates that the geometry of the constellation has a similar impact even if the combination GPS+Galileo gives a better GDOP thanks to a better repartition of visible satellites. In other words, the improvement of the GDOP is not sufficient to correct the loss in the pseudo range accuracy to be better than the Galileo accuracy in the position level.

2.3.8. Conclusion

This chapter gives two different applications of the use of the IPRE concept: the traditional method considering measurements of IGS stations and the simulation method using random generation of individual errors using an a priori UERE budget. The results obtained confirms what is expected for Galileo and for a combined GPS+ Galileo constellation. The combination of both constellations even if it gives better results than the GPS alone is still below the accuracy expected for Galileo. The combination accuracy is bounded by both the accuracies of GPS and Galileo. But in fact the availability of both constellations gives more chance to track at least 4

		obe2	nya1	ntus
Bias (m)	GPS	2.347	1.113	9.533
	GAL	1.325	-0.150	8.580
	COM	1.755	0.403	9.009
σ (m)	GPS	2.968	2.262	7.500
	GAL	2.497	1.495	7.447
	COM	2.752	1.973	7.486
RMS (m)	GPS	3.784	2.521	12.130
	GAL	2.827	1.503	11.361
	COM	3.264	2.013	11.713

Table 2.11.: Statistical results for the IPRE at pseudo range level

satellites in conditions like positioning in urban canyon for example where only a small zone of sky is visible. Another advantage is the improvement of the availability of RAIM algorithms, providing not only the detection of faulty satellites but also their exclusion giving thus more robustness to the navigation system i.e. more integrity. This argument for the combined Galileo and GPS constellation has many different applications and will involve a lot of interest especially in Safety of life applications. However, if a user is interested more in the accuracy, then the use of Galileo alone will provide certainly the best results because pseudo ranges are less erroneous. Probably in a majority of applications, a compromise has to be found between high accuracy and high integrity/availability. The combined GPS+Galileo constellation would give the best results in both accuracy and integrity when the GPS satellites are tending to provide the same level of performance at the pseudo range level as the Galileo system is going to do and this is what would be planed using the modernized GPS constellation.

2.4. Example: the GNSS Orbit Errors

In this section, we are considering the special case of ephemeris error as we observed in the precedent sections that the projection of the orbital error in the position domain showed a bias in the vertical direction that was actually not expected.

In this section we are going to look more in details the characteristic of this kind of error and try to explain the origin of the observed bias.

The user while receiving the navigation message from the visible satellites, calculate first the position of the satellite according to the Keplerian parameters contained in

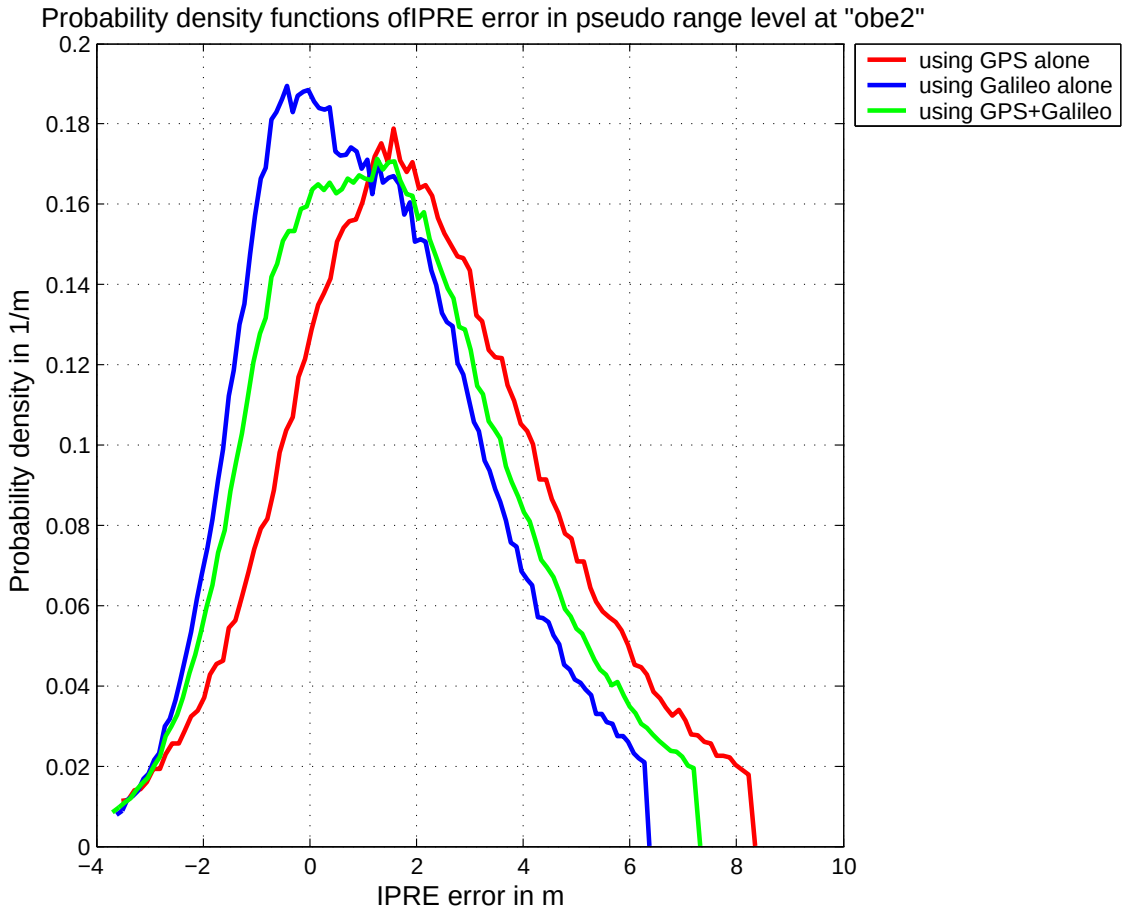

Figure 2.23.: Probability densities of IPRE

the message in the Earth Centered Earth Fixed (ECEF) coordinate system. These Keplerian parameters are determined on ground by a network of monitoring stations observing the same satellite (using an Inverted GNSS approach with reference stations playing the role of satellites and the considered satellite position being the unknown of the multilateration problem). These parameters are determined for a specific time called the time of ephemeris (toe). This is the reference time for which the Keplerian parameters best describe the real satellite position. This set of parameters is updated every two hours and the position of the satellite is calculated at any time by propagating this set of parameters as detailed in the GPS ICD 200C document.
The International GNSS Service provides several products generated by post processing from large number of observations at different reference stations. These post processed data are very precise and are generally used as a reference to calculate the individual error sources of the pseudo-range (rapid and ultra rapid precise orbits and final orbit for ephemeris errors and SV clock errors, precise ionosphere maps in IONEX format for ionosphere error...). For the ephemeris error, the use of precise

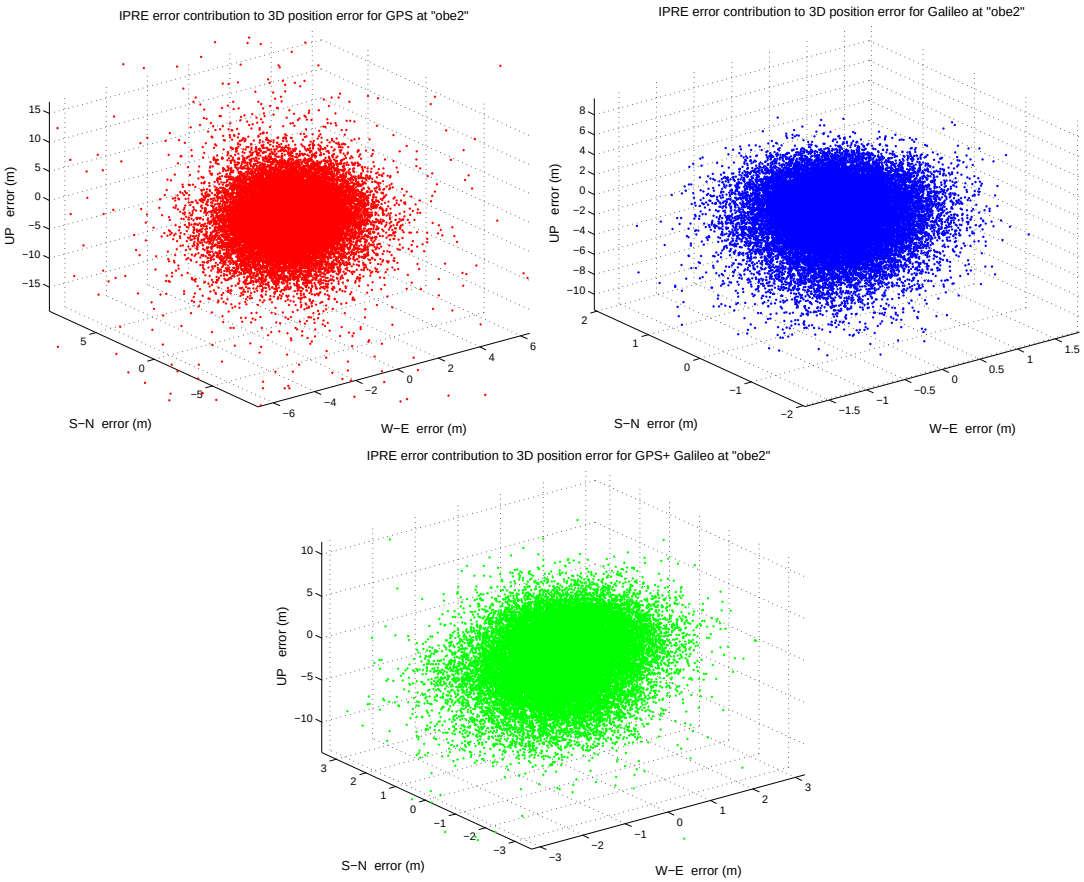

Figure 2.24.: 3D position error at obe2 using the GPS constellation

final satellite orbits and clock provided by the sp3 files is considered.

2.4.1. The sp3 reference data

IGS provides precise final orbits and clock information in sp3 format. The content of these files are ECEF coordinates of all GPS satellites every 15 minutes. These data are based on post-processed measurements considering precise orbital models and forces applied to the satellite. Furthermore the processing of a large number of observations for each satellite from a network of precisely located stations contributes to decrease the uncertainty of the orbit.

2.4.2. Phase Center Center of Gravity Offset (PCCGO)

For some of GNSS satellites, the sp3 files uses as a reference for the position of the satellites the center of mass of the satellite rather than the phase center of the transmission antenna as it is for the broadcasted navigation message. For these satellites,

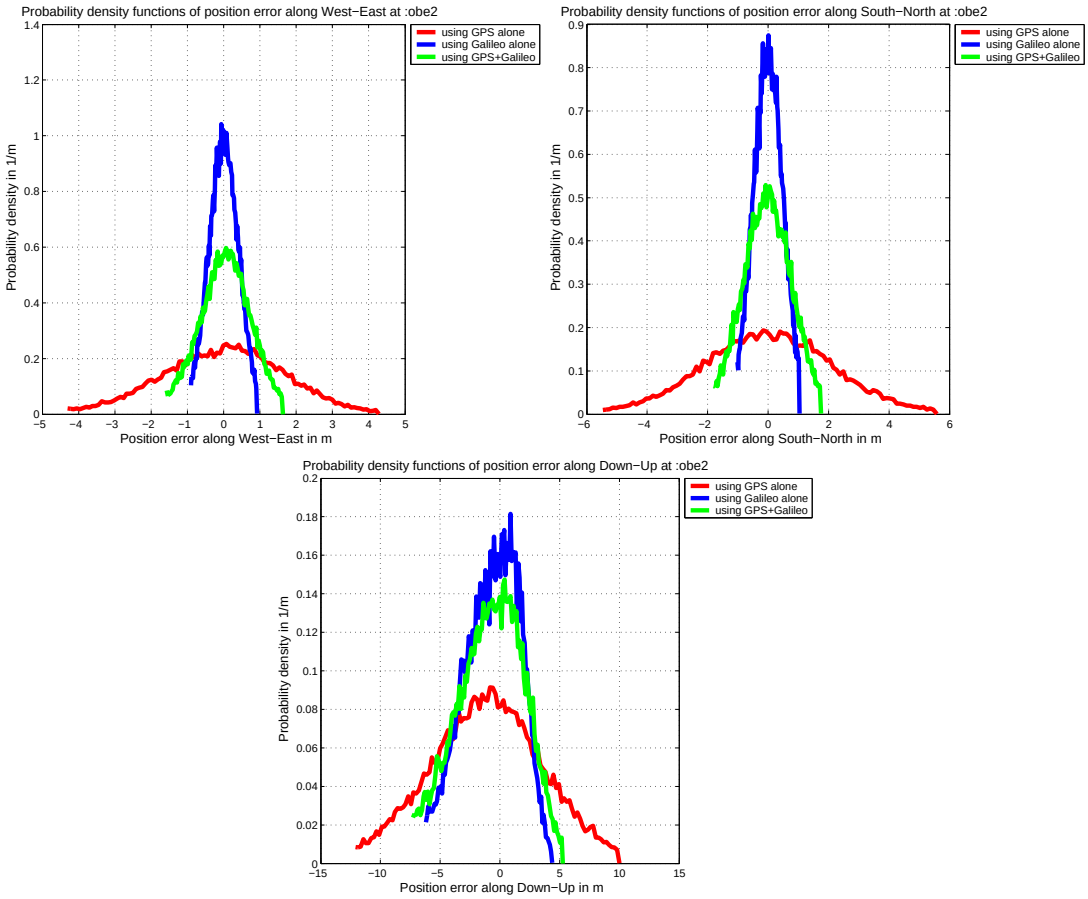

Figure 2.25.: Probability densities of position error along West-East

the ephemeris error (estimated minus reference) should apply this correction. This is what we define as the phase center-center of gravity offset (PCCGO). This offset is provided for all GPS satellites in a satellite body centered coordinate system for example from the National Geo-spatial Intelligence Agency based on post processing GPS observations from 17 identified reference stations. This PCCGO must be applied in order to compare broadcasted ephemeris and precise ephemeris. These corrections are given in a satellite body centered coordinate system. Δx, Δy, Δz represent respectively the along track, cross track and radial component of the offset. These offsets differs from one satellite to another.

2.4.3. Measurements of orbit errors

A first step consists of calculating the position of the satellites from broadcasted ephemeris data into ECEF coordinates (see Fig. 2.26). This step is detailed in the GPS interface control document(ICD) and is briefly explained in the appendix 4 of the document [ARI00]. In fact, the positions of the satellites using broadcasted ephemeris data correspond to the position of the phase center of the sending antenna.

A second step consists of applying the PCCGO to the satellite position calculated in the first step. The PCCGO must first be expressed also in the ECEF coordinate system.
The third and last step consists of calculating the difference between the precise ephemeris and the corrected broadcasted ephemeris. The result is expressed in both ECEF coordinate system and in a satellite body frame coordinate system. A motivation for the error in the satellite body frame coordinate system is to better identify non conservative errors (those errors that are growing after each satellite revolution).

2.4.4. PCCGO in ECEF coordinate system

The satellite position is expressed in ECEF coordinate system. Therefore PCCGO must be also expressed in ECEF coordinate system. From the Keplerian parameters provided in the broadcasted ephemeris (see [ARI00]), it is possible to define the rotations to be used for the RAC/ECEF transformation. First of all let us define the general 3D rotation matrix around each principal axis. Let us suppose that the rotation angle is θ

$$R_1(\theta) = \begin{pmatrix} 1 & 0 & 0 \\ 0 & \cos(\theta) & \sin(\theta) \\ 0 & -\sin(\theta) & \cos(\theta) \end{pmatrix}.$$

$$R_2(\theta) = \begin{pmatrix} \cos(\theta) & 0 & -\sin(\theta) \\ 0 & 1 & 0 \\ \sin(\theta) & 0 & \cos(\theta) \end{pmatrix}.$$

$$R_3(\theta) = \begin{pmatrix} \cos(\theta) & \sin(\theta) & 0 \\ -\sin(\theta) & \cos(\theta) & 0 \\ 0 & 0 & 1 \end{pmatrix}.$$

let us call $\mathbf{I}_{ACR}$ the unit vector in the satellite body frame coordinate system corresponding to the Along track, Cross track and Radial directions (ACR). Let us call $\mathbf{I}_{ECEF}$ the unit vector in the ECEF coordinate system. The relation between these two coordinate systems can be defined as follows:

$$\mathbf{I}_{ECEF} = R_3(-\Omega_c) \cdot R_1(-I) \cdot R_3(-u_c) \cdot \mathbf{I}_{ACR} \tag{2.32}$$

Where u_c is the corrected argument of latitude, I is the angle of inclination and Ω_c the corrected right ascension of the ascending node calculated as follow:

$$\Omega_c = \Omega_0 + \left(\dot{\Omega} - \dot{\Omega}_e\right) t_k - \dot{\Omega}_e \cdot t_{oe} \tag{2.33}$$

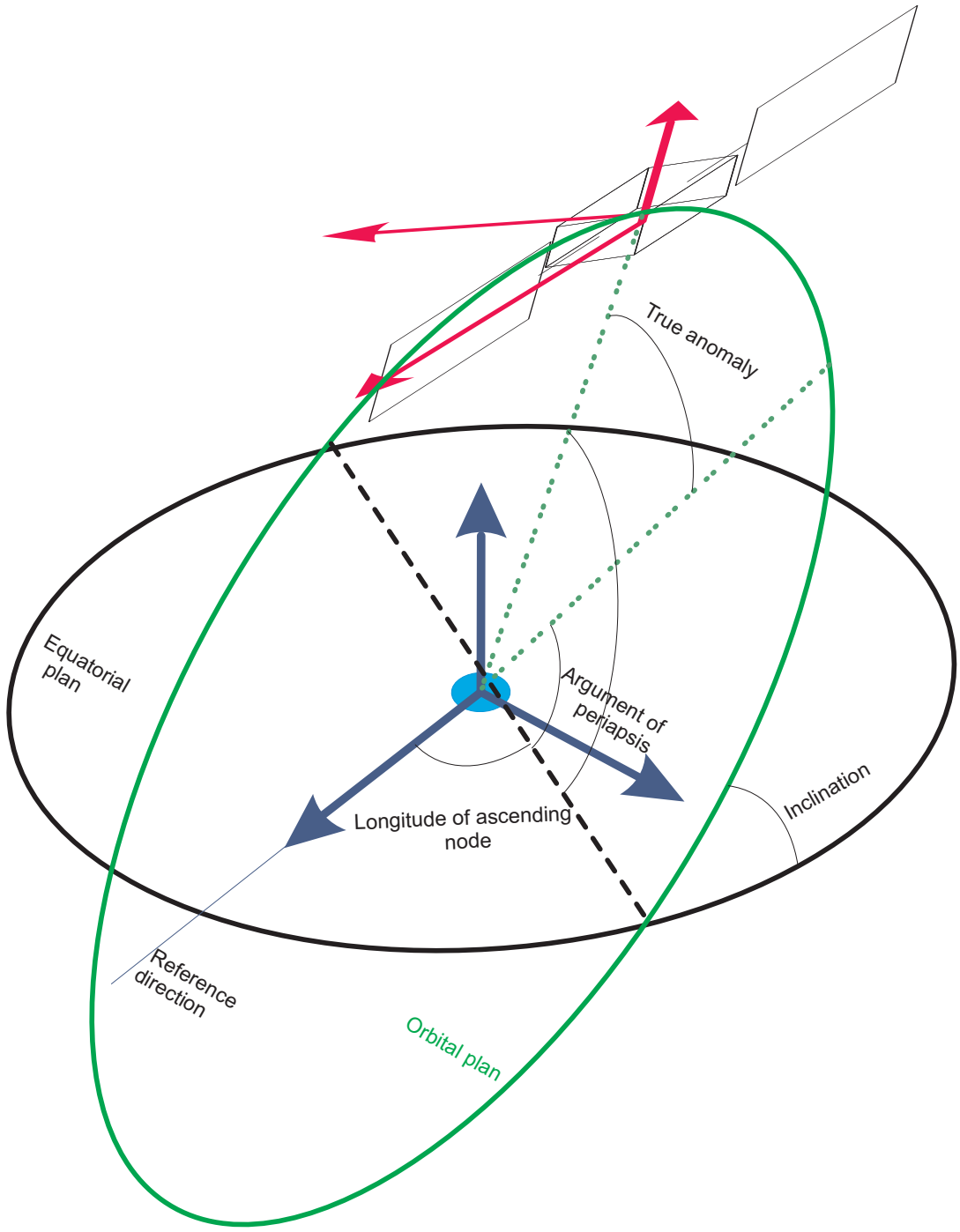

Figure 2.26.: Orbit representation using Keplerian parameters

Where Ω_0 is the right ascension of the ascending node at reference time, $\dot{\Omega}$ is the change rate of the right ascension; $\dot{\Omega}_e$ is the change rate of the earth's rotation;t_k is the calculation time; and t_oe is the reference time of the ephemeris parameters.

The new vector PCCGO in ECEF coordinate system can be expressed for each satellite by applying the rotations defined above see [ME06] for more details.

$$PCCGO^i_{ECEF} = R_3\left(-\Omega^i_c\right) \cdot R_1\left(-I^i\right) \cdot R_3\left(-u^i_c\right) \cdot PCCGO^i_{ACR} \tag{2.34}$$

2.4.5. Measurement results

The period of measurement considered is from 11th of October 2009 Midnight till 31st of October 2009 at 11:45. We used a sampling period of measurement of 15 minutes and the orbit error analysis is done at orbit level as a first step and then considers a user reference position at Oberpfaffenhofen in Germany for their projection in the line of sight to study the impact at pseudo range level.
During the period of measurements, 3 satellites where declared unavailable during at least 1 epoch. We decided not to consider these satellites in our analysis. These satellites have the pseudo random noise (PRN) numbers:1,8,24. Satellite number 1 was even unavailable during the complete period of measurements. These PRN numbers are identification numbers for each GNSS satellite. As all satellites are broadcasting using signals at the same frequency the user receiver need to identify the satellite to track the signal and therefore correlate with each available codes. This is usually what is applied for code division multiple access (CDMA) systems
In Fig. 2.27 and Fig. 2.28, we plotted first the error in radial, along track and cross track (RAC) coordinate system without correcting the PCCGO for each satellite and in the second graphic, we plotted the error after correction.

The resulting remaining bias seems to be corrected only for the radial direction. Although this is the main contribution to the position error budget, It is surprising that biases remain in both other directions. As the PCCGO didn't correct for these biases, a possible explanation of this result in along track especially is the high uncertainty of the satellite position in this direction. The high velocity of a satellite provides a proportionally high uncertainty in the direction of the speed vector which can impact a potential user especially when the satellite is at low elevation for which the projection of the along track component contribution of the error is the highest. Nevertheless this need to be investigated more in details.

In order to have a better idea of the error behavior, we selected one good and one bad satellite with respect to their remaining orbit errors. We choose to focus on PRN#4 (bad) and PRN#7 (good).

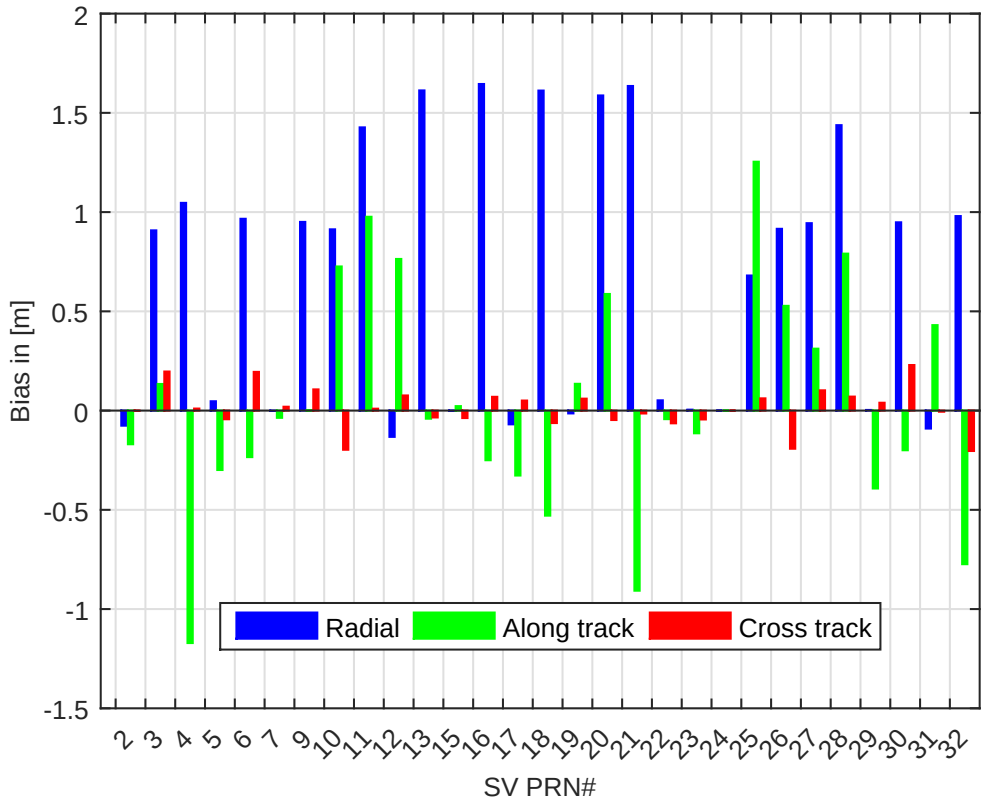

Figure 2.27.: Orbit mean error without correction in RAC coordinate system for the period 11-31 October 2009

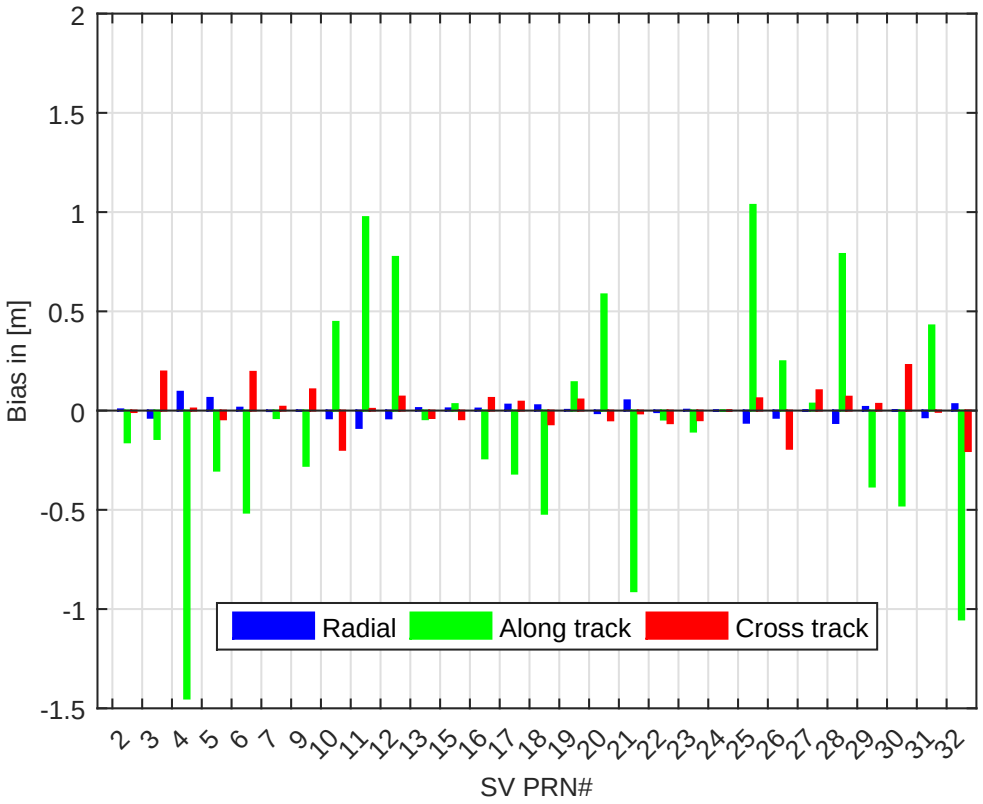

Figure 2.28.: Orbit mean error with correction in RAC coordinate system for the period 11-31 October 2009

2.4.5.1. Orbital error analysis in satellite body frame

Orbital errors show as expected different types of behavior between directions (radial, along track, cross track) and also differences between satellites (see Fig. 2.29).

It appears that the data show periodicity. If we zoom in one day (Oct. 11 2009 for example), these periodicities appears to be correlated with the period of the satellite orbit. Fig. 2.30 represent the radial error. If we look in details it appears that 2 effects are superimposed: The orbital periodicity of half a day and the dataset sampling period (2 hours).

PCCGO does not improve the accuracy in the along track direction. One of a possible reason for that is the high level of uncertainty in the direction of the satellite motion. Still it does not explain the reason for the systematic bias. Another probable reason is the satellite clock uncertainty. In fact the along track error is directly influenced by the true anomaly which is strongly depend on the speed of the satellite. With a speed of almost 4 km/s, this means that a very small uncertainty will be magnified in a large amount.

The cross track component as the along track has only a limited impact in the pseudo range error budget. The error seems to be also corrected, with a remaining residual bias of 1 to 2 meters. There is clearly a deterministic effect that still can be eliminated in the navigation message. Maybe for that, it would be necessary either to increase the update rate of the orbit parameters or to add additional parameters to the model. A cost benefit analysis would help to take the right decision in order to improve the performance of the overall system.

After investigations, it appears that PRN#4 is a block IIA satellite with operational date Nov. 22, 1993 (one of the oldest operational satellite) using a rubidium clock (switch from cesium to rubidium frequency standard from Sept. 13 to Sept. 21 1998).
Concerning PRN#7, it appears that this satellite belongs to block II-RM providing civilian signals L1C and L2C with operational date: Mar. 24, 2008 this is one of the newest satellite with a rubidium clock as master clock. These information can be found under ftp://tycho.usno.navy.mil/pub/gps/gpsb2.txt

2.4.5.2. Projection in the line of sight

In order to analyze the impact of the orbit error in a pseudo range calculation, one has to choose a position of a user (for example Oberpfaffenhofen in Germany with the following longitude, latitude and height respectively 11.3000 48.1000 651.0000 m) and for this user, determine at each time the line of sight vector. We just have to project the orbit error in the line of sight by applying a scalar product and we analyze the result. We consider an elevation mask of 5 degrees.

Fig. 2.31 and Fig. 2.32 are to be compared with Fig. 2.27 and Fig. 2.28. It stresses the fact that the sole reduction of the radial error by extracting the PCCGO provides

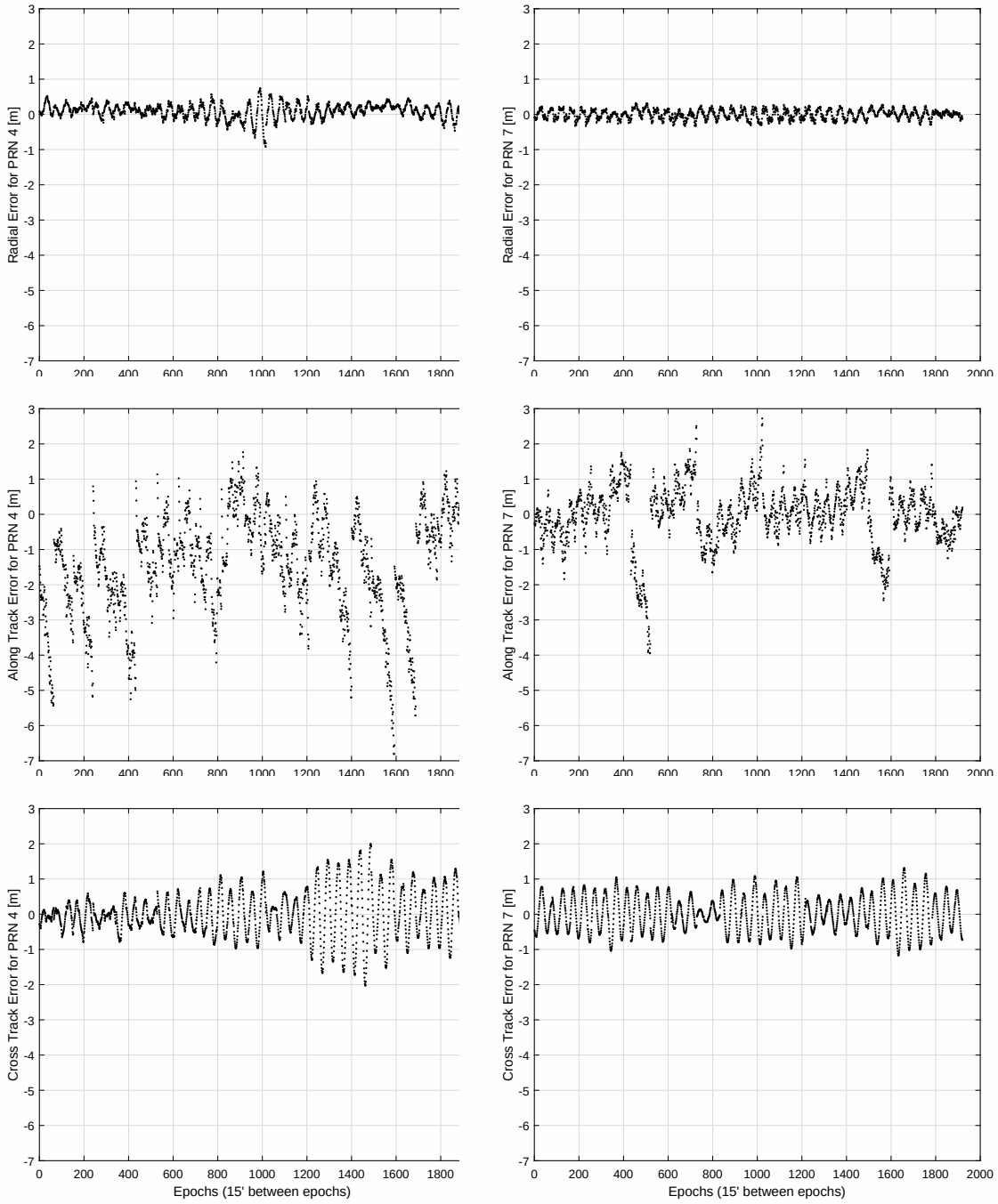

Figure 2.29.: Orbit errors in body frame reference system for PRN 4 and PRN 7

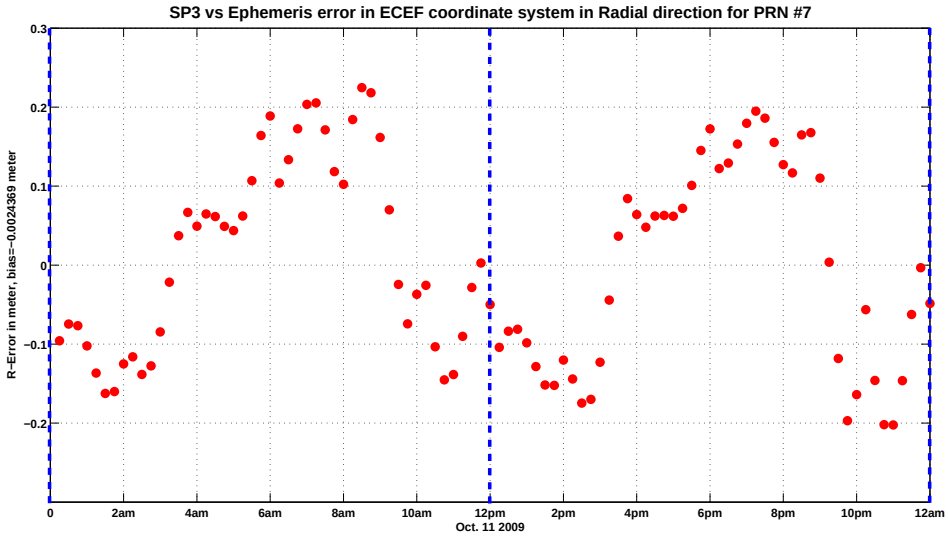

Figure 2.30.: Radial error for PRN#7 on Oct. 11 2009

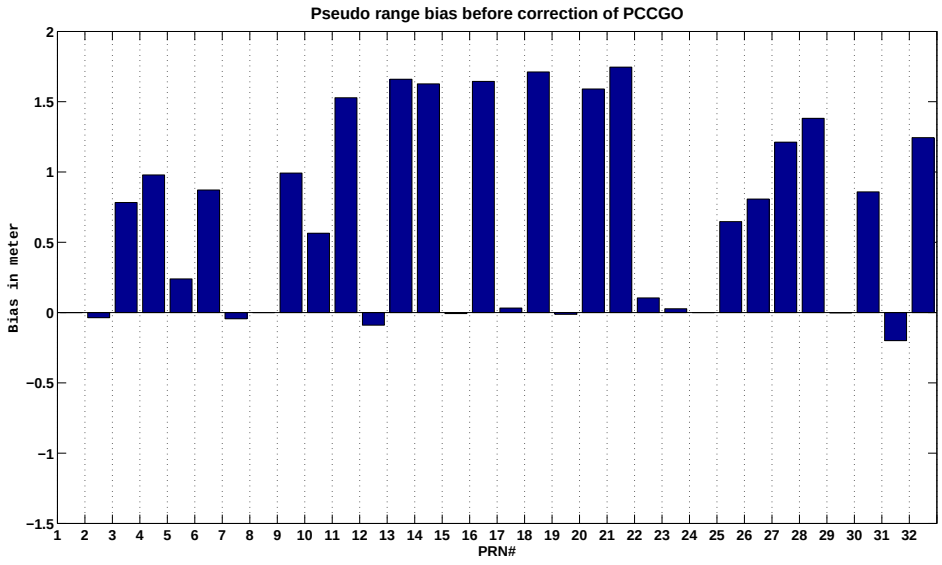

Figure 2.31.: Orbit error projected in the pseudo range before correction of the PCCGO

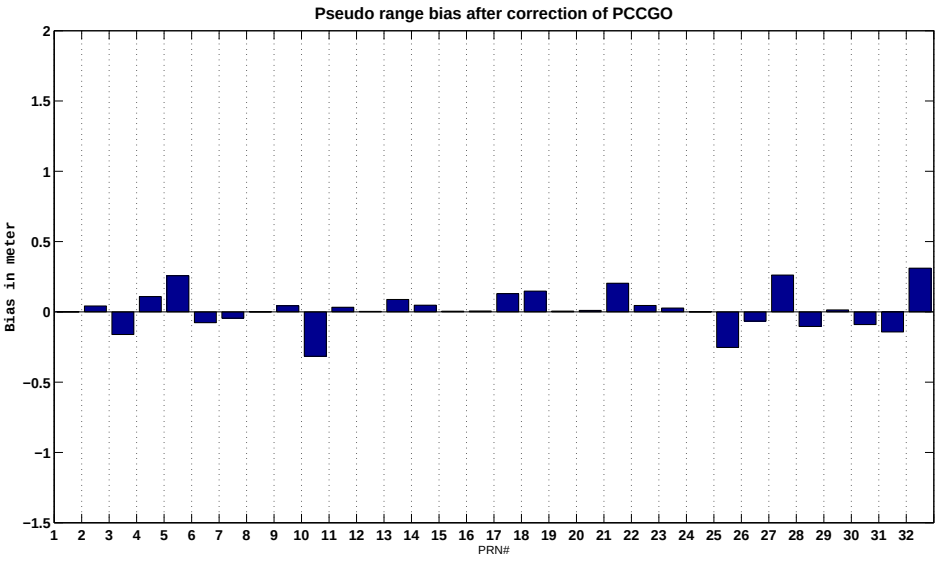

Figure 2.32.: Orbit error projected in the pseudo range after correction of the PCCGO

a very satisfactory result. The Along track and the cross track components of the orbit error are a lot reduced after projection in the line of site direction.
One could study these biases for different locations of user. The conclusion should not change fundamentally because the principal contribution of the orbit error at pseudo range level will still remain the radial one.
As a conclusion for this section, the PCCGO correction is necessary in order to eliminate the major bias contributor to the orbit error. But the PCCGO is not the only bias source, it appears that there are still deterministic errors that are although not constant are still providing a deterministic pattern. This should be subject to additional investigations and propositions for orbit model improvements should be suggested. This activity is beyond the scope of this thesis.

2.5. Code Carrier Smoothing Algorithm

In the previous sections, only raw pseudo range observations of the L1 C/A code signal were used. A GNSS receiver uses a DLL and a PLL to characterize the signal channel and estimate both the magnitude and the rate of change of the pseudo range. The accumulated Doppler constitute the phase observation of the signal received and provide an additional information for the user. A phase expressed in integer number of cycles and a fraction of a cycle is provided to the user. It appears that the fraction part of the cycle is very precise and the range calculated using this phase is very precise especially because the level of multipath and receiver noise is approximately ten times smaller than the level of multipath and receiver noise

experienced by the pseudo ranges generated by the code measurements.

The idea of using both Code and Phase measurements to improve precision and accuracy was first suggested by Ronald Hatch in [Hat82].

The Hatch filter is recalled here:

Let us call $\rho_{u,n}^{(k)}$ and $\Phi_{u,n}^{(k)}$ the code range (resp. phase range) of the signal coming from satellite k to the user u at epoch n, and $\widetilde{\rho}_{u,n-1}^{(k)}$ the smoothed code range at epoch $n-1$. The smoothed code range at epoch n is defined iterativelly using the following equation:

$$\widetilde{\rho}_{u,n}^{(k)} = \alpha\rho_{u,n}^{(k)} + (1-\alpha)\left[\widetilde{\rho}_{u,n-1}^{(k)} + \left(\Phi_{u,n}^{(k)} - \Phi_{u,n-1}^{(k)}\right)\right] \tag{2.35}$$

with $\alpha = \frac{1}{\tau}$ and with τ being the time constant of the filter. All components of the equation are using the distance unit i.e. meter.

Let's write the observation equations:

$$\rho_u^{(k)} = r_u^{(k)} + c\left(\delta t_u - \delta t^{(k)}\right) + I_u^{(k)} + T_u^{(k)} + \mathcal{E}_u^{(k)} \tag{2.36}$$

This equation is directly derived from 2.6.

And for the phase observation translated in a pseudo range unit we have:

$$\Phi_u^{(k)} = \lambda\phi_u^{(k)} - \lambda\phi^{(k)} + \lambda N_u^{(k)} + c\left(\delta t_u - \delta t^{(k)}\right) - I_u^{(k)} + T_u^{(k)} + \eta_u^{(k)} \tag{2.37}$$

with $\phi_u^{(k)}$ being the phase of the signal at user level, $\phi^{(k)}$the phase of the signal while leaving the transmitting antenna of the satellite, $N_u^{(k)}$ the integer number of cycles from satellite to user (called the integer ambiguity), $\eta_u^{(k)}$ the phase multipath and thermal receiver noise, λ the carrier wavelength and the other notations as defined in sec. 2.2. The negative sign for the ionosphere delay in 2.37 is because the phase is advanced when the signal crosses the ionosphere with the same magnitude as for the code delay.

2.5.1. Continuous Form of the Hatch Filter Equation

The Hatch filter 2.35 can then be fed with the observation models described above:

Let us call $\widetilde{\rho}_u^{(k)}(t)$ the smoothed code with the phase at the epoch t.

The Hatch filter can be written as follows:

$$\widetilde{\rho}_u^{(k)}(t+dt) = \alpha\rho_u^{(k)}(t+dt) + (1-\alpha)\left[\widetilde{\rho}_u^{(k)}(t) + \left(\Phi_u^{(k)}(t+dt) - \Phi_u^{(k)}(t)\right)\right] \quad (2.38)$$

We choose to represent the continuous form of the filter in order to use the theory of stochastic differential equation. In that case $\alpha = \frac{dt}{\tau_h}$ with τ_h the time constant of the Hatch filter.

Equation 2.38 can be rewritten as follows:

$$\widetilde{\rho}_u^{(k)}(t+dt) = \frac{dt}{\tau_h}\rho_u^{(k)}(t+dt) + \left(1 - \frac{dt}{\tau_h}\right)\left[\widetilde{\rho}_u^{(k)}(t) + \left(\Phi_u^{(k)}(t+dt) - \Phi_u^{(k)}(t)\right)\right] \quad (2.39)$$

We assume that between t and $t+dt$, the ionosphere, troposphere delays and the clock delays to GPS time (satellite and receiver) are constant.

The last term of equation 2.38 can be written in the following form:

$$\Phi_u^{(k)}(t+dt) - \Phi_u^{(k)}(t) = \lambda\left(\dot{\phi}_u^{(k)} - \dot{\phi}^{(k)}\right)dt + d\eta_t \quad (2.40)$$

With η_t being an auto-regressive first order process AR(1) taking into consideration time correlations and that can be written as the solution of the following stochastic differential equation in continuous form:

$$d\eta_t = -\frac{1}{\tau_\eta}\eta_t dt + \sigma_\eta dW_t \quad (2.41)$$

This process is also called a centered Ornstein-Uhlenbeck (OU) process (with parameters $1/\tau_\eta$ and σ_η) representing a more realistic noise model than the usual white Gaussian Noise process. The parameters should be chosen such that they over-bound the true receiver noise process.

We then replace this expression in 2.38 and obtain the following equation:

$$d\widetilde{\rho}_u^{(k)}(t) = \left[\frac{1}{\tau_h}\left(\rho_u^{(k)}(t+dt) - \widetilde{\rho}_u^{(k)}(t)\right) + \lambda\left(\dot{\phi}_u^{(k)} - \dot{\phi}^{(k)}\right)\right]dt + d\eta_t \quad (2.42)$$

All other terms are negligible.

We rearrange equation 2.42

$$d\widetilde{\rho}_u^{(k)}(t) = \frac{1}{\tau_h}\left[\left(\rho_u^{(k)}(t+dt) + \lambda\tau_h\left(\dot{\phi}_u^{(k)} - \dot{\phi}^{(k)}\right)\right) - \widetilde{\rho}_u^{(k)}(t)\right]dt + d\eta_t \tag{2.43}$$

In this expression we can recognize a variation of an Ornstein-Uhlenbeck (OU) process with parameters $\left(\theta, \mu, \sigma_{\widetilde{\rho}}\right)$ with

$$\begin{aligned}\theta &= \frac{1}{\tau_h}\\ \mu &= \left(\rho_u^{(k)}(t+dt) + \lambda\tau_h\left(\dot{\phi}_u^{(k)} - \dot{\phi}^{(k)}\right)\right)\\ \sigma_{\widetilde{\rho}} &= \sigma(\eta)\end{aligned}$$

The particularity of this OU-process is that the mean is time dependent and the driving noise is also an OU-process with parameters $\left(\frac{1}{\tau_\eta}, 0, \sigma_\eta\right)$.

We can also decompose $\rho_u^{(k)}(t+dt)$ to let appear the timely varying values and the noise with respect to the pseudo range at a prior time epoch t:

$$\rho_u^{(k)}(t+dt) = r_u^{(k)}(t) + dr_u^{(k)}(t) + c\left(\delta t_u - \delta t^{(k)}\right)(t) + I_u^{(k)}(t) + T_u^{(k)}(t) + \mathcal{E}_u^{(k)}(t) \tag{2.44}$$

We use the property that the ionosphere and the troposphere delays do not change during dt and the noise $\mathcal{E}_u^{(k)}(t)$ is stationary which implies that the process is invariant with respect to a shift in time. These assumptions can be revisited during the study if we consider ionosphere storms for example introducing strong temporal gradients.

Finally we can simplify 2.44:

$$\rho_u^{(k)}(t+dt) = \bar{\rho}_u^{(k)}(t) + dr_u^{(k)}(t) + \mathcal{E}_u^{(k)}(t) \tag{2.45}$$

With $\bar{\rho}_u^{(k)}(t) = r_u^{(k)}(t) + c\left(\delta t_u - \delta t^{(k)}\right)(t) + I_u^{(k)}(t) + T_u^{(k)}(t)$

We keep the "deterministic" part of the code observation in the first term of the Hatch filter and the "noise" part is extracted from this first term.

We consider a more generalized form of the code noise $\mathcal{E}_u^{(k)}$ (in the same way as for the phase noise) and set $\mathcal{E}_u^{(k)}(t)\,dt = d\mathcal{E}_t$, where $\mathcal{E}_t$ being an AR(1) process with parameters $\left(\frac{1}{\tau_\mathcal{E}}, 0, \sigma_\mathcal{E}\right)$.

$$d\mathcal{E}_t = -\frac{1}{\tau_\mathcal{E}}\mathcal{E}_t dt + \sigma_\mathcal{E} dV_t \tag{2.46}$$

We can rewrite the first order development of the Hatch filter equation as follows:

$$d\widetilde{\rho}_u^{(k)}(t) = \frac{1}{\tau_h}\left[\left(\bar{\rho}_u^{(k)}(t) + dr_u^{(k)}(t) + \lambda\tau_h\left(\dot{\phi}_u^{(k)} - \dot{\phi}^{(k)}\right)\right) - \widetilde{\rho}_u^{(k)}(t)\right]dt + \frac{1}{\tau_h}\mathcal{E}_t dt + d\eta_t \tag{2.47}$$

with $\mathcal{E}_t dt = -\tau_{\mathcal{E}} d\mathcal{E}_t + \tau_{\mathcal{E}}\sigma_{\mathcal{E}} dV_t$

Finally we have:

$$d\widetilde{\rho}_u^{(k)}(t) = \frac{1}{\tau_h}\left[\mu_u^{(k)}(t) - \widetilde{\rho}_u^{(k)}(t)\right]dt + \frac{\tau_{\mathcal{E}}}{\tau_h}\left(-d\mathcal{E}_t + \sigma_{\mathcal{E}} dV_t\right) + d\eta_t \tag{2.48}$$

with $\mu_u^{(k)}(t) = \left(\bar{\rho}_u^{(k)}(t) + dr_u^{(k)}(t) + \lambda\tau_h\left(\dot{\phi}_u^{(k)} - \dot{\phi}^{(k)}\right)\right)$

2.5.2. Resolution of the Hatch Filter Equation

We will treat the only case where the noise is Gaussian distributed.

In that case the solution of the Hatch filter equation is also Gaussian distributed for any given epoch t. It is sufficient to calculate the mean and the variance of the process for each epoch. We can calculate the correlation with respect to time of the process solution of the stochastic differential equation (SDE).

$$\widetilde{\rho}_u^{(k)}(t) = \int_0^t d\widetilde{\rho}_u^{(k)}(s) + \widetilde{\rho}_u^{(k)}(0) \tag{2.49}$$

We apply the Itō Lemma (see [Oks07]) to the function $f\left(\widetilde{\rho}_u^{(k)}(t), t\right) = \widetilde{\rho}_u^{(k)}(t)\, e^{\frac{t}{\tau_h}}$

$$df\left(\widetilde{\rho}_u^{(k)}(t), t\right) = \frac{1}{\tau_h} e^{\frac{t}{\tau_h}} \widetilde{\rho}_u^{(k)}(t)\, dt + e^{\frac{t}{\tau_h}} d\widetilde{\rho}_u^{(k)}(t) \tag{2.50}$$

$$df\left(\widetilde{\rho}_u^{(k)}(t), t\right) = \frac{1}{\tau_h} e^{\frac{t}{\tau_h}} \mu_u^{(k)}(t)\, dt + e^{\frac{t}{\tau_h}}\left[\frac{\tau_{\mathcal{E}}}{\tau_h}\left(-d\mathcal{E}_t + \sigma_{\mathcal{E}} dV_t\right) + d\eta_t\right] \tag{2.51}$$

Let's consider the initial time corresponding to the first observation of the satellite (either when the satellite appears at the horizon or after recovering a satellite after

a loss of lock of the signal). We also assume that between the initial time to the actual epoch t there is no loss of signal lock.

the integral from 0 to t of df is:

$$\widetilde{\rho}_u^{(k)}(t)\, e^{\frac{t}{\tau_h}} = \widetilde{\rho}_u^{(k)}(0) + \int_0^t e^{\frac{s}{\tau_h}} \mu_u^{(k)}(s)\, \frac{ds}{\tau_h} + \int_0^t e^{\frac{s}{\tau_h}} \left[\frac{\tau_{\mathcal{E}}}{\tau_h} \left(-d\mathcal{E}_s + \sigma_{\mathcal{E}} dV_s \right) + d\eta_s \right] \quad (2.52)$$

We develop the expression for $d\mathcal{E}_t$ and $d\eta_t$.

we apply the Itō Lemma to the functions $f_{\mathcal{E}}(\mathcal{E}_t, t) = \mathcal{E}_t e^{\frac{t}{\tau_{\mathcal{E}}}}$ and $f_\eta(\eta_t, t) = \eta_t e^{\frac{t}{\tau_\eta}}$.

$$df_\epsilon(\mathcal{E}_t, t) = \frac{1}{\tau_{\mathcal{E}}} e^{\frac{t}{\tau_{\mathcal{E}}}} \mathcal{E}_t dt + e^{\frac{t}{\tau_{\mathcal{E}}}} d\mathcal{E}_t \quad (2.53)$$

We recall that $d\mathcal{E}_t = -\frac{1}{\tau_{\mathcal{E}}} \mathcal{E}_t dt + \sigma_{\mathcal{E}} dV_t$

Equation 2.53 becomes:

$$df_{\mathcal{E}}(\mathcal{E}_t, t) = \sigma_{\mathcal{E}} e^{\frac{t}{\tau_{\mathcal{E}}}} dV_t \quad (2.54)$$

We can integrate from 0 to t and obtain:

$$\mathcal{E}_t e^{\frac{t}{\tau_{\mathcal{E}}}} = \mathcal{E}_0 + \int_0^t \sigma_{\mathcal{E}} e^{\frac{s}{\tau_{\mathcal{E}}}} dV_t \quad (2.55)$$

we divide the left and right side by $e^{\frac{t}{\tau_{\mathcal{E}}}}$ and we finally obtain:

$$\mathcal{E}_t = \mathcal{E}_0 e^{\frac{-t}{\tau_{\mathcal{E}}}} + \sigma_{\mathcal{E}} \int_0^t e^{\frac{s-t}{\tau_{\mathcal{E}}}} dV_s \quad (2.56)$$

($\sigma_{\mathcal{E}}$ does not depend on s and therefore can be extracted from the integral).

Using the same method we obtain:

$$\eta_t = \eta_0 e^{\frac{-t}{\tau_\eta}} + \sigma_\eta \int_0^t e^{\frac{s-t}{\tau_\eta}} dW_s \quad (2.57)$$

Let's consider the initial time corresponding to the first observation of the satellite (either when the satellite appears at the horizon or after recovering from a loss of

lock of the signal). We also assume that between the initial time to the actual epoch t there is no loss of signal lock.

the integral from 0 to t of df is:

$$\widetilde{\rho}_u^{(k)}(t)\, e^{\frac{t}{\tau_h}} = \widetilde{\rho}_u^{(k)}(0) + \int_0^t e^{\frac{s}{\tau_h}} \mu_u^{(k)}(s) \frac{ds}{\tau_h} + \int_0^t e^{\frac{s}{\tau_h}} \left[\frac{\tau_{\mathcal{E}}}{\tau_h} \left(-d\mathcal{E}_s + \sigma_{\mathcal{E}} dV_s \right) + d\eta_s \right] \tag{2.58}$$

The last integral term can be developed:

Let's apply the integration by parts formula:

$$\underbrace{\int_0^t e^{\frac{s}{\tau_h}} \left[\frac{\tau_{\mathcal{E}}}{\tau_h} \left(-d\mathcal{E}_s + \sigma_{\mathcal{E}} dV_s \right) + d\eta_s \right]}_{C} = \underbrace{\left[e^{\frac{s}{\tau_h}} \left[\frac{\tau_{\mathcal{E}}}{\tau_h} \left(-\mathcal{E}_s + \sigma_{\mathcal{E}} V_s \right) + \eta \right] \right]_0^t}_{A} - \underbrace{\int_0^t e^{\frac{s}{\tau_h}} \left[\frac{\tau_{\mathcal{E}}}{\tau_h} \left(-\mathcal{E}_s + \sigma_{\mathcal{E}} V_s \right) + \eta_s \right] \frac{ds}{\tau_h}}_{B} \tag{2.59}$$

We replace $\mathcal{E}_t$ and η_t by their expressions (Equations 2.56 and 2.57) in A and B:

$$A = e^{\frac{t}{\tau_h}} \left[\frac{\tau_{\mathcal{E}}}{\tau_h} \left(-\mathcal{E}_t + \sigma_{\mathcal{E}} V_t \right) + \eta_t \right] + \frac{\tau_{\mathcal{E}}}{\tau_h} \mathcal{E}_0 - \eta_0 \tag{2.60}$$

$$A = e^{\frac{t}{\tau_h}} \left[\frac{\tau_{\mathcal{E}}}{\tau_h} \left(-\mathcal{E}_0 e^{\frac{-t}{\tau_{\mathcal{E}}}} - \sigma_{\mathcal{E}} \int_0^t e^{\frac{s-t}{\tau_{\mathcal{E}}}} dV_s + \sigma_{\mathcal{E}} V_t \right) + \eta_0 e^{\frac{-t}{\tau_\eta}} + \sigma_\eta \int_0^t e^{\frac{s-t}{\tau_\eta}} dW_s \right] + \frac{\tau_{\mathcal{E}}}{\tau_h} \mathcal{E}_0 - \eta_0 \tag{2.61}$$

After simplification we obtain:

$$A = \frac{\tau_{\mathcal{E}}}{\tau_h} \mathcal{E}_0 \left(1 - e^{\frac{t}{\tau_h} - \frac{t}{\tau_{\mathcal{E}}}} \right) - \eta_0 \left(1 - e^{\frac{t}{\tau_h} - \frac{t}{\tau_\eta}} \right) + \frac{\tau_{\mathcal{E}}}{\tau_h} \sigma_{\mathcal{E}} e^{\frac{t}{\tau_h}} \left(V_t - \int_0^t e^{\frac{s-t}{\tau_{\mathcal{E}}}} dV_s \right) + \sigma_\eta e^{\frac{t}{\tau_h}} \int_0^t e^{\frac{s-t}{\tau_\eta}} dW_s \tag{2.62}$$

or:

$$A = \frac{\tau_{\mathcal{E}}}{\tau_h} \mathcal{E}_0 \left(1 - e^{-\frac{t}{\tau_{\mathcal{E}}^\star}} \right) - \eta_0 \left(1 - e^{-\frac{t}{\tau_\eta^\star}} \right) + \frac{\tau_{\mathcal{E}}}{\tau_h} \sigma_{\mathcal{E}} e^{\frac{t}{\tau_h}} \left(V_t - \int_0^t e^{\frac{s-t}{\tau_{\mathcal{E}}}} dV_s \right) + \sigma_\eta e^{\frac{t}{\tau_h}} \int_0^t e^{\frac{s-t}{\tau_\eta}} dW_s$$

(2.63)

with $\tau_{\mathcal{E}}^{\star} = \frac{\tau_h \tau_{\mathcal{E}}}{\tau_h - \tau_{\mathcal{E}}}$ and $\tau_{\eta}^{\star} = \frac{\tau_h \tau_{\eta}}{\tau_h - \tau_{\eta}}$

We can simplify $V_t - \int_0^t e^{\frac{s-t}{\tau_{\mathcal{E}}}} dV_s$, indeed by applying the integration by parts formula to the second term, we have:

$$\begin{aligned} V_t - \int_0^t e^{\frac{s-t}{\tau_{\mathcal{E}}}} dV_s &= V_t - \left[e^{\frac{s-t}{\tau_{\mathcal{E}}}} V_s \right]_0^t + \frac{1}{\tau_{\mathcal{E}}} \int_0^t e^{\frac{s-t}{\tau_{\mathcal{E}}}} V_s ds \\ &= V_t - \left(e^{\frac{t-t}{\tau_{\mathcal{E}}}} V_t - e^{\frac{0-t}{\tau_{\mathcal{E}}}} V_0 \right) + \frac{1}{\tau_{\mathcal{E}}} \int_0^t e^{\frac{s-t}{\tau_{\mathcal{E}}}} V_s ds \\ &= V_t - (V_t - 0) + \frac{1}{\tau_{\mathcal{E}}} \int_0^t e^{\frac{s-t}{\tau_{\mathcal{E}}}} V_s ds \\ &= \frac{1}{\tau_{\mathcal{E}}} \int_0^t e^{\frac{s-t}{\tau_{\mathcal{E}}}} V_s ds \end{aligned} \tag{2.64}$$

We finally express A as follows:

$$A = \frac{\tau_{\mathcal{E}}}{\tau_h} \mathcal{E}_0 \left(1 - e^{-\frac{t}{\tau_{\mathcal{E}}^{\star}}} \right) - \eta_0 \left(1 - e^{-\frac{t}{\tau_{\eta}^{\star}}} \right) + \frac{\sigma_{\mathcal{E}}}{\tau_h} e^{\frac{t}{\tau_h}} \int_0^t e^{\frac{s-t}{\tau_{\mathcal{E}}}} V_s ds + \sigma_{\eta} e^{\frac{t}{\tau_h}} \int_0^t e^{\frac{s-t}{\tau_{\eta}}} dW_s \tag{2.65}$$

We are going now to develop the expression of B:

$$\begin{aligned} B &= \int_0^t e^{\frac{s}{\tau_h}} \left(\frac{\tau_{\mathcal{E}}}{\tau_h} \left(-\mathcal{E}_0 e^{\frac{-s}{\tau_{\mathcal{E}}}} - \sigma_{\mathcal{E}} \int_0^s e^{\frac{u-s}{\tau_{\mathcal{E}}}} dV_u + \sigma_{\mathcal{E}} V_s \right) + \eta_0 e^{\frac{-s}{\tau_{\eta}}} + \sigma_{\eta} \int_0^s e^{\frac{u-s}{\tau_{\eta}}} dW_u \right) \frac{ds}{\tau_h} \\ &= \int_0^t e^{\frac{s}{\tau_h}} \left(\frac{\tau_{\mathcal{E}}}{\tau_h} \left(-\mathcal{E}_0 e^{\frac{-s}{\tau_{\mathcal{E}}}} + \frac{\sigma_{\mathcal{E}}}{\tau_{\mathcal{E}}} \int_0^s e^{\frac{u-s}{\tau_{\mathcal{E}}}} V_u du \right) + \eta_0 e^{\frac{-s}{\tau_{\eta}}} + \sigma_{\eta} \int_0^s e^{\frac{u-s}{\tau_{\eta}}} dW_u \right) \frac{ds}{\tau_h} \end{aligned} \tag{2.66}$$

$$\begin{aligned} B = -\mathcal{E}_0 \frac{\tau_{\mathcal{E}}}{\tau_h^2} \int_0^t e^{\frac{-s}{\tau_{\mathcal{E}}^{\star}}} ds + \frac{\sigma_{\mathcal{E}}}{\tau_h^2} \int_0^t e^{\frac{-s}{\tau_{\mathcal{E}}^{\star}}} \int_0^s e^{\frac{u}{\tau_{\mathcal{E}}}} V_u du ds + \\ + \frac{\eta_0}{\tau_h} \int_0^t e^{\frac{-s}{\tau_{\eta}^{\star}}} ds + \frac{\sigma_{\eta}}{\tau_h} \int_0^t e^{\frac{-s}{\tau_{\eta}^{\star}}} \int_0^s e^{\frac{u}{\tau_{\eta}}} dW_u ds \end{aligned} \tag{2.67}$$

$$\begin{aligned} B = -\frac{\tau_{\mathcal{E}}}{\tau_h} \mathcal{E}_0 \frac{\tau_{\mathcal{E}}}{\tau_h - \tau_{\mathcal{E}}} \left(1 - e^{\frac{-t}{\tau_{\mathcal{E}}^{\star}}} \right) + \frac{\sigma_{\mathcal{E}}}{\tau_h^2} \int_0^t e^{\frac{-s}{\tau_{\mathcal{E}}^{\star}}} \int_0^s e^{\frac{u}{\tau_{\mathcal{E}}}} V_u du ds - \\ + \eta_0 \frac{\tau_{\eta}}{\tau_h - \tau_{\eta}} \left(1 - e^{\frac{-t}{\tau_{\eta}^{\star}}} \right) + \frac{\sigma_{\eta}}{\tau_h} \int_0^t e^{\frac{-s}{\tau_{\eta}^{\star}}} \int_0^s e^{\frac{u}{\tau_{\eta}}} dW_u ds \end{aligned} \tag{2.68}$$

by combining equations 2.65 and 2.68, we obtain ($C = A - B$):

$$C = \mathcal{E}_0 \frac{\tau_\mathcal{E}}{\tau_h - \tau_\mathcal{E}} \left(1 - e^{\frac{-t}{\tau_\mathcal{E}^\star}}\right) - \eta_0 \frac{\tau_h}{\tau_h - \tau_\eta} \left(1 - e^{\frac{-t}{\tau_\eta^\star}}\right) +$$
$$+ \frac{\sigma_\mathcal{E}}{\tau_h} \left(e^{\frac{t}{\tau_h}} \int_0^t e^{\frac{s-t}{\tau_\mathcal{E}}} V_s ds - \frac{1}{\tau_h} \int_0^t e^{\frac{-s}{\tau_\mathcal{E}^\star}} \int_0^s e^{\frac{u}{\tau_\mathcal{E}}} V_u du ds \right) +$$
$$+ \frac{\sigma_\eta}{\tau_h} \left(\tau_h e^{\frac{t}{\tau_h}} \int_0^t e^{\frac{s-t}{\tau_\eta}} dW_s - \int_0^t e^{\frac{-s}{\tau_\eta^\star}} \int_0^s e^{\frac{u}{\tau_\eta}} dW_u ds \right) \quad (2.69)$$

we divide each side of equation 2.58 by $e^{\frac{-t}{\tau_h}}$ and obtain:

$$\widetilde{\rho}_u^{(k)}(t) = \widetilde{\rho}_u^{(k)}(0) e^{\frac{-t}{\tau_h}} + \int_0^t e^{\frac{s-t}{\tau_h}} \mu_u^{(k)}(s) \frac{ds}{\tau_h} + C e^{\frac{-t}{\tau_h}} \quad (2.70)$$

with

$$C e^{\frac{-t}{\tau_h}} = \mathcal{E}_0 \frac{\tau_\mathcal{E}}{\tau_h - \tau_\mathcal{E}} e^{\frac{-t}{\tau_h}} \left(1 - e^{\frac{-t}{\tau_\mathcal{E}^\star}}\right) - \eta_0 \frac{\tau_h}{\tau_h - \tau_\eta} e^{\frac{-t}{\tau_h}} \left(1 - e^{\frac{-t}{\tau_\eta^\star}}\right) +$$
$$+ \frac{\sigma_\mathcal{E}}{\tau_h} \left(e^{\frac{t}{\tau_h}} \int_0^t e^{\frac{s-t}{\tau_\mathcal{E}}} V_s ds - \frac{1}{\tau_h} \int_0^t e^{\frac{-s}{\tau_\mathcal{E}^\star}} \int_0^s e^{\frac{u}{\tau_\mathcal{E}}} V_u du ds \right) e^{\frac{-t}{\tau_h}} +$$
$$+ \frac{\sigma_\eta}{\tau_h} \left(\tau_h e^{\frac{t}{\tau_h}} \int_0^t e^{\frac{s-t}{\tau_\eta}} dW_s - \int_0^t e^{\frac{-s}{\tau_\eta^\star}} \int_0^s e^{\frac{u}{\tau_\eta}} dW_u ds \right) e^{\frac{-t}{\tau_h}} \quad (2.71)$$

We assume that all random variables are over-bounded by Gaussian distributions and $\widetilde{\rho}_u^{(k)}(0), \mathcal{E}_0, \eta_0, dV_t$ and dW_t for all t are independent.

As a consequence, $\widetilde{\rho}_u^{(k)}(t)$ is Gaussian distributed for each epoch t and therefore it is sufficient to determine its expectation and variance to determine the whole distribution. We want to estimate $E\left[\widetilde{\rho}_u^{(k)}(t)\right]$ and $V\left[\widetilde{\rho}_u^{(k)}(t)\right]$ for any t.

$$E\left[\widetilde{\rho}_u^{(k)}(t)\right] = E\left[\widetilde{\rho}_u^{(k)}(0)\right] e^{\frac{-t}{\tau_h}} + \int_0^t e^{\frac{s-t}{\tau_h}} \mu_u^{(k)}(s) \frac{ds}{\tau_h} + E[C] e^{\frac{-t}{\tau_h}} \quad (2.72)$$

with

$$E[C] e^{\frac{-t}{\tau_h}} = E[\mathcal{E}_0] \frac{\tau_\mathcal{E}}{\tau_h - \tau_\mathcal{E}} e^{\frac{-t}{\tau_h}} \left(1 - e^{\frac{-t}{\tau_\mathcal{E}^\star}}\right) - E[\eta_0] \frac{\tau_h}{\tau_h - \tau_\eta} e^{\frac{-t}{\tau_h}} \left(1 - e^{\frac{-t}{\tau_\eta^\star}}\right) \quad (2.73)$$

The variance is by definition $\mathcal{V}\left[\widetilde{\rho}_u^{(k)}(t)\right] = E\left[\left(\widetilde{\rho}_u^{(k)}(t) - E\left[\widetilde{\rho}_u^{(k)}(t)\right]\right)^2\right]$

Let's define the following notation for a random variable X we set $\check{X} = X - E[X]$

$$\begin{aligned}\overset{\vee}{\widetilde{\rho}}_u^{(k)}(t) = \overset{\vee}{\widetilde{\rho}}_u^{(k)}(0)\, e^{\frac{-t}{\tau_h}} + \check{\mathcal{E}}_0 \frac{\tau_\mathcal{E}}{\tau_h - \tau_\mathcal{E}} e^{\frac{-t}{\tau_h}}\left(1 - e^{\frac{-t}{\tau_\mathcal{E}^\star}}\right) - \check{\eta}_0 \frac{\tau_h}{\tau_h - \tau_\eta} e^{\frac{-t}{\tau_h}}\left(1 - e^{\frac{-t}{\tau_\eta^\star}}\right) + \\ + \frac{\sigma_\mathcal{E}}{\tau_h}\left(\int_0^t e^{\frac{s-t}{\tau_\mathcal{E}}} V_s ds - \frac{e^{\frac{-t}{\tau_h}}}{\tau_h}\int_0^t e^{\frac{-s}{\tau_\mathcal{E}^\star}}\int_0^s e^{\frac{u}{\tau_\mathcal{E}}} V_u du ds\right) + \\ + \frac{\sigma_\eta}{\tau_h}\left(\tau_h \int_0^t e^{\frac{s-t}{\tau_\eta}} dW_s - e^{\frac{-t}{\tau_h}}\int_0^t e^{\frac{-s}{\tau_\eta^\star}}\int_0^s e^{\frac{u}{\tau_\eta}} dW_u ds\right) \quad (2.74)\end{aligned}$$

We apply an integration by parts for the terms in dW_s and dW_u in order to let appear classical Riemann integrals.

We have

$$\begin{aligned}\int_0^t e^{\frac{s-t}{\tau_\eta}} dW_s &= \left[e^{\frac{s-t}{\tau_\eta}} W_s\right]_0^t - \frac{1}{\tau_\eta}\int_0^t e^{\frac{s-t}{\tau_\eta}} W_s ds \\ &= W_t - \frac{1}{\tau_\eta}\int_0^t e^{\frac{s-t}{\tau_\eta}} W_s ds \quad (2.75)\end{aligned}$$

So we have

$$\begin{aligned}\overset{\vee}{\widetilde{\rho}}_u^{(k)}(t) = \overset{\vee}{\widetilde{\rho}}_u^{(k)}(0)\, e^{\frac{-t}{\tau_h}} + \check{\mathcal{E}}_0 \frac{\tau_\mathcal{E}}{\tau_h - \tau_\mathcal{E}} e^{\frac{-t}{\tau_h}}\left(1 - e^{\frac{-t}{\tau_\mathcal{E}^\star}}\right) - \check{\eta}_0 \frac{\tau_h}{\tau_h - \tau_\eta} e^{\frac{-t}{\tau_h}}\left(1 - e^{\frac{-t}{\tau_\eta^\star}}\right) + \\ + \frac{\sigma_\mathcal{E}}{\tau_h}\left(\int_0^t e^{\frac{s-t}{\tau_\mathcal{E}}} V_s ds - \frac{e^{\frac{-t}{\tau_h}}}{\tau_h}\int_0^t e^{\frac{-s}{\tau_\mathcal{E}^\star}}\int_0^s e^{\frac{u}{\tau_\mathcal{E}}} V_u du ds\right) + \\ + \frac{\sigma_\eta}{\tau_h}\left(\tau_h W_t - \frac{\tau_h}{\tau_\eta}\int_0^t e^{\frac{s-t}{\tau_\eta}} W_s ds - e^{\frac{-t}{\tau_h}}\int_0^t e^{\frac{-s}{\tau_\eta^\star}}\left[W_s - \frac{1}{\tau_\eta}\int_0^s e^{\frac{u}{\tau_\eta}} W_u du\right] ds\right) \quad (2.76)\end{aligned}$$

And after simplification of the last term we obtain:

$$\overset{\vee}{\widetilde{\rho}}_u^{(k)}(t) = \overset{\vee}{\widetilde{\rho}}_u^{(k)}(0)\, e^{\frac{-t}{\tau_h}} + \check{\mathcal{E}}_0 \frac{\tau_{\mathcal{E}}}{\tau_h - \tau_{\mathcal{E}}} e^{\frac{-t}{\tau_h}} \left(1 - e^{\frac{-t}{\tau_{\mathcal{E}}^{\star}}}\right) - \check{\eta}_0 \frac{\tau_h}{\tau_h - \tau_\eta} e^{\frac{-t}{\tau_h}} \left(1 - e^{\frac{-t}{\tau_\eta^{\star}}}\right) +$$
$$+ \frac{\sigma_{\mathcal{E}}}{\tau_h} \left(\int_0^t e^{\frac{s-t}{\tau_{\mathcal{E}}}} V_s ds - \frac{e^{\frac{-t}{\tau_h}}}{\tau_h} \int_0^t e^{\frac{-s}{\tau_{\mathcal{E}}^{\star}}} \int_0^s e^{\frac{u}{\tau_{\mathcal{E}}}} V_u du ds \right) +$$
$$+ \sigma_\eta \left(W_t - \int_0^t \left[\frac{1}{\tau_\eta} e^{\frac{s-t}{\tau_\eta}} + \frac{1}{\tau_h} e^{\frac{s-t}{\tau_h}} e^{\frac{-s}{\tau_\eta}} \right] W_s ds + \frac{1}{\tau_\eta \tau_h} \int_0^t \int_0^s e^{\frac{u-s}{\tau_\eta} + \frac{s-t}{\tau_h}} W_u du ds \right) \tag{2.77}$$

Taking into account the fact that the random variables are independent, a cross product of two different random variables or integral of random variable will have its expectation being zero. In fact this assumption is for $\overset{\vee}{\widetilde{\rho}}_u^{(k)}(0)$ and for $\check{\mathcal{E}}_0$ not true because the filter take the code measurements as a starting point. In fact these variable are not only dependent, they are taken as the same. Let's consider for more generality, that they are processed independently.

$$V\left[\widetilde{\rho}_u^{(k)}(t)\right] = E\left[\left(\overset{\vee}{\widetilde{\rho}}_u^{(k)}(t)\right)^2\right] = V\left[\widetilde{\rho}_u^{(k)}(0)\right] e^{\frac{-2t}{\tau_h}} +$$
$$+ V[\mathcal{E}_0] \left(\frac{\tau_{\mathcal{E}}}{\tau_h - \tau_{\mathcal{E}}}\right)^2 e^{\frac{-2t}{\tau_h}} \left(1 - e^{\frac{-t}{\tau_{\mathcal{E}}^{\star}}}\right)^2 + V[\eta_0] \left(\frac{\tau_h}{\tau_h - \tau_\eta}\right)^2 e^{\frac{-2t}{\tau_h}} \left(1 - e^{\frac{-t}{\tau_\eta^{\star}}}\right)^2 +$$
$$+ \frac{\sigma_{\mathcal{E}}^2}{\tau_h^2} E\left[\left(\underbrace{\int_0^t e^{\frac{s-t}{\tau_{\mathcal{E}}}} V_s ds - \frac{e^{\frac{-t}{\tau_h}}}{\tau_h} \int_0^t e^{\frac{-s}{\tau_{\mathcal{E}}^{\star}}} \int_0^s e^{\frac{u}{\tau_{\mathcal{E}}}} V_u du ds}_{D_t} \right)^2 \right] +$$
$$+ \sigma_\eta^2 E\left[\left(\underbrace{W_t - \int_0^t \left[\frac{1}{\tau_\eta} e^{\frac{s-t}{\tau_\eta}} + \frac{1}{\tau_h} e^{\frac{s-t}{\tau_h}} e^{\frac{-s}{\tau_\eta}} \right] W_s ds + \frac{1}{\tau_\eta \tau_h} \int_0^t \int_0^s e^{\frac{u-s}{\tau_\eta} + \frac{s-t}{\tau_h}} W_u du ds}_{P_t} \right)^2 \right]$$

Let's develop the expression inside the first expectation: $D_t = \int_0^t e^{\frac{s-t}{\tau_{\mathcal{E}}}} V_s ds - \frac{e^{\frac{-t}{\tau_h}}}{\tau_h} \int_0^t e^{\frac{-s}{\tau_{\mathcal{E}}^{\star}}} \int_0^s e^{\frac{u}{\tau_{\mathcal{E}}}} V_u du ds$
See in Appendix the analytical form of $E[D_t^2]$.
In a similar way we determine $E[P_t^2]$

$$P_t = \tau_h W_t - \frac{\tau_h}{\tau_\eta} \int_0^t e^{\frac{s-t}{\tau_\eta}} W_s ds - e^{\frac{-t}{\tau_h}} \int_0^t e^{\frac{-s}{\tau_\eta^{\star}}} \left(e^{\frac{s}{\tau_\eta}} W_s - \frac{1}{\tau_\eta} \int_0^s e^{\frac{u}{\tau_\eta}} W_u du \right) ds$$
$$= \tau_h W_t - \int_0^t \left(\frac{\tau_h}{\tau_\eta} e^{\frac{s-t}{\tau_\eta}} + e^{\frac{s-t}{\tau_h}} \right) W_s ds + \frac{1}{\tau_\eta} \int_0^t \int_0^s e^{\frac{u-s}{\tau_\eta} + \frac{s-t}{\tau_h}} W_u du ds \tag{2.78}$$

See in Appendix the analytical form of $E[P_t^2]$.

Finally we can express the variance of the Hatch filter with respect to the parameters of the problem. As this expression is very long, we don't rewrite it here (See Appendix C)

2.6. Conclusion

This chapter describes the characterization of the individual errors for stand alone global positioning services and their impact in positioning performances. The major contribution made is the introduction of the notion of IPRE and its statistical analysis when used for single constellation GPS [BPH05a] and dual constellation using GPS and Galileo [BHS05a, BHS05b]. This notion is going to be applied for integrity monitoring algorithm developed in the next chapter and for the differential correction modes using augmentation to GNSS constellation.
Additionally we developed a closed form of the Hatch filter performance function of the time constant of the filter, the variance of the code and phase multipath and noise and the time using the general theory of stochastic differential equations applied to Gaussian overbounds of the errors.

3. Investigation of Autonomous Fault Detection

3.1. Introduction

The IPRE (Instantaneous Pseudo Range Error) provides not only a level of instantaneous error but also a "look up table" from which a co-variance matrix of satellites on visibility can be extracted. The method will be detailed later in this chapter. This means that at each time step, the user is able to calculate an empirical co-variance matrix of the visible satellites based on one year measurements from an IGS station. The generated look up table is defined regionally (around the station used for data collection). This means that the satellite configuration (which repeats itself almost every day for GPS) is assumed not to change within a radius of approximately 50 km around the co-variance measurement site. We will see in the next section why it is so important to be inside this area. A first part of this chapter will consist of presenting the standard Receiver Autonomous Integrity Monitoring (RAIM) algorithm and the assumptions considered then a second part will consist of modeling the co-variance matrix of pseudo range noise for a given location. A second part will be dedicated to the description of the RAIM algorithms used in this chapter with a special emphasize on the integration of a generalized noise model. In a third part, we will present the simulation test cases that have been chosen. In a last part, we will present the results and we will draw some conclusions of the impact of a GPS/Galileo constellation on RAIM availability and performances.

3.2. RAIM algorithm

As a minimum configuration of a receiver for aviation, the GNSS receiver should provide a standalone single frequency GPS RAIM algorithm and a good description of this algorithm can be found in [SC101]. A summary of the description is given hereafter (see [CCH+06] for more details).
There are 3 different functions that are expected from a RAIM algorithm: to detect possible faulty pseudo ranges, to exclude the faulty pseudo ranges and to provide a fault free confidence measure in the position domain to fulfill some alert limit and integrity risk requirements. We will focus mainly on the fault free confidence measure

function of the RAIM algorithm in this chapter based on chi-squared distribution technique as developed in[WE95] [BC98].

The standard RAIM algorithm uses an over-determined solution (more than 4 measurements) to perform a self-consistency check on the satellite measurements.

Starting with the linearized GNSS measurement equation as described in sec. 2.2:

$$\rho = \mathbf{G}x + \Delta\rho \tag{3.1}$$

Where x is the four (or five, when using Galileo $\begin{pmatrix} x_1 & x_2 & x_3 & \delta t_{GPS} & \delta t_{Gal} \end{pmatrix}^T$ with $\begin{pmatrix} x_1 & x_2 & x_3 \end{pmatrix}$ being the spatial coordinate of the user, δt_{GPS} being the receiver bias to the GPS system time and δt_{Gal} being the receiver bias to the Galileo system time). $\Delta\rho$ is the Gaussian overbound of the pseudo range error vector and ρ is the vector of pseudo ranges.

The vector of observations can be described as the sum of a first term function of the unknown position and receiver clock delay and a residual error of observations.

A weighted least square estimate of the unknown vector is expressed as follows:

$$\hat{x} = \left(\mathbf{G}^T\mathbf{W}\mathbf{G}\right)^{-1}\mathbf{G}^T\mathbf{W}\rho = \mathbf{S}\rho \tag{3.2}$$

$\mathbf{W} = \mathbf{C}^{-1}$ is the weighting matrix with $\mathbf{C}$ being the covariance matrix of the pseudo-range error.

$$\hat{\rho} = \mathbf{G}\hat{x} \tag{3.3}$$

The position error made when using the least squares algorithm is given by

$$e_{WGS84} = \Delta x = \hat{x} - x$$

$$e_{WGS84} = \mathbf{S}\rho - x$$

$$e_{WGS84} = \mathbf{S}(\mathbf{G}x + \Delta\rho) - x$$

$$e_{WGS84} = \mathbf{S}\Delta\rho$$

Because x is given in the WGS84 ECEF referential, the error is defined in this referential too. And since it is more convenient to work in the user local coordinate

system (East North Up) (ENU) a transformation (rotation) $\mathbf{T}_{WGS84}^{ENU}$ needs to be applied.

$$e_{ENU} = \mathbf{T}_{WGS84}^{ENU} e_{WGS84}$$

Thus

$$e_{ENU} = \mathbf{T}_{WGS84}^{ENU} \mathbf{S} \Delta\rho$$

$$e_{ENU} = \mathbf{M} \Delta\rho \tag{3.4}$$

With $\mathbf{M} = \mathbf{T}_{WGS84}^{ENU} \mathbf{S}$. This expression allows us to define both e_{ENU}^{h} the horizontal error vector and e_{ENU}^{v} the vertical error vector such that

$$e_{ENU}^{h} = \begin{pmatrix} e_{ENU}(1) \\ e_{ENU}(2) \end{pmatrix}$$

And

$$e_{ENU}^{v} = e_{ENU}(3)$$

Moreover it comes,

$$V\left[e_{ENU}\right] = \mathbf{T}_{WGS84}^{ENU} \mathbf{S} \mathbf{C} \mathbf{S}^{T} \mathbf{T}_{WGS84}^{ENU^{T}}$$

And we note

$$V\left[e_{ENU}\right] = \begin{pmatrix} \sigma_{e_E}^2 & \sigma_{e_E e_N} & \sigma_{e_E e_U} & \sigma_{e_E e_{dt}} \\ \sigma_{e_N e_E} & \sigma_{e_N}^2 & \sigma_{e_N e_U} & \sigma_{e_N e_{dt}} \\ \sigma_{e_U e_E} & \sigma_{e_U e_N} & \sigma_{e_U}^2 & \sigma_{e_U e_{dt}} \\ \sigma_{e_{dt} e_E} & \sigma_{e_{dt} e_N} & \sigma_{e_{dt} e_U} & \sigma_{e_{dt}}^2 \end{pmatrix}$$

Since the measurement noise covariance matrix is considered to be general, we can no longer separate the expected positioning errors into dilution of precision parameters and UERE. We choose to express new confidence parameters,

- the expected global accuracy is:
$$\sqrt{\sigma_{e_E}^2 + \sigma_{e_N}^2 + \sigma_{e_U}^2 + \sigma_{e_{dt}}^2}$$
- the expected position accuracy is:
$$\sqrt{\sigma_{e_E}^2 + \sigma_{e_N}^2 + \sigma_{e_U}^2}$$
- the expected horizontal accuracy is:
$$\sqrt{\sigma_{e_E}^2 + \sigma_{e_N}^2}$$
- the expected vertical accuracy is:
$$\sigma_{e_U}$$
- the expected time accuracy is:
$$\sigma_{e_{dt}}$$

3.2.1. Generalized single fault detection [Gas05]

One of the most important RAIM function is to be able to detect faulty satellites using self-consistency check of visible pseudo ranges. For that purpose, we will use, like in the RAIM method developed in ([CCH+06] pp. 346-353), the least squared residual as a test statistics.

the least square residuals can be expressed by:

$$w = \rho - \hat{\rho} = \rho - \mathbf{S}\rho = [\mathbf{I}_n - \mathbf{S}]\,\rho = \mathbf{Q}\rho \tag{3.5}$$

When no faults are observed the over-bounded Gaussian distribution of each element of w is centered around zero. A fault in one satellite is modeled as a bias in the satellite range.

replacing ρ by its expression in equation 3.1 we have:

$$w = \mathbf{Q}\Delta\rho \tag{3.6}$$

so we have:

$$w = \mathbf{Q}\rho = \mathbf{Q}\Delta\rho \tag{3.7}$$

we then proceed with a parity transformation of the observation vector. This transformation can be obtained using a QR decomposition of the geometry matrix $\mathbf{G}$. The matrix obtained by this transformation $\mathbf{P}$ called the parity transformation matrix is a $(n-4) \times n$ matrix and we set $\mathbf{p} = \mathbf{P}\rho$. The rows of $\mathbf{P}$ has the following properties:

- they are mutually orthogonal
- they are of magnitude one
- they are mutually orthogonal to the column of $\mathbf{G}$

So with these properties, if $\Delta\rho$ has independent random elements and are normally distributed, then:

$$\mathbf{p} = \mathbf{P}w \tag{3.8}$$

$$\mathbf{p} = \mathbf{P}\Delta\rho \tag{3.9}$$

$$\mathbf{p}^T\mathbf{p} = w^T w \tag{3.10}$$

For error detection, it is easier to work with $\mathbf{p}$ than with w. But working with $\mathbf{p}$ reduces the dimension of the tests but necessitate to make a QR decomposition which can be for large number of visible satellites intensive processing. Working with w has the disadvantage of having measurements in it which makes the error detection not straight forward but the processing time is reduced.

It has been demonstrated that if $\mathbf{C} = \sigma^2\mathbf{I}$ the square norm of the residuals follows a χ^2 law with $N-4$ degrees of freedom ([Bro92]). The problem in our case is that the diagonal elements of the covariance matrix of noise are different for each satellite and that the range errors are correlated. Thus the assumption that $\|w\|^2$ is following a χ^2 law is no longer true.

But, since the covariance matrix $\mathbf{C}$ is by definition definite positive, we can do a Cholesky decomposition of it. So it exists one unique non-singular lower triangular matrix $\mathbf{A}$ such that:

$$\mathbf{C} = \mathbf{A}\mathbf{A}^T$$

According to this property, we can define a new vector of measurement noise, ε', following a normal $\mathcal{N}(0, \mathbf{I}_N)$ law such that ε follows the same law as $\mathbf{A}\varepsilon'$. Moreover it comes:

$$\begin{aligned}
\rho &= \mathbf{G}x + \Delta\rho \\
\rho &= \mathbf{G}x + \mathbf{A}\Delta\rho' \\
\mathbf{A}^{-1}\rho &= \mathbf{A}^{-1}\mathbf{G}x + \Delta\rho' \\
\rho' &= \mathbf{G}'x + \Delta\rho'
\end{aligned}$$

From this new measurement model, where $V[\Delta\rho'] = \mathbf{I}$ we can form new LS residuals,

$$\begin{aligned}
w' &= \rho' - \hat{\rho}' \\
w' &= \mathbf{A}^{-1}w
\end{aligned}$$

Thanks to the definition of $\Delta\rho'$, the square norm of the random variable w' is following a χ^2 distribution with $N-4$ degrees of freedom. We are now able to select the error detection threshold T_d by inverting the cumulative density function (CDF) of $\|w'\|^2$.
This transformation is my personal contribution and the adaptations of classical methods of RAIM in the rest of this chapter is also my personal contribution.

3.2.2. Protection levels (see definition in chapter 1)

To compute the protection levels we have to see first how an error affects the LS residuals vector w',

$$w' = \mathbf{A}^{-1}\mathbf{Q}\Delta\rho$$
$$\|w'\| = \Delta\rho^T\mathbf{Q}^T\mathbf{A}^{-T}\mathbf{A}^{-1}\mathbf{Q}\Delta\rho$$
$$\|w'\| = \Delta\rho^T\mathbf{Q}_{w'}\Delta\rho$$

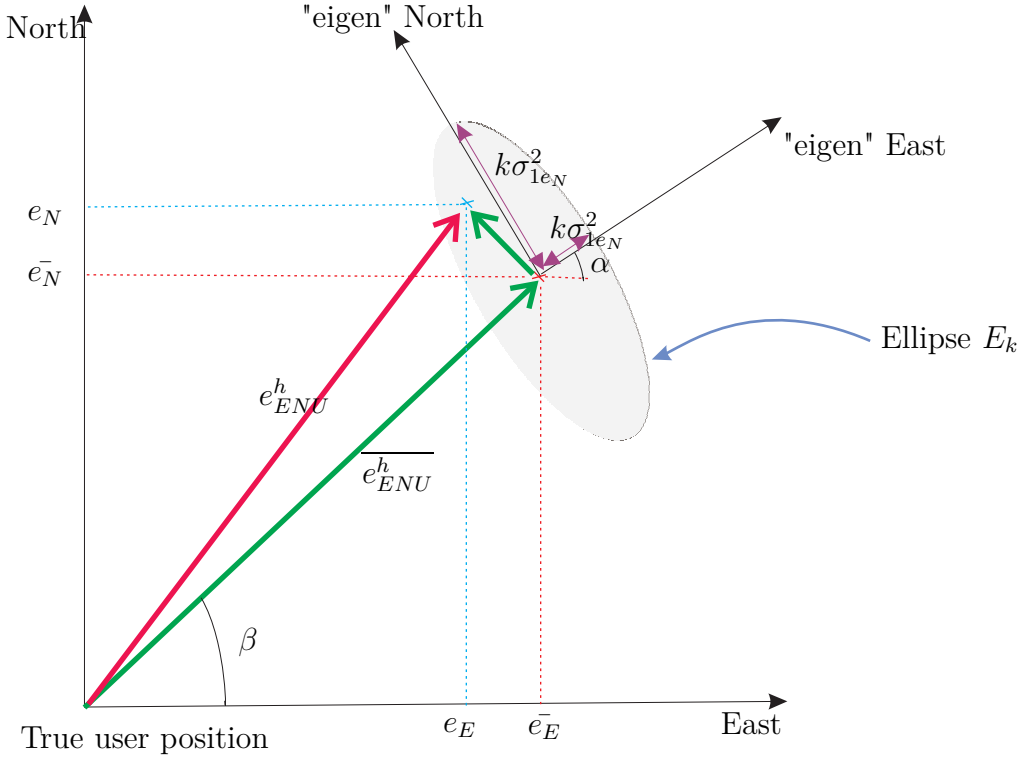

Figure 3.1.: Failure impact on the horizontal user position

A faulty satellite is characterized by a bias b in its pseudo range. We note $E[\Delta\rho] = \theta$ the expectation value of the random pseudo-range noise vector. If there is a failure in one[1] of the visible satellites it comes:

$$\theta = \begin{pmatrix} 0 \\ \vdots \\ b \\ \vdots \\ 0 \end{pmatrix}$$

[1]We only consider one satellite failure in our analysis, this hypothesis is of course a bit restrictive because in real operational conditions the environment may induce several biases on measurements.

with b in the i^{th} satellite. Thus

$$\|w'\|^2 = \mathbf{Q}_{w'}(i,i)b^2$$

b is set as an unknown. A test based on assumed integrity risk and continuity requirements will define the minimum detectable bias that fulfill these requirements and this is the basis for the protection level estimation.

3.2.3. Horizontal Protection Level

If we consider the horizontal solution error e^h_{ENU}, it can be shown that (equation 3.4)

$$\|e^h_{ENU}\|^2 = (\mathbf{M}(1,i)^2 + \mathbf{M}(2,i)^2)b^2$$

Thus

$$\|e^h_{ENU}\|^2 = \frac{\mathbf{M}(1,i)^2 + \mathbf{M}(2,i)^2}{\mathbf{Q}_{w'}(i,i)}\|w'\|^2$$

where $\mathbf{M} = \mathbf{T}^{ENU}_{WGS84}\mathbf{S}$ The quantity $\sqrt{\frac{\mathbf{M}(1,i)^2+\mathbf{M}(2,i)^2}{\mathbf{Q}_{w'}(i,i)}}$ is called the horizontal slope (H-Slope) and the i index tells us that it is dependent on the satellite we have supposed to fail. So, with the no noise assumption ($\varepsilon = \theta$) the horizontal value that we can protect is

$$\text{HPL} = \max_{i=1\ldots N} \text{HSlope}(i) \times T_d$$

In this equation T_d represent the detection threshold for the test statistic: If the test statistic remains below this threshold, it means that no error is detected and we assume that there is no detectable fault. If the test statistic is larger than this threshold, then we declare that there is a faulty satellite in the set of visible ones. This detection threshold is determined using the probability of false alarm that the system is required not to overcome (requirement for a given operation).

But in reality the noise will spread the horizontal solution around the previous value. This spreading effect is represented in Fig. 3.1 by the ellipse. The definition of the HPL induces that there is a missed alert when the horizontal solution error is lower than the HPL value because of a too noisy environment. Let P_{md} denote this probability of missed detection.

$$P_{md} = 1 - p$$

Where p is the probability to be *inside* the ellipse. Thus the value of HPL should be set to the distance between the user true position and the furthest point from

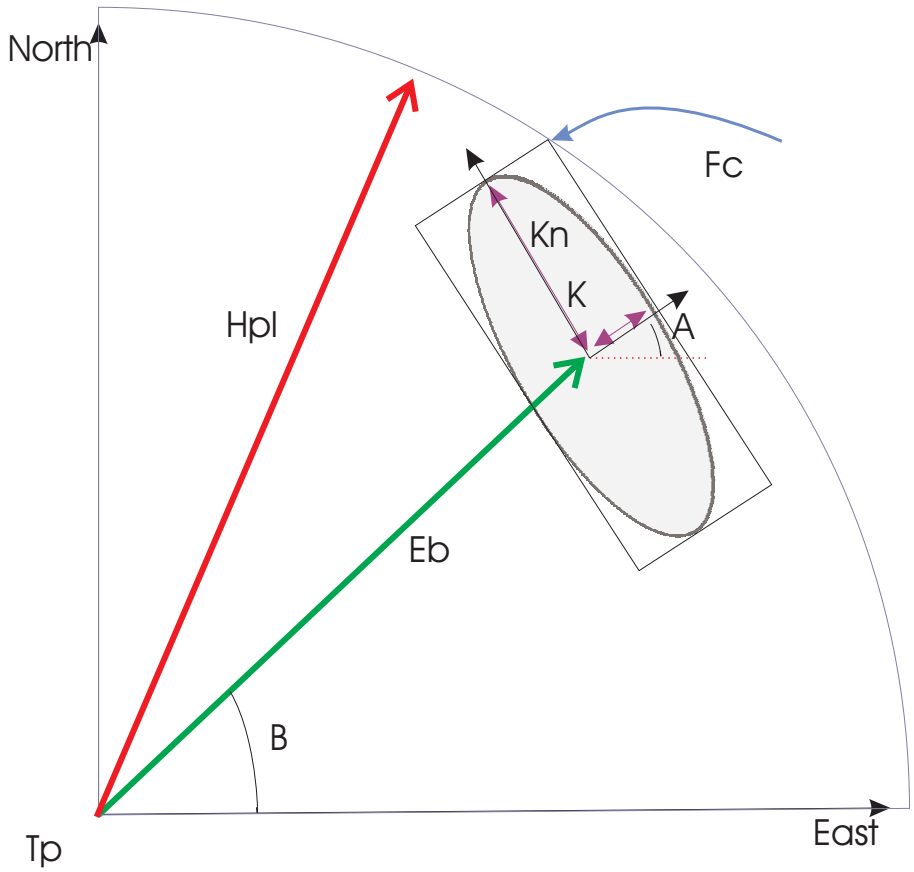

Figure 3.2.: Horizontal Protection Level practical value [You01]

the origin inside the ellipse. This means that the HPL should theoretically be the radius of the circle centered at the true position which is tangent to the ellipse. Analytically, this value is complicated to obtain and we use the estimation proposed in [You01].

The idea is to be a little bit more conservative than by considering the tangent to the ellipse and take, instead of the furthest point inside the ellipse, the furthest point of the smallest rectangle that contains the noise ellipse. This rectangle is represented in Fig. 3.2. The value of HPL is found by a vector decomposition of the OM_1 distance ($OM_1 = \|\overrightarrow{OM_1}\|$).

$$\overrightarrow{OM_1} = \overrightarrow{OC} + \overrightarrow{C\hat{A}} + \overrightarrow{AM_1} \tag{3.11}$$

Thus,

$$\begin{aligned} \|OM_1\|^2 &= \|\overrightarrow{OC}\| + \|\overrightarrow{C\hat{A}}\| + \dots \\ &\dots + \|\overrightarrow{AM_1}\| + 2\overrightarrow{OC}.\overrightarrow{C\hat{A}} + \dots \\ &\dots + 2\overrightarrow{OC}\overrightarrow{AM_1} + 2\overrightarrow{C\hat{A}}\overrightarrow{AM_1} \end{aligned}$$

With (see Fig. 3.2):

- $OC = ARP$
- $CA = k\sigma_{1e_N}$
- $AM_1 = k\sigma_{1e_e}$
- $\overrightarrow{OC} \cdot \overrightarrow{CA} = OC \cdot CA \sin(\beta - \alpha)$
- $\overrightarrow{OC} \cdot \overrightarrow{AM_1} = OC \cdot AM_1 \cos(\beta - \alpha)$
- $\overrightarrow{CA} \cdot \overrightarrow{AM_1} = 0$

So,

$$HPL = \sqrt{\begin{array}{c} ARP^2 + k^2\sigma_{1e_e}^2 + k^2\sigma_{1e_N}^2 + \dots \\ \dots + 2kARP[\sigma_{1e_N}|\sin(\beta - \alpha)| + \dots \\ \cdots + \sigma_{1e_e}|\cos(\beta - \alpha)|] \end{array}}$$

With,

$$k = \sqrt{-2\log(1-p)}$$

3.2.4. Vertical Protection Level

In similar way we can define a $VSlope$ linking the test statistic to the norm of the vertical solution error,

$$\|e^v_{ENU}\| = VSlope(i)\|w_n\|$$

Where $VSlope(i) = \sqrt{\frac{(M(3,i)^2)(N-4)}{Q_{w'}(i,i)}}$. The upper-bound value for $\|e^v_{ENU}\|$ is,

$$\|e^v_{ENU}\| \leq \max_{i=1\dots N} VSlope(i)$$

The VPL value in a no noise environment can be obtained thanks to,

$$VPL = VSlope_{max} \times T_d$$

In considering the noise, the VPL value is much easier to evaluate than the HPL because the vertical error is one-dimensional Gaussian variable.

$$e^v_{ENU} \sim \mathcal{N}(\overline{e^v_{ENU}}, \sigma^2_{e_U})$$

In our case we fix

$$\overline{e^v_{ENU}} = VSlope_{max} \times T_d \tag{3.12}$$

Thus the expression of VPL can be defined by

$$VPL = VSlope_{max} \times T_d + \alpha(P_{md}) \times \sigma_{e_U} \tag{3.13}$$

where $\alpha(p)$ represents the threshold for which we have all realization of a $\mathcal{N}(0,1)$ law below this threshold with a probability p. Thus we have,

$$p = Pr(X \leq \alpha) = \int_{\infty}^{\alpha} pdf(x)dx \tag{3.14}$$

where $pdf(x)$ is the probability density function for a $\mathcal{N}(0,1)$ law:

$$pdf(x) = \frac{1}{\sqrt{2\pi}} e^{-\frac{1}{2}x^2} \tag{3.15}$$

Thus,

$$p = \int_{\infty}^{\alpha} \frac{1}{\sqrt{2\pi}} e^{-\frac{1}{2}x^2} dx \tag{3.16}$$

The probability of missed detection is the probability to have the VPL value below the vertical error. This means that,

$$p = 1 - P_{md}$$

We have,

$$P_{md} = 1 - \int_{\infty}^{\alpha} \frac{1}{\sqrt{2\pi}} e^{-\frac{1}{2}x^2} dx \tag{3.17}$$

$$P_{md} = \frac{1}{2} - \int_{0}^{\alpha} \frac{1}{\sqrt{2\pi}} e^{-\frac{1}{2}x^2} dx \tag{3.18}$$

$$1 - 2P_{md} = 2\int_{0}^{\alpha} \frac{1}{\sqrt{2\pi}} e^{-\frac{1}{2}x^2} dx \tag{3.19}$$

$$1 - 2P_{md} = erf(\frac{\alpha}{\sqrt{2}}) \tag{3.20}$$

where $\text{erf}(u) = \frac{2}{\sqrt{\pi}} \int_0^u e^{-t^2} dt$. Hence we found the expression of $\alpha(P_{md})$:

$$\alpha(P_{md}) = \sqrt{2}\text{erf}^{-1}(1 - 2P_{md}) \tag{3.21}$$

And finally,

$$VPL = VSlope_{max} \times T_d + \ldots$$
$$\ldots + \sqrt{2}\text{erf}^{-1}(1 - 2P_{md}) \times \sigma_{e_U}$$

THE REST OF THIS CHAPTER IS A PERSONAL CONTRIBUTION

3.3. Regional covariance matrix of pseudo range errors

The model of covariance matrix usually taken as input for the majority of RAIM algorithms is a simple but usually said representative model of pseudo range error. As given in the introduction, one of the aims of this work is to make this covariance matrix as much representative as we can of the real pseudo range noise faced by a single frequency receiver. We do not only take into account the variations according to the elevation angle but also the cross correlations of the pseudo range errors derived from two satellites with different azimuth and elevation angles. In this section, we will first introduce the error measurements using the concept of IPRE (Instantaneous Pseudo Range Error) developed in [BPH05b] and then the practical method used to develop the regional covariance matrix of pseudo range noise. We will end this section by giving an Example of covariance matrix calculated at a given epoch at Oberpfaffenhofen near Munich (Germany).

3.3.1. The statistical analysis

The results from one year measurements of the IPRE vs. time (see precedent chapter for the expression of the IPRE) of all visible satellites for each time step is the basis to generate the covariance matrix of errors. We have a statistical process (IPRE) depending on three variables: the epoch, the elevation angle (El) and the azimuth (Az). An approach per class is adopted here and all visible satellites are considered. The idea here is to use all available measurements from all satellites and to distribute these measurements into 3 D classes (IPRE, El, Az). In order to get a representative statistics, we merge all observations at all epochs and for all satellites together. This means that we consider classes of elevation angle, classes of azimuth angle and classes of IPRE. In a first step we distribute all the measurement samples into classes.

Variables	Lower bound	Upper bound	Class width
IPRE	-15 m	15 m	0.25 m
Elevation	5°	90°	5°
Azimuth	0°	360°	10°

Table 3.1.: Field of variables

We want to generate the covariance matrix of the variable $(IPRE\,|El, Az)$: The IPRE given the elevation angle and the azimuth. The covariance study will be done with respect to (El, Az). The covariance is an inter (El, Az) class covariance with respect to the $IPRE$ variable (see Tab. 3.1 for the range of the variable classes).

n_{ijk} is the number of points belonging to the class i of elevation angle, the class j of azimuth and the class k of IPRE.

Let's take two satellites on visibility A and B whose elevation and azimuth classes are (i, j) and (i', j') respectively, the covariance between these satellite errors is calculated as follows:

$$Cov\,(A,B) = \frac{1}{N_{iji'j'}} \sum_k \sqrt{n_{ijk} n_{i'j'k}} \Big(IPRE_k - \overline{IPRE_{ij}} \Big) \Big(IPRE_k - \overline{IPRE_{i'j'}} \Big) \tag{3.22}$$

with

$$N_{iji'j'} = \sum_k \sqrt{n_{ijk} n_{i'j'k}}$$

$$\overline{IPRE_{ij}} = \frac{1}{N_{ij-}} \sum_k n_{ijk} IPRE_k$$

$$N_{ij-} = \sum_k n_{ijk}$$

This approach differs from the classical covariance of time series variables. The reason for that is that considering time series rather than the approach per IPRE class would have induced a huge period of measurement to have a representative statistics. This expression provides a 4D look up table (For each 2D point in the (El, Az) space, the covariance matrix is the covariance of the IPRE of that point with respect to the IPRE of any other point (El, Az) point in the (El, Az) space) that will be used to constitute the covariance matrix of observations for each epoch.

Fig. 3.3 is a graphical representation of the 4D look up table for a given epoch. in z axis is the value of the covariance term of a considered (Elevation, Azimuth) represented by a the red arrow with respect to any other (El, Az) point in the space. The blue arrows represent for a given epoch the location of the other visible satellites for a given epoch and the magnitude in the z axis at the blue arrow location represent the covariance term between the satellite located at this location with respect to the satellite located at the red arrow level. This look up table is available for a region around the considered IGS station for which the constellation of satellites at every epoch is considered the same. This "regional" covariance matrix of noise observables depends also on the correction algorithms considered in the model of single frequency receiver. In our case we considered the Klobuchar model for ionosphere delay correction and the MOPS model for the troposphere delay correction.

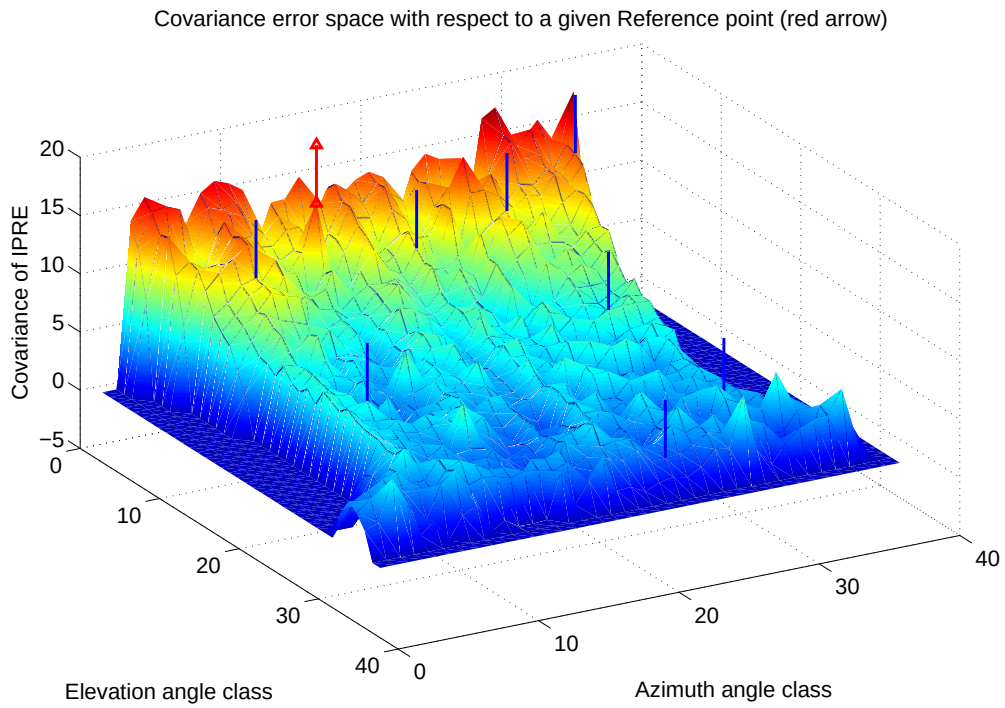

Figure 3.3.: Example of surface of covariance

3.4. Simulation scenarios

The error model has been generated for a single frequency absolute positioning receiver using the MOPS tropospheric correction model at Oberpfaffenhofen (near Munich) during the year 2003, no filtering of pseudo range has been made. We define 3 test cases used as input of RAIM algorithm:

- TC1=Generalized covariance matrix with measured variances and covariances
- TC2=Diagonal covariance matrix with measured variances for all satellites in view
- TC3=Diagonal covariance matrix with constant variance (maximal value of all satellites in view)

We use 2 constellation scenarios:

- C1=GPS alone
- C2=GPS+ Virtual Galileo Constellation

The Virtual Galileo Constellation (VGC) is adopted in our study. It consists of the GPS constellation observed at two different epochs (offset of 2 hours) [Fen05] in order to easily simulate an additional constellation for which the look up table of the regional covariance matrix would apply (see Fig. 3.4). The aim of this scenario is to see the impact of increasing the number of satellites with respect to the RAIM

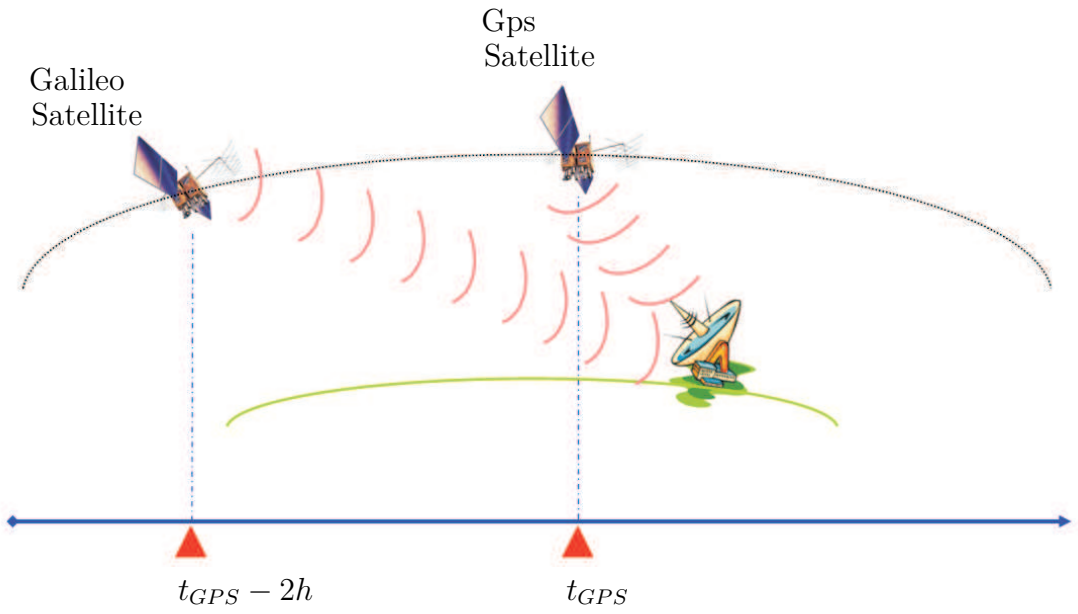

Figure 3.4.: Virtual Galileo Constellation [Fen05]

performance.

3.5. Results of the simulations

In this section, we are going to comment the HPL and VPL obtained for different test cases and different constellations configurations as defined above. We considered one day of measurements with a sampling period of 1 minute. A RAIM simulator (RaimSim) developed by DLR under a C/C++ environment has been used to process the data. The graphics are obtained using MATLAB.

Fig. 3.5 and Fig. 3.6 shows clearly an improvement of the protection levels. The Vertical component is of particular interest since this parameter is generally the most critical one because the air navigation requirements from APV1 to CAT. III (as specified in Tab. 1.1) are always considering very stringent vertical alarm limit.

Fig. 3.7 shows for a combined GPS+Galileo constellation that the improvement from TC2 to TC1 is not so obvious. The high level of fluctuations for TC1 is showing a limit of our model. A test using a different time offset (between GPS and VGC) should be done to state whether the covariance matrix or the geometry matrix are badly conditioned.

Fig. 3.8 shows the same type of behavior as previously. Nevertheless the use of a diagonal matrix with an elevation dependency is giving good results in comparison with TC3 which is obviously a too conservative case.

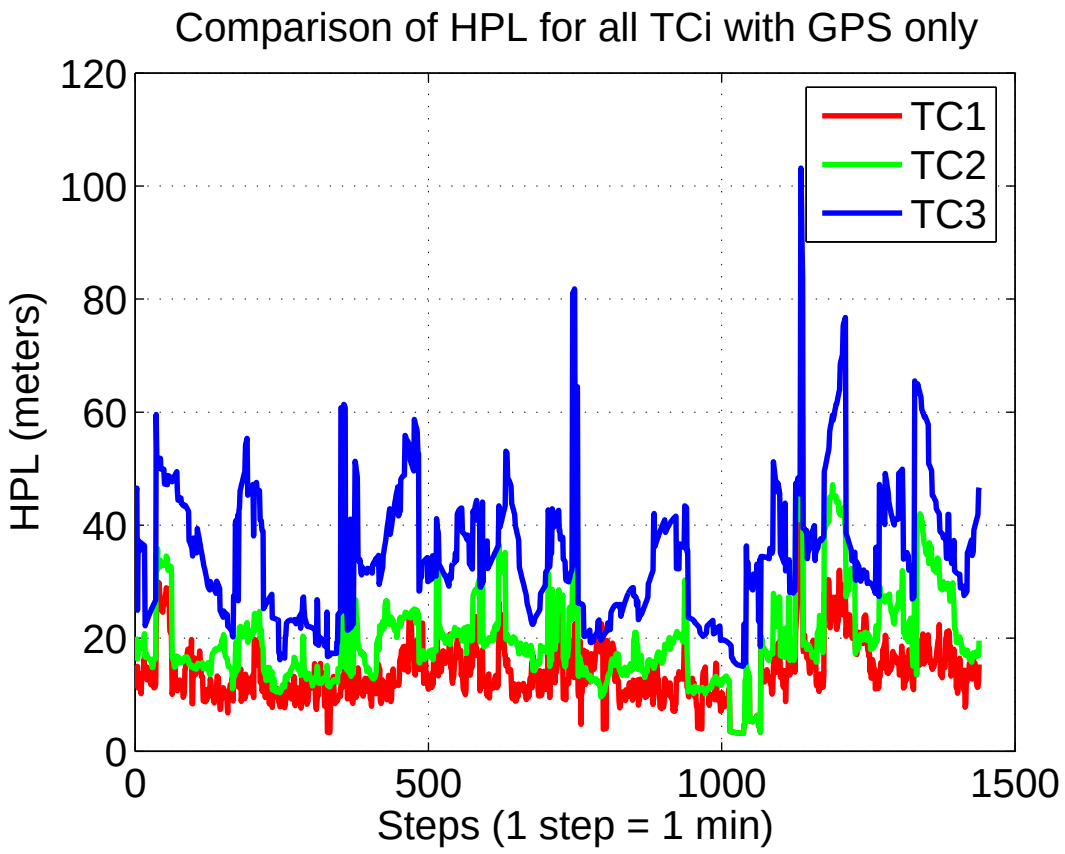

Figure 3.5.: HPL for all test cases and using GPS only

In Fig. 3.9 and Fig. 3.10 we can observe the impact of augmenting the number of visible satellites in the protection levels. As expected C2 gives better results for both HPL and VPL. The C2 curve is shifted with comparison to the C1 curve, this was done to take into account the 2 hours offset between GPS and VGC.

3.6. Discussion of the Results

The results obtained are encouraging in the sense that a better knowledge of the error behavior of pseudo range observables implies a better estimation of the protection levels. This better knowledge of the error is a result of a measurement campaign of the covariance matrix during one year. In the actual form of our 4D look up table, The availability of this matrix cannot exceed a certain area. That's why we choose to denominate it as a "regional" covariance matrix. By taking a dual constellation GPS and Galileo, and considering that Galileo observables are facing the same level of pseudo range noise, the protection levels are decreasing just by considering more satellites on visibility. The hypotheses considering only one faulty satellite could be

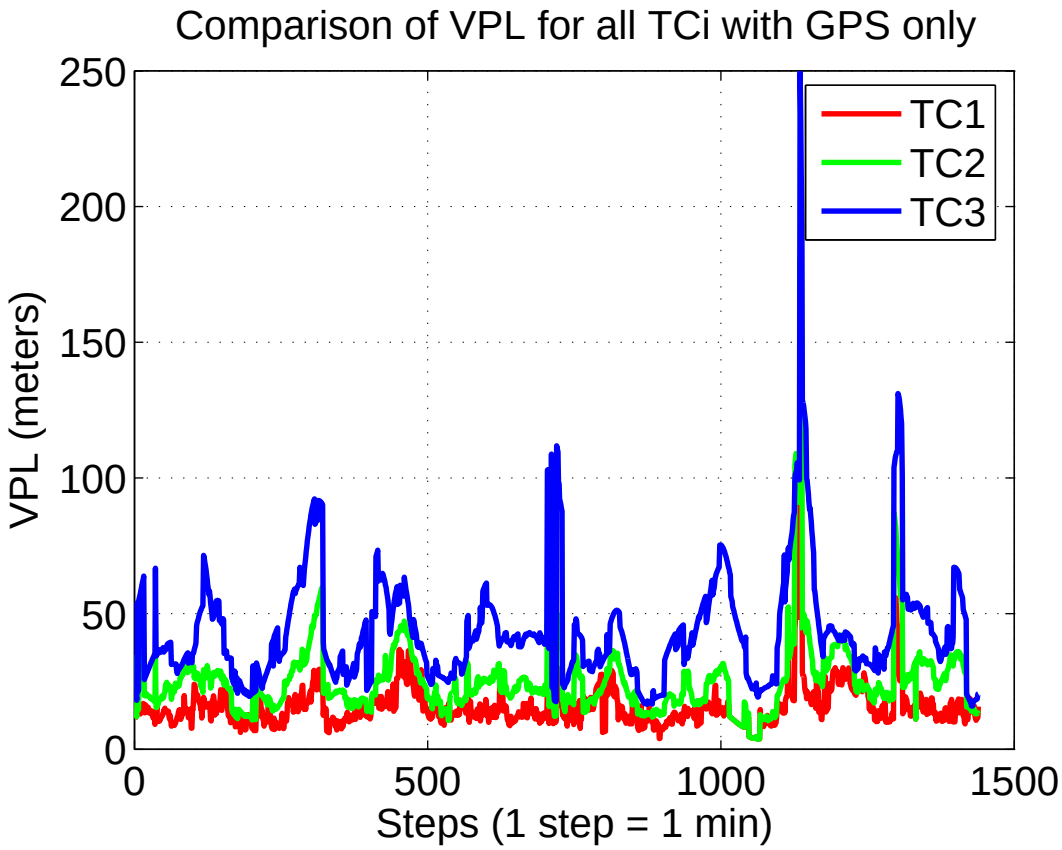

Figure 3.6.: VPL for all test cases and using GPS only

discussed when 2 constellations are taken into account. In fact the probability of a multiple failure is higher and thus should be considered in the future. It would be interesting to consider a lower level of noise for Galileo as specified in [Zap02]. In that case, a combined covariance matrix of noise has to be set. In any case the generalized RAIM algorithms using a Cholesky decomposition of the covariance matrix is a promising technique and is ready to take the advantages of using the Galileo constellation.

3.7. Conclusion and major contribution

In this chapter, we introduced the impact of a better knowledge of the range error behavior (using a regional generalized covariance matrix approach based on the IPRE concept described in the first chapter) with respect to residual based RAIM performances. This constitutes the major contribution made with respect to a residual based RAIM approach and the major results have been summarized in [BG05]. An additional investigation was made for RAIM when the pseudo ranges are deferentially corrected using local reference station [NBHP07]. This approach is generalized

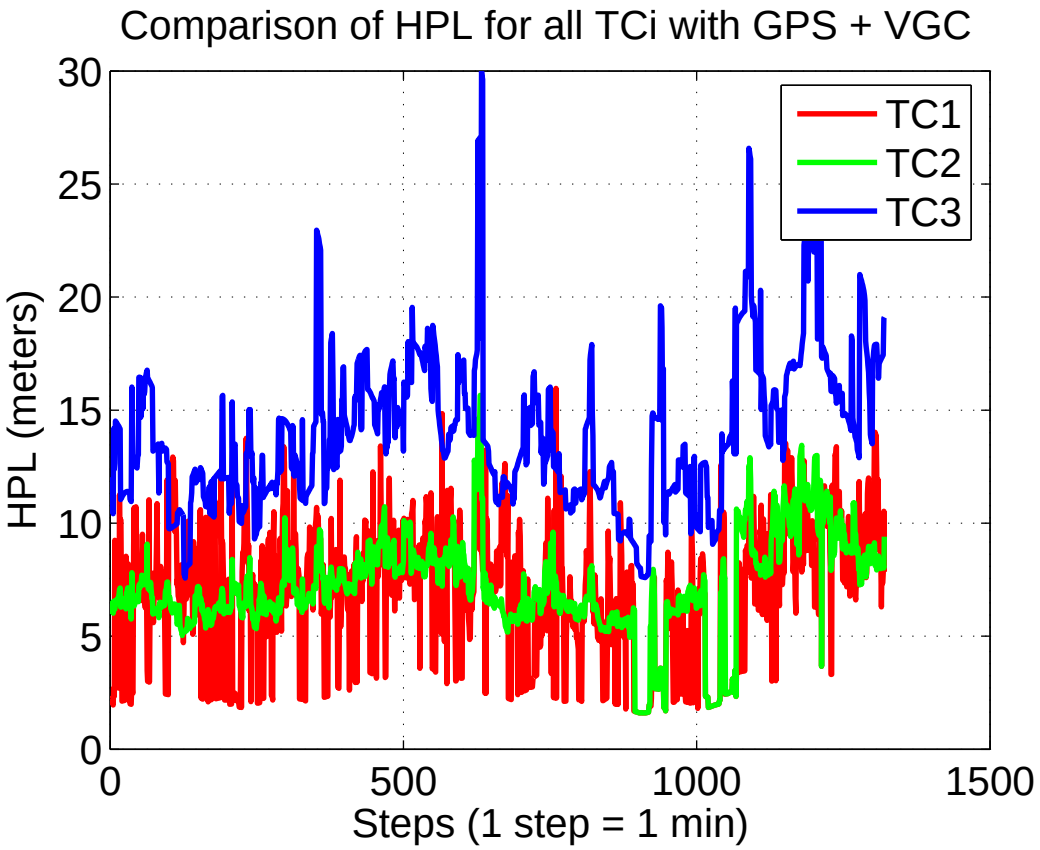

Figure 3.7.: HPL for all test cases and using GPS + VGC

and detailed in the next chapter.

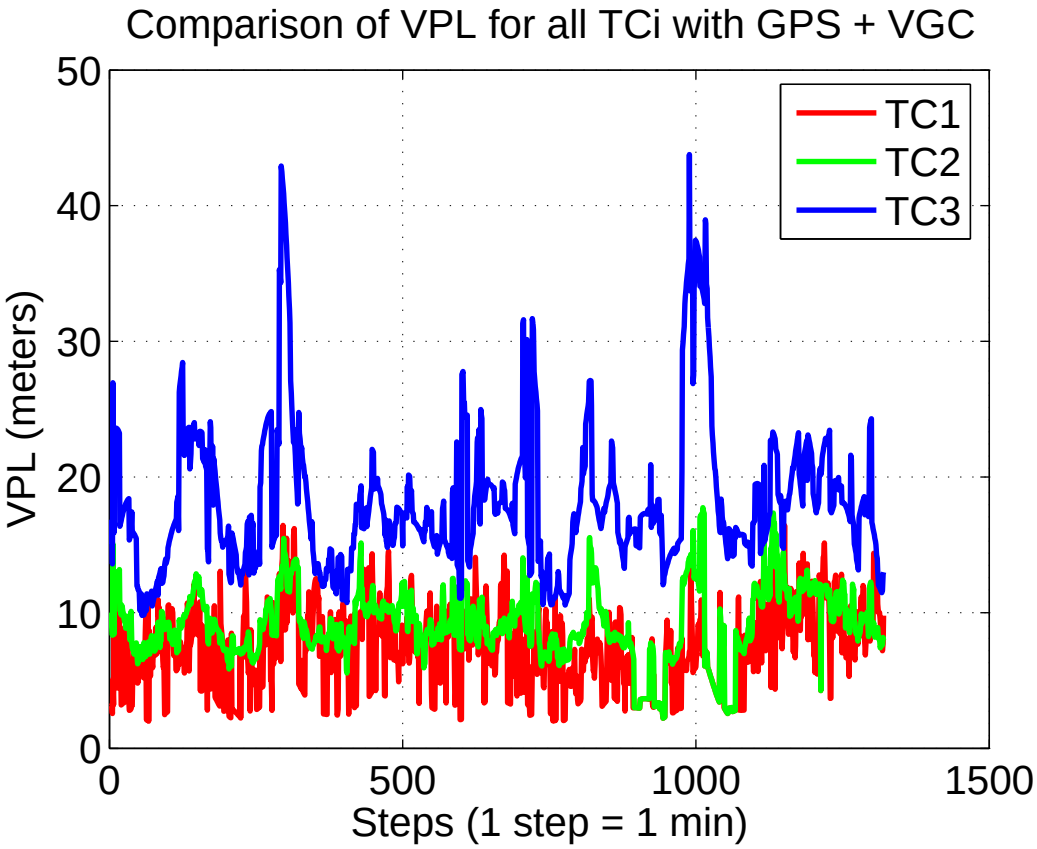

Figure 3.8.: VPL for all test cases and using GPS + VGC

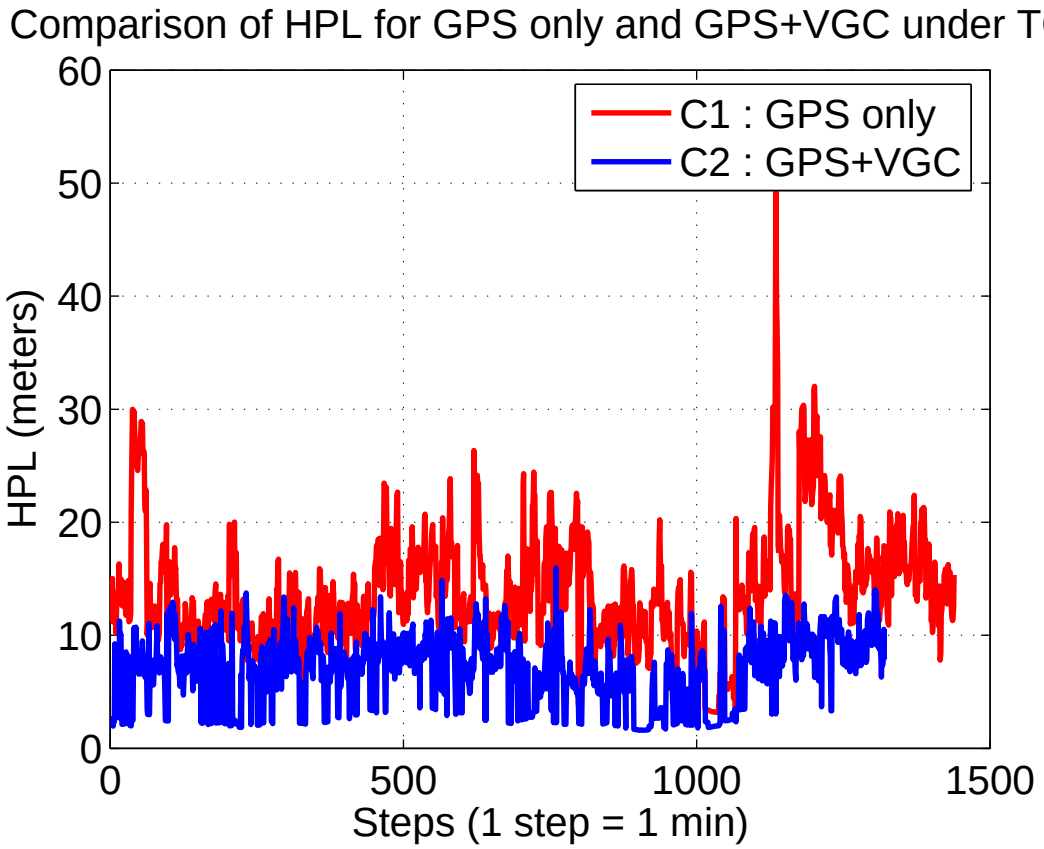

Figure 3.9.: HPL for TC1 using GPS only and GPS + VGC

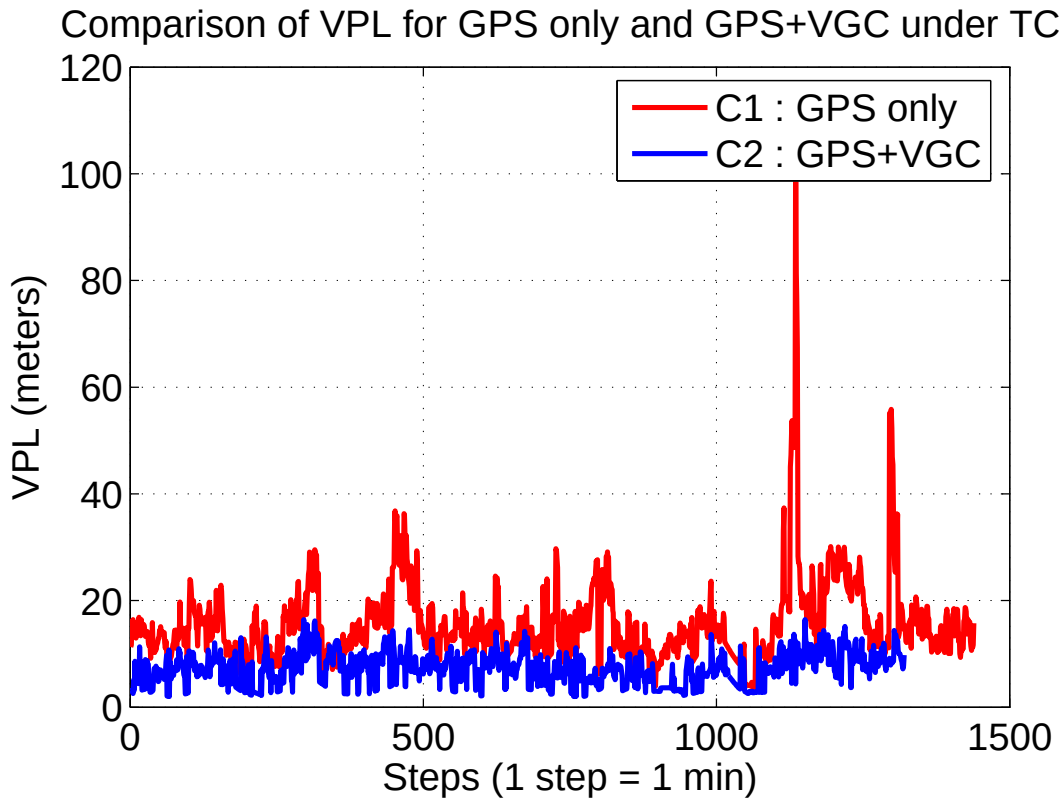

Figure 3.10.: VPL for TC1 using GPS only and GPS + VGC

4. GNSS Positioning Integrity using Augmentations

4.1. Introduction

The IPRE concept is extended to include also differential correction methods for both SBAS and GBAS. In this chapter we consider augmentation systems to the navigation satellite systems whose main objective is to improve accuracy and integrity of the pseudo-ranging performance. In this chapter, the IPRE concept developed in chapter 2 is adapted to the SBAS-corrected pseudo ranges and the performance are evaluated. In a second part of this chapter, GBAS based on dual constellation dual frequency scenario is investigated and the performances are assessed. And in a third part, an ionosphere gradient monitor is investigated in depth with a proposal for an architecture.

4.2. SBAS Performance Assessment using IPRE

4.2.1. Introduction

European GALILEO, the modernized GPS or advanced augmentation systems like the American WAAS or the European EGNOS announces the establishment of new applications and services with a higher expectations for positioning accuracy, integrity and continuity. For special applications, e.g. precision approaches in aviation, very stringent requirements on the system performance are already defined, which can be reached only by the complementary utilization of the above mentioned systems. For the establishment of a suitable environment to combine monitoring aspects of different systems the DLR Institute of Communications and Navigation has developed in cooperation with the German aerospace company Jena-Optronik GmbH the so called Experimentation and Verification Network (EVNet) over the last three years.
This section presents a performance processing facility using a Network Integrity Monitoring Platform applied to EGNOS.

This section is organized as follows:
In the first part a description of the EVNet will be done followed by the description

of the Network Integrity Monitoring Platform. In a third part we will describe the algorithms applied for our study: A first case without EGNOS by using RAIM algorithms and a second case using EGNOS.
We will then present the results obtained and we will conclude with the performances obtained and about the applicability of this Network Integrity Monitoring Platform for Galileo.

4.2.2. Experimentation and Verification Network (EVnet)

The EVNet is a combined system of hardware and software components to acquire, monitor, distribute and archive GNSS raw data as well as additional information like e.g. meteorological data via internet connections. Besides, this network offers the ability to test and tune new processing algorithms and methods under consideration of specific user and application oriented requirements (e.g. error bounds, integrity level).

The network consists of the following four main elements:

- A set of at maximum 50 Sensor Stations at different locations worldwide;
- A Central Processing and Control Facility (CPCF) act as heart of the whole system facility, controlled by different administrator and operator authorities and responsible for all communications aspects between the involved components;
- An External Processing Facilities on different locations, which can be integrated to distribute the computing power of high computing applications and that offer the opportunity for external partners of the EVnet to bring in own processing software products;
- A set of user components (Customers or Clients) which can get an access on data and products broadcasted by the CPCF.

As shown in Fig. 4.1 data streams coming from the sensor stations at first pass the Central Processing and Control Facility (CPCF). There a broadcasting system is running that acts as a device to receive and distribute data streams to different clients like "normal" user components or external processing facilities. The broadcaster software is an enhanced and adapted version of the ICECAST streamer (ICECAST is a well known free streaming server for the distribution of audio streams). Depending on the user requirements these streams can be processed to higher level products and disseminated to the clients using the same common distribution mechanism, too. Therefore internal (CPCF Processing Center) or external (External Processing Facilities) computing power can be used. The administration of all services is controlled by a combined administrator and operator tool.

The operating tool offers the access to real-time data streams on a per-sensor level. In addition to this, the operator can set permission rights for all data streams

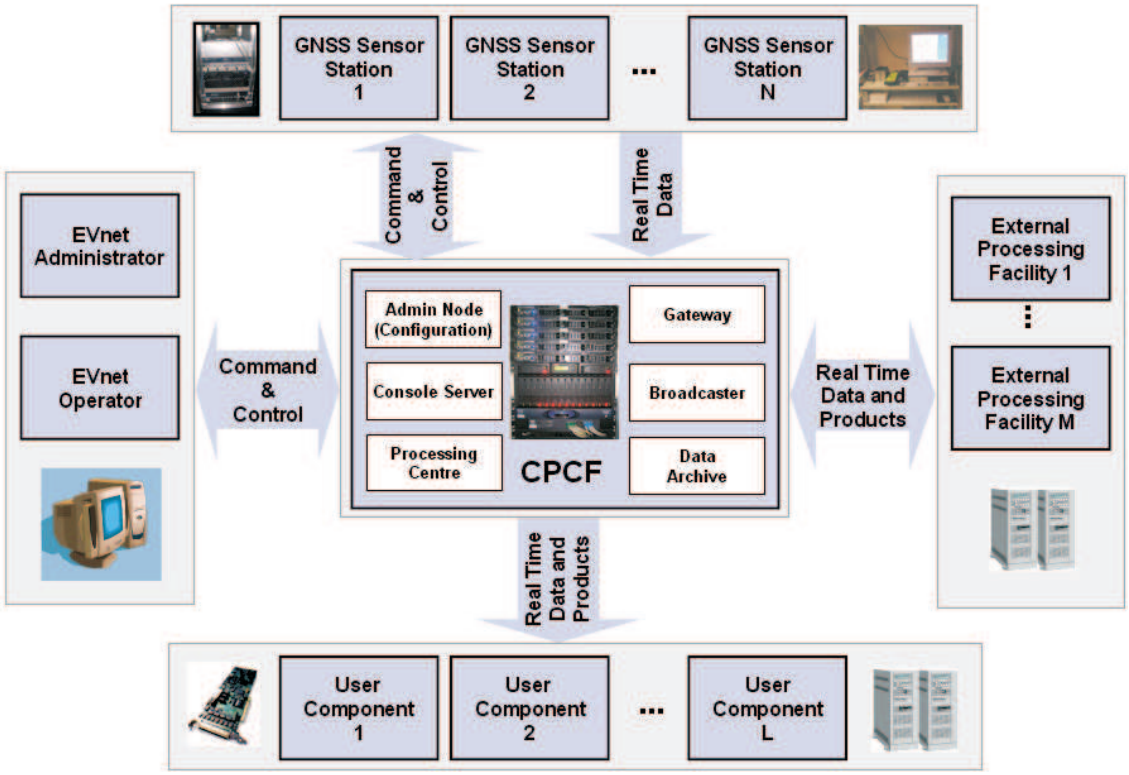

Figure 4.1.: EVnet main components

coming from the sensors or from the processing facilities on a per-user level. To automatically store real-time data streams or specific subsets of the data an archive with a capacity of nearly 3 TByte is implemented. This archive also provides a WWW front-end which allows the download of archived data via a conventional browser. A more detailed description of the architecture and the technical realization of each of the components can be found in [NSKH04]. To support the performance analysis described in this paper and to provide required monitoring architecture for the distribution of GNSS as well as augmented data, the EVnet was tuned to be operated for the reception, processing, and distribution of data coming from spatial distributed combined GPS/EGNOS receivers on the following 4 locations (see also Fig. 4.2):

Table 4.1.: Used EVnet stations (rough coordinates)

Location	Country	Latitude	Longitude
Neustrelitz	North-Germany	53^o	13^o
Munich	South-Germany	48^o	11^o
Toulouse	France	44^o	1^o
Kiruna	Sweden	68^o	20^o

Figure 4.2.: Station Network

Each of these sensor stations is equipped with a Javad EGGD two frequency high rate GPS/GLONASS receiver located as mentioned in Tab. 4.1. Additional equipment comprises environmental sensors to acquire meteorological data and IT components like e.g. Server-PC, UPS (unbreakable power supply), and Console Server. During the measurement campaign the EVnet kernel station software at each sensor location permanently sent data in the following format to the CPCF see Tab. 4.2.

4.2.3. The Network Integrity Monitoring Platform

The Network Integrity Monitoring Platform (NIMP) allowing real time monitoring in a near future (used in a post processing mode for the moment) is allocated to an external processing facility as shown in Fig. 4.3.

The tasks fulfilled by this Platform are summarized in Fig. 4.4. The red arrows represent the outputs corresponding to final or intermediate results. The black arrows represent the logical link between modules of the NIMP or the input required by the NIMP. Let's describe each part:

Table 4.2.: Supported data at each sensor level

Type of data	Description	Data Rate
GPS raw data	CA-code raw pseudo-range [m]	50 Hz
	P1-code raw pseudo-range [m]	
	P2-code raw pseudo-range [m]	
	L1 raw carrier phase [cyc]	
	L2 raw carrier phase [cyc]	
	L1 raw Doppler [cyc/s]	
	L2 raw Doppler [cyc/s]	
	CA signal to noise ratio [dB]	
	L1 signal to noise ratio [dB]	
	L2 signal to noise ratio [dB]	
	CA amplitude [none]	
	L1 amplitude [none]	
	L2 amplitude [none]	
EGNOS data	EGNOS correction data	1 Hz

4.2.3.1. Outputs of the NIMP

The main outputs are the fault free protection levels and their relation with an application requirements. These are essentially provided under the form of Stanford diagrams (developed by the GPS Lab of Stanford University and described further in this chapter see caption of Fig. 4.6) and also but not represented here as time series. Then some intermediate outputs could also be provided like: Time series of pseudo range errors at each station and for a given mode of processing (single frequency, dual frequency, with Satellite Based Augmentation System corrections, with Ground Based Augmentation System using Carrier Smoothing or -Real Time Kinematics). These time series of pseudo range errors could be used outside the NIMP for monitoring the quality of measurements over time or simply to estimate the accuracy of a given mode. Another intermediate output is a 4D Look Up Table containing a 2 by 2 covariance terms (this will be developed later in this chapter) for which a graphical representation is the so called covariance space of pseudo range error generated by one satellite. Another one represents the so called regional covariance matrix of pseudo range error that can be generated for each epoch for a given constellation geometry (elevation and azimuth of the satellites on visibility).

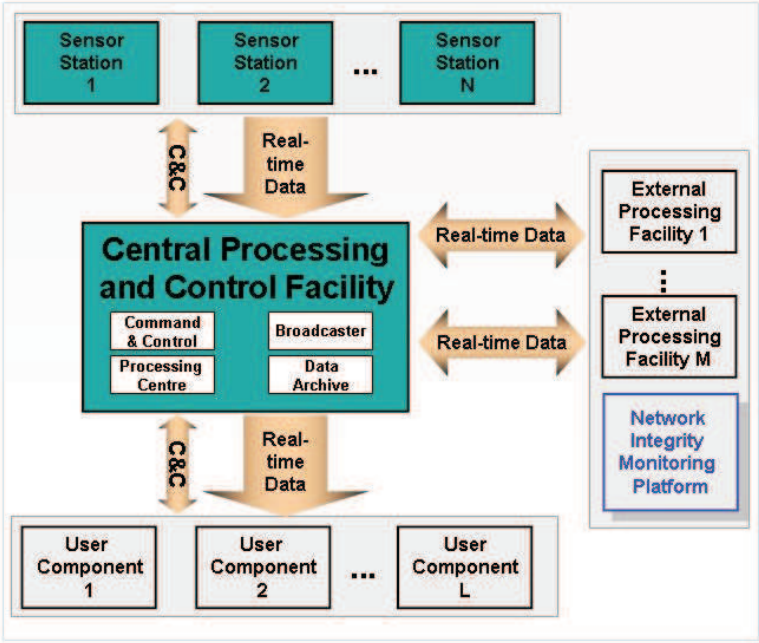

Figure 4.3.: EVNet with The Network Integrity Monitoring Platform

4.2.3.2. Inputs of the NIMP

From the EVNet we are able to access in a near real time as written above the observations (code and phase) for each monitored station. With the navigation files and the geostationary satellite messages for SBAS, they represent the necessary inputs for the platform.

4.2.3.3. The IPRE module

This module is the implementation of the algorithms described in sec. 2.2.

4.2.3.4. The statistic analysis part (modules: IPRED, 4DLUT and RCMPRE)

The results from one week measurements of the IPRE vs. time of all visible satellites for each time step is stored in an IPRE Database (IPRED) and is used as the basis to generate the covariance matrix of error.

The IPRE database is then used to build up a 4D look up table (4DLUT) that will be used to constitute the Regional Covariance Matrix of Pseudo Range Error (RCM-

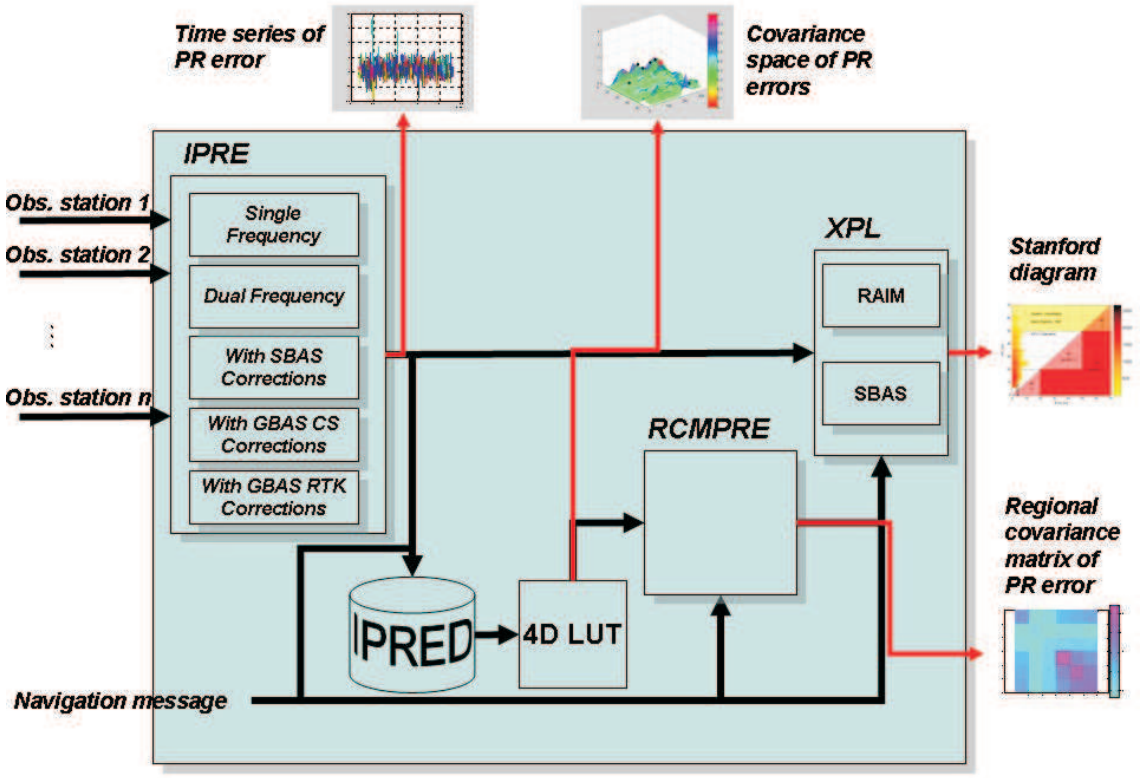

Figure 4.4.: The Network Integrity Monitoring Platform

PRE) for each epoch and for each given set of satellites on visibility as described in sec. 3.3.1.

Fig. 4.5 represents in z axis the value of the covariance term of a the pseudo range error of visible satellites (black diamonds) in the covariance space generated by a specific satellite (red diamond). This look up table is available for a region around the considered EVNet station for which the constellation of satellites at every epoch is considered the same. This "regional" covariance matrix of noise observables depends also on the correction algorithms considered in the model of single frequency receiver. In our case we considered the Klobuchar model for ionosphere delay correction and the MOPS model (see [RTC06]) for the troposphere delay correction for the case without EGNOS.

4.2.3.5. The XPL module

The XPL module performs VPL and HPL for any given mode of operation. The protection levels considered are generally the so-called “fault free” protection levels

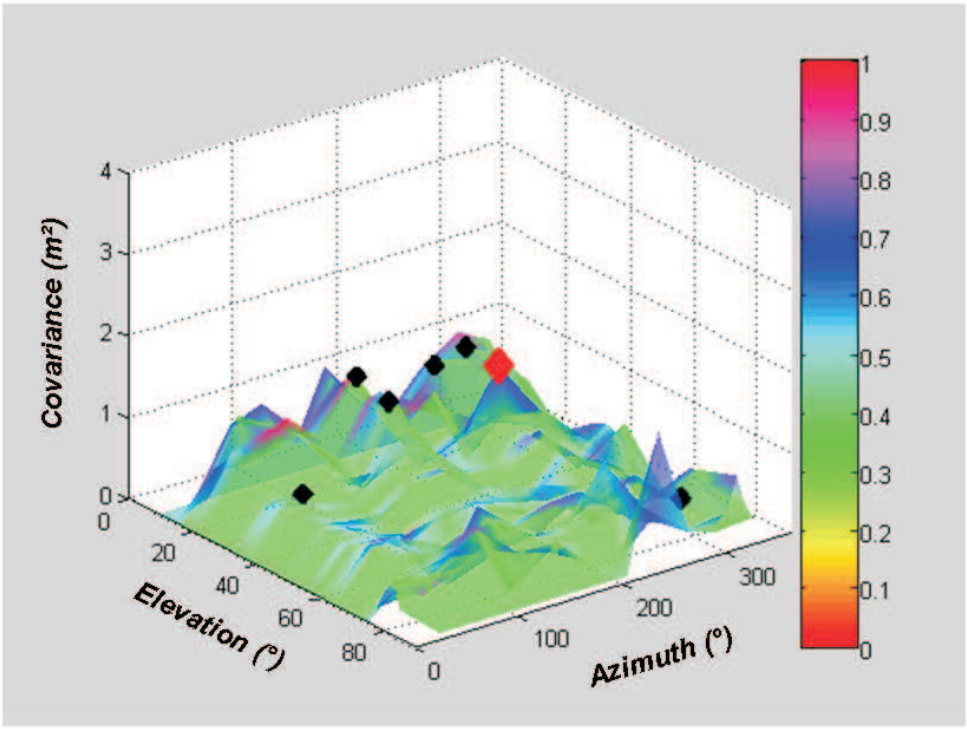

Figure 4.5.: Example of a covariance space surface generated by one satellite for a given epoch using IPRE with EGNOS corrections at Oberpfaffenhofen

but will be extended to protection levels for fault detection and exclusion using RAIM. Still the algorithm for RAIM is presented in detail in the following section.

4.2.4. Description of the EGNOS Protection Levels

Satellite based augmentation system (SBAS) like EGNOS, WAAS, and MSAS enhance GPS by providing differential correction messages and additional ranging signals. Similar to the US system WAAS EGNOS employs geostationary satellites (GEO) to broadcast its service messages by modulating them onto GPS L1 C/A like ranging signals. Once EGNOS is fully operational it will consist out of three geostationary satellites. Currently, EGNOS is in the operational readiness review phase [LWG05] while ESTB is still providing corrections via the SBAS satellite AOR-E (Atlantic Ocean Region East). During the time measurements where carried out AOR-E broadcasted the most meaningful corrections to the observations and therefore only those were considered.

From the user point of view EGNOS improves positioning accuracy of GPS satellites above the service area and provides information about the reliability of the

position solution. The principle steps applied by the user will be shortly reviewed here whereas [RTC06] serves as a detailed reference. The accuracy improvement is obtained by applying ionospheric I, long term satellite Δu_{SV} and fast satellite clock corrections. The ionospheric delays I_v provided by EGNOS describe the delay the signal would experience in vertical direction and the user applies an elevation dependent mapping function $I = m(E)I_v$ to obtain the delay of the i-th satellite signal. The long term corrections include both differential ephemeris Δr_{sv} and satellite clock corrections. In case of a large change of ephemeris errors satellite velocity and clock drift corrections can be broadcast. However, for the considered time period AOR-E transmitted only clock and radial ephemeris corrections what only slightly decreases navigation accuracy. As can be seen in

$$SISRE = \sqrt{(0.980R - Clk)^2 + 0.141^2(A^2 + C^2)}$$

the radial satellite errors R mainly affects the signal in space range errors (SISRE) and the along track and cross track components have only a small impact on positioning accuracy [WR03, PSJ96]. Together with the fast pseudorange corrections PRC the messages form a consistent set where the long term corrections are slowly changed in order to produce only small navigation errors if messages could not be received.

In addition EGNOS also sends information about the reliability of the accuracy the user observes. This is established through over bounding the errors by Gaussian distributions what establishes the user to obtain the variance of the k^{th} satellite with

$$\sigma_k^2 = \sigma_{k,flt}^2 + \sigma_{k,UIRE}^2 + \sigma_{k,tropo}^2 + \sigma_{k,air}^2,$$

where $\sigma_{k,flt}^2$ account for the accuracy provided through fast and long term correction and their decorrelation. $\sigma_{k,UIRE}^2$ can also be computed from the transmitted EGNOS messages and reflects the ionospheric errors whereas $\sigma_{k,tropo}^2$ is defined in [RTC06]. $\sigma_{k,air}^2$ which depends on receiver noise and multipath errors was computed from the observations. With the K variances σ_k^2 a diagonal weighting matrix $W_{i,i} = \sigma_k^2$ is set up that is used in a weighted least squares position solution [EWP+96].

To compute a position confidence bound, commonly referred to as protection level, the variances are propagated dependent on the actual geometry to the position domain. In vertical direction the obtained standard deviation d in the position domain of the Gaussian overbound is then multiplied by K_v (e.g. 5.33) to achieve the wished level of integrity (e.g. 10^{-7})

$$VPL = K_V \cdot d.$$

To get a representative status of the performances of EGNOS, we considered observations during mid of march 2006. Since EGNOS was at this time not fully operational, message type 2 was replaced by type 0, which corresponds to a don't

use flag for safety critical applications. For the recorded EGNOS messages some testing seemed to be conducted, as for the long term corrections from 22:00 to 24:00 UTC the issue of data (IOD) of some messages indicated the applicability of old GPS ephemeris data. For this reason the messages during these periods were not taken into account. With the observed data we obtained for the accuracy of the measured pseudo range $\sigma_\rho \approx 1.5$m.

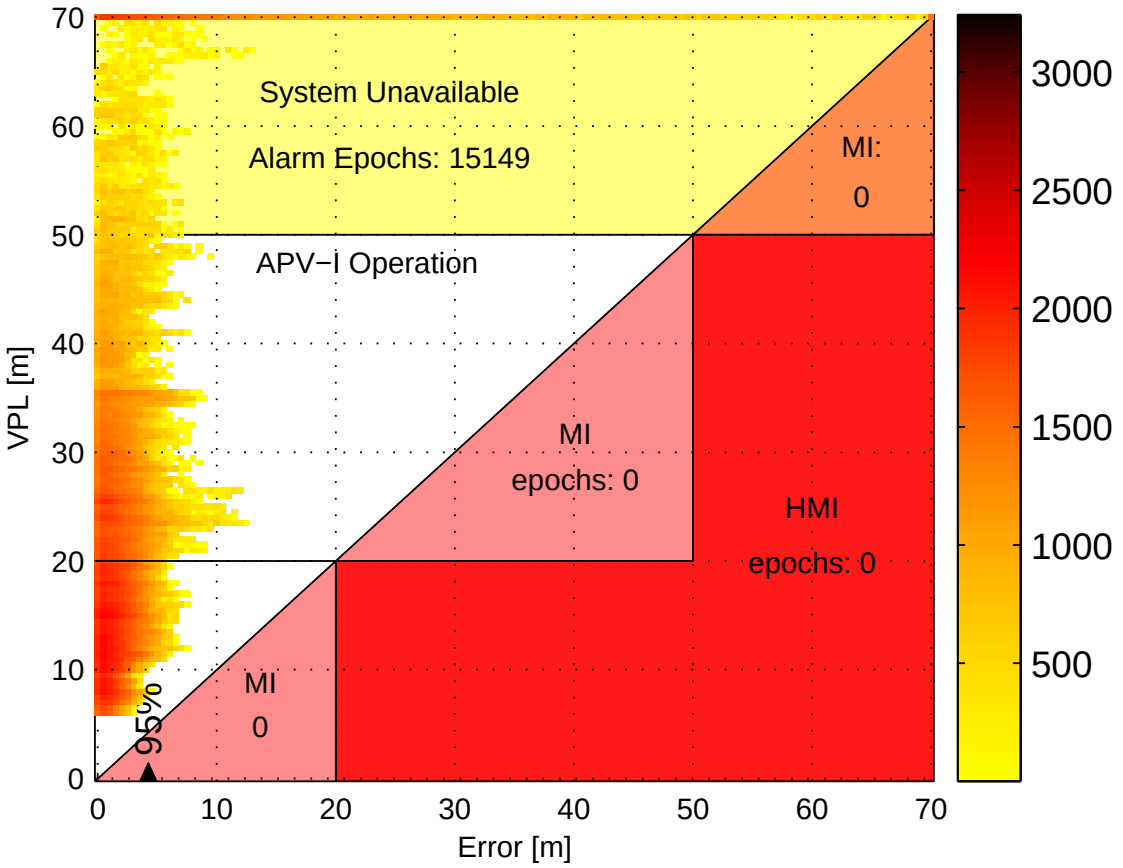

Figure 4.6.: Histogram of vertical protection level (VPL) versus vertical position error (Stanford plot) obtained for the EVNet station located in Oberpfaffenhofen during 4 days in March with PRN 120 for $K_V = 5.33$.

The integrity performance of EGNOS is shown in Fig. Fig. 4.6. As illustrated, the positioning algorithm is in a proper navigation state, if the horizontal position error and the protection level is below the alarm limit (here 40m). Since at no time the protection level has been lower than the actual error, neither Misleading Information (MI) nor undesired hazardous MI (HMI) have been present to the user. However, the position has been flagged as ”don’t use” for APV-I operations for 15149 epochs which corresponds to an availability of 95.6 percent.

4.2.5. Results for one week measurements

THE WORK DESCRIBED IN THIS SECTION IS MY PERSONAL CONTRIBUTION.

In this part, we briefly represent the results of our measurements corresponding to the period of 4 days using 1 second of epoch intervals.

4.2.5.1. Position error distribution with EGNOS

In this section, the position error has been calculated using the observation data of each station and the results are as follows.

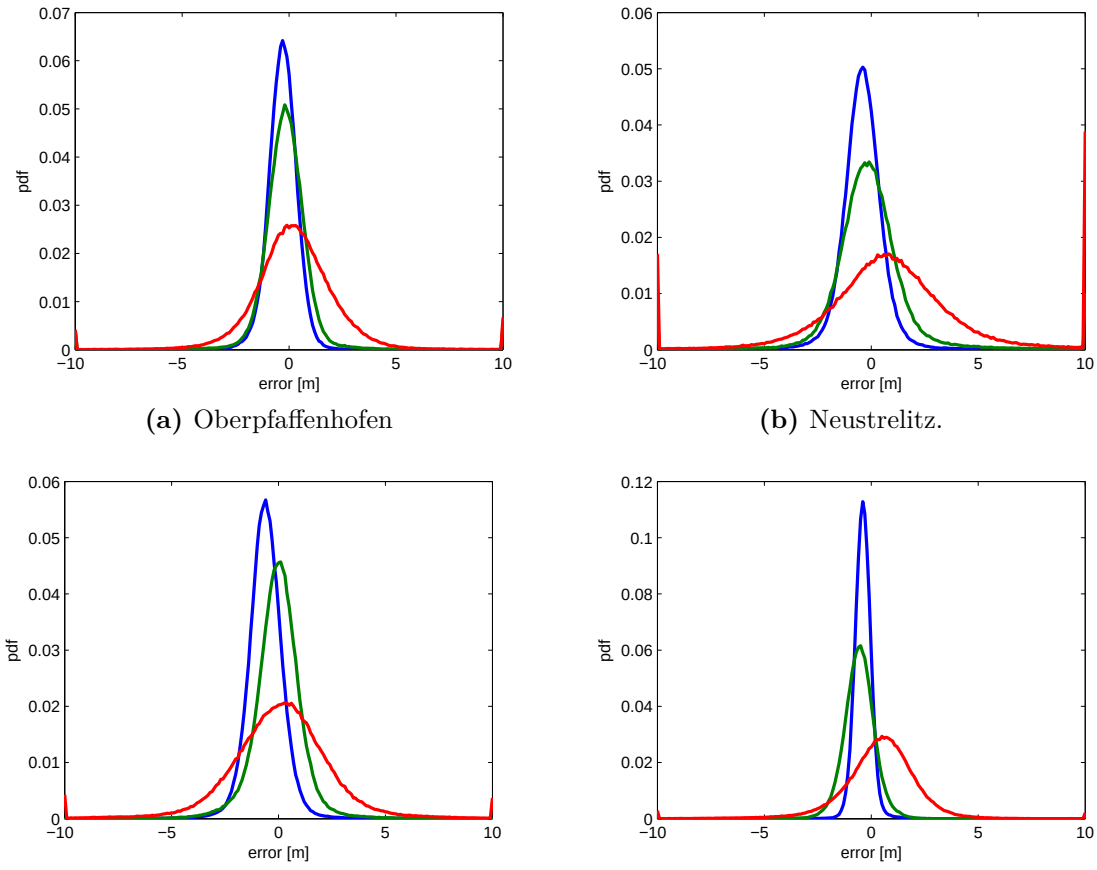

(a) Oberpfaffenhofen

(b) Neustrelitz.

(c) Toulouse.

(d) Kiruna.

Figure 4.7.: Probability density functions of the position error (East in blue, North in green and Vertical in red) obtained for the selected EVNet stations

From these results (see 4.7a to 4.7d), we can conclude that the vertical error component has the highest variance which is coherent to what we usually observed. Generally the distributions are usually slightly biased. This can be easily explained

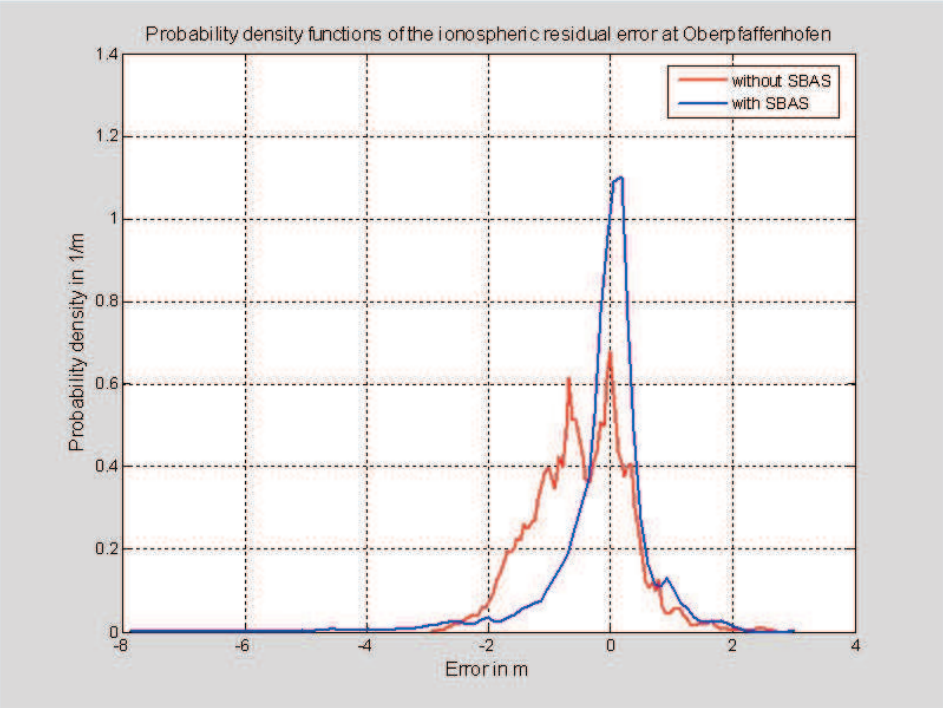

Figure 4.8.: Probability density functions of the ionospheric residual error with and without EGNOS obtained for the EVNet station located at Oberpfaffenhofen.

by the short period of observation, which cannot be considered as representative of the averaged behavior.
While comparing the results between stations, it appears that the accuracy at the Kiruna Station is slightly better than for the other stations especially for the horizontal component. One explanation is the high number of satellites visible at this high latitude and with a relatively low elevation angle which imply a short horizontal dilution of precision. Nevertheless the vertical dilution of precision is higher and we would have expected a higher error in the vertical direction with respect to the other stations. But one has to take into account not only the geometry of the constellation but also the level of pseudo range noise which can impact a lot the the position error. One has to consider the level of multipath which is highly depending on the environment of the antenna. A general remark concerns the weak improvement of the accuracy while using EGNOS (PRN 120). But as mentioned earlier, the ephemeris corrections where not applied during the considered period of measurement. The improvement is mainly due to the ionospheric corrections as can be observed in Fig. 4.8

4.2.5.2. Fault free vertical protection levels with and without EGNOS

Protection levels without EGNOS In this part the protection levels were calculated without considering EGNOS corrections. This gives a level of pseudo range error higher than with EGNOS especially concerning the ionospheric residual error.

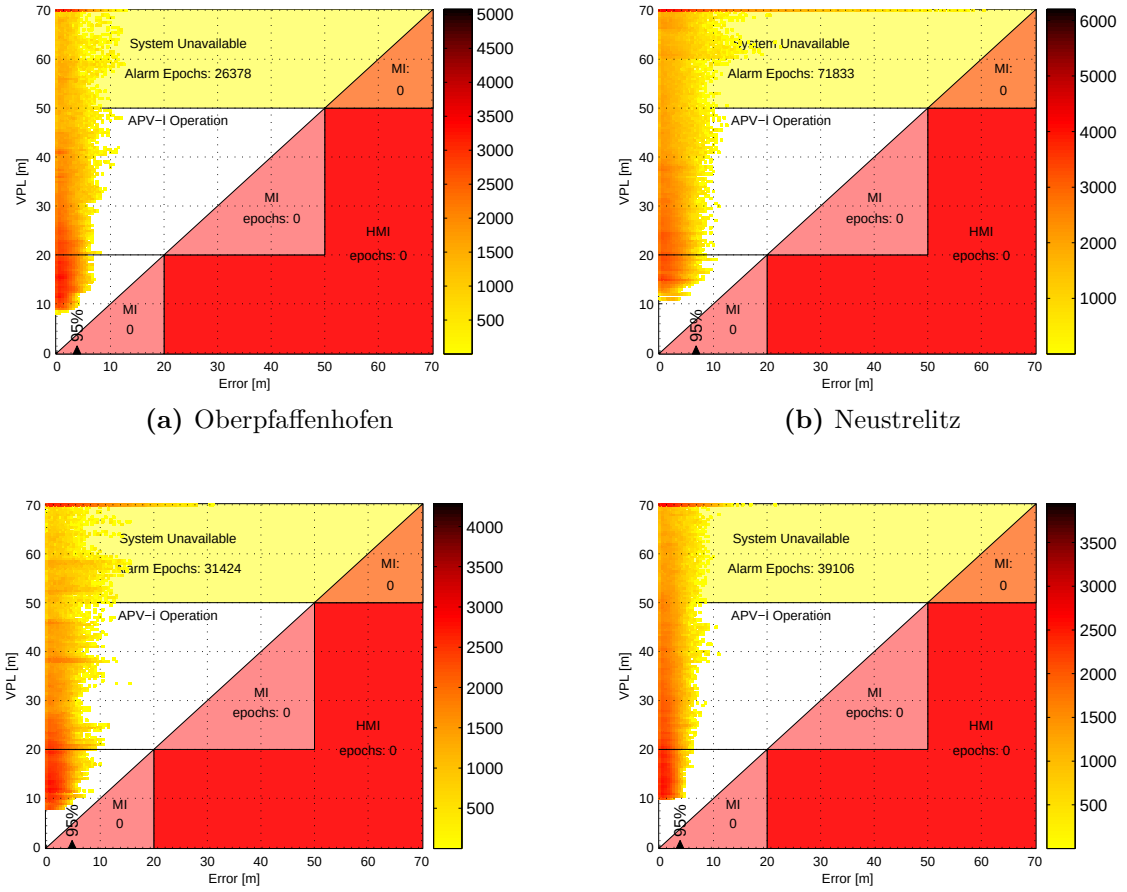

(a) Oberpfaffenhofen

(b) Neustrelitz

(c) Toulouse

(d) Kiruna

Figure 4.9.: Stanford plot for VPL without EGNOS for the selected EVNet stations using $K_V = 5.33$

Without the use of EGNOS and the variance of errors is high, this has the consequence to provide large protection levels. As expected GPS alone can provide the level of integrity corresponding to APV-I. The availability of APV-I is hardly more than 70% (see 4.9a to 4.9d).

Protection levels with EGNOS EGNOS provides corrections to satellite pseudo ranges. This system has the advantage of reducing the major contributions to satellite pseudo range biases which are the ionosphere delays and the satellite orbits and

clock errors. As a result, the corresponding IPRE are much reduced at a level that enables precision approach services. Although the service does not provide misleading information, the availability of APV-I performance is still insufficient (see 4.10a to 4.10d).

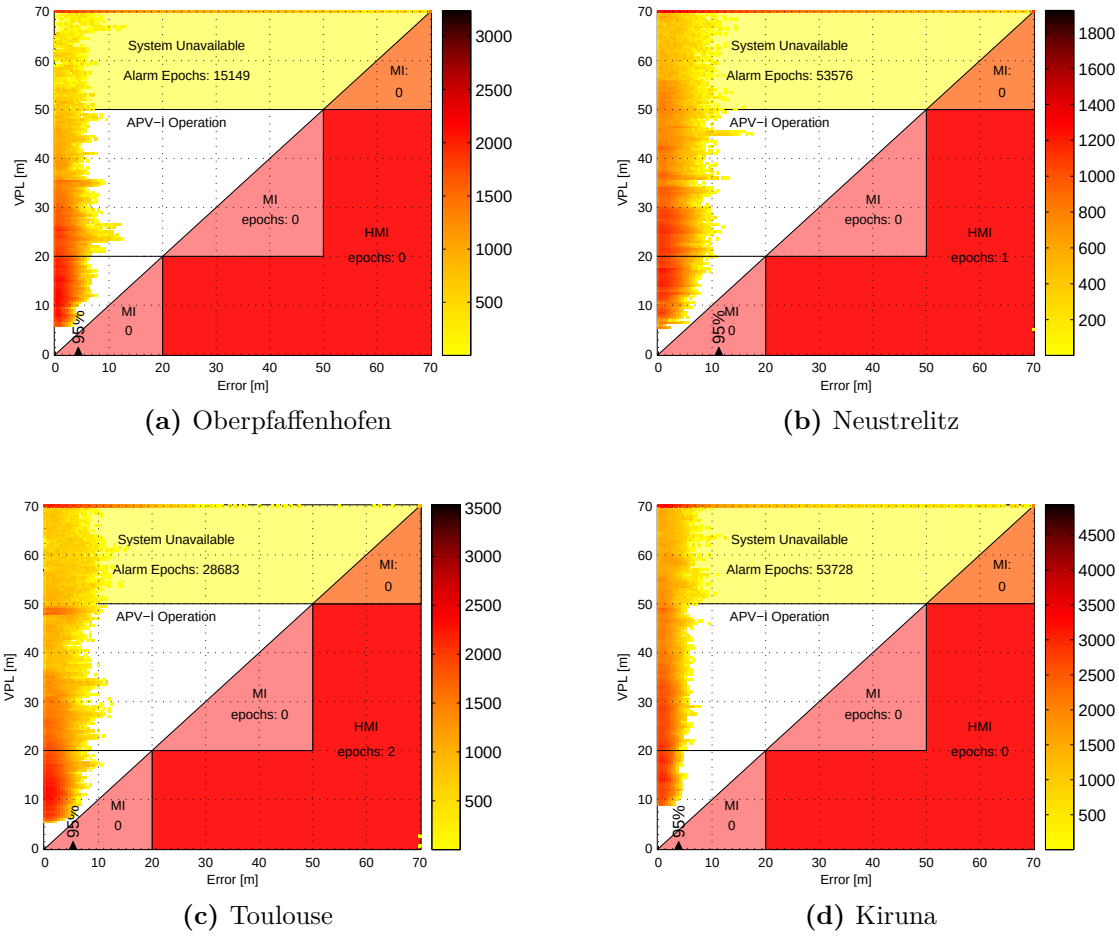

(a) Oberpfaffenhofen **(b)** Neustrelitz

(c) Toulouse **(d)** Kiruna

Figure 4.10.: Stanford plot for VPL with EGNOS for the selected EVNet stations using $K_V = 5.33$.

4.2.6. Conclusion

It was illustrated that the implementation of the Experimentation and Verification Network provides the possibility to acquire, process and distribute high rate GNSS raw data. This enables new approaches concerning the rapid performance assessment of GNSS raw data. The development of specific processing algorithm as part of the EVNet itself or as part of routines integrated into external processing facilities and

their easy on the fly integration offers the possibility to use the EVNet within the scope of validation purposes and the development of local elements for existing and future GNSS.

4.3. GBAS Dual Frequency GPS-Galileo Performance Analysis

4.3.1. Introduction

It is well known that severe ionosphere gradient is the main threat for GBAS while considering precision landing of CAT III. The use of Dual frequency techniques can mitigate this threat and even suppress it. Two smoothing techniques have been studied see [KPRE06]. This section will investigate the impact of Galileo constellation in the availability of CAT III performances with respect to different ionosphere gradient scenarios and considering the smoothing techniques defined in [KPRE06]. A first part of the subsection will introduce the general assumptions considered in the simulations and the scenario of the simulations. A second part will recall the smoothing techniques and the satellite selection strategy. The third part will present the results of the simulation and the analysis. At the end we will draw some conclusions with respect to future dual frequency, dual constellation GBAS architectures.

4.3.2. GBAS Architecture and Hypothesis

4.3.2.1. GBAS Architecture

Future GBAS systems will use multi-frequency multi-constellation to enable precision landing of category III. Different configurations are considered but the general architecture standardized in [RTC04] although for single frequency GBAS, will be kept for dual frequency GBAS. It is supposed that the ground subsystem is monitoring both GPS and Galileo constellations and provides the corrections of all satellites in view to the user. A short description of the architecture is presented in Fig. 4.11.

The use of 2 constellations and 2 frequencies will automatically increase the information to be sent to the user through the VHF Data Broadcast (VDB) link. It is assumed that the maximum capacity of broadcast through the VDB link is not reached and that the general structure of the message is not modified.

4.3.2.2. Constellation hypothesis

For our simulation, GPS will use 28 satellites (corresponding to almanac data in 2005) and Galileo is plan to have 30 satellites (use of the most recent planned

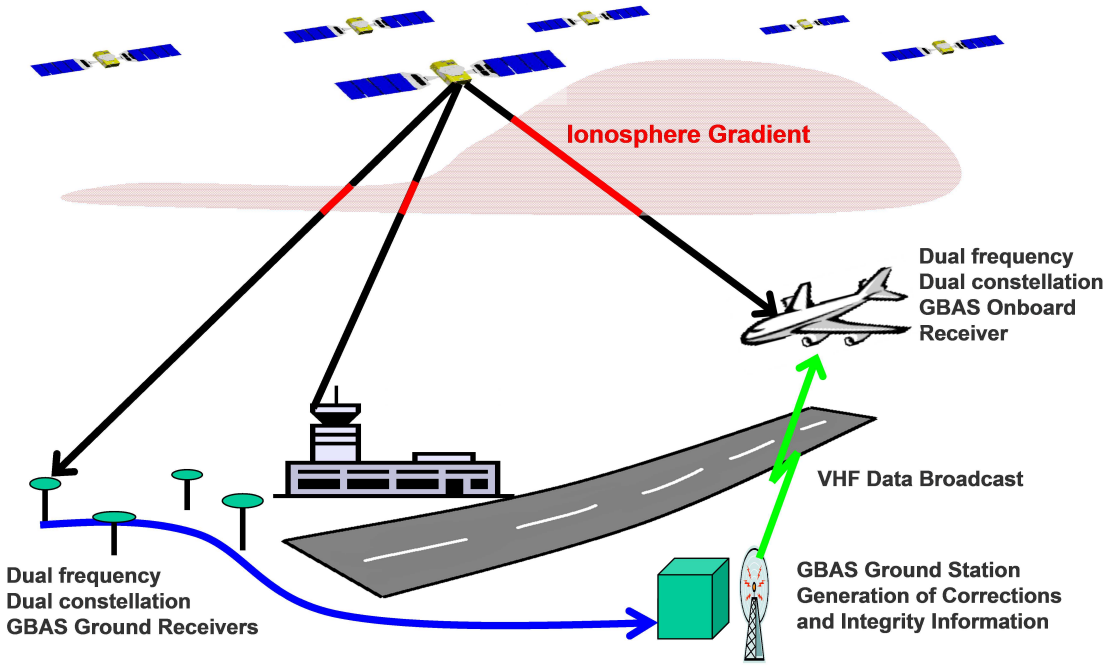

Figure 4.11.: GBAS Baseline Architecture

almanac data)

4.3.2.3. Error model

For Galileo, the error models considered are derived from [Zap02]. While comparing with GPS standard values [RTC04] it appears that the error levels are in the same order of magnitude as for Galileo (see Fig. 4.12).

To avoid the impact of the error model in the analysis of the results, we decided to use for Galileo and for GPS the same error models i.e the one provided in [Zap02].

4.3.3. Dual Frequency Smoothing Filters

Two smoothing techniques defined in [KPRE06] are considered: The ionosphere free smoothing and the divergence free smoothing technique. We recall below these algorithms. The adaptation is made to support GPS with 28 satellites and Galileo with 30 satellites. Concerning the used frequencies, for GPS, it is assumed the use of L1 and L5 for which we have access to code and phase and for Galileo, it is assumed the use of E1 and E5a. The choice of Galileo E5a is motivated for receiver design reasons $f_{L5} = f_{E5a}$ for the combined constellation case.

The general low pass filter architecture represented in Fig. 4.13 and inspired by [KPRE06] is a general representation of a filter for GNSS. The Hatch filter intensively studied in chapter 2 can be schematically represented using the same scheme.

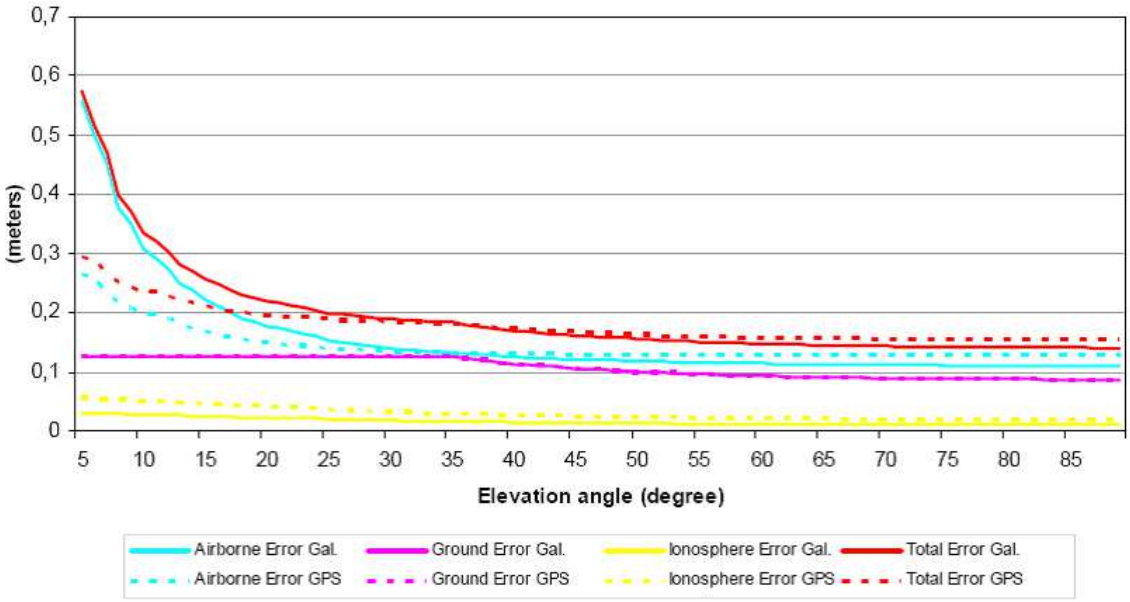

Figure 4.12.: Residual error for single frequency vs. elevation

Ψ is a raw code observation or a combination of code observations expressed in meter. Θ is a raw phase observation or a combination of phase observations expressed in meter. Before using the low pass filter, it is important to suppress all the possible biases or the highly correlated effects. Therefore the first operation is to get ride of the geometry range and the change of range due to the movement of the user relative to the satellite. χ is the "geometry free combination". The geometry is retrieved after the smoothing by adding again the phase combination.

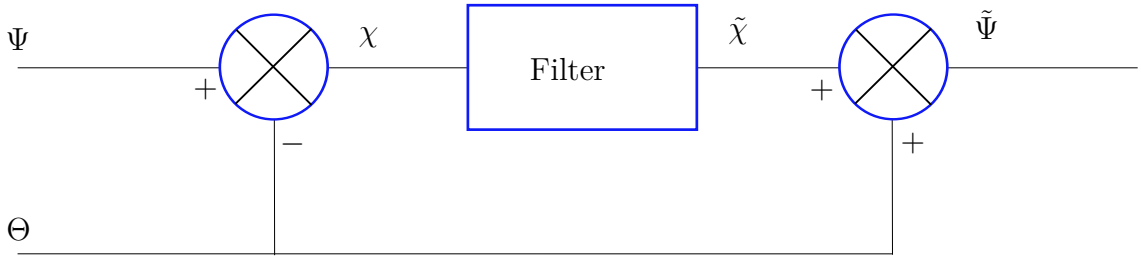

Figure 4.13.: General low pass filter architecture

4.3.3.1. General Expression of the Carrier Smoothing

In discrete time domain, the smoothing filter can be written in a recursive way:

$$\tilde{\chi}_{k+1} = \frac{\tau - \Delta t}{\tau}\tilde{\chi}_k + \frac{\Delta t}{\tau}\chi_{k+1} \tag{4.1}$$

where τ is the smoothing time constant.

We can express this formula as a differential equation:

$$\tilde{\chi}_{k+1} - \tilde{\chi}_k = \frac{-\Delta t}{\tau}\tilde{\chi}_k + \frac{\Delta t}{\tau}\chi_{k+1} \tag{4.2}$$

$$\frac{\Delta\tilde{\chi}_k}{\Delta t} = -\frac{1}{\tau}\tilde{\chi}_k + \frac{1}{\tau}\chi_{k+1} \tag{4.3}$$

We then can express the time continuous form of this formula in Laplace domain:

$$s\mathcal{L}\left(\tilde{\chi}\left(t\right)\right) - \tilde{\chi}\left(0\right) = -\frac{1}{\tau}\mathcal{L}\left(\tilde{\chi}\left(t\right)\right) + \frac{1}{\tau}\mathcal{L}\left(\chi\left(t\right)\right) \tag{4.4}$$

were $\mathcal{L}\left(\tilde{\chi}\left(t\right)\right)$ is the Laplace transform of $\tilde{\chi}\left(t\right)$.

If we consider $\tilde{\chi}\left(0\right) = \chi\left(0\right) = \chi_0$ we obtain the following formula which is also the characteristic of a low pass filter:

$$\mathcal{L}\left(\tilde{\chi}\left(t\right)\right) = \frac{1}{\tau s + 1}\mathcal{L}\left(\chi\left(t\right)\right) + \frac{\tau}{\tau s + 1}\chi_0 \tag{4.5}$$

The inverse Laplace transform (noted $\mathcal{L}^{-1}$) of this equation give the evolution in time domain of the filter:

$$\tilde{\chi}\left(t\right) = \mathcal{L}^{-1}\left(\frac{1}{\tau s + 1}\right) * \chi\left(t\right) + \chi_0\mathcal{L}^{-1}\left(\frac{\tau}{\tau s + 1}\right) \tag{4.6}$$

where $*$ represents the convolution operator.

$$\tilde{\chi}\left(t\right) = \frac{1}{\tau}\exp\left(-\frac{t}{\tau}\right) * \chi\left(t\right) + \chi_0\exp\left(-\frac{t}{\tau}\right) \tag{4.7}$$

We can use the definition of the convolution of two functions f and g:

$$f * g\left(t\right) = \int_0^t f\left(t - r\right) g\left(r\right) dr \tag{4.8}$$

We set $f(t) = \exp\left(-\frac{t}{\tau}\right)$ and $g(t) = \chi(t)$
so we have:

$$\tilde{\chi}(t) = \frac{1}{\tau}\int_0^t \exp\left(\frac{r-t}{\tau}\right)\chi(r)\,dr + \chi_0 \exp\left(-\frac{t}{\tau}\right) \tag{4.9}$$

We see that when t is "large" enough, the second term of this equation is negligible with respect to the first term. In this case, we obtain the same expression as in [KPRE06]. In our approach we consider also the transition phase of the filter therefore this term is not neglected.

We use the same notations as in [KPRE06] for the transfer function we have:

$$F(s) = \frac{1}{\tau s + 1} \tag{4.10}$$

So the smoothed code measurement can be written as follows:

$$\mathcal{L}\left(\tilde{\Psi}(t)\right) = F(s)\,\mathcal{L}(\chi(t)) + \tau F(s)\,\chi_0 + \mathcal{L}(\Theta(t)) \tag{4.11}$$

This is a general expression for the filter which can apply for all combinations considered in this thesis.

4.3.3.2. Single Frequency Carrier Smoothing Filter

As already presented in Chapter 3, the single frequency carrier smoothing technique or Hatch filter reduces the level of code noise significantly by using the phase observation difference in time. In this case we would have:

$$\Psi = \rho_{L1} \tag{4.12}$$

and we have:

$$\Theta = \Phi_{L1} \tag{4.13}$$

$$\chi = \Psi - \Theta = \rho_{L1} - \Phi_{L1} \tag{4.14}$$

The observation equations can be written in a simplified form as follows:

$$\rho_{L1} = \mu + I_{L1} + \mathcal{E}_{L1} \tag{4.15}$$

where μ represents the non frequency depend terms including the the geometric range, the troposphere delay and the clock offsets, $\mathcal{E}_{L1}$ represents the code error residuals (essentially the code noise and multipath) and I_{L1} represents the first order ionosphere delay experienced by the code on L1.

equivalently we have:

$$\Phi_{L1} = \mu - I_{L1} + N_{L1} + \eta_{L1} \tag{4.16}$$

where N_{L1} represent the distance corresponding to the integer cycle ambiguity experienced by the phase on L1, η_{L1} represent the phase error residuals (essentially the phase noise and multipath).

In our case, the input of the filter can be written as follows:

$$\chi = 2I_{L1} + \mathcal{E}_{L1} - N_{L1} \tag{4.17}$$

In this expression, we neglect the phase error η_{L1} because we have $\eta_{L1} \ll \mathcal{E}_{L1}$

So in Laplace domain the output of the filter can be written as follows (we omit t and we simplify $F(s)$ into F):

$$\mathcal{L}(\tilde{\chi}) = 2F\mathcal{L}(I_{L1}) + F\mathcal{L}(\mathcal{E}_{L1}) - \mathcal{L}(N_{L1}) + \tau F\chi_0 \tag{4.18}$$

We consider that the integer ambiguity does not change with respect to time, which assumes that there is no loss of lock and no cycle slips during the filtering process.

So finally the code smoothed can be written as follows:

$$\mathcal{L}\left(\tilde{\Psi}\right) = \mathcal{L}(\tilde{\rho}_{L1}) = \mathcal{L}(\mu) + (2F-1)\mathcal{L}(I_{L1}) + F\mathcal{L}(\mathcal{E}_{L1}) + \tau F\chi_0 \tag{4.19}$$

4.3.3.3. Divergence Free (D-Free) Smoothing Filter

We keep the code in L1 and we provide a phase combination of both frequencies as follows:

$$\Psi = \rho_{L1} \tag{4.20}$$

$$\Theta = \Phi_{L1} - \frac{2}{\alpha}\left(\Phi_{L1} - \Phi_{L5}\right) \tag{4.21}$$

with $\alpha = 1 - \frac{f_{L1}^2}{f_{L5}^2}$

This combination provides a suitable propriety which is presented hereafter:

We recall that the first order ionosphere delay is proportional to the inverse of the frequency squared:

$I_{L1} = \frac{A}{f_{L1}^2}$ with A being a constant and symmetrically $I_{L5} = \frac{A}{f_{L5}^2}$.

The carrier phase observation is defined as follows:

$$\Phi_{L1} = \mu - \frac{A}{f_{L1}^2} + N_{L1} + \eta_{L1} \tag{4.22}$$

after development and simplification of Equation 4.21, we obtain:

$$\Theta = \mu + I_{L1} + N_{L1} - \frac{2}{\alpha}\left(N_{L1} - N_{L5}\right) + \eta_{L1} - \frac{2}{\alpha}\left(\eta_{L1} - \eta_{L5}\right) \tag{4.23}$$

We have then

$$\chi = \mathcal{E}_{L1} - N_{L1} + \frac{2}{\alpha}\left(N_{L1} - N_{L5}\right) \tag{4.24}$$

For the same reason as before, the carrier phase residual combination is neglected when compared to the code residual error.

Compared to Equation 4.17, the Ionospheric term is fully canceled before the filter. This has the advantage of getting rid of the ionosphere divergence introduced by the temporal smoothing. Therefore this smoothing type is called divergence free smoothing.

The other steps of the filter can be modeled as follows:

$$\mathcal{L}(\tilde{\chi}) = F\mathcal{L}(\mathcal{E}_{L1}) - \mathcal{L}(N_{L1}) + \frac{2}{\alpha}(\mathcal{L}(N_{L1}) - \mathcal{L}(N_{L5})) + \tau F\chi_0 \tag{4.25}$$

$$\mathcal{L}\left(\tilde{\Psi}\right) = \mathcal{L}(\tilde{\rho}_{L1}) = \mathcal{L}(\mu) + \mathcal{L}(I_{L1}) + F\mathcal{L}(\mathcal{E}_{L1}) + \tau F\chi_0 \tag{4.26}$$

Compared to the single frequency smoothing filter, we have no ionospheric divergence any more.

4.3.3.4. Ionosphere Free (I-Free) Smoothing Filter

In this smoothing filter the ionosphere is eliminated from both the phase and the code observation by applying an ionosphere free combination.

$$\Psi = \rho_{L1} - \frac{1}{\alpha}(\rho_{L1} - \rho_{L5}) \tag{4.27}$$

$$\Theta = \Phi_{L1} - \frac{1}{\alpha}(\Phi_{L1} - \Phi_{L5}) \tag{4.28}$$

Using the same notations as before, we have:

$$\rho_{L1} = \mu + \frac{A}{f_{L1}^2} + \mathcal{E}_{L1} \tag{4.29}$$

$$\rho_{L5} = \mu + \frac{A}{f_{L5}^2} + \mathcal{E}_{L5} \tag{4.30}$$

so,

$$\Psi = \mu + \frac{A}{f_{L1}^2} - \frac{1}{1 - \frac{f_{L1}^2}{f_{L5}^2}}\left(\frac{A}{f_{L1}^2} - \frac{A}{f_{L5}^2}\right) + \mathcal{E}_{L1} - \frac{1}{\alpha}(\mathcal{E}_{L1} - \mathcal{E}_{L5}) \tag{4.31}$$

and after simplifications we obtain:

$$\Psi = \mu + \mathcal{E}_{L1} - \frac{1}{\alpha}(\mathcal{E}_{L1} - \mathcal{E}_{L5}) \tag{4.32}$$

In this combination, the ionosphere is "virtually" eliminated. In fact, this linear combination cancels out the first order ionosphere delay.

We can observe at this stage one of the drawback of this method: the combination of decorrelated code noise and multipath can reach several meters. much higher than the single frequency residual code noise.

For the phase observation, we use the same combination as for the code and obtain:

$$\Theta = \mu + N_{L1} - \frac{1}{\alpha}\left(N_{L1} - N_{L5}\right) + \eta_{L1} - \frac{1}{\alpha}\left(\eta_{L1} - \eta_{L5}\right) \tag{4.33}$$

The code minus carrier after neglecting the phase noise combination can be written as follows:

$$\chi = \Psi - \Theta = \mathcal{E}_{L1} - \frac{1}{\alpha}\left(\mathcal{E}_{L1} - \mathcal{E}_{L5}\right) - N_{L1} + \frac{1}{\alpha}\left(N_{L1} - N_{L5}\right) \tag{4.34}$$

The other steps of the filter can be modeled as follows:

$$\mathcal{L}\left(\tilde{\chi}\right) = F\mathcal{L}\left(\mathcal{E}_{L1} - \frac{1}{\alpha}\left(\mathcal{E}_{L1} - \mathcal{E}_{L5}\right)\right) - \mathcal{L}\left(N_{L1}\right) + \frac{1}{\alpha}\left(\mathcal{L}\left(N_{L1}\right) - \mathcal{L}\left(N_{L5}\right)\right) + \tau F\chi_0 \tag{4.35}$$

$$\mathcal{L}\left(\tilde{\Psi}\right) = \mathcal{L}\left(\tilde{\rho}_{L1}\right) = \mathcal{L}\left(\mu\right) + F\mathcal{L}\left(\mathcal{E}_{L1} - \frac{1}{\alpha}\left(\mathcal{E}_{L1} - \mathcal{E}_{L5}\right)\right) + \tau F\chi_0 \tag{4.36}$$

We observe that the ionosphere delay is eliminated and the code noise combination is filtered to a certain level depending on the characteristic of the noise process and the time constant of the filter.

4.3.4. Vertical Protection Level Equation and Availability Equation

The critical dimension is the vertical component of the position. There are two reasons to focus on this direction:

1. Requirements for precision approach are essentially related to the vertical guidance.
2. The vertical dilution of precision is generally predominant when compared to the two other perpendicular directions.

The equation is based on the vertical protection level equation already developed for single frequency GBAS (see [RTC04]).

$$\mathrm{VPL} = k_{\mathrm{ffmd}}\sigma_V \tag{4.37}$$

where σ_V is the standard deviation of the Gaussian overbound of the vertical error and k_{ffmd} is the multiplication parameter derived from the fault free probability of missed detection.

$$\sigma_V = \sqrt{\sum_{i=1}^{n} S_{\mathrm{Vert},i}^2 \sigma_i^2} \tag{4.38}$$

$$\mathbf{S} = \left(\mathbf{G^T W G}\right)^{-1}\mathbf{G^T W} \tag{4.39}$$

$S_{\mathrm{Vert},i}$ is the projection of the i^{th} pseudo range in the vertical direction.

$\mathbf{S}$ is the pseudo-inverse matrix of the observation equation.

σ_i is the standard deviation of the Gaussian overbound of the fault free pseudo range residual error relative to satellite i.

These errors are estimated after smoothing and after differential corrections.

4.3.4.1. VPL for D-Free

For D-free, the spatial component of the ionosphere gradient is not eliminated and appears as a bias in the residual error. As described in [KPRE06], either a perfect monitoring of the ionosphere gradient can be made and the protection levels can be increased in order to take into account the inflation of the ionosphere gradient or there is no perfect monitoring of the ionosphere gradient and in that case the integrity can't be guaranteed at all. An interesting integrity concept was proposed by Hiroyuki Konno in his paper [KPRE06]. He suggested adding the bias due to the spatial ionosphere gradient in the VPL in the case of a perfect monitoring of the ionosphere gradient. Thus the VPL can be written in the following form:

$$\mathrm{VPL}_{H0} = k_{\mathrm{ffmd}} \underbrace{\sqrt{\sum_{i=1}^{n} S_{\mathrm{Vert},i}^2 \left(\sigma_{\mathrm{Dfree\text{-}gnd},i}^2 + \sigma_{\mathrm{Trop}}^2 + \sigma_{\mathrm{Dfree\text{-}air},i}^2\right)}}_{A} + \underbrace{\sum_{j=1}^{M} S_{\mathrm{Vert},j}\frac{\partial I_j}{\partial x}d}_{B} \tag{4.40}$$

In this equation, the standard deviations $\sigma_{\text{Dfree-gnd},i}$ and $\sigma_{\text{Dfree-air},i}$ correspond to the residual errors for the divergence free smoothing solution after application of differential corrections. M is the number of affected satellites (affected by a gradient), d is the estimated horizontal distance between the user and the GBAS reference point, and $\frac{\partial I_j}{\partial x}$ is the spatial ionosphere gradient relative to affected satellite j.

It is important to notice that "perfect" monitoring means with a very "small" uncertainty because all uncertainties in B will necessary be modeled as random value and has to be moved to A and inflated to be consistent with the acceptable probability of missed detection (k_{ffmd}). This protection level concept will necessary be updated to take into account the monitoring uncertainty. It is possible, that finally the protections levels resulting from this consideration will even be higher than the protection level of the ionosphere free combination.

4.3.4.2. VPL for I-Free

For I-free, the first order ionosphere delay is eliminated. In that case, the protection level equation will be based on a nominal error inflation only (the B term in VPL equation for D-Free is canceled). But the price to pay is an increase of $\sigma_{Ifree-gnd}$ and $\sigma_{Ifree-air}$ which are based on code multipath and code noise combinations in two different frequencies.

$$\text{VPL}_{H0} = k_{\text{ffmd}} \sqrt{\sum_{i=1}^{n} S_{\text{Vert},i}^2 \left(\sigma_{\text{Ifree-gnd},i}^2 + \sigma_{\text{Trop}}^2 + \sigma_{\text{Ifree-air},i}^2\right)} \tag{4.41}$$

In this equation, $\sigma_{\text{Ifree-gnd},i}$ and $\sigma_{\text{Ifree-air},i}$ represent the standard deviation of the Gaussian overbound of respectively the residual ground receiver error and the residual airborne receiver error after applying the ionosphere free smoothing and the differential corrections.

4.3.5. Performance Metric

For all presented algorithms, the availability considers only the VPL compared to the VAL (as defined in chapter 1) for CAT III (5.3 m) representing the Cat III "ILS- look alike". This assumes no failure at any satellite of the constellation. In the reality one has to consider an a priori probability of satellite failure. Nevertheless the impact of a satellite failure for a combined Galileo-GPS constellation is limited thanks to a large number of visible satellites. This is not the case for a single constellation for which a failure in one satellite can drive to availability problem.

4.3.6. Spatial Ionospheric Gradient Scenario

While considering divergence free smoothing, the ionosphere residual error due to spatial ionosphere gradient can't be eliminated. For our simulations, we define the ionosphere scenario as follows (see Fig. 4.14):

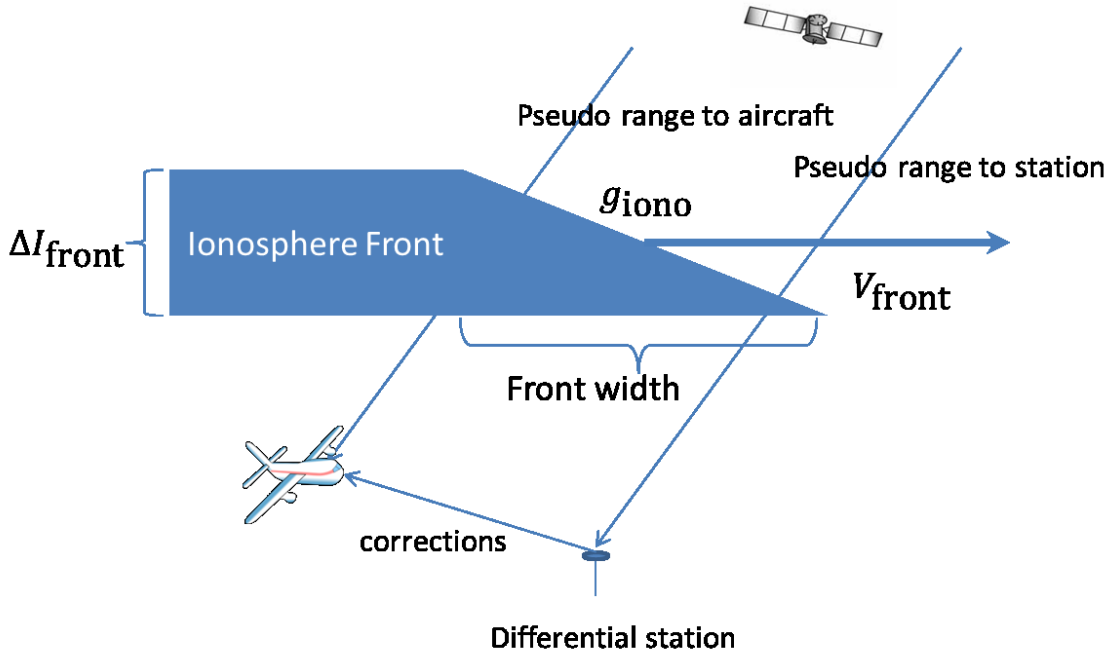

Figure 4.14.: Ionospheric Gradient Model. The ionospheric gradient represents the slope of the front which is the ionosphere delay difference between the highest and the lowest level ΔI_{front}divided by the front width.

In a single layer ionosphere model, the ionosphere medium is equivalent to a layer located at 350 km above the earth surface and concentrates the whole electron density. The intersection of the line of sight signal with the ionosphere layer is called the ionosphere pierce point (IPP). We consider the following scenario: Each visible satellite (from user and ground receiver) generates 2 IPPs (one relative to the airplane ligne of sight and the other one relative to the ground reference station). The total electron content TEC difference between both ligne of sights induces an ionosphere residual error. The altitude of the ionosphere equivalent layer is negligible with respect to the altitude of the satellite; therefore the baseline between user and receiver is considered equivalent to the position difference of the IPPs.

The distribution of the total electron content (TEC) gradients at the ionosphere equivalent layer is generally not homogeneous. A detail investigation of the physical behavior of these gradients needs to be done but is not the aim of this work. In this chapter a conservative approach will consider a spatial ionosphere gradient defined in an area (sector) centered in the IPP of the most critical satellite (i.e. the

satellite providing the largest impact on user position) of the all in view constellation. Fig. 4.15 describes this approach. An ionosphere gradient is defined with respect to a given satellite, the frequency of the ranging signal and a pair user- ground sation with a known baseline distance. It is the ionosphere delay difference divided by the baseline distance and it is expressed in [mm/km].

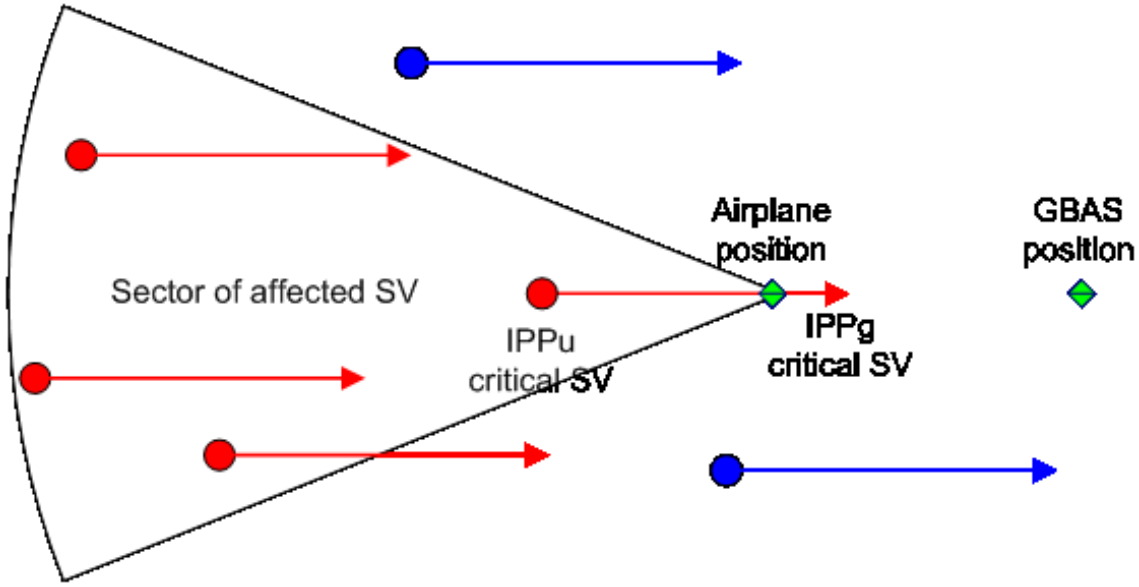

Figure 4.15.: Ionospheric Threat Scenario with IPPu being the IPP at user level with respect to the most critical satellite (arrow tail), IPPg the IPP for the ground station with respect to the same most critical satellite (arrowhead). The arrows represent the baseline vector with respect to each satellite. The red arrows correspond to the affected satellites.

A worst case for the airplane landing direction considers a trajectory in the opposite direction to the defined sector of affected satellites. The angle defining the sector will be considered as a parameter in our simulation (30°) and characterized by an azimuth range centered in the azimuth angle of the critical satellite.

4.3.7. Simulation Scenario

The objective of this work is to test for any satellite geometry and for a worst case ionosphere gradient if the GBAS system performances can fulfill the CAT III requirements.

For simplification and in order to limit the dimension of the problem, the position of the user remains constant during the 10 days of simulation, the ionosphere threat is considered stationary (no temporal gradient is considered). Only the satellites are moving using downloaded almanacs for GPS and modeled almanacs for Galileo.

While considering divergence free smoothing, the ionosphere residual error due to spatial ionosphere gradient remains in the residual. The ionosphere scenario defined above is considered.

Another important aspect is the design of the time stability of the carrier smoothing filter. Fig. 4.16 shows a sequence of pseudo range residual measurement after ionosphere free smoothing. The red line represents the residual range error of satellite 3 of the Galileo constellation which has the highest range error when visible. When the satellite raise from the horizon (5° elevation mask), the filter begins to smooth the pseudo range. After a certain time, the smoothing filter is stable. It appears that around 100 second latency is necessary in order to have an error below 1m. This 100 seconds latency will therefore be used in our study i.e. new satellites appearing in the horizon will be considered in the navigation solution only after 100 seconds of smoothing. We considered for both frequencies a carrier phase noise modeled as a white Gaussian noise of 1cm standard deviation. We didn't assume any cycle slip and the integer ambiguity is constant in any 0.5 second of the simulation. The consecutive time difference will therefore eliminate the integer ambiguity.

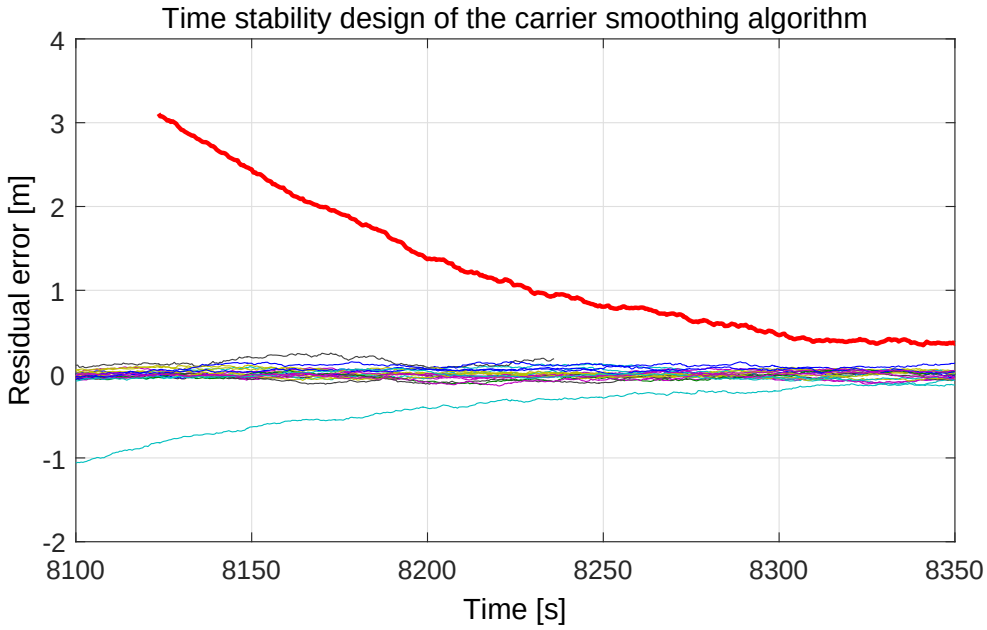

Figure 4.16.: Pseudo range residual error after ionosphere free smoothing for each visible satellites using a smoothing time of 100 seconds. The pseudo range residual in red corresponds to a new acquired satellite starting with a a residual error of 3 meters and converging to residual error of around 0.5 m at the end of the simulation period.

4.3.8. Simulation Setup

The simulations to compute the protection levels and availability of the GBAS system were taken at time steps of 0.5 seconds for a period of ten days from December 17th, 2005 to December 27th, 2005. The assumed position of the GBAS station was chosen to be at Blagnac Airport in Toulouse, France (Latitude: 43.5786 North, Longitude: 1.3760 West, Height: 220m). The simulation considered a fixed user position (Lat 43.6730 N, Long 1.3164 W, Height 449 meters) (constant baseline: 5km, but constellation varying). For calculating residual errors, the requirements appropriate for CAT III were assumed, i.e. four available GBAS reference stations, the GBAS Service Level F, the airborne accuracy designator B, and the airframe multipath designator B. The satellite positions used for the simulations were in the case of GPS taken from a YUMA almanac file, and in the case of Galileo from the last available planed almanac data.

In this chapter, a maximum ionosphere gradient of 350 mm/km is considered.

4.3.9. Simulation Results and Analysis

We present the results of our simulations. Only the case of vertical ionosphere gradient of 350 mm/km has been presented here. This case corresponds to an extreme ionosphere storm that is rarely observed. The response of GBAS for different configurations (Dual constellation I-free and D-free using best VDOP technique or all in view) is presented and compared with the use of a single constellation.

4.3.9.1. Single frequency GPS and Galileo GBAS

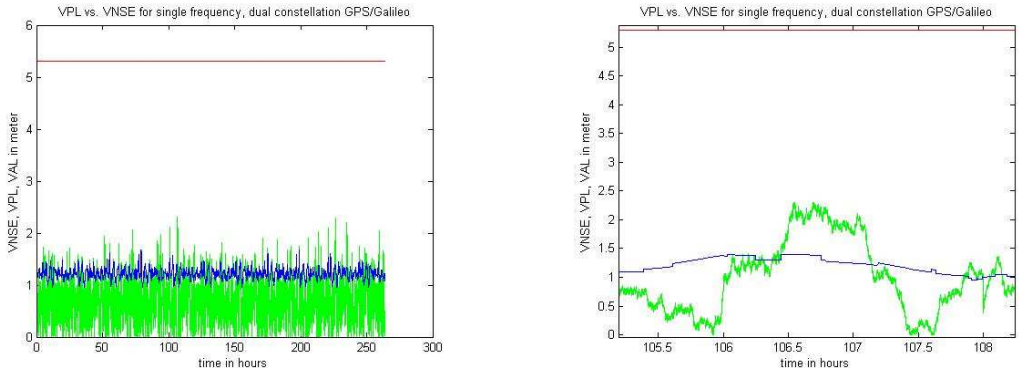

(a) Single frequency scenario **(b)** Zoom single frequency scenario

Figure 4.17.: VPL (blue) and VNSE (green) results compared to VAL (red) for the single frequency scenario using all in view GPS and Galileo satellites

In 4.17a, we represent the Vertical Alert Limit (VAL), the Vertical Protection Level (VPL) and the Vertical Navigation System Error (VNSE) (see chapter 1 for the definition of these parameters) corresponding to the single frequency GBAS scenario. It has to be noticed that no temporal ionosphere gradient has been simulated. Therefore the level of noise is low. This scenario is considered as "fault free".

Nevertheless, the vertical protection level is very often below the vertical error. This means that a lot of misleading information occurred. The protection level concept considered in this case cannot protect the user against ionosphere anomalies. A zoom in a worst case time window shows the limitations of the performances of the GBAS system while using only one frequency:

4.17b shows clearly a decorrelation between the error and the protection level. Even without considering a temporal gradient of the ionosphere which would have led to a drift and a time shift after applying the carrier smoothing filter, the error can still reach a very high level. And misleading information can lead to hazardous misleading information (in this sequence of time, the error can reach more than 2 meters).

4.3.9.2. Dual frequency D-Free using GPS and Galileo

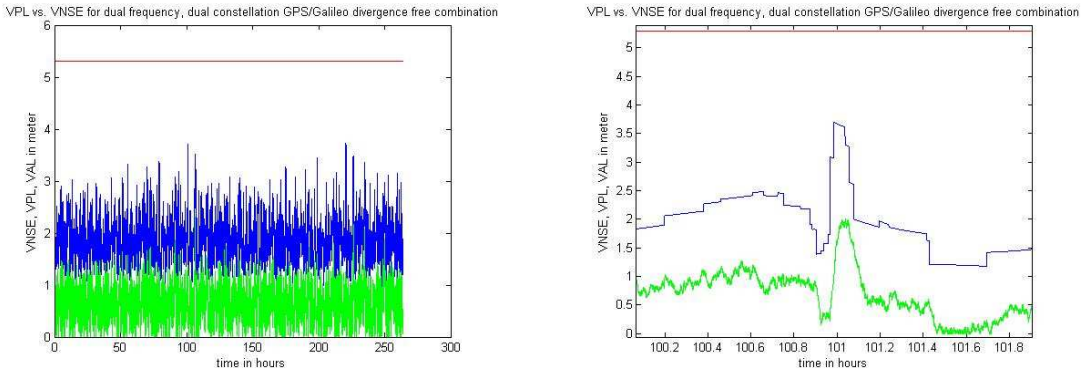

(a) D-Free scenario **(b)** Zoom D-Free scenario

Figure 4.18.: VPL (blue) and VNSE (green) results compared to VAL (red) for the D-Free scenario using all in view GPS and Galileo satellites

In this scenario, the user is assumed to receive from the VDB link (which is the data link from the GBAS station to the GBAS users and containing the pseudo range corrections, the range rate corrections and integrity monitoring information) the spatial ionosphere gradient monitored on ground.

In this case, the spatial gradient is supposed to be perfectly monitored on ground and the user considers this effect while calculating his VPL. It appears that even if the protection level is never exceeded by the vertical error, the gap is sometimes very short as we can see if we zoom in the worst geometry period:

The VPL seems to follow quite optimally the vertical error (see 4.18a and 4.18b). The error is strongly influenced by the spatial ionosphere bias for satellites located in the sector of influence of the ionosphere storm.

Even if the Gap between the protection level and the user error is small, the ground monitoring of the ionosphere provides sufficient information to over bound the error at user level.

By looking in details, the VPL equation as specified above supposes a perfect monitoring of the spatial ionosphere gradient.

4.3.9.3. Dual frequency I-Free using GPS and Galileo

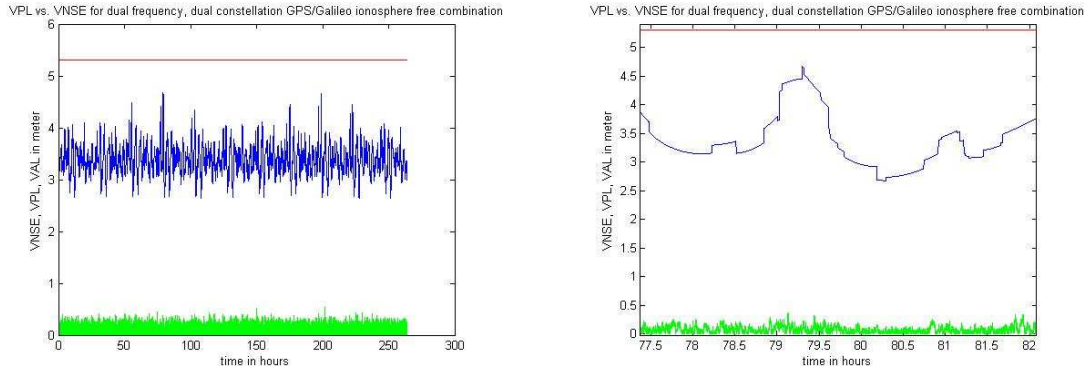

(a) I-Free scenario **(b)** Zoom I-Free scenario

Figure 4.19.: VPL (blue) and VNSE (green) results compared to VAL (red) for the I-Free scenario using all in view GPS and Galileo satellites

For the ionosphere free combination, the ionosphere error is completely eliminated at receiver level. The affected satellites will behave exactly like the other satellites. The price to pay is a higher level of noise due to the combination of code observations in L1 and in E5a/L5.

In 4.19a and 4.19b, it can be observed that the error is much lower than the protection level. A zoom in a worst geometry region shows the evaluation of the error with respect to the protection level.

In contrary to the D-Free case, there is no apparent correlation between the error and the protection level. The carrier smoothing filter is providing very good results and maintains the error below 0.5 meter.

4.3.9.4. I-Free Combination using limited number of visible satellites

For this simulation scenario, we took into consideration limited number of channels: 24 (6 GPS and 6 Galileo dual frequency satellites). Thus we choose among all visible

GPS satellites 6 satellites and the same for Galileo. The best VDOP test is made after grouping all satellites.

We considered only the ionosphere free combination for this best VDOP scenario. Fig. 4.20 and Fig. 4.21 represent the VAL vs. VPL vs. VNSE during the whole duration of the simulation and after zooming.

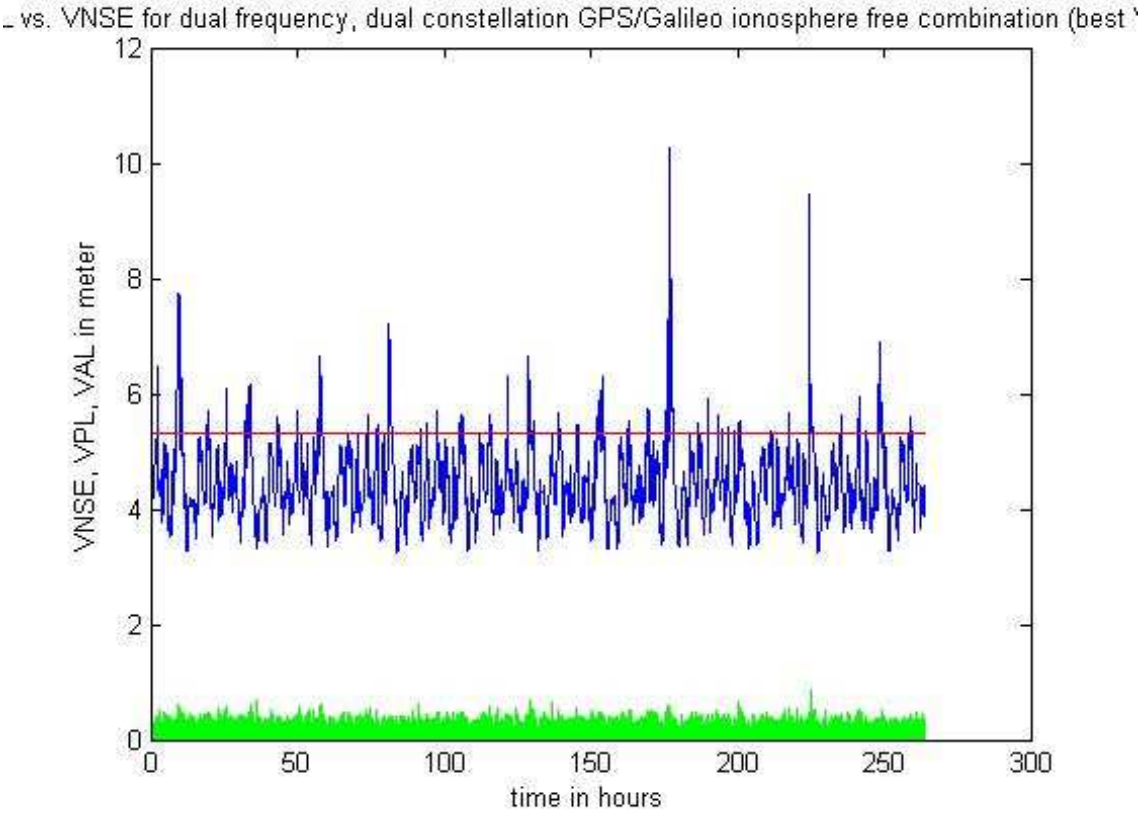

Figure 4.20.: I-Free VPL and VNSE using best 6 GPS and best 6 Galileo satellites

Although the level of error remains very low, the protection level exceeds the alarm limit for CAT III. When low number of satellites is considered, the protection level is very sensitive to the geometry variations. A zoom in the worst case VPL region shows better the width of unavailability:

These results show that a reduction of visible satellites provides a poor geometry and thus a too high protection level.

By varying the maximum number of satellite (12, 14, 16), we show that the protection level can be improved.

An important aspect consists of removing the satellites that could have a bad quality of data or for which the probability of outage is very high (see Fig. 4.22).

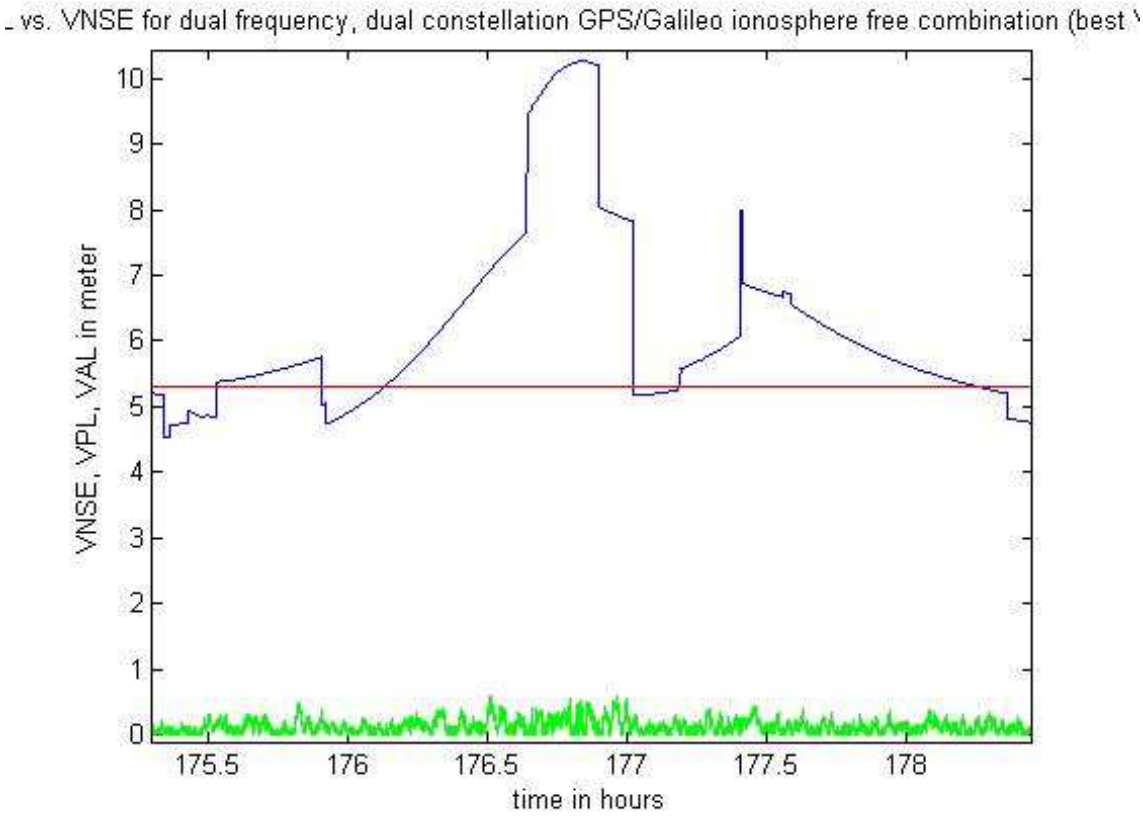

Figure 4.21.: Zoom of I-Free VPL and VNSE using best 6 GPS and best 6 Galileo satellites

4.3.9.5. Availability of Protection Levels

Aviation requirements include availability of required performance. For Cat III, the service must provide an availability of 99.9 to 99.999% of the time.

This availability include signal availability, navigation integrity and continuity of the service.

This study considers only the protection level which is a measure of integrity. Therefore the availability represents only the percentage of time the protection level is below the alert limit see Tab. 4.3.

For D-Free it appears that for 43 epochs, the VNSE is higher than the vertical protection level. This is very surprising and need to be investigated further. A possible cause of that is the effect of the initial deviation of the smoothing filter.

The most robust solution remains the ionosphere free combination using dual frequency. The divergence free combination provides an optimized overbound but necessitate an ionosphere monitor on ground.

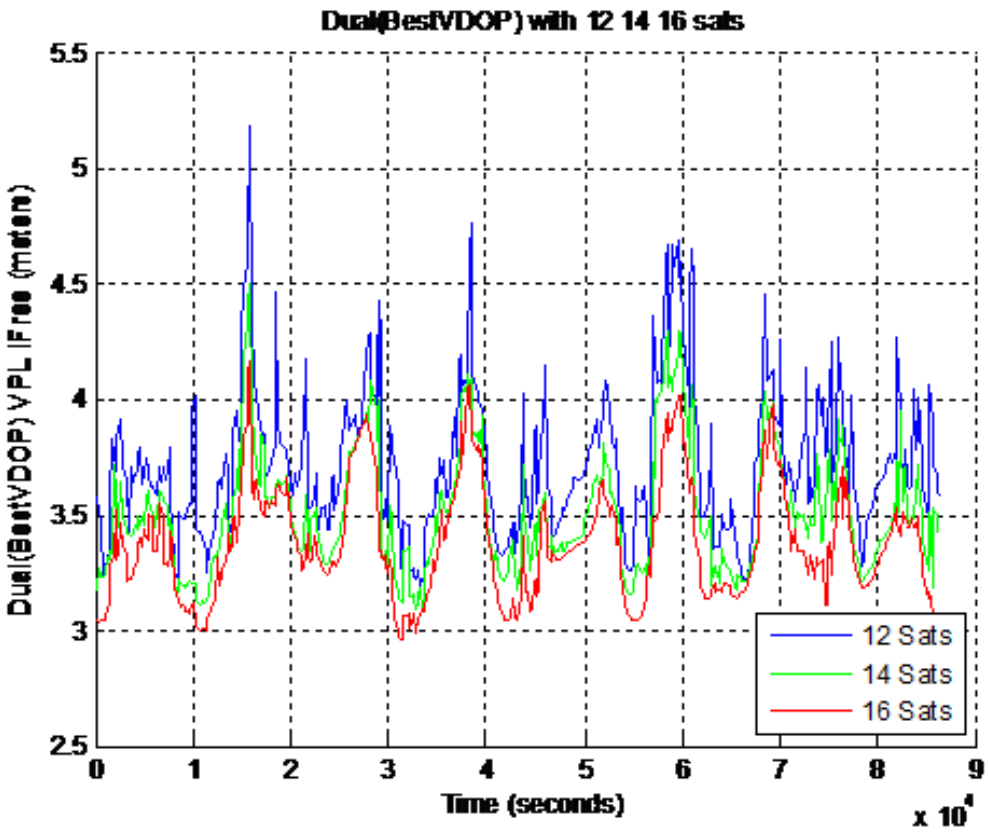

Figure 4.22.: I-Free protection level using limited number of satellites and best VDOP

4.4. Single Frequency Ground Ionosphere Gradient Monitor

THE WORK DESCRIBED IN THIS SECTION IS MY PERSONAL CONTRIBUTION

The Ground Based Augmentation System Testbed developed by DLR uses three receivers with separations of 740, 760 and 770 m from each other (see Fig. 4.32). In this section we explore the capabilities of the absolute ionosphere gradient monitor as proposed in [KYP+10] and adapt it for the multi-receiver (>2) case. Initially, we present the dual baseline ionosphere gradient monitor and we define the variables and parameters of the problem. Then we investigate the performance achieved with the existing architecture of 3 receivers. Then, we adapt the monitor for the existing configuration of the GBAS test bed and analyze the performance results of this configuration. In the next part of this section, we investigate the special case of co-linearly distributed receivers and propose optimal separation strategies when using 3 or 4 aligned receivers. In the last part of the section, we investigate

Scenario	Misleading information (in %) (epochs)	Availability (in %)
Single frequency	7.09 (134685)	100
D-free	0.023 (43)	100
I-free	0	100
I-free using best VDOP	0	91.85

Table 4.3.: Availability of protection level for different smoothing strategies. The second column (Misleading information) is defined as the percentage number of epochs the error is larger than the protection level. This happens when the system is not protected against a given threat in this case against strong ionosphere gradients. The third column (Availability) is the percentage of times the alert limit for the given phase of flight is larger than the protection level. For single frequency for

the ionosphere gradient as a diffusion process and determine the sensitivity of the monitor performance to the errors in the diffusivity coefficient of the ionosphere gradient. A conclusion summarizes the results obtained and the main contributions to the thesis.

4.4.1. Dual baseline absolute slant ionosphere gradient monitor

The absolute slant ionosphere gradient monitor proposed in [KYP+10] is based on single frequency double difference carrier phase observations. Assuming a precise knowledge of the receivers positions (and thus their baseline separation vector), it is possible to determine double difference residual biases like the ionospheric decorrelation between 2 receivers. These biases can be estimated as long as they are not within the measurement uncertainty to an integer multiple of a wavelength. In the following, we keep the same notations as in [KYP+10] and describe the dual baseline absolute slant ionosphere gradient monitor.

We start with the observation equations for the phase observation as already presented in equation 2.37 that we recall here:

$$\Phi_u^{(k)} = \lambda\phi_u^{(k)} - \lambda\phi^{(k)} + \lambda N_u^{(k)} + c\left(\delta t_u - \delta t^{(k)}\right) - I_u^{(k)} + T_u^{(k)} + \eta_u^{(k)} \tag{4.42}$$

this equation corresponds to a single pair (satellite k and user u)

The elementary architecture of the double difference carrier phase ionosphere monitor is composed of 2 reference receivers i and j observing a pair of satellites k

and l. Each reference receiver observe both satellites and we can build up 2 phase observations for each satellite. We therefore have for each epoch:

$$\Phi_i^{(k)} = \lambda\phi_i^{(k)} - \lambda\phi^{(k)} + \lambda N_i^{(k)} + c\left(\delta t_i - \delta t^{(k)}\right) - I_i^{(k)} + T_i^{(k)} + \eta_i^{(k)} \tag{4.43}$$

$$\Phi_j^{(k)} = \lambda\phi_j^{(k)} - \lambda\phi^{(k)} + \lambda N_j^{(k)} + c\left(\delta t_j - \delta t^{(k)}\right) - I_j^{(k)} + T_j^{(k)} + \eta_j^{(k)} \tag{4.44}$$

$$\Phi_i^{(l)} = \lambda\phi_i^{(l)} - \lambda\phi^{(l)} + \lambda N_i^{(l)} + c\left(\delta t_i - \delta t^{(l)}\right) - I_i^{(l)} + T_i^{(l)} + \eta_i^{(l)} \tag{4.45}$$

$$\Phi_j^{(l)} = \lambda\phi_j^{(l)} - \lambda\phi^{(l)} + \lambda N_j^{(l)} + c\left(\delta t_j - \delta t^{(l)}\right) - I_j^{(l)} + T_j^{(l)} + \eta_j^{(l)} \tag{4.46}$$

ODTS errors can be eliminated using for each satellite the single difference of observations from each receiver. We can build from the four equations above the following 2 single difference equations:

$$\Delta\Phi_{ij}^{(k)} \triangleq \Phi_i^{(k)} - \Phi_j^{(k)} = \lambda\Delta\phi_{ij}^{(k)} + \lambda\Delta N_{ij}^{(k)} + c\Delta\delta t_{ij} - \Delta I_{ij}^{(k)} + \Delta T_{ij}^{(k)} + \Delta\eta_{ij}^{(k)} \tag{4.47}$$

$$\Delta\Phi_{ij}^{(l)} \triangleq \Phi_i^{(l)} - \Phi_j^{(l)} = \lambda\Delta\phi_{ij}^{(l)} + \lambda\Delta N_{ij}^{(l)} + c\Delta\delta t_{ij} - \Delta I_{ij}^{(l)} + \Delta T_{ij}^{(l)} + \Delta\eta_{ij}^{(l)} \tag{4.48}$$

Receiver biases can then be eliminated by differentiating 4.47 with 4.48 to obtain the double difference carrier phase equation:

$$\Delta^2\Phi_{ij}^{(kl)} \triangleq \Delta\Phi_{ij}^{(k)} - \Delta\Phi_{ij}^{(l)} = \lambda\Delta^2\phi_{ij}^{(kl)} + \lambda\Delta^2 N_{ij}^{(kl)} - \Delta^2 I_{ij}^{(kl)} + \Delta^2 T_{ij}^{(kl)} + \Delta^2\eta_{ij}^{(kl)} \tag{4.49}$$

It appears as illustrated in Fig. 4.23 that the single difference can be expressed as the scalar product of the baseline with the unit vector for the corresponding satellite:

$$\Delta\Phi_{ij}^{(k)} = \mathbf{b}_{ij} \cdot \mathbf{e}^{(k)} \tag{4.50}$$

$$\Delta\Phi_{ij}^{(l)} = \mathbf{b}_{ij} \cdot \mathbf{e}^{(l)} \tag{4.51}$$

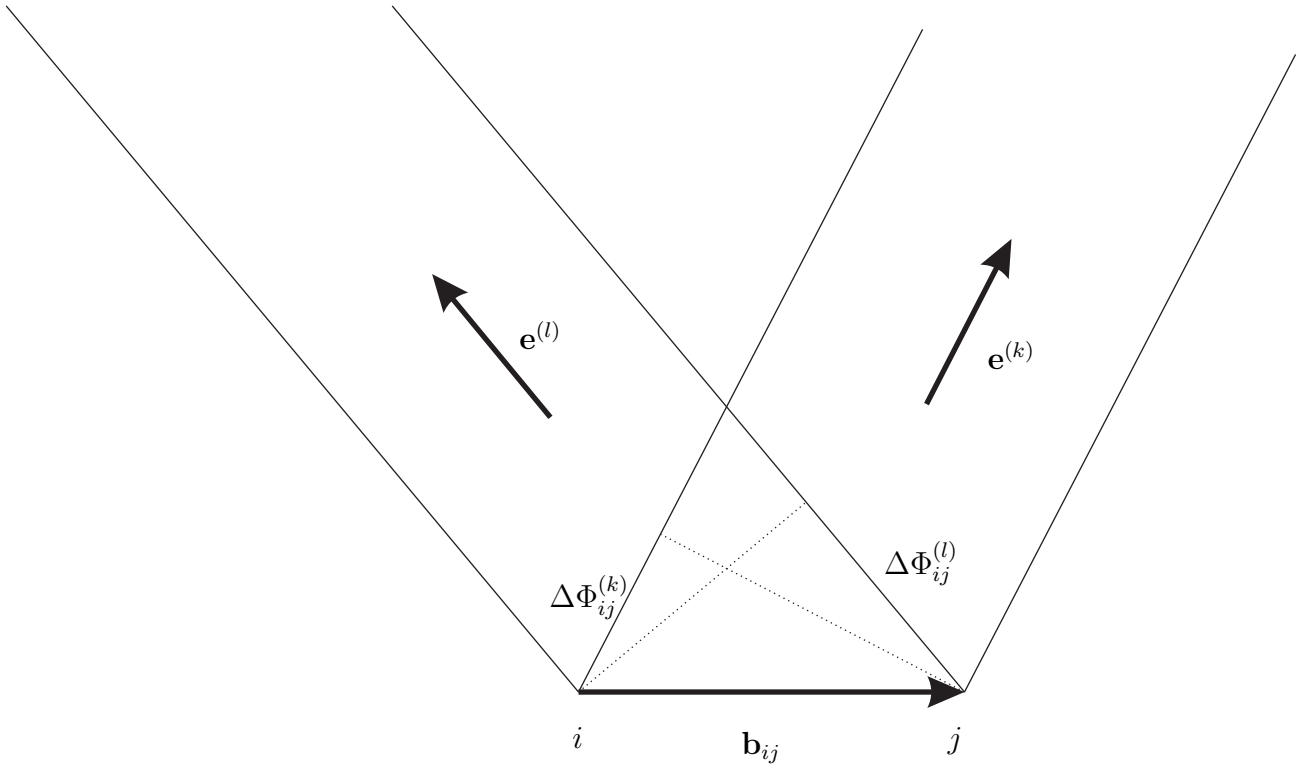

Figure 4.23.: Geometric representation of the double difference carrier phase observation with $\mathbf{e}^{(k)}$ respectively $\mathbf{e}^{(l)}$ being the unit vectors from receiver i or j to satellite k respectively l, $\mathbf{b}_{ij}$ is the baseline vector from receiver i to receiver j, $\Delta\Phi_{ij}^{(k)}$ respectively $\Delta\Phi_{ij}^{(l)}$ being the single carrier phase difference relative to satellite k respectively l.

So we have:

$$\Delta^2\Phi_{ij}^{(kl)} = \mathbf{b}_{ij} \cdot \left(\mathbf{e}^{(k)} - \mathbf{e}^{(l)}\right) = \mathbf{b}_{ij} \cdot \Delta\mathbf{e}^{(kl)} \tag{4.52}$$

And replacing $\Delta^2\Phi_{ij}^{(kl)}$ by $\mathbf{b}_{ij} \cdot \Delta\mathbf{e}^{(kl)}$ in 4.49 gives:

$$\mathbf{b}_{ij} \cdot \Delta\mathbf{e}^{(kl)} = \lambda\Delta^2\phi_{ij}^{(kl)} + \lambda\Delta^2 N_{ij}^{(kl)} - \Delta^2 I_{ij}^{(kl)} + \Delta^2 T_{ij}^{(kl)} + \Delta^2\eta_{ij}^{(kl)} \tag{4.53}$$

The double difference integer ambiguity $\Delta^2 N_{ij}^{(kl)}$ can take positive or negative integer values. We assume in the whole section this term as an unknown and by convention and in order to fit with notations in [KYP+10] to assume $\Delta^2 N_{ij}^{(kl)} = -\Delta^2 n_{ij}^{(kl)}$. The single difference ionosphere gradient $\Delta I_{ij}^{(k)}$ can be expressed using the ionosphere

spatial gradient $\alpha_{ij}^{(k)}$ and the norm of the baseline vector $\mathbf{b}_{ij}$. We have then $\Delta I_{ij}^{(k)} = \alpha_{ij}^{(k)} \|\mathbf{b}_{ij}\|$. If we assume that the reference satellite l is not affected by a gradient, we have $\alpha_{ij}^{(l)} = 0$ and therefore $\Delta^2 I_{ij}^{(kl)} = \alpha_{ij}^{(k)} \|\mathbf{b}_{ij}\|$.

If additionally we assume that due to the short baseline considered, the troposphere has no spatial variations, we have $\Delta^2 T_{ij}^{(kl)} = 0$. Based on these assumptions and by grouping the "measurable" parameters in the left hand and the unknown parameters in the right hand, we have:

$$\lambda\Delta^2\phi_{ij}^{(kl)} - \mathbf{b}_{ij} \cdot \Delta\mathbf{e}^{(kl)} = \lambda\Delta^2 n_{ij}^{(kl)} + \alpha_{ij}^{(k)} \|\mathbf{b}_{ij}\| + \Delta^2\eta_{ij}^{(kl)} \tag{4.54}$$

The left hand side can be measured at each epoch and is composed of $\Delta^2\phi_{ij}^{(kl)}$ the double difference carrier phase measurement between receiver i and receiver j, the differential receiver to satellite unit vector $\Delta\mathbf{e}^{(kl)}$ (which can be determined using the navigation message of the considered satellites) and the baseline vector between the receivers $\mathbf{b}_{ij}$.

The right hand side of the equation is unknown and corresponds to the sum of the double difference carrier phase cycle ambiguity $\Delta^2 n_{ij}^{(kl)}$, the ionosphere gradient $\alpha_{ij}^{(k)}$ between receiver i and j times the norm of the baseline vector $\mathbf{b}_{ij}$, and the double difference carrier phase residual error $\Delta^2\eta_{ij}^{(kl)}$ whose distribution is overbounded by the Gaussian distribution with standard deviation $\sigma_{ij}^{(kl)}$.

Let's denote $\sigma_i^{(k)}$ the standard deviation of the Gaussian over-bounded carrier phase residual error (noise and multipath) of receiver i for the signal coming from satellite k. In order to study the sensitivity of the monitor performances to receiver carrier phase error, we keep the standard deviation of each receiver independent and we define $r_{ij}^{(k)} = \frac{\sigma_j^{(k)}}{\sigma_i^{(k)}}$ the standard deviation ratio between receiver j and receiver i (taken as reference) with respect to satellite k. Let's call $\sigma_{ij}^{(kl)}$ the standard deviation of the double difference phase error $\Delta^2\eta_{ij}^{(kl)}$ when considering receiver j, receiver i and satellite k, satellite l. Then we have the relation:

$$\sigma_{ij}^{(kl)} = \sqrt{2\left(1 + r_{ij}^{(k)2}\right)}\sigma_i^{(k)} \tag{4.55}$$

Furthermore, we assume that the phase residual errors are independent from satellite to satellite with respect to one receiver and independent from receiver to receiver with respect to one satellite (we assume that the baseline is sufficiently large to fulfill this assumption). We also assume that the errors or, more precisely, the error over-bounds are Gaussian distributed.

Since our interest is to monitor the ionosphere gradient component in the direction of the runway for an aircraft in an "ILS-look alike" approach, it is necessary to project

the individual test statistics by projecting the baselines in the runway direction as will be explained later while considering the GBAS test bed located in Braunschweig airport.

4.4.2. Measurement and Simulation Form of the Test Statistic

The aim of a ionosphere gradient monitor is to detect an ionosphere gradient that can be a threat for GBAS. Equation 4.54 suggests to use the following test statistic (see [KYP+10]):

$$s_{ij}^{(kl)} = \lambda\Delta^2\phi_{ij}^{(kl)} - \mathbf{b}_{ij}\cdot\Delta\mathbf{e}^{(kl)} - \lambda\text{round}\left(\frac{\Delta^2\phi_{ij}^{(kl)} - \mathbf{b}_{ij}\cdot\Delta\mathbf{e}^{(kl)}}{\lambda}\right) \tag{4.56}$$

where round is the function that rounds to the nearest integer. This form is called the "measurement form" of the test statistic because it is only based on actual measurements from receivers and the knowledge of the satellite ephemeris. This is also what should be implemented for a real time processing of the monitor. The following form is preferred in the rest of this section because it is better suitable for a performance and sensitivity analysis and is what we call the "simulation form" of the test statistic:

$$s_{ij}^{(kl)} = \lambda\Delta^2 n_{ij}^{(kl)} + \alpha_{ij}^{(k)}\left\|\mathbf{b}_{ij}\right\| + \Delta^2\eta_{ij}^{(kl)} - \lambda\text{round}\left(\frac{\lambda\Delta^2 n_{ij}^{(kl)} + \alpha_{ij}^{(k)}\left\|\mathbf{b}_{ij}\right\| + \Delta^2\eta_{ij}^{(kl)}}{\lambda}\right) \tag{4.57}$$

$\Delta^2 n_{ij}^{(kl)}$is an integer and it will vanish from $s_{ij}^{(kl)}$.

$$s_{ij}^{(kl)} = \alpha_{ij}^{(k)}\left\|\mathbf{b}_{ij}\right\| + \Delta^2\eta_{ij}^{(kl)} - \lambda\text{round}\left(\frac{\alpha_{ij}^{(k)}\left\|\mathbf{b}_{ij}\right\| + \Delta^2\eta_{ij}^{(kl)}}{\lambda}\right) \tag{4.58}$$

The advantage of using the test statistic suggested is the non necessity to solve the integer ambiguity. The price to pay is to have an ambiguity in the estimation of the ionosphere gradient $\alpha_{ij}^{(k)}$ as we will see later.

$s_{ij}^{(kl)}$ is defined in the interval $\Omega = \left[-\frac{\lambda}{2}, \frac{\lambda}{2}\right]$. We assume that $\alpha_{ij}^{(k)}$ takes its values in the interval $[-2000, 2000]$ mm/km. We implicitly consider that the probability to have an ionosphere gradient $\left|\alpha_{ij}^{(k)}\right| \geq 2000$ is equal to 0. If we call $f_{\eta|\alpha}$ the probability density function of $\alpha_{ij}^{(k)}\left\|\mathbf{b}_{ij}\right\| + \Delta^2\eta_{ij}^{(kl)}$, which is a normal distribution with mean $\alpha_{ij}^{(k)}\left\|\mathbf{b}_{ij}\right\|$ and a variance $\sigma_{ij}^{(kl)2}$, the probability density function $f_{s|\alpha}$ of s_{ij} given that a gradient $\alpha_{ij}^{(k)}$ is present can be written as follows:

$$f_{s|\alpha} : \Omega \Rightarrow \mathbb{R}^+$$
$$f_{s|\alpha}(x) = \sum_{n\in\mathbb{Z}} f_{\eta|\alpha}(x + n\lambda) \tag{4.59}$$

$\mathbb{R}^+$ being the half positive real line. Equation 4.59 maps the non centered Gaussian distribution in the domain of definition of $f_{s|\alpha}$ (Ω). If we partition the line $\mathbb{R}$ in segments of length λ, $f_{s|\alpha}$ is the sum of all segments of the function $f_{\eta|\alpha}$ defined in these intervals.

We can show that $\int_\Omega f_{s|\alpha}(x)dx = 1$:

$$\int_\Omega f_{s|\alpha}(x)dx = \sum_{n\in\mathbb{Z}} \int_{-\frac{\lambda}{2}}^{\frac{\lambda}{2}} f_{\eta|\alpha}(x + n\lambda)dx \tag{4.60}$$
$$= \sum_{n\in\mathbb{Z}} \int_{\lambda\left(n-\frac{1}{2}\right)}^{\lambda\left(n+\frac{1}{2}\right)} f_{\eta|\alpha}(y)dy \tag{4.61}$$
$$= \sum_{n\in\mathbb{Z}} \left[F_{\eta|\alpha}\left(\lambda\left(n+\frac{1}{2}\right)\right) - F_{\eta|\alpha}\left(\lambda\left(n-\frac{1}{2}\right)\right)\right] \tag{4.62}$$
$$= F_{\eta|\alpha}(+\infty) - F_{\eta|\alpha}(-\infty) \tag{4.63}$$
$$= 1 \tag{4.64}$$

with $F_{\eta|\alpha}$ being the cumulative density function.

The shape of the distribution is driven by the standard deviation $\sigma_{ij}^{(kl)}$ and $\alpha_{ij}^{(k)} \|\mathbf{b}_{ij}\|$: For small $\sigma_{ij}^{(kl)}$ and α, the shape of the distribution is close to a centered Gaussian distribution. For large $\sigma_{ij}^{(kl)}$, $f_{s|\alpha}$ is close to a uniform density function with value $\frac{1}{\lambda}$ in the interval of definition of the function. The product $\alpha_{ij}^{(k)} \|\mathbf{b}_{ij}\|$ defines the shift of the probability density function inside Ω . Fig. 4.24 is an example of the probability density function of the test statistics for a very large value (28.67 mm) of $\sigma_{ij}^{(kl)}$.

The distribution of the test statistic is not Gaussian. The values taken by the test statistic are reduced in a finite interval Ω, i.e. for constantly growing $\alpha_{ij}^{(k)} \|\mathbf{b}_{ij}\|$ from 0 to 2λ for example, the maximum of $f_{s|\alpha}$ is growing from 0 up to $\frac{\lambda}{2}$, jumping back to $-\frac{\lambda}{2}$, increasing again up to $\frac{\lambda}{2}$ and jumping back again to $-\frac{\lambda}{2}$ and stop at 0.
The non detectable area (central region of s_{ij}) is periodic and the detectable set is periodic too. Therefore we will prefer the term "set of detectable gradients" rather than "minimum detectable gradients".

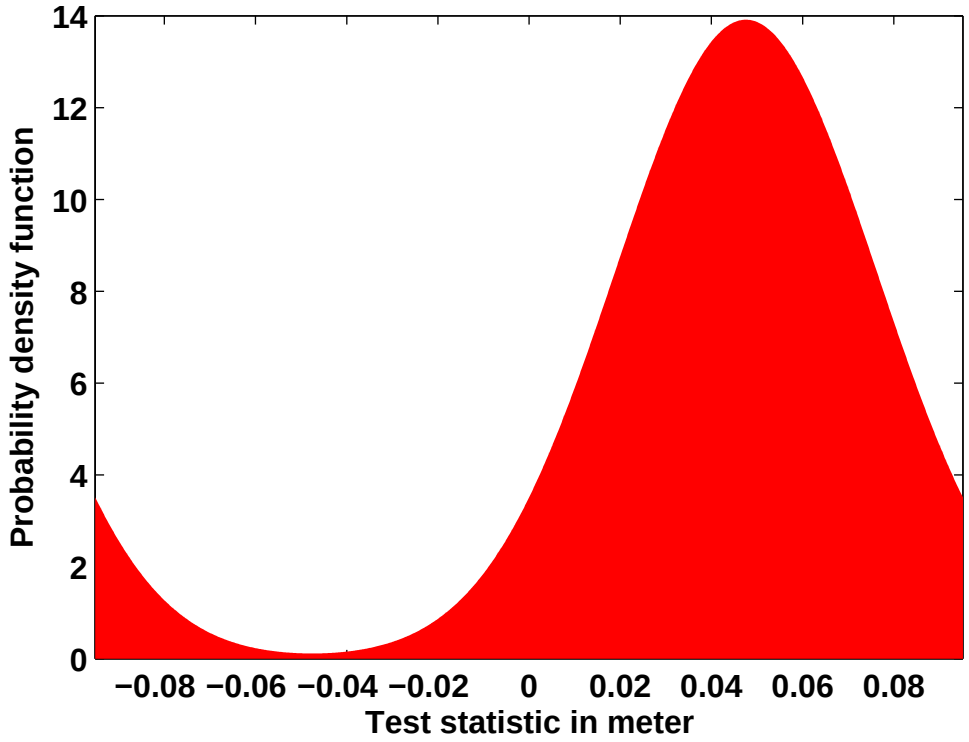

Figure 4.24.: Density function of the test statistic $f_{s|\alpha}$ when using a double difference carrier phase residual error standard deviation of $\sigma_{ij}^{(kl)} = 28.67$ mm, an ionosphere gradient of $\alpha = 216$ mm/km and a baseline $\|\mathbf{b}_{ij}\| = 220$m.

4.4.3. Set of Detectable Ionosphere Gradients

We define the null-hypothesis (H_0) as being the hypothesis that $\alpha_{ij}^{(k)} \|\mathbf{b}_{ij}\|$ is equal to an integer number of wavelength λ.

Given the probability of false alarm (for numerical application we choose 10^{-4}, for a detail justification see [KYP+10]) and the test statistic distribution corresponding to the H_0 hypothesis, we can determine the threshold $T_{fa} \in \Omega$ as follows:

$$\int_{-T_{fa}}^{T_{fa}} f_{s|0}(x)dx = 1 - P_{\text{fa}} \tag{4.65}$$

Where $f_{s|0}$ is the density of H_0.

A gradient α can be detected if the following relation is verified:

$$\int_{-T_{fa}}^{T_{fa}} f_{s|\alpha}(x)dx \leq P_{\text{md}} \tag{4.66}$$

Where P_{md} is the probability of missed detection (for numerical application we choose 10^{-4}, for a detail justification see [KYP+10]). $f_{s|\alpha}$ is the probability density function of the H_1 hypothesis (defined as the hypothesis of having $\alpha_{ij}^{(k)} \|\mathbf{b}_{ij}\|$ not equal to an integer number of wavelength λ).

The set of α verifying this relation is defined as the set of detectable gradients. This is a function of the baseline between two receivers, the level of the double difference carrier phase residual error, the probability of false alarm and the probability of missed detection. Fig. 4.25 shows the left border of the set of detectable gradients represented by the abscissa of the maximum of the density function in red divided by the baseline. When the density function of the H_1 hypothesis is shifted in the right, the function is truncated at $\frac{\lambda}{2}$ and the truncated part is thrown to the left.

From the equation above, there exists a factor K_{σ_η} such that the set of detectable gradients can be written as follows:

$$\begin{aligned}\mathcal{G} = \bigcup_{n\in\mathbb{Z}} \Bigg\{ &\left[\frac{\lambda}{\|\mathbf{b}_{ij}\|}\left(n - \frac{1}{2}\right), \frac{\lambda n - K_{\sigma_\eta}\sigma_{ij}^{(kl)}}{\|\mathbf{b}_{ij}\|} \right] \cup \\ &\cup \left[\frac{\lambda n + K_{\sigma_\eta}\sigma_{ij}^{(kl)}}{\|\mathbf{b}_{ij}\|}, \frac{\lambda}{\|\mathbf{b}_{ij}\|}\left(n + \frac{1}{2}\right) \right] \Bigg\}\end{aligned} \tag{4.67}$$

$\sigma_{ij}^{(kl)}$ is the double difference carrier phase error residual standard deviation. It characterizes the quality of the receiver and antenna. The first term correspond to the left side of the availability area, and the second corresponds to the right side. When $\sigma_{ij}^{(kl)}$ is increasing, the left border of the first term and the right border of the second term, do not change, the right border of the first term is decreasing until it

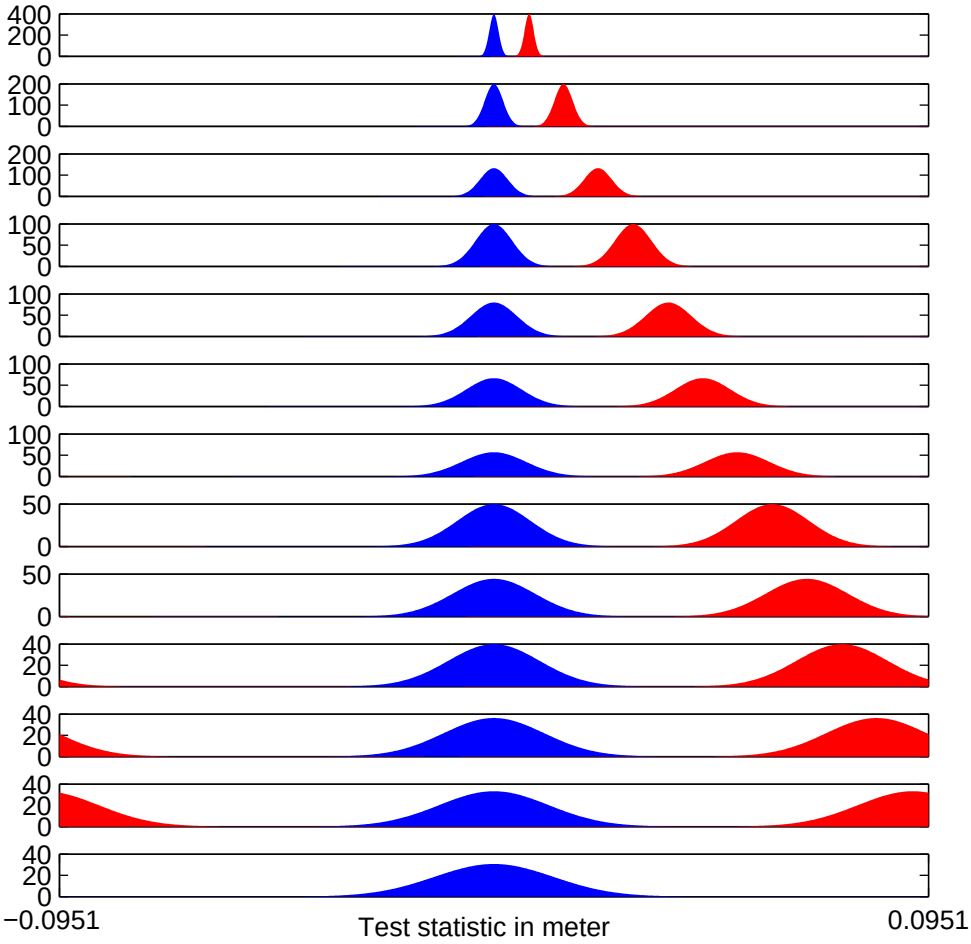

Figure 4.25.: Probability density function of the H_0 hypothesis in blue and H_1 in red. The test statistic s_{ij} in the x axis takes values in $\left[-\frac{\lambda}{2}, \frac{\lambda}{2}\right]$. The location of the maximum of the H_1 density function corresponds to the left border of the set of detectable gradients multiplied by the baseline. From top to bottom $\sigma_{ij}^{(kl)} = 1$ to 13 mm with a step of 1 mm and using a baseline of $\|\mathbf{b}_{ij}\| = 220$m. For $\sigma_{ij}^{(kl)} = 13$ mm, the set of detectable gradient is void.

vanishes for $\sigma_{ij}^{(kl)} = \frac{\lambda}{2K_{\sigma_\eta}}$, in a symmetric way, the left border of the second term is increasing until the second term vanishes for the same value $\sigma_{ij}^{(kl)} = \frac{\lambda}{2K_{\sigma_\eta}}$.

if we replace n by $n+1$, the set $\mathcal{G}$ remains unchanged and the second interval in the union operator for n can be merged with the first interval for $n+1$ leading to the following expression:

$$\mathcal{G} = \bigcup_{n\in\mathbb{Z}} \left\{ \left[\frac{\lambda n + K_{\sigma_\eta}\sigma_{ij}^{(kl)}}{\|\mathbf{b}_{ij}\|}, \frac{\lambda(n+1) - K_{\sigma_\eta}\sigma_{ij}^{(kl)}}{\|\mathbf{b}_{ij}\|} \right] \right\} \tag{4.68}$$

This expression is better suited for further discussion. We obtain the same expression as in [BDLK10a] by replacing K_{σ_η} by $k_{\text{ffd}} + k_{\text{md}}$. For small values of $\sigma_{ij}^{(kl)}$, K_{σ_η} and $k_{\text{ffd}} + k_{\text{md}}$ are the same. For large values $\sigma_{ij}^{(kl)}$, K_{σ_η} is greater than $k_{\text{ffd}} + k_{\text{md}}$.

A gradient α is detectable by the monitor whose baseline is $\|\mathbf{b}_{ij}\|$ if it fulfills the following relation for any integer n:

$$\frac{\lambda n + K_{\sigma_\eta}\sigma_{ij}^{(kl)}}{\|\mathbf{b}_{ij}\|} \leq \alpha \leq \frac{\lambda(n+1) - K_{\sigma_\eta}\sigma_{ij}^{(kl)}}{\|\mathbf{b}_{ij}\|} \tag{4.69}$$

We can see in this expression, that for different baselines, we obtain different areas of availability of the monitor. For individual monitors, the set of detectability is periodic with a periodicity $\frac{\lambda}{\|\mathbf{b}_{ij}\|}$. In the same way the set of undetectable gradients is also periodic with same periodicity. The periodicity is inversely proportional to the baseline length of the considered monitor. To detect any gradient in the [300, 2000] mm/km range, unless $\sigma_{ij}^{(kl)} = 0$, it is necessary to use a combination of several receiver pairs with different baseline lengths. The objective is to define an architecture of multiple baselines that can detect all gradients between 300 and 2000 mm/km with the largest $\sigma_{ij}^{(kl)}$. Fig. 4.26, 4.27 and 4.28 give the detection areas for three different baselines. The largest baseline provides the shortest period of the gradient detection area. The choice of the baselines is going to be presented in the next chapter.

4.4.4. ASIGMA Detectability Area

We would like to find the optimal baseline that allows 100% detectability in the range $300 - 2000$ mm/km using the receivers with the highest $\sigma_{ij}^{(kl)}$ values. The availability areas of the monitor ASIGMA_{1i} (Absolute Slant Ionospheric Gradient Monitor Architecture between receiver RR_1 and receiver RR_i) are defined using 4.69. This equation is defined for any integer n. We can observe that if $\sigma_{ij}^{(kl)} = 0$, for any α there exist an integer n for which $\frac{\lambda n}{\|\mathbf{b}_{ij}\|} \leq \alpha \leq \frac{\lambda(n+1)}{\|\mathbf{b}_{ij}\|}$ and such an ideal monitor with

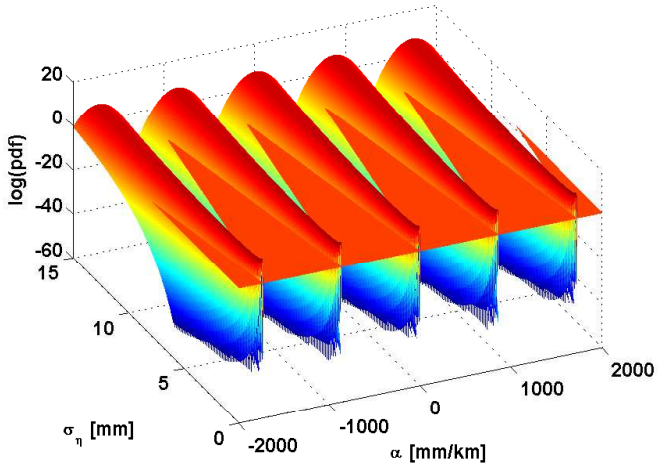

Figure 4.26.: Probability density surface of the H_0 hypothesis mapped in the slant ionosphere gradient range [-2000,2000] mm/km. The planar layer in red represent the set of detectable gradients considering a probability of false alarm and of missed detection of 10^{-4} and a baseline of 221 m

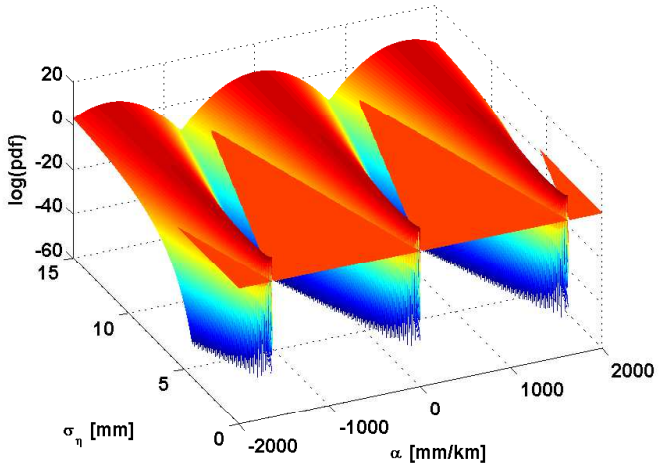

Figure 4.27.: Same as for the previous figure with a baseline of 117 m.

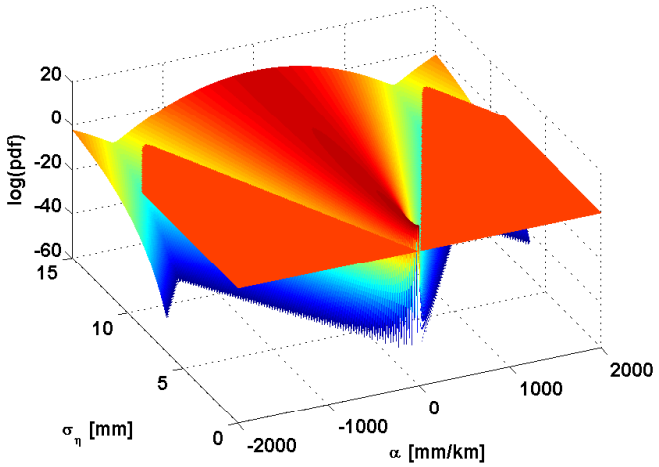

Figure 4.28.: Same as for the previous figure with a baseline of 61.9 m.

no carrier phase error would have 100% detectability. The minimum of $\sigma_{ij}^{(kl)}(\alpha)$ for which we have 100% of detectability is obtained for $\alpha = \frac{\lambda n}{\|\mathbf{b}_{ij}\|} \equiv \breve{\alpha}_n$. The minimum of $\sigma_{ij}^{(kl)}(\alpha)$ for which we have 0% detectability is obtained for $\sigma_{ij}^{(kl)} = \frac{\lambda}{2K_{\sigma_\eta}} \equiv \widehat{\sigma}$. It is interesting to notice that this is a constant. This is obtained for $\alpha = \frac{\lambda(n+1/2)}{\|\mathbf{b}_{ij}\|} \equiv \widehat{\alpha}_n^i$. The function $\sigma_{ij}^{(kl)}(\alpha) = g_i(\alpha)$ delimiting the area of availability of the monitor ASIGMA_{1i} is a periodically piece wise linear function that can be written in the following form :

$$\sigma_{ij}^{(kl)}(\alpha) = \frac{\widehat{\sigma}}{\widehat{\alpha}_n^i - \breve{\alpha}_n^i} \cdot \left(\alpha - \widehat{\alpha}_n^i\right) + \widehat{\sigma} \quad \breve{\alpha}_n^i \leq \alpha \leq \widehat{\alpha}_n^i \tag{4.70}$$

$$\sigma_{ij}^{(kl)}(\alpha) = \frac{\widehat{\sigma}}{\breve{\alpha}_{n+1}^i - \widehat{\alpha}_n^i} \cdot \left(\widehat{\alpha}_n^i - \alpha\right) + \widehat{\sigma} \quad \widehat{\alpha}_n^i \leq \alpha \leq \breve{\alpha}_{n+1}^i \tag{4.71}$$

The period of the monitor is $T^i = \breve{\alpha}_{n+1}^i - \breve{\alpha}_n^i = \frac{\lambda}{\|\mathbf{b}_{ij}\|}$. See Fig. 4.29 for a graphical description of the availability area of the monitor. This representation will be used during the whole section.

4.4.5. Application to DLR's GBAS Testbed

The Absolute Slant Ionosphere Gradient Monitor Architecture (ASIGMA) measures the gradient in the baseline directions which are not necessarily aligned with the runway. Fig. 4.31 describes this schematically:

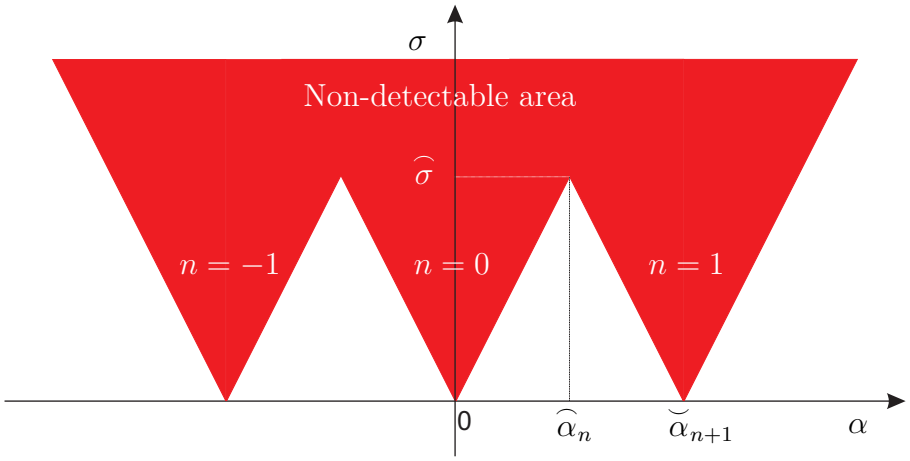

Figure 4.29.: ASIGMA performance metric. Area of availability (white) plotted using double difference carrier phase error standard deviation versus the slant ionosphere gradient magnitude. In red is the non detectability area for the given parameters.

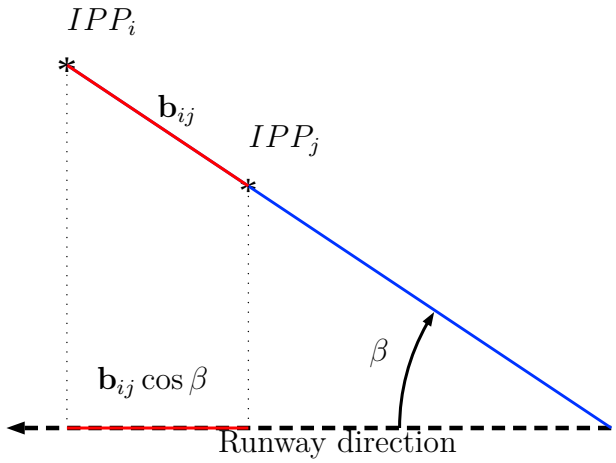

Figure 4.30.: Ionosphere gradient monitor projection in the runway direction

In Fig. 4.30, we assume that a monitor observe the ionosphere gradient between the IPP_i and IPP_j that we call α_{ij}.

So we have $\alpha_{ij} = \frac{\Delta I_{ij}}{\|\mathbf{b}_{ij}\|}$. We assume that the front we want to detect is perpendicular to the runway direction and that the magnitude of the ionosphere gradient of the front is the ionosphere difference divided by the projected baseline in the runway direction. This is generally a more conservative approach as the projected baseline is shorter when $\beta \neq 0$.

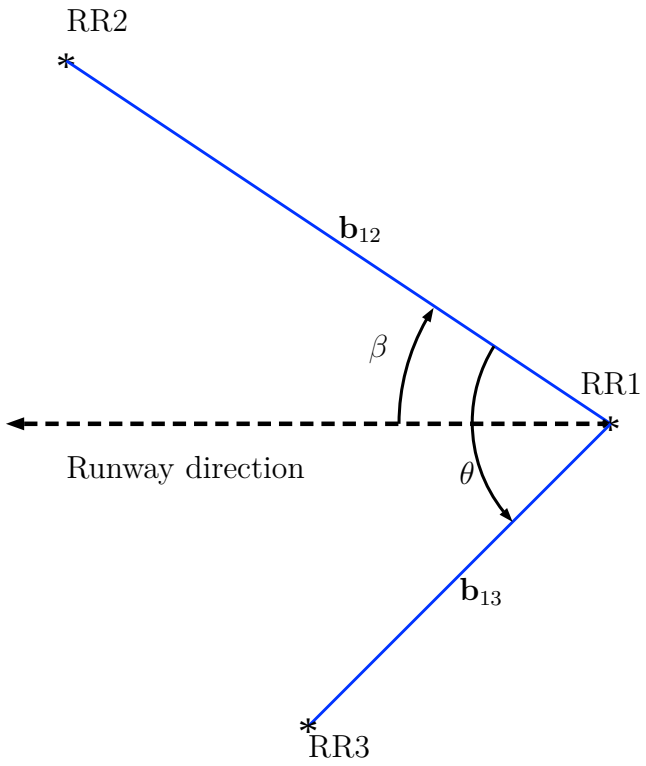

Figure 4.31.: General configuration scheme and notations. $\mathbf{b}_{ij}$ is the baseline vector defined by the reference receiver RR_i and RR_j . β is the angle between b_{12} and the runway direction, θ is the angle between the two baselines

From Fig. 4.31 we have $\alpha_{12}^0 = \frac{\alpha_{12}}{\cos\beta}$ and $\alpha_{13}^0 = \frac{\alpha_{13}}{\cos(\theta-\beta)}$ if we call α_{12}^0 and α_{13}^0 the gradients in the runway direction.

For each baseline, an absolute ionosphere gradient monitor using the test statistic as defined in [KYP+10] can be implemented. We assume that these monitors are independent and that each ionosphere gradient detected by one of them is projected into the runway direction. One needs to be careful with the fact that the monitor can't observe directly the gradient in the runway direction but only the components in the direction of the baseline. An extreme case is a baseline perpendicular to the runway. This would drive to an infinite gradient when projected in the direction of the runway. Therefore the angles θ and β should be kept as close as possible to zero.

The detectable ionosphere gradients are those fulfilling the following inequalities:

$$\frac{\lambda n + (k_{ffd} + k_{md})\,\sigma_{12}}{\mathbf{b}_{12}\cos\beta} < \alpha_{12}^{0} < \frac{\lambda\,(n+1) + (k_{ffd} + k_{md})\,\sigma_{12}}{\mathbf{b}_{12}\cos\beta} \tag{4.72}$$

$$\frac{\lambda n' + (k_{ffd} + k_{md})\,\sigma_{13}}{\mathbf{b}_{13}\cos\left(\theta - \beta\right)} < \alpha_{13}^{0} < \frac{\lambda\,(n'+1) + (k_{ffd} + k_{md})\,\sigma_{13}}{\mathbf{b}_{13}\cos\left(\theta - \beta\right)} \tag{4.73}$$

with n and n' being independent integers, λ is the wavelength of the considered signal, k_{ffd} is the inflation factor for fulfilling the required probability of false alarm and k_{md} is the inflation factor for fulfilling the required probability of missed detection. Details can be found in [KYP+10].These expressions are symmetric with respect to n and n'.

For our simulations, we used the actual receiver locations of the DLR's GBAS Testbed as shown in Fig. 4.32. This GBAS Test bed (stand 2010) is composed of 3 receivers with a plan to install a 4^{th} one.

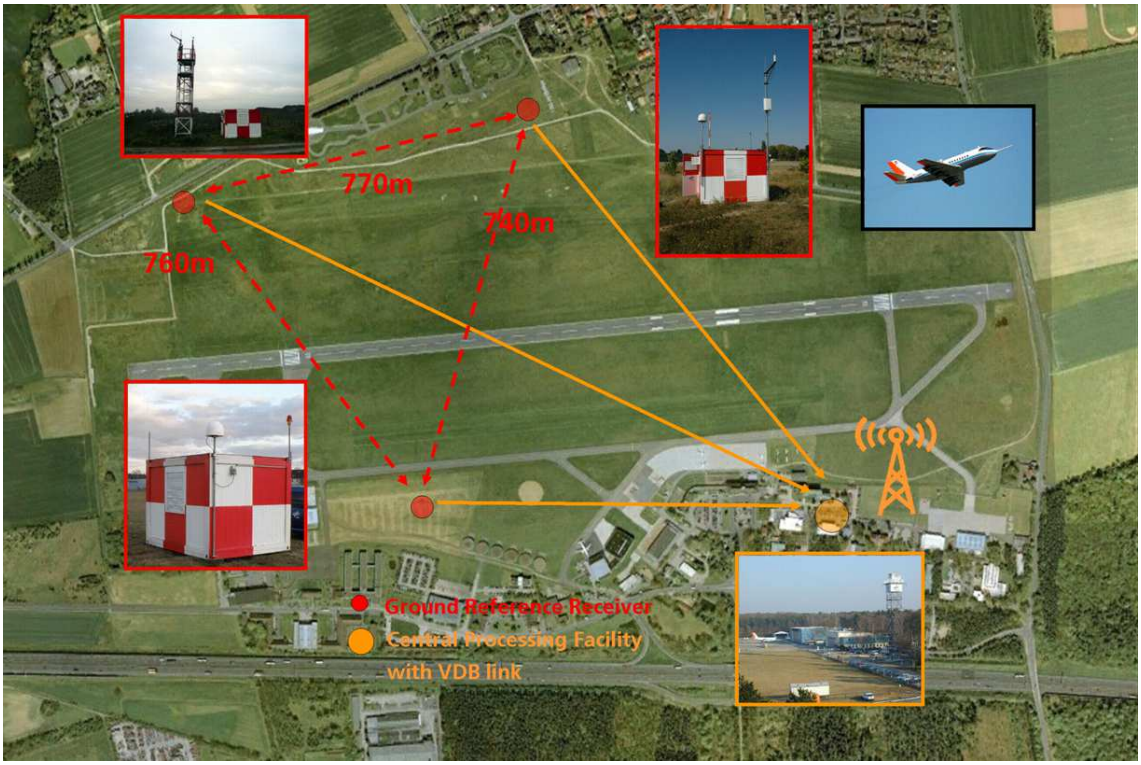

Figure 4.32.: GBAS reference receiver location at Braunschweig airport (status 2010)

The locations of the receivers in ECEF coordinate system are given in Tab. 4.4:

Table 4.4.: Receivers' locations in ECEF coordinates

Receiver	X in m	Y in m	Z in m
RR1	3840619.039	715604.228	5024909.863
RR2	3840835.113	714861.969	5024848.587
RR3	3841202.939	715429.959	5024488.675

From these locations we can determine the lengths of the baselines as well as the angles between baselines and runway direction.

There are 2 different approaches for taking benefit of both monitors:

- A slant ionosphere gradient is considered detected if at least one monitor can detect it (minimize the missed detection probability)
- A slant ionosphere gradient is considered detected only if both monitors simultaneously detect it (minimize the false alarm probability)

These two different approaches represent extreme cases for a combined dual baseline monitor i.e their application gives upper and lower performance bounds.

4.4.6. Simulation and Analysis of Results

The sensitivity of the monitor performance with respect to the receiver accuracy is plotted in 4.33a and in 4.33b.

The largest baseline b_{12} provides the largest availability at the GBAS test-bed. As only the region $300 - 2000$ mm/km is relevant for GAST-D [ICA06], we decided to show only this area in all our results. As geometry screening ([LLP+06, HM07]) would induce an unacceptable level of unavailability of the system, the extreme ionosphere gradients must be monitored in an efficient way. Studies have been conducted to analyze the impact of an ionosphere monitor in GBAS applications ([HM09]) and drive to the fact that in certain circumstances an absolute ionosphere gradient is necessary.

4.33c and 4.33d show the monitor results with the logic as defined in the previous paragraph. 4.33c shows results of detectability when both monitors can detect (represented by $\cap$) and 4.33d shows the detectability area when at least one monitor can detect (represented by $\cup$)

Both 4.33c and 4.33d show a loss of periodicity at least for the range of interest. The availability area is better in 4.33d than in 4.33c, as expected.

The impact of an additional monitor with a different baseline reduces the area of undetectability. An important aspect is the minimum σ for which 100% of the gradients in the range $300 - 2000$ mm/km are detectable. This minimum $\sigma \approx 1$ mm

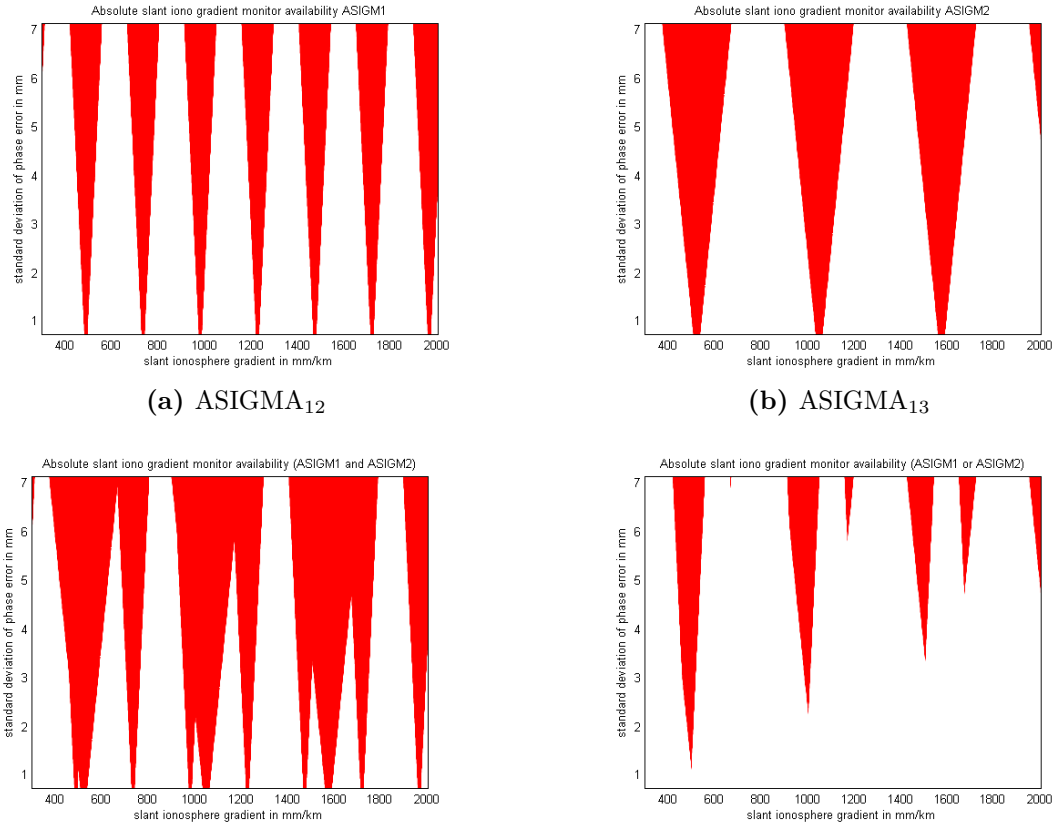

(a) ASIGMA_{12} **(b)** ASIGMA_{13}

(c) $\text{ASIGMA}_{12} \cap \text{ASIGMA}_{13}$ **(d)** $\text{ASIGMA}_{12} \cup \text{ASIGMA}_{13}$

Figure 4.33.: Absolute slant ionospheric gradient monitor availability function of standard deviation of phase error for baseline or combination of baselines. The red areas corresponds to non detectability regions of the monitors. The plots represents the double difference carrier phase standard deviation σ_η function of the slant ionospheric gradient α for $P_{\text{fa}} = P_{\text{md}} = 10^{-4}$

is shown in 4.33d for the DLR GBAS Testbed. This is an important parameter as this will provide requirements for the antennas, receivers and level of multipath in the neighborhood of the antennas. The baseline for the additional antenna should be chosen in a way that the minimum σ that provides 100% detectability is as large as possible. From 4.33d, an additional monitor with a maximum detectability around 500 mm/km will improve significantly the minimum allowed carrier phase double difference residual error to achieve 100% detectability.

4.4.7. Optimal linear distribution of monitors

We consider in this section that the receivers are all aligned and parallel to the runway. Let m be the total number of receivers with $m > 2$. Let's fix the largest

baseline $b_{1m} = B$ and consider one of the receivers at the edge to be the reference receiver. Fig. 4.34 shows a schematic description of this configuration.

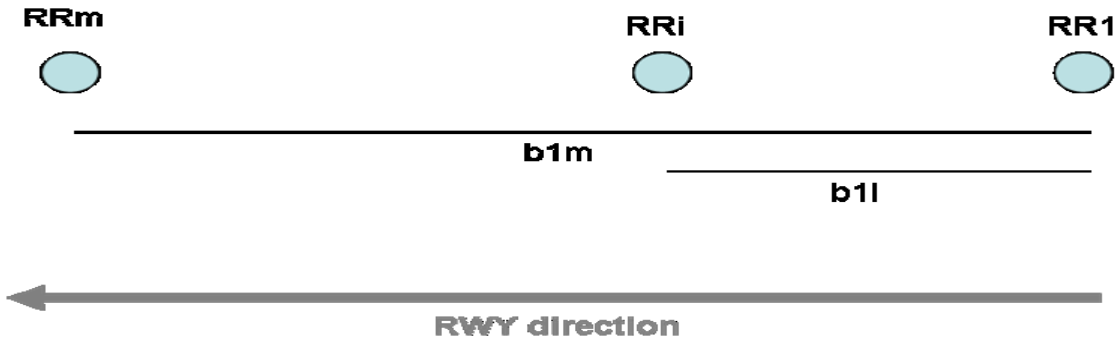

Figure 4.34.: Schematic description of the linear distribution of receivers and notations

Let us assume that the receivers have all the same performances: $\sigma_i = \sigma_j = \frac{1}{2}\sigma \quad \forall \{i,j\} \in \{1,2,\cdots,m\}^2$ where we have inserted the factor $\frac{1}{2}$ for simplification of algebraic calculus. We define b_{1i} to be the baseline from receiver 1 to receiver i. Let's define the baseline ratio $\eta_i = b_{1i}/B$. There are $m-1$ ratios to be considered with $0 = \eta_1 \leq \eta_i \leq \eta_m = 1$.

4.4.7.1. Optimal Distribution in the Case of 2 Monitors

The combination of two monitors provide us with an availability area which is a combination of both parametric curves defined above. The intersection points between the different lines can be calculated as follow. If we identify the first monitor with index i and the second one with index j and the integer ambiguity for monitor i being n_i and monitor j being n_j: The intersection is given for $\sigma^i(\alpha) = \sigma^j(\alpha)$. A first step is to identify the periodicity of the combined monitor: This is the largest common divisor of the periodicity of both individual ones. This is a function of the baselines. The largest common divisor is the product of both periods. One property of these intersecting points is that the border of the availability will switch from one monitor to the other.

For $m = 3$, we keep B and η_2 as variable. We search the optimal $B^\star$ of B and $\eta_2^\star$ of η_2 that maximize the level of double difference carrier phase error and maintaining a 100% detectability of an absolute slant ionosphere gradient in the range $300 - 2000$ mm/km. A gradient must be at least detected by one monitor to be considered within the detection range by the whole system. The second possible combination (detectability when all monitors detect) is not considered in this section.

The optimal problem, defined through the objective function that we want to maximize is taken as the carrier phase error that provides 100% of detectability in the

range $300 - 2000$ mm/km. The aim is to find the baselines that drive to this maximum and the value of the objective function at this optimum. The determination of this optimum is done numerically by considering discrete values for each baseline. The functions defined by 4.70 and 4.71 are calculated for each discretized baseline and for each integer values corresponding to the 300-2000 mm/km range. The monitors are then combined by taking the maximum values of the functions corresponding to each monitor for each slant ionosphere gradient. For each discrete value of the baselines we find the minimum of $\sigma(\alpha)$ for which 100% of detectability is guarantied. The results are plotted in Fig. 4.35.

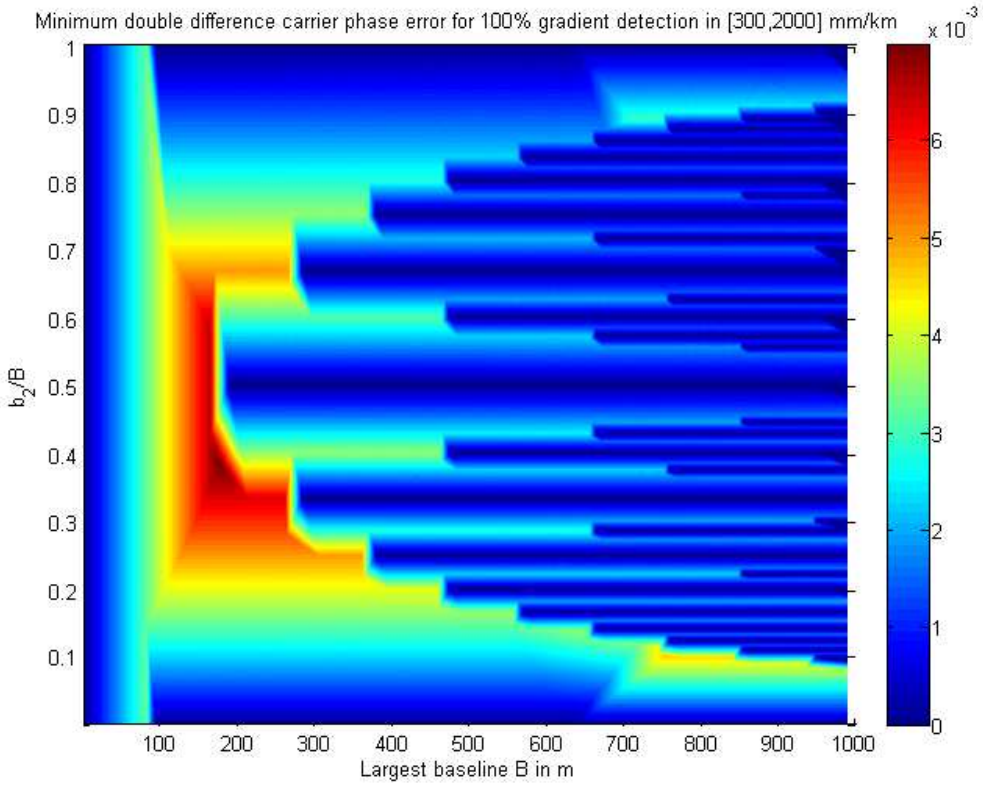

Figure 4.35.: Maximum standard deviation carrier phase error (color scale from 0 to 7 mm) that provides 100 % detectability in the range $300 - 2000$ mm/km function of the largest baseline in meter in the x axis and b_2/B in the y axis

We can notice in Fig. 4.35 a superposition of symmetric trend with respect to $b2/B$ and a dis-symmetric trend probably due to the dis-symmetry of the range of slant ionosphere gradients. For B below 82 meters, there is an independence with respect to η_2. For $B \geq 190$ m and $\eta_2 = 0.5$ (receiver in the middle of the interval), σ takes very low values and this architecture although symmetrical should be avoided. The values fund for the optimum are: $\sigma^\star = 6,97$ mm, $B^\star = 177$ m and $\eta_2^\star = 0.387$. This configuration provides the detectability area shown in Fig. 4.36:

The high level of double difference carrier phase noise allowed ($\sigma^\star$) can be achieved

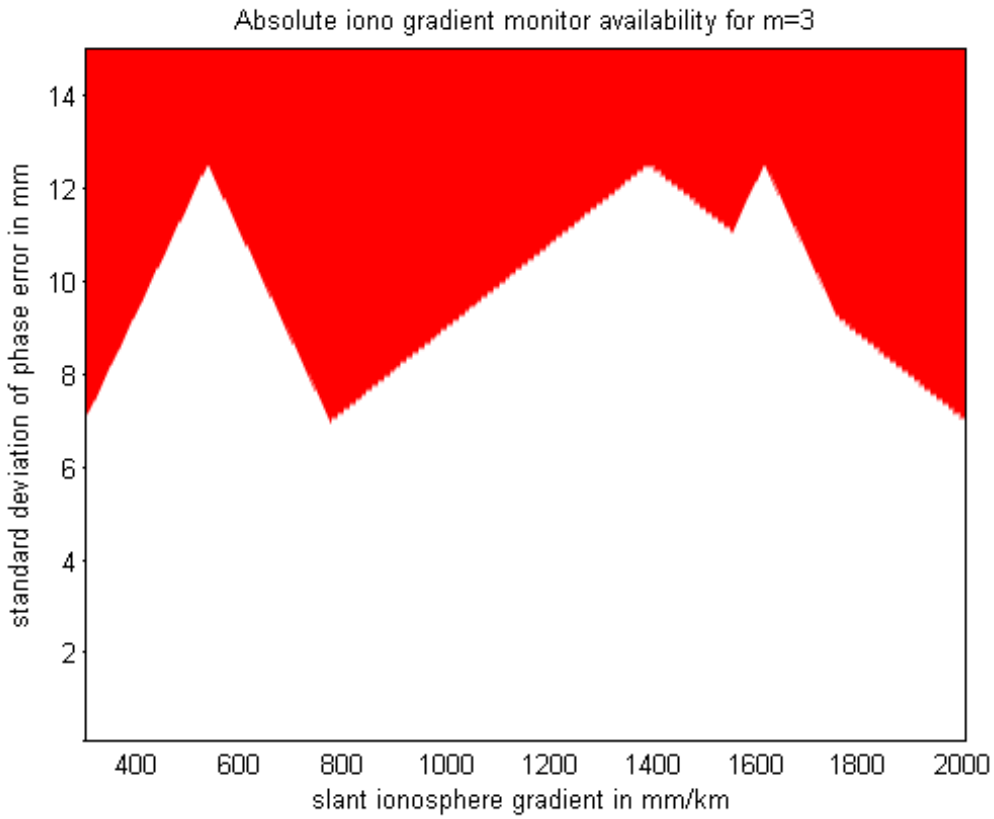

Figure 4.36.: Slant ionosphere gradient detection area for $m = 3$ receivers optimally linearly distributed.

with a well calibrated antenna. The sitting criteria should take into consideration the multipath environment as usual. Attention should be paid to the possible multipath correlation between RR_1 and RR_2 due to the shorter baseline.

If we apply these results to propose a possible location of a 4^{th} receiver at Braunschweig research airport to achieve GAST-D requirements and consider the receivers RR_1 and RR_2 for the largest baseline ($B \simeq 770$ m), the optimal location for RR_4 would be 77 m from RR_1 and the maximum allowed double difference carrier phase error standard deviation would be $4,5$ mm to achieve 100% of ionosphere gradient detectability.

4.4.7.2. Optimal Distribution in the Case of 3 Monitors

For $m = 4$ and assuming all 4 receivers are aligned. We find the following optimal surfaces:

The optimum is obtained for $\sigma^\star = 8,65$ mm, $B^\star = 221$ m, $\eta_2^\star = 0.28$ and $\eta_3^\star = 0.53$.

The result is a maximum tolerable carrier phase error and it provides the detectabil-

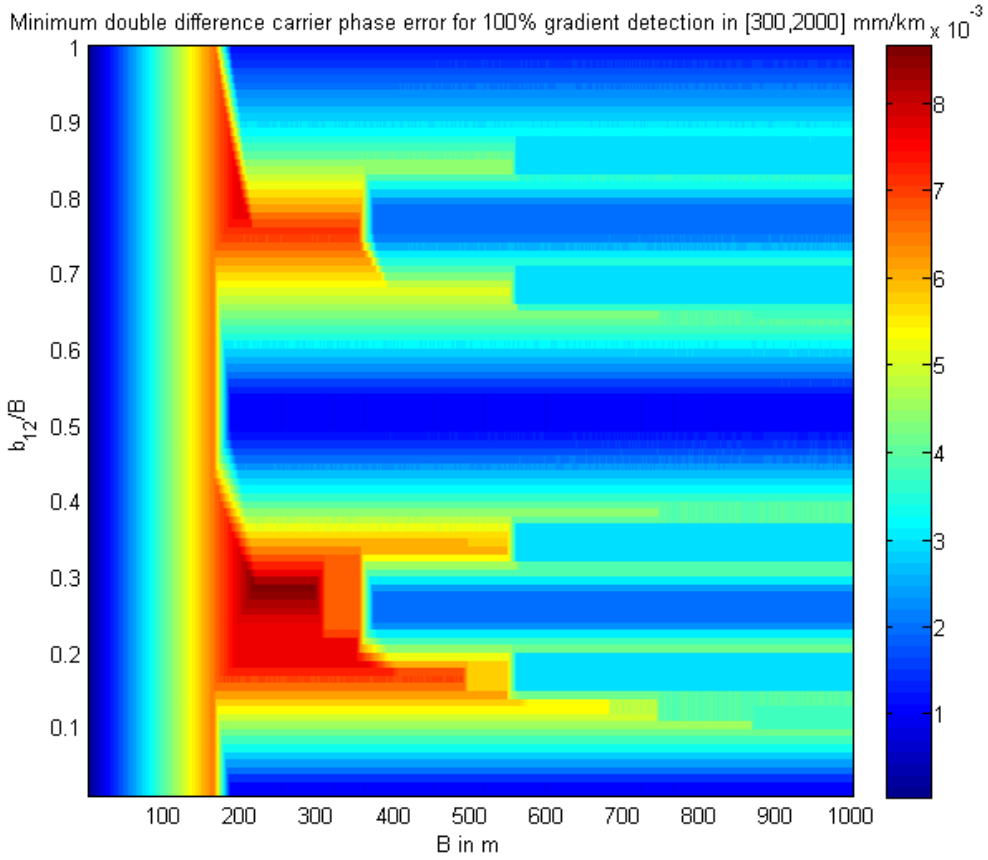

Figure 4.37.: Minimum carrier phase error for 100% gradient detection $\sigma_{\eta_3^\star}(B, \eta_2)$

ity area plotted in Fig. 4.40.

As expected the addition of one receiver provides higher maximum allowable double difference carrier phase error and the maximum baseline remains acceptable for a majority of airports.

4.4.7.3. Optimal Baseline Search Algorithm

Let's consider m being the number of monitors of the ASIGMA$_m$ configuration as drawn in Fig. 4.41. We have stated in [BDLK10a] that ideally each individual monitor should be parallel to the runway direction. From the previous section, we observed that the set of detectable gradients is periodic with a periodicity inversely proportional to the baseline of the considered monitor. The detection area refers in this section to the local gradient, i.e. the gradient experienced by the monitors.

In this section we assume that the double difference carrier phase residual error is the same for all monitors. (We assume the same receiver configuration, the same

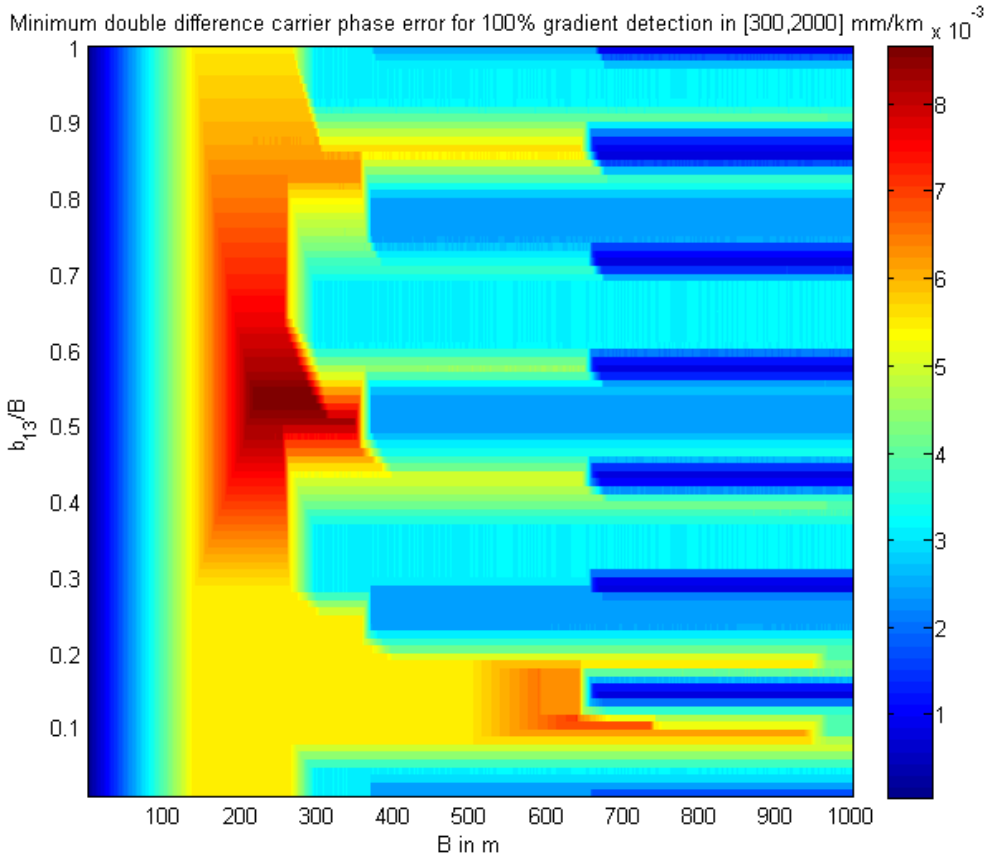

Figure 4.38.: Minimum carrier phase error for 100% gradient detection $\sigma_{\eta_2^\star}(B, \eta_3)$

antenna type and the same multipath environment) and we set for simplification: $\sigma_{ij}^{(kl)} = \sigma_\eta$

In [BDLK10a] we observe that for 3 and 4 optimally distributed receivers, the 300 mm/km detection is given by the largest baseline (ascending detection border of the monitor), and the 2000 mm/km detection is ensured by the shortest baseline (first descending detection border of the monitor).
For 3 receivers and therefore 2 monitors, the largest baseline is suited for the detection at 300 mm/km, but not up to 2000 mm/km. Therefore it is necessary that at least 2 monitors are in use. Fig. 4.42 is generated using 3 optimally distributed monitors as already obtained in [BDLK10a]. we can see that the optimal σ_η that we note $\sigma_\eta^\star$ is reached for 300 mm/km and 2000 mm/km in the case of 3 monitors. We observe the same for 2 monitors (see [BDLK10a]) .

We propose to define a simple formula to calculate the baselines of the monitors that provide the largest detection area.

We define $b_1 = B$ being the largest baseline and $b_i = \rho_i B$ the i-th baseline of ASIGMA$_m$. We consider that the the baselines are sorted from the largest to

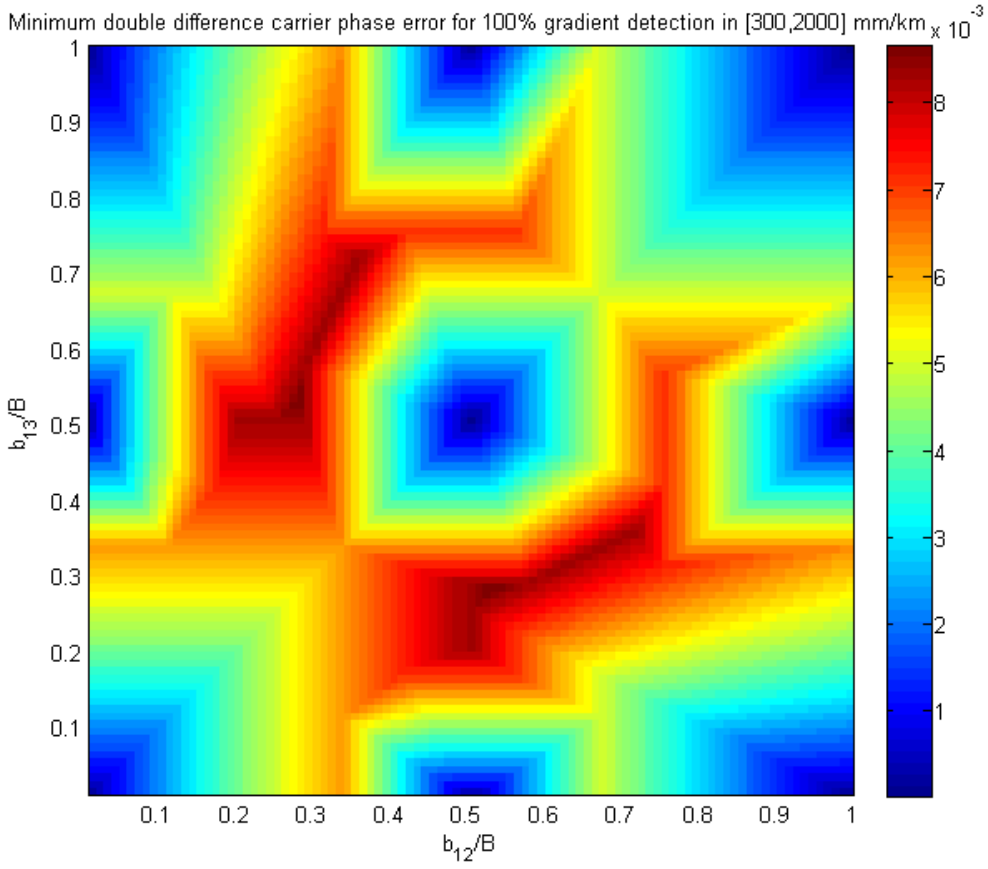

Figure 4.39.: Minimum carrier phase error for 100% gradient detection $\sigma_{B^\star}(\eta_2, \eta_3)$

the smallest one. By convention we define b_m as being the smallest baseline. In [BDLK10a] we observe for three monitors that $b_3^\star = \rho_3^2 B$ and $b_2^\star = \rho_3 B$ with $\rho_3 = 0.53$ approximately. It is tempting to generalize this rule for m monitors by writing:

$$\forall\, i \in \{1, \cdots, m\},\ b_i^\star = (\rho_m)^{i-1} B \tag{4.74}$$

We would have $b_m = (\rho_m)^{m-1} B$. From equation 4.69 and from the observation made above, we have for the right edge of the domain of detection required:

$$K_{\sigma_\eta}\sigma_\eta = \lambda - 2000 \times 10^{-6} (\rho_m)^{m-1} B \tag{4.75}$$

and for the left edge:

$$K_{\sigma_\eta}\sigma_\eta = 300 \times 10^{-6} B \tag{4.76}$$

From these equations, we obtain:

$$\rho_m = \left(\frac{\frac{\lambda}{B} - 300 \times 10^{-6}}{2000 \times 10^{-6}} \right)^{\frac{1}{m-1}} \tag{4.77}$$

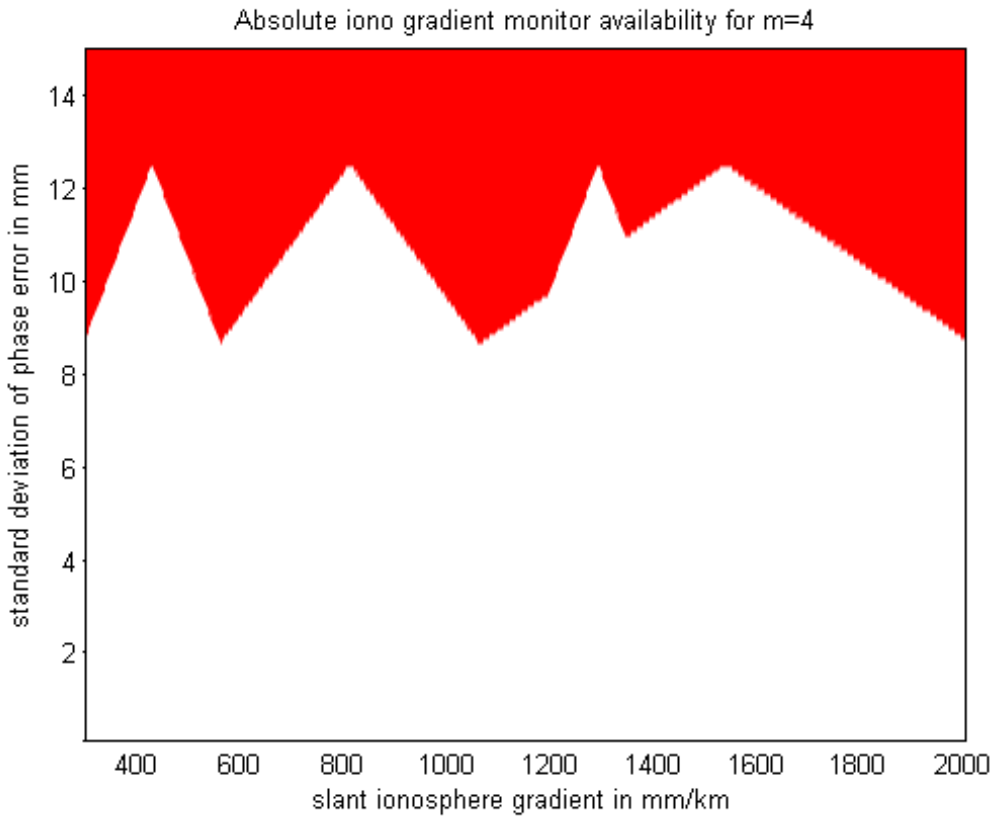

Figure 4.40.: Slant ionosphere gradient detection area for $m = 4$ receivers optimally distributed

This expression of ρ_m is parametrized by the largest baseline B.

This simplifies considerably the optimization problem for m monitors when $m \gg 1$. It is sufficient to make a search along the largest baseline B, the other baselines are directly calculated using 4.74 and 4.77.

4.4.8. Ionosphere Gradient as a Diffusion Process

Let's consider the optimal configuration with 4 receivers and the gradient range from $[-2000, +2000]$ mm/km (see Fig. 4.43for the detectability area).

At the optimal standard deviation of the phase error (The maximum that provides 100% detectability in the area $[-2000, -300] \cup [300, 2000]$ mm/km). Although it is not required to extend the monitor detection area to the region $[-300, 300]$ mm/km, the risk of having an effective gradient resulting in an unacceptable differential error due to a decorrelation of the gradient observed by the monitor and the effective gradient experienced by the GBAS system may constraint us to pay more attention

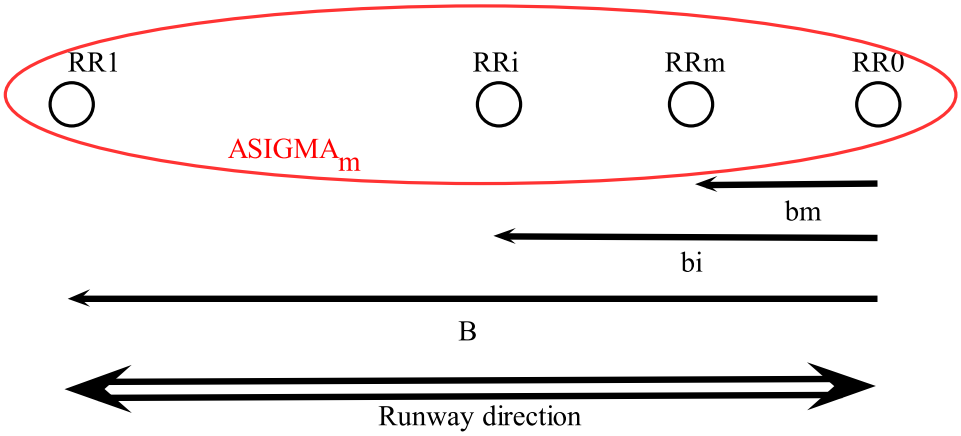

Figure 4.41.: ASIGMA$_m$ configuration using $m+1$ reference receivers (RR). RR$_0$ is set by convention as the reference receiver for all individual monitors, b_i is the baseline between RR$_0$ and RR$_i$. we call B the largest baseline (between RR$_0$ and RR$_1$)

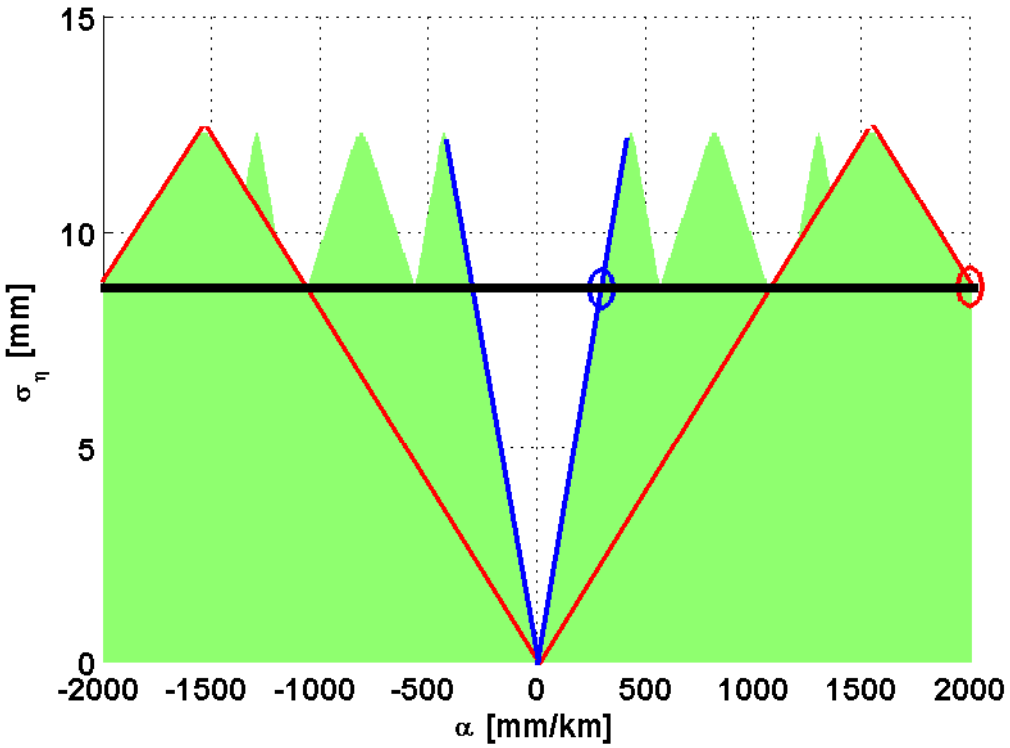

Figure 4.42.: Set of detectable gradients in green. The minimum σ_η that provides full detectability in [300,2000] mm/km gradient range is represented with a bold black line. In blue the border of the monitor with the largest baseline and in red the one with the shortest baseline. The baselines used are $b_1^\star = 221$ m, $b_2^\star = 117$ m, $b_3^\star = 62$ m and for that we obtain $\sigma_\eta^\star = 8.65$ mm.

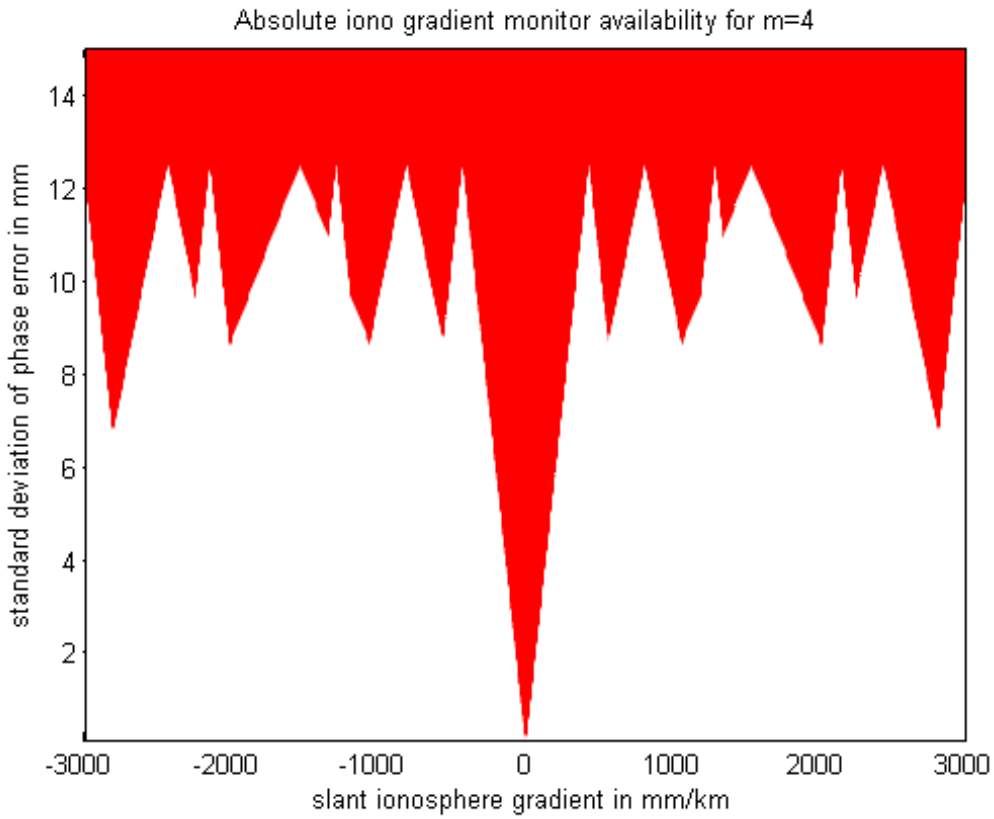

Figure 4.43.: Slant ionosphere gradient detection area for $m = 4$ receivers optimally distributed

to this area. The justification of this concern is based on the hypothesis usually admitted by the civil aviation community which describes the ionosphere threat as a locally constant gradient. In this section we take into consideration a spatial Taylor expansion of the ionosphere delay in a neighborhood of a reference point. This approximation is justified only if the effect of the second order expansion is negligible. The aim of this section is to precisely study the sensitivity of the proposed ionosphere gradient monitor to second order terms.

4.4.8.1. Diffusion model of the ionosphere Gradient

Let I_x be the ionosphere delay experienced by a satellite-user range located at a distance x from a reference point considered as the origin of the one dimensional spatial axis of interest. Let I_0 be the ionosphere delay at this reference point. For x located in a neighborhood of the reference point and provided that the ionosphere delay is twice differentiable at the reference point, we can write the Taylor expansion

as follows:

$$I_x = I_0 + x\frac{\partial I}{\partial x}(0) + \frac{x^2}{2}\frac{\partial^2 I}{\partial x^2}(0) + o\left(x^3\right)$$

We define the effective gradient as follows:

$$\alpha_{\text{eff}}(x) \equiv \frac{I_x - I_0}{x} \tag{4.78}$$

which can be written using the Taylor expansion suggested above and by introducing the same notation for the ionosphere gradient as before (α_x) at distance x,

$$\alpha_{\text{eff}}(x) = \alpha_0 + \frac{x}{2}\frac{\partial \alpha}{\partial x}(0) + o\left(x^2\right) \tag{4.79}$$

In the preceding equation, either the monitoring equipment can provide an estimation of the derivative of the ionosphere gradient at the reference point or we have to consider this as a random variable. Let's define $\frac{\partial \alpha}{\partial x}(0) = \xi_{0x}$ being a centered normal random variable with $V[\xi_0] = \sigma^2_{\alpha'_0}$. If we neglect the higher order terms for the expectation and the variance calculus, we have:

$$E[\alpha_{\text{eff}}] = \alpha_0$$

and

$$V[\alpha_{\text{eff}}] = \frac{x^2}{4}\sigma^2_{\xi_0}$$

This approach considers only the derivative of the ionosphere gradient at the reference point being a random variable. What happens if the derivative of the ionosphere gradient cannot any more be considered as a constant in the neighborhood for which the Taylor expansion applies but as a random variable. For simplicity we consider the derivative of the ionosphere gradient being modeled by a bias term (drift of the gradient) and a centered White Gaussian Noise process:

$$\frac{d\alpha_x}{dx} = \beta + \xi_x \tag{4.80}$$

with $\xi_x \sim \mathcal{N}\left(0, \sigma^2_\xi\right)$ for which the variance σ^2_ξ and the bias β are considered constant. The variation of these parameters will be considered later for the sensitivity analysis.

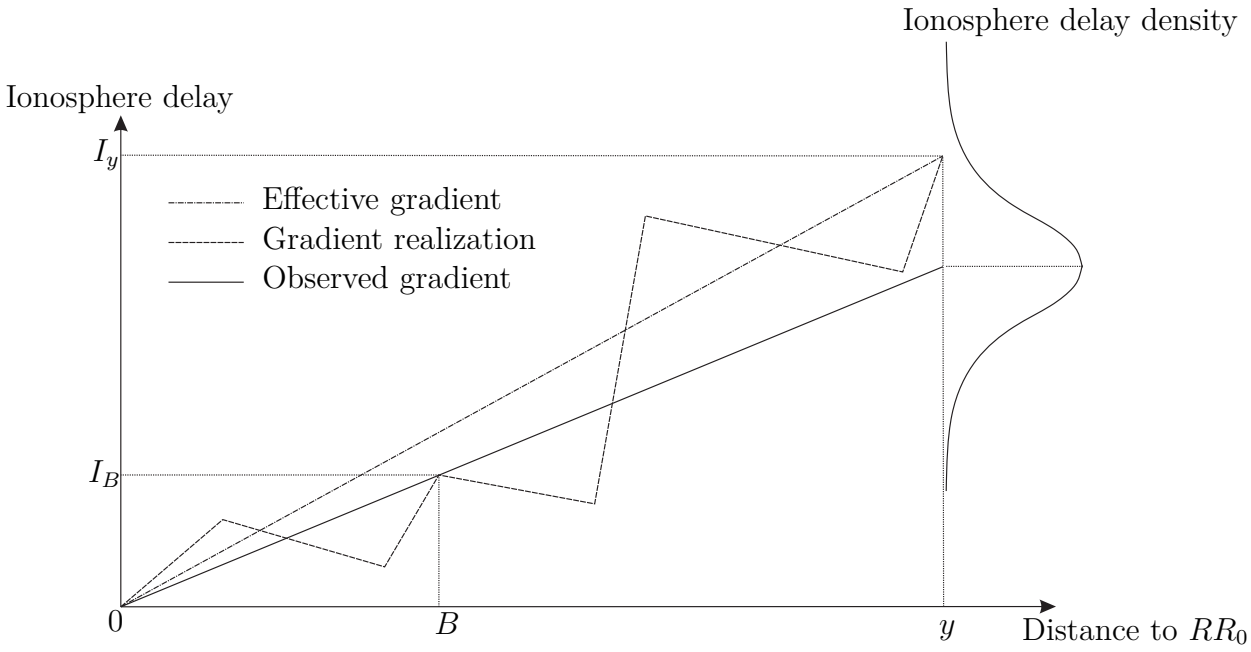

Figure 4.44.: Representation of the effective gradient

Let's write the equation above in a differential form:

$$d\alpha_x = \beta dx + \sigma_\xi dB_x \tag{4.81}$$

Where B_x is the one dimension Brownian motion in the direction of interest with a diffusion coefficient $\frac{\sigma_\xi^2}{2}$. Let I_y be the Ionosphere delay experienced by the signal coming from a given satellite to the aircraft. Let I_0 be the ionosphere delay experienced by the signal coming from the same satellite to the GBAS station. Let y be the distance between the aircraft and the GBAS reference receiver RR_0 (only the horizontal component) see Fig. 4.44.

From 4.78, we can express $I_x - I_o$ taking into account the expression of the infinitesimal gradient defined by 4.81:

$$\alpha_{\text{eff}}(y) = \frac{\int_0^y \alpha_x dx}{y} \tag{4.82}$$

$$\alpha_{\text{eff}}(y) = \frac{\int_0^y (\alpha_0 + \beta x + \sigma_\xi B_x)\, dx}{y} \tag{4.83}$$

$$\alpha_{\text{eff}}(y) = \frac{y\alpha_0 + \frac{y^2}{2}\beta + \sigma_\xi \int_0^y B_x dx}{y} \tag{4.84}$$

For characterization of the effective gradient, we propose to calculate its expectation and variance. Let's call $\alpha_{O\text{eff}y}$ the effective ionospheric gradient overbound for an aircraft located at distance y from the reference receiver. The integral form of 4.81 can be written as follows considering the conservative value $\alpha_{O\text{eff}y}$ based on the maximum value of the diffusion parameters: the maximum drift $\beta_{\max}$ and the maximum diffusion coefficient $\frac{\sigma^2_{\xi\max}}{2}$.

$$\alpha_{O\text{eff}y} = \alpha_0 + \frac{y}{2}\beta_{\max} + \frac{\sigma_{\xi\max}}{y}\int_0^y B_x dx \tag{4.85}$$

$$E\left[\alpha_{O\text{eff}y}\right] = \alpha_0 + \frac{y}{2}\beta_{\max}$$

And the variance:

$$\mathrm{V}\left[\alpha_{O\text{eff}y}\right] = \frac{\sigma^2_{\xi\max}}{y^2} E\left[\left(\int_0^y B_x dx\right)^2\right]$$

By applying the integration by part formula for $\int_0^y B_x dx$ we obtain:

$$\mathrm{V}\left[\alpha_{O\text{eff}y}\right] = \frac{\sigma^2_{\xi\max}}{y^2} E\left[\left(yB_y - \int_0^y x dB_x\right)^2\right]$$

$$\frac{y^2}{\sigma^2_{\xi\max}}\mathrm{V}\left[\alpha_{O\text{eff}y}\right] = E\left[y^2 B_y^2 + \left(\int_0^y x dB_x\right)^2 - 2yB_y\int_0^y x dB_x\right]$$

$$\frac{y^2}{\sigma^2_{\xi\max}}\mathrm{V}\left[\alpha_{O\text{eff}y}\right] = y^2 E\left[B_y^2\right] + E\left[\left(\int_0^y x dB_x\right)^2\right] - 2yE\left[B_y\int_0^y x dB_x\right]$$

We have $E\left[B_y^2\right] = y$ (Property of Brownian motions) and using the Ito isometry, the second term can be written as follows:

$$E\left[\left(\int_0^y x dB_x\right)^2\right] = E\left[\int_0^y x^2 dx\right] = \frac{y^3}{3}$$

The integral in the third term can be determined by applying the 1-dimensional Ito-formula:

$$d\left(xB_x\right) = B_x dx + x dB_x$$

which can be written in an integral form:

$$yB_y = \int_0^y B_x dx + \int_0^y x dB_x$$

or:

$$\int_0^y x dB_x = yB_y - \int_0^y B_x dx$$

$$E\left[B_y \int_0^y x dB_x\right] = E\left[B_y \left(yB_y - \int_0^y B_x dx\right)\right]$$

$$E\left[B_y \int_0^y x dB_x\right] = y^2 - \int_0^y E\left[B_y B_x\right] dx$$

$$E\left[B_y \int_0^y x dB_x\right] = y^2 - \int_0^y \left(x \wedge y\right) dx = y^2 - \frac{y^2}{2}$$

Finally we have:

$$\frac{y^2}{\sigma^2_{\xi\,\max}} \mathrm{V}\left[\alpha_{O\mathrm{eff}y}\right] = y^3 + \frac{y^3}{3} - 2y\left(y^2 - \frac{y^2}{2}\right) = \frac{y^3}{3}$$

Finally the variance of the effective gradient is:

$$\mathrm{V}\left[\alpha_{O\mathrm{eff}y}\right] = \frac{y}{3}\sigma^2_{\xi\,\max} \tag{4.86}$$

We can write the expression of the observed gradient at the monitor level function of the effective gradient:

$$\alpha_0 = \alpha_{O\mathrm{eff}y} - \frac{y}{2}\beta_{\max} - \frac{\sigma_{\xi\,\max}}{y}\int_0^y B_x dx \tag{4.87}$$

These results have been compared with those obtained with simulations and the results have been plotted in Fig. 4.45. The simulations have been conducted by generating randomly (using Matlab's random generator functions) sample paths solution of equation 4.85. As we can see inFig. 4.45, the theory matches perfectly with the simulations.

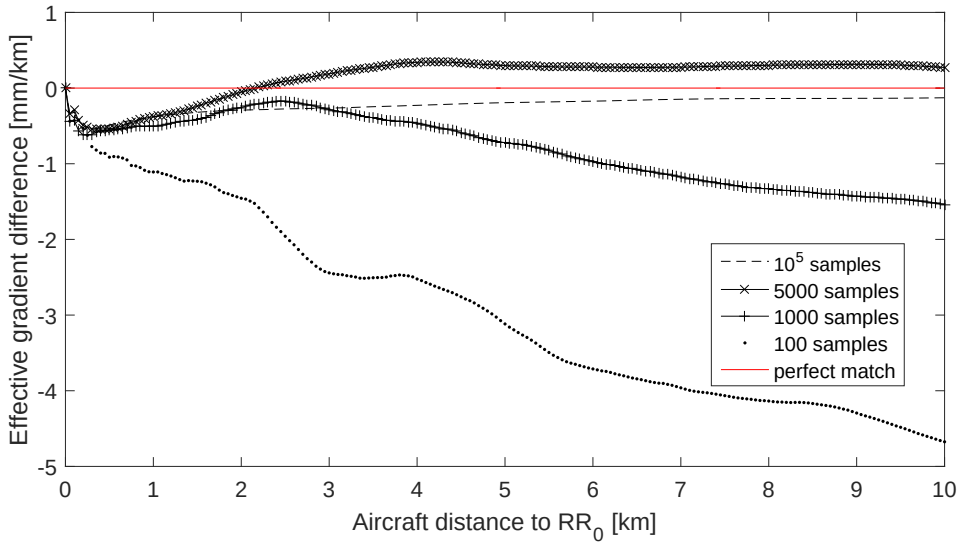

Figure 4.45.: Validation of α_{Oeffy} using simulations with $\beta_{\max} = 0$ [mm/km^2], $\alpha_0 = 300$ [mm/km], $\sigma_{\xi\,\max} = 850$ [mm/km^2] and $K_{\sigma_\eta} = 7.6$ (corresponding to $P_{\text{md}} = P_{\text{ffd}} = 10^{-4}$)

4.4.9. Propagation of non detectable gradient area

The range $[-300, +300]\,mm/km$ corresponds to the gradient range that cannot and until now must not be detected by the absolute slant ionosphere gradient monitor on ground. This requirement is for the effective gradient, i.e. the one corresponding to the slant ionosphere residual delay divided by the baseline between the aircraft and the GBAS location (the reference of the pseudo range corrections). Admitting that the gradient observed at the GBAS station is the same as the effective gradient is a strong assumption. In the last section we show that taking a very simple model of a gradient uncertainty diffusion (Brownian motion) makes available the assumption of a constant gradient. The undetectable area is increased and becomes $\left[-300 - (k_{ffd} + k_{md})\,\sigma_\alpha\sqrt{\frac{y}{3}}, 300 + (k_{ffd} + k_{md})\,\sigma_\alpha\sqrt{\frac{y}{3}}\right]$.

If we want to guaranty with 10^{-9} that the non detectable area of the effective gradient remains $[-300, 300]\,mm/km$, it will be necessary to increase the detectable

area of the ground monitor to the level

$$\left[-2000, -300 + (k_{ffd} + k_{md})\,\sigma_\alpha\sqrt{\frac{y}{3}}\right] \cup \left[300 - (k_{ffd} + k_{md})\,\sigma_\alpha\sqrt{\frac{y}{3}}, 2000\right] \quad (4.88)$$

This will give additional constraints for either the location of the monitoring receivers or the level of acceptable residual noise and therefore the quality of the antennas and receivers. The largest baseline provides the limitation to −300 to 300 mm/km. It would be possible to reduce this area by adding a new receiver that build a larger baseline than what we originally have. Depending on the maximal gradient dispersion (σ_α), one should place the receiver at a suited location.

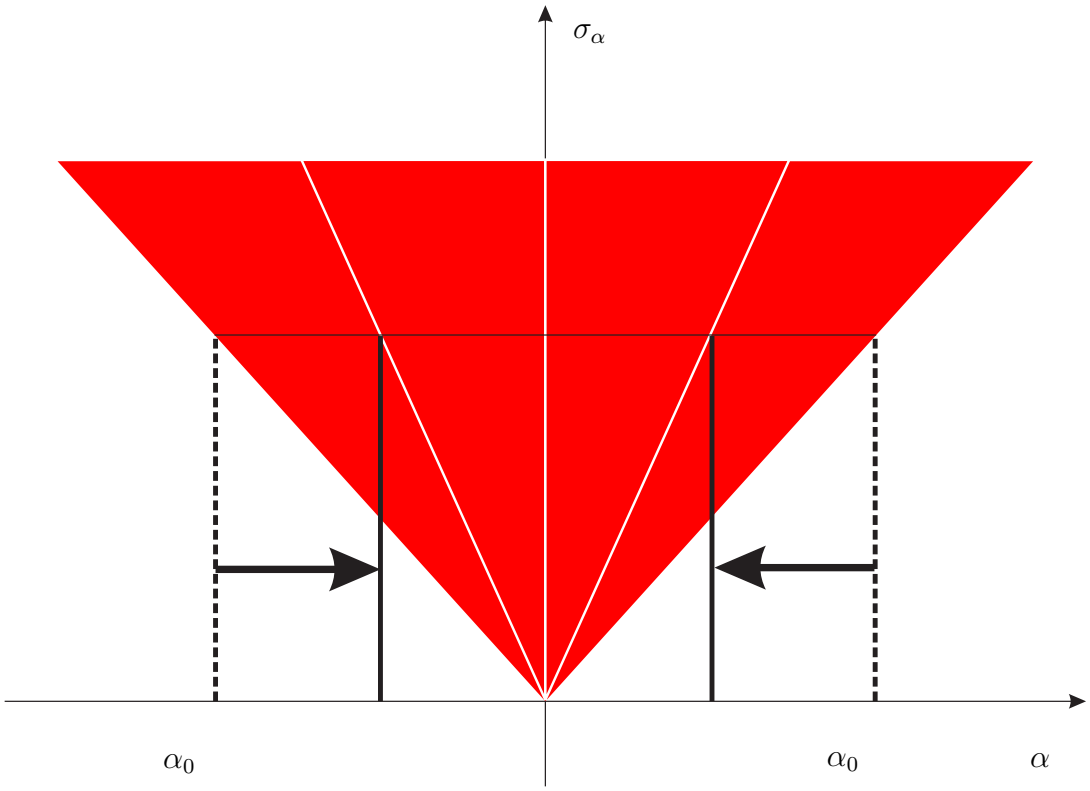

Figure 4.46.: Enlarged baseline strategy. By increasing the largest baseline, we can reduce the minimum detectable gradient to count for the diffusion of the ionosphere gradient at user level

Fig. 4.46 assumes a constant level of receiver performances ($\sigma_{\Delta\phi}$). The second strategy consist of reducing the level of double difference carrier phase noise and keeping the same location of receivers (see Fig. 4.47). These two approaches have an impact in the monitor architecture and may introduce strong constraints for the GBAS implementation.

In this area, we assumed a Brownian like diffusion process for the gradient. This is a an assumption that will need to be checked using real observations. The aim

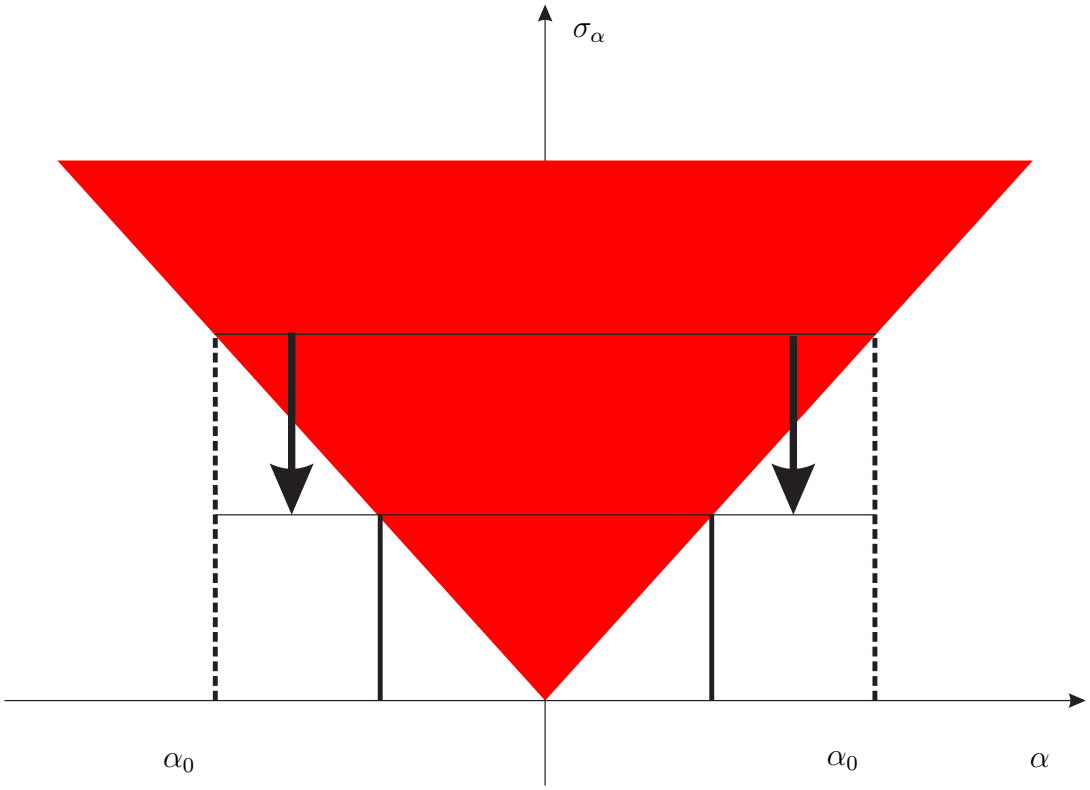

Figure 4.47.: Reduced carrier noise strategy. By reducing the double difference carrier phase error (i.e. by choosing higher performance antennas for example) we can reduce the minimum detectable gradient to count for the diffusion of the ionosphere gradient at user level

of this section is to try to analyze the impact of uncertainty in the definition of the gradient. A sensitivity analysis can show two results: Either the performance parameters are very sensitive to the diffusion coefficients or they aren't. If not, this would mean that it is not necessary to investigate further the level of uncertainty. If yes, this means that there is a need to investigate further. The further investigations consist of setting a permanent mini network located in a small size area (a radius of 10 km) trying to estimate statistically σ_α especially its dependency with α.

4.4.10. Sensitivity Analysis of the Largest Baseline to σ_α

For a given $\sigma^\star_\phi$, the detection of the lower bound ionosphere gradient is given by the monitor with the largest baseline. In that case the lower bound ionosphere gradient can be written as a function of $\sigma^\star$, and the largest baseline $B^\star$. Let $\alpha_{\min}$ be the lower

bound of the gradient. Let rewrite the equation giving the border of detectability:

$$\sigma^i(\alpha) = \frac{\widehat{\sigma}}{\widehat{\alpha}_n^i - \breve{\alpha}_n^i} \cdot \left(\alpha - \widehat{\alpha}_n^i\right) + \widehat{\sigma} \quad \breve{\alpha}_n^i \leq \alpha \leq \widehat{\alpha}_n^i \tag{4.89}$$

For $n = 0$ we have: $\breve{\alpha}_0^i = 0$, $\widehat{\alpha}_0^i = \frac{\lambda}{2B}$ and $\widehat{\sigma} = \frac{\lambda}{2(k_{\text{ffd}}+k_{\text{md}})}$.
We have then:

$$\sigma(\alpha) = \frac{\lambda}{2(k_{\text{ffd}} + k_{\text{md}})\frac{\lambda}{2B}} \cdot \left(\alpha - \frac{\lambda}{2B}\right) + \frac{\lambda}{2(k_{\text{ffd}} + k_{\text{md}})} \quad 0 \leq \alpha \leq \frac{\lambda}{2B} \tag{4.90}$$

$$\sigma(\alpha) = \frac{B}{(k_{\text{ffd}} + k_{\text{md}})} \cdot \left(\alpha - \frac{\lambda}{2B}\right) + \frac{\lambda}{2(k_{\text{ffd}} + k_{\text{md}})} \quad 0 \leq \alpha \leq \frac{\lambda}{2B} \tag{4.91}$$

$$\sigma(\alpha) = \frac{B}{(k_{\text{ffd}} + k_{\text{md}})} \cdot \alpha \quad 0 \leq \alpha \leq \frac{\lambda}{2B} \tag{4.92}$$

We have for the optimal case:

$$\sigma_\phi^\star = \frac{B^\star}{(k_{\text{ffd}} + k_{\text{md}})} \cdot \alpha_{\min}^\star \tag{4.93}$$

Let $\alpha_0 = 300$ mm/km, we can observe that $\alpha_{\min}^\star \approx \alpha_0$. For the 4 receivers configuration, $\alpha_{\min}^\star = 297.5$ mm/km. We can interpret this margin as being the authorized diffusion of the ionosphere gradient uncertainty with respect to the distance. If we set $\sigma_\alpha^\star$ being the authorized diffusion of the gradient uncertainty for the optimal configuration, we have:

$$\sigma_\alpha^\star = \frac{\sqrt{3/y}}{k_{\text{ffd}} + k_{\text{md}}}(\alpha_0 - \alpha_{\min}^\star) \quad \alpha_{\min}^\star < \alpha_0 \tag{4.94}$$

For $y = 10$ km for example a numerical application for the case of 4 optimally aligned receivers shows that $\sigma_\alpha^\star = 0.1826$ mm/km$^{3/2}$ which is a very small value.

Is it sufficient to protect an aircraft equipped with a GBAS system against large gradients? A better knowledge of the second ionosphere derivative is necessary especially for the gradients close to α_0. If the ionosphere gradient decorrelation has

a standard deviation larger than $\sigma_\alpha^\star$, the largest baseline must be extended. In order not to lose the optimality, a fifth receiver may be necessary to be installed.

Let assume that an independent permanent network of stations provides an estimation of this decorrelation being $\hat{\sigma}_\alpha > \sigma_\alpha^\star$. The baseline between the reference and the fifth receiver B_α is a function of the optimal configuration.

From the following relation:

$$\sigma_\phi = \frac{b}{k}\alpha_b$$

From now on, we set $k \equiv k_{\text{ffd}} + k_{\text{md}}$. b is the baseline, α_b is the minimum detectable gradient for the monitor whose baseline is b, and σ_ϕ is the standard deviation of the carrier phase error for the considered receivers, assuming that every receivers have the same carrier phase error level. The relation between $\hat{\sigma}_\alpha$ and α_b is given by:

$$\hat{\sigma}_\alpha = \frac{\sqrt{3/y}}{k}\left(\alpha_0 - \alpha_b\right)$$

Thus:

$$\alpha_b = \alpha_0 - k\sqrt{\frac{y}{3}}\hat{\sigma}_\alpha$$

We can express b function of $\hat{\sigma}_\alpha$:

$$b = \frac{k\sigma_\phi}{\alpha_0 - k\sqrt{\frac{y}{3}}\hat{\sigma}_\alpha} \tag{4.95}$$

The sensitivity to $\hat{\sigma}_\alpha$ of the baseline is the partial derivative of the baseline with respect to $\hat{\sigma}_\alpha$:

$$\frac{\partial b}{\partial \hat{\sigma}_\alpha} = k\sqrt{\frac{y}{3}}\frac{k\sigma_\phi}{\left(\alpha_0 - k\sqrt{\frac{y}{3}}\hat{\sigma}_\alpha\right)^2} \tag{4.96}$$

We see that b and its derivative with respect to $\hat{\sigma}_\alpha$ tend to infinity when $\hat{\sigma}_\alpha^\infty = \frac{\alpha_0}{k}\sqrt{\frac{3}{y}}$. In fact for high values of b, it is necessary to add other receivers in order to fully cover the gradient range $[\alpha_b, \alpha_0]$.

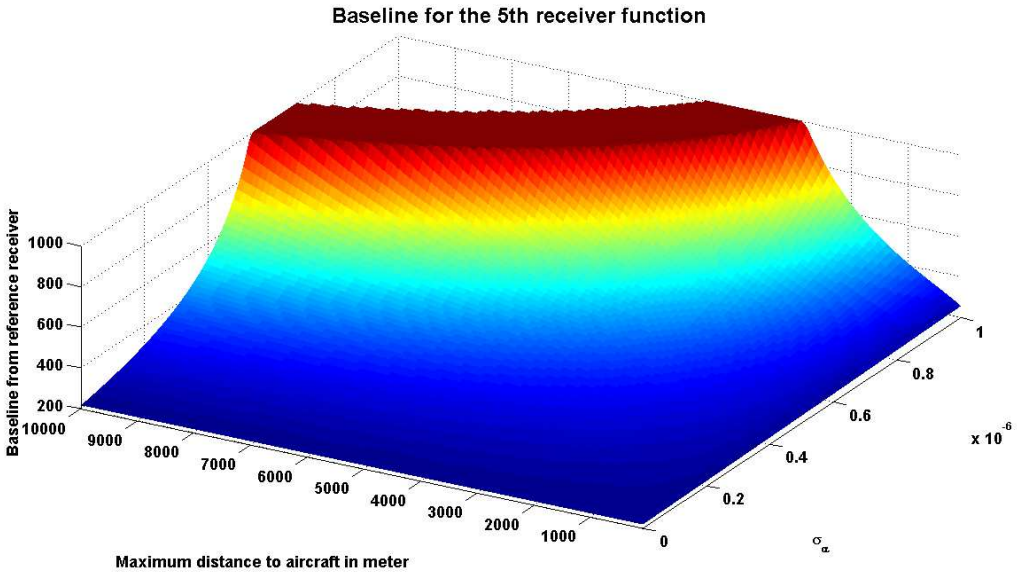

Figure 4.48.: Baseline in function of maximum distance to aircraft and gradient uncertainty

4.4.11. Sensitivity Analysis of the Carrier Phase Error to σ_α

In this section, we consider the architecture of the aligned monitors constant. We adopt the second strategy: to reduce the carrier phase error in order to enlarge the range of observability of the gradient monitor. We recall the equation giving the baseline function of $\hat{\sigma}_\alpha$:

$$b = \frac{k\sigma_\phi}{\alpha_0 - k\sqrt{\frac{y}{3}}\hat{\sigma}_\alpha} \tag{4.97}$$

Let's consider this time the baseline $B^\star$ as the largest baseline of the monitors. σ_ϕ can be expressed function of $\hat{\sigma}_\alpha$:

$$\sigma_\phi = \frac{B^\star}{k}\left(\alpha_0 - k\sqrt{\frac{y}{3}}\hat{\sigma}_\alpha\right) \tag{4.98}$$

The partial derivative with respect to $\hat{\sigma}_\alpha$ is:

$$\frac{\partial\sigma_\phi}{\partial\hat{\sigma}_\alpha} = B^\star\sqrt{\frac{y}{3}} \tag{4.99}$$

As in the previous chapter $\hat{\sigma}_\alpha^\infty = \frac{\alpha_0}{k}\sqrt{\frac{3}{y}}$ is a limit case. The unique solution while fixing all parameters constant is to set $\sigma_\phi = 0$. This is of course not possible due to the residual carrier phase errors that cannot be eliminated.

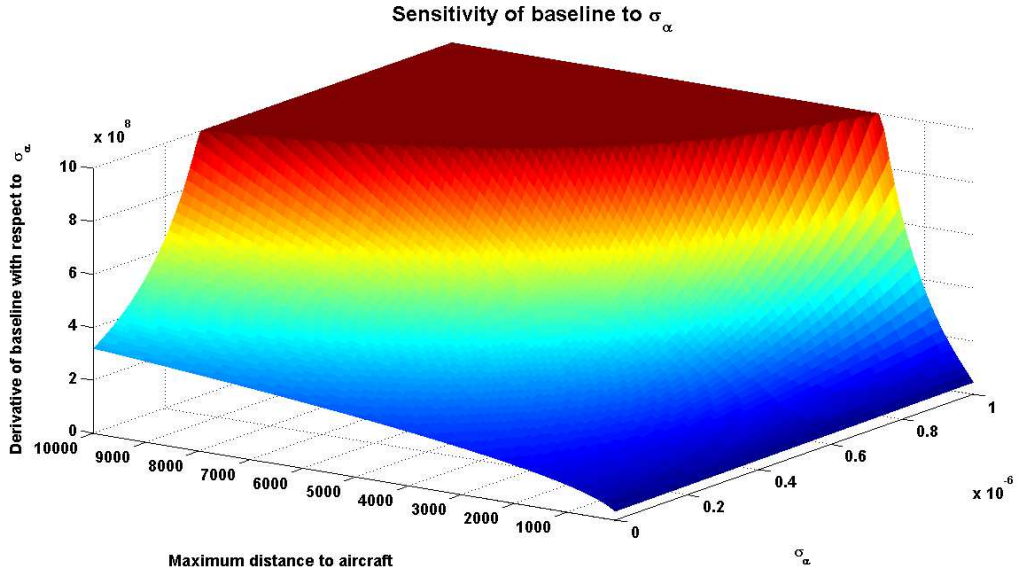

Figure 4.49.: Sensitivity of Baseline in function of maximum distance to aircraft and gradient uncertainty

4.4.12. Estimation of the Ionosphere Gradient Derivative

This section will investigate a method to estimate this second derivative using a permanent mini-network of receivers.

In the previous chapter, it has been shown that for some values of σ_α the required monitor baseline can be very sensitive to this value.

The diversity of ionosphere situations and the lack of observability of effects that influence the ionosphere total electron content makes it difficult to provide a deterministic behavior of the gradient derivative. Rather than trying to solve the dynamic equations describing the behavior of the ionosphere, we opt to a statistical approach using a permanent network of dual frequency reference receivers able to measure in at least 3 different aligned points close enough to have a good estimate of the local derivatives of the ionosphere delay but far enough in order to avoid multipath correlations. This should provide us the measurement equipment for which we will base our safety analysis.

Depending on the behavior of the ionosphere second spatial derivative, the requirements for the ground monitor could be impacted and as a consequence its architecture would need to be adapted. In fact the largest baseline may have to be extended.

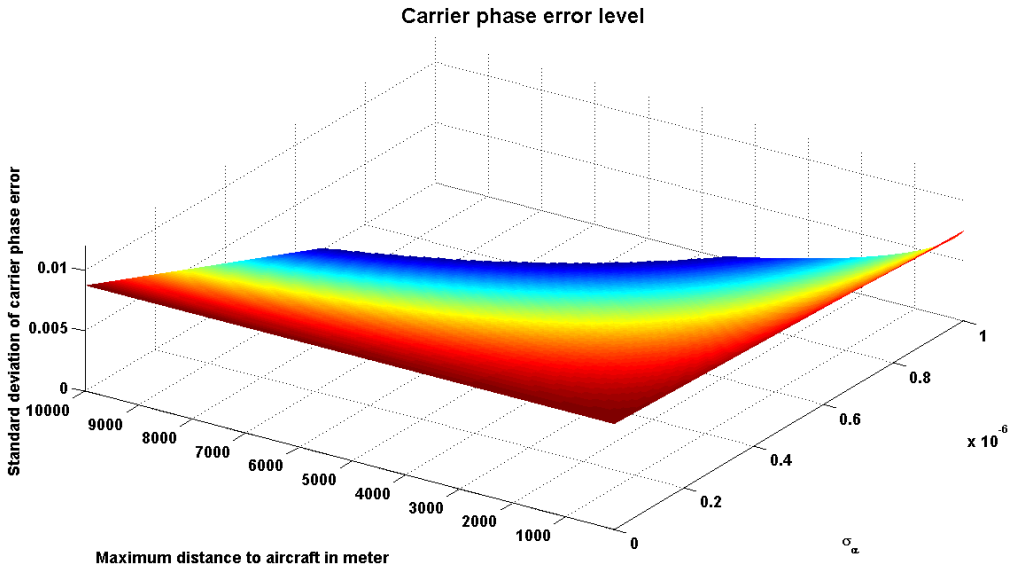

Figure 4.50.: Carrier phase error in function of maximum distance to aircraft and gradient uncertainty

4.4.13. Sensitivity using Error Structures

The aim of this section is to use the error structures developed in [Bou03] to determine the sensitivity of the optimal baseline to non direct observability of the effective gradient.

Another approach consists of defining the uncertainty in the gradient measured by the ground monitor as an error that propagates through the model defined by the following equation:

$$d\alpha_x = \sigma_\alpha dB_{\alpha x} \tag{4.100}$$

The erroneous quantity is σ_α. The problem we propose to solve is to study the sensitivity of the baseline and the carrier phase error with respect to an error in this quantity. For that we use the approach with error structures.

Let's represent the error on the quantity σ_α by $\Delta\sigma_\alpha$. We recall the expression of b:

$$b = \frac{k\sigma_\phi}{\alpha_0 - k\sqrt{\frac{y}{3}}\sigma_\alpha}$$

We first define an error structure on σ_α: $S = \left([0, 2\times10^{-6}], \mathcal{B}\left([0, 2\times10^{-6}]\right), \mathbb{P}, \mathbb{D}, \Gamma : u \to u'^2\right)$ (see Appendix B). We want to determine the quadratic error on b given the error on

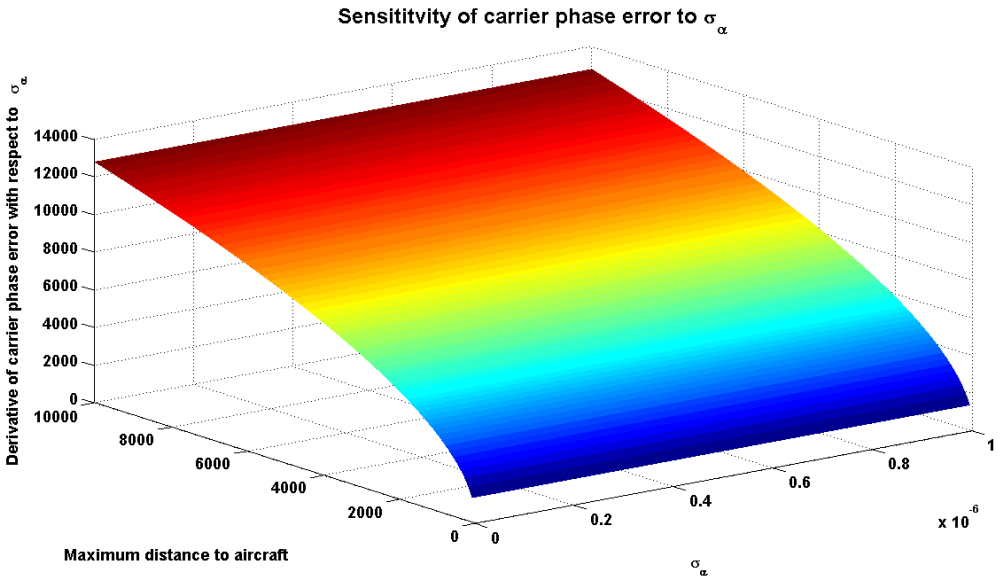

Figure 4.51.: Sensitivity of Carrier phase error in function of maximum distance to aircraft and gradient uncertainty

σ_α. An error on σ_α could be basically a lack of information provided by a permanent network. The chain rule provides the following quadratic error on b provided that $b \in \mathbb{D}$.

$$\Gamma\left[b\left(\sigma_\alpha\right)\right] = \left(\frac{\partial b}{\partial \sigma_\alpha}\right)^2 \Gamma\left[\sigma_\alpha\right] \tag{4.101}$$

$$\Gamma\left[b\left(\sigma_\alpha\right)\right] = \left(k\sqrt{\frac{y}{3}}\frac{k\sigma_\phi}{\left(\alpha_0 - k\sqrt{\frac{y}{3}}\sigma_\alpha\right)^2}\right)^2 \Gamma\left[\sigma_\alpha\right] \tag{4.102}$$

We assume that the variance of σ_α is independent of α. We should keep this as a simplification, as the ionosphere is a complex middle that obeys electrodynamics laws. The investigations of the physical behavior of the ionosphere and its modeling is not the aim of this thesis.

This means that the sensitivity to an error in σ_α is simply the first order derivative of error in b with respect to σ_α.

$$\frac{\partial \Gamma\left[b\left(\sigma_\alpha\right)\right]}{\partial \Gamma\left[\sigma_\alpha\right]} = \left(k\sqrt{\frac{y}{3}}\frac{k\sigma_\phi}{\left(\alpha_0 - k\sqrt{\frac{y}{3}}\sigma_\alpha\right)^2}\right)^2 \tag{4.103}$$

This is to be compared with the equation obtained in the previous chapter:

$$\frac{\partial b}{\partial \hat{\sigma}_\alpha} = k\sqrt{\frac{y}{3}}\frac{k\sigma_\phi}{\left(\alpha_0 - k\sqrt{\frac{y}{3}}\hat{\sigma}_\alpha\right)^2} \tag{4.104}$$

The results are the same (Γ being a variance operator, the expression is squared). An advantage of using the error structures approach is to be able to find a chain law for the propagation of the bias using a second order derivative (taking into account not only the bias but also the Γ). As presented in the chapter 2, the chain rule of the bias can be expressed as follows:

$$A\left[\Phi\left(F_1, F_2, ..., F_p\right)\right] = \sum_i \Phi_i^{'}\left(F_1, F_2, ..., F_p\right) A\left[F_i\right] + \frac{1}{2}\sum_{i,j} \Phi_{ij}^{"}\left(F_1, F_2, ..., F_p\right) \Gamma\left[F_i, F_j\right] \tag{4.105}$$

Applied to b and assuming that σ_α is the only erroneous variable, we have:

$$A\left[b\left(\sigma_\alpha\right)\right] = \frac{\partial b}{\partial \sigma_\alpha}\left(\sigma_\alpha\right) A\left[\sigma_\alpha\right] + \frac{1}{2}\frac{\partial^2 b}{\partial \sigma_\alpha^2}\left(\sigma_\alpha\right) \Gamma\left[\sigma_\alpha\right] \tag{4.106}$$

We have:

$$\frac{\partial b}{\partial \sigma_\alpha} = k\sqrt{\frac{y}{3}}\frac{k\sigma_\phi}{\left(\alpha_0 - k\sqrt{\frac{y}{3}}\sigma_\alpha\right)^2}$$

and:

$$\frac{\partial^2 b}{\partial \sigma_\alpha^2} = 2k^2\frac{y}{3}\frac{k\sigma_\phi}{\left(\alpha_0 - k\sqrt{\frac{y}{3}}\sigma_\alpha\right)^3}$$

Thus:

$$A\left[b\left(\sigma_\alpha\right)\right] = k\sqrt{\frac{y}{3}}\frac{k\sigma_\phi}{\left(\alpha_0 - k\sqrt{\frac{y}{3}}\sigma_\alpha\right)^2} A\left[\sigma_\alpha\right] + k^2\frac{y}{3}\frac{k\sigma_\phi}{\left(\alpha_0 - k\sqrt{\frac{y}{3}}\sigma_\alpha\right)^3}\Gamma\left[\sigma_\alpha\right] \tag{4.107}$$

$$A\left[b\left(\sigma_\alpha\right)\right] = k\sqrt{\frac{y}{3}}\frac{k\sigma_\phi}{\left(\alpha_0 - k\sqrt{\frac{y}{3}}\sigma_\alpha\right)^2}\left(A\left[\sigma_\alpha\right] + \frac{k\sqrt{\frac{y}{3}}}{\left(\alpha_0 - k\sqrt{\frac{y}{3}}\sigma_\alpha\right)}\Gamma\left[\sigma_\alpha\right]\right) \tag{4.108}$$

Assuming that the error on σ_α is unbiased, due to non-linearity of b, a bias appears due to the error variance on σ_α. It is to be noticed that for both Γ and A there is a singularity for the curve defined by $y = 3\left(\frac{\alpha_0}{k\sigma_\alpha}\right)^2$

In the following we are going to show the numerical results when simulating the errors on σ_α using for example a centered normal distribution with a standard deviation of 10^{-9} m/m^2. The chain rule of the error propagation is based on a second order Taylor expansion for both the variance and the bias operator which apply in a neighborhood of the reference point considered. The graphical representation of the required baseline with respect to the maximum distance to aircraft and to the diffusion coefficient of the ionosphere gradient is shown in Fig. 4.52.

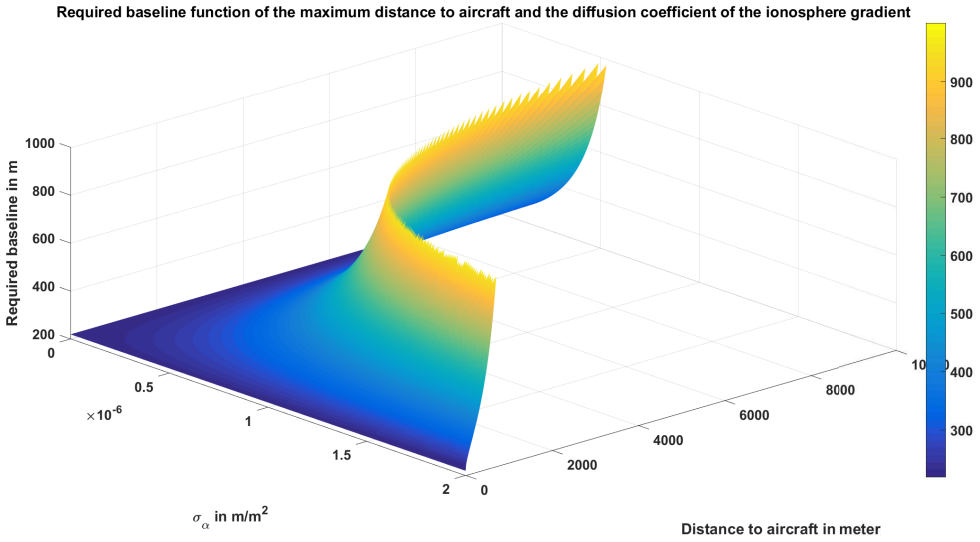

Figure 4.52.: Surface of required baseline

4.53a and 4.53b show a strong sensitivity of the required baseline to errors on σ_α when approaching the curve defined by $y = 3\left(\frac{\alpha_0}{k\sigma_\alpha}\right)^2$. Due to a strong non-linearity while approaching this curve, a bias appears in the required baseline even if the error on σ_α is centered.

4.5. Conclusion and major contributions

In the first two sections of this chapter, we investigated the impact of pseudo range errors with respect to GNSS performances when considering augmentations [BSS05,

BGN06, BRM08b, MJB+08b, MJB08a, MBD09, DBR09a, BMJ+08, BRM08a, BRWM08, DBM09, MBJ+09, RBDM09, BDLK10b, DMA+10, DBR09b, DBRP10, HSB+10, BS05]. SBAS performance has been assessed considering the use of instantaneous pseudo range error approach. The IPRE concept provides statistics to the NIMP (Network Integrity Monitoring Platform) that is used to evaluate the performance of SBAS using accumulated measurements. The third subsection analyses an ionosphere gradient monitoring technique candidate for GBAS GAST-D. This constitutes the major contribution made by the author to this chapter [BDF+10, BRMP11, BM12]. In this part a sensitivity analysis has been made to different parameters to test the stability of the solution to non precise estimation of the ionosphere gradient model parameters.

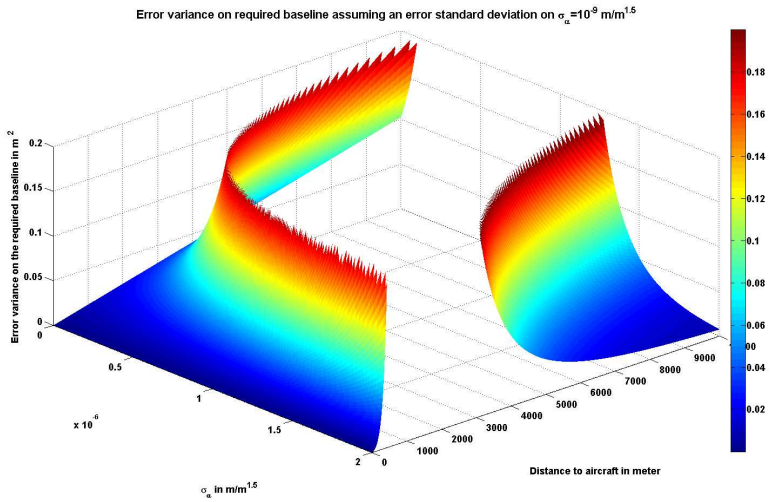

(a) Error variance of the required baseline

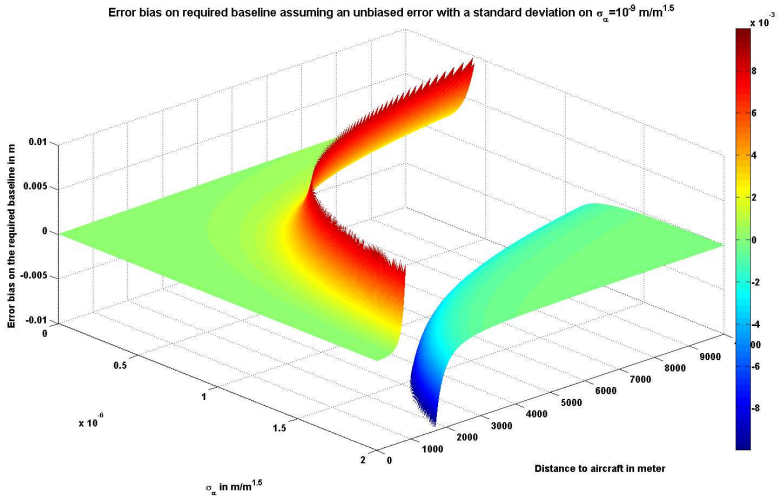

(b) Error bias of the required baseline

Figure 4.53.: Sensitivity analysis of the required baseline assuming an error on $\sigma_\alpha = 10^{-9}\mathrm{m}/m^2$

5. GNSS Positioning Integrity using Inertial Sensors

THE WORK DESCRIBED IN THIS CHAPTER IS MY PERSONAL CONTRIBUTION.

5.1. Introduction

Although GNSS signals are available almost everywhere, there are specific scenarios especially during surface movement of aircraft or for car or train navigation where the signals are either blocked by obstacles, reflected by surrounding objects or jammed by radio frequency interference due to other emitting equipment in the vicinity of the user. Possible additional sensors that can overcome this problem is the use of inertial measurement units. The inertial measurement units sense the accelerations in 3 directions and the angle rates also with respect to 3 orthogonal axis. Alone, the inertial measurement unit provides only a relative position that drifts with respect to time due to the accumulation of errors while integrating the acceleration measurements at position level. But in combination with GNSS, the performance can reach a very high level of accuracy.

The aim of this chapter is to estimate the performance in terms of accuracy and integrity of a navigation solution based on the use of inertial sensors. Under specific assumptions and for a 1D problem, a close form of the bias and variance propagation is suggested.

Inertial error models have been widely discussed in the literature. According to [GE04], however it is sufficient for low-cost sensors to use a simplified version. Given that the misalignment of the different measuring axes are known:

$$\hat{s}(t) = (1 + s_f)s(t) + b(t), \tag{5.1}$$

where $\hat{s}(t)$ is the measured sensor output, i.e an angular turn rate or a 1-D acceleration. The true value of this quantity is denoted as $s(t)$. This true quantity can be used as the input acceleration in simulations. This is possible to simulate different type of scenarios as for example vibrations or constant acceleration, deceleration. An ideal sensor would measure directly $s\,(t)$ but in the model and due to sensor imperfections, the output of the sensor has a proportional to the true quantity part

(including a scaling factor s_f) and an additive drift depending on time: $b(t)$. The latter can be modeled by a constant offset b_0 as well as a time varying component $b_1(t)$ and a noise b_w.

$$b\left(t\right) = b_0 + b_1\left(t\right) + b_w \tag{5.2}$$

We can assume that the offset is corrected by an initial calibration of the sensors. Additionally, the noise is assumed to be Gaussian distributed with zero-mean and a variance σ_w^2. The time-varying component is represented by a 1st-order Gauss-Markov process which can be expressed mathematically by

$$\dot{b}_1(t) = -\frac{1}{\tau} b_1(t) + n_{b_1}, \tag{5.3}$$

where τ is the time constant of the Gauss-Markov process and n_{b_1} is a noise which can be assumed to be Gaussian distributed with zero mean and variance σ_g^2. It is also known as an Ornstein-Uhlenbeck process in financial mathematics with $\frac{1}{\tau}$ the rate of mean reversion and with volatility σ_g (see sec. A.3)

5.2. Error Propagation Equation

5.2.1. The Generator of the Error Diffusion Process

Let's consider only a one dimensional translational acceleration (without attitude change). The position of the mobile can be determined using only one accelerometer or the combination of redundant accelerometers in the direction of the acceleration. We simplify the Equation (5.1) to obtain:

$$\hat{s}(t) = (1 + s_f)s(t) + b_0 + b_1(t) + b_w, \tag{5.4}$$

Let $\delta\hat{s}(t)$ be the deviation of the measured acceleration with respect to the true acceleration or the input acceleration:

$$\delta\hat{s}\left(t\right) = \hat{s}\left(t\right) - s(t) \tag{5.5}$$

The equation verified by $\delta\hat{s}(t)$ is derived from Equation 5.4:

$$\delta\hat{s}(t) = s_f s(t) + b_0 + b_1(t) + b_w \tag{5.6}$$

The time-varying bias $b_1(t)$ is solution of the stochastic differential Equation (5.3).

If we rewrite the equation 5.3 in a differential way (Ito form) and introducing the one-dimensional Brownian motion B_t we obtain:

$$db_{1t} = -\frac{1}{\tau} b_{1t} dt + \sigma_g dB_{gt}. \tag{5.7}$$

The vertical deviation of the speed $\delta\hat{v}(t)$ is the integral of the measured acceleration deviation $\delta\hat{s}(t)$.

$$d\delta\hat{v}_t = (s_f s(t) + b_0 + b_{1t})\,dt + \sigma_w dB_{wt} \tag{5.8}$$

And the vertical position deviation can be written in the following form:

$$d\delta\hat{x}_t = \delta\hat{v}_t dt \tag{5.9}$$

Let define $X_t = (b_{1t} \quad \delta\hat{v}_t \quad \delta\hat{x}_t)^T$ as the state vector of our problem.

The Stochastic differential equation can be written in the following form:

$$dX_t = \beta_t(X_t)\,dt + \sigma dB_t \tag{5.10}$$

with $\beta_t(X_t) = \left(-\frac{1}{\tau}b_{1t} \quad s_f s(t) + b_0 + b_{1t} \quad \delta\hat{v}_t\right)^T$, $\sigma = \begin{pmatrix} \sigma_g & 0 & 0 \\ 0 & \sigma_w & 0 \end{pmatrix}^T$ and $dB_t = (dB_{gt} \quad dB_{wt})^T$.

It can be seen that under the considered assumptions X_t is an Ito diffusion process characterized by a drift $\beta_t(X_t)$ and a diffusion matrix: $\frac{1}{2}\sigma\sigma^T$. The Generator of the diffusion process can be written in the following general form:

$$Af(x) = \sum_i \beta_i(x)\frac{\partial f}{\partial x_i} + \frac{1}{2}\sum_{i,j}\left(\sigma\sigma^T\right)_{i,j}(x)\frac{\partial^2 f}{\partial x_i \partial x_j} \tag{5.11}$$

Which in our case can be written as follows:

$$Af(x) = -\frac{1}{\tau}b_1\frac{\partial f}{\partial b_1} + \left[(1+s_f)s(t) + b_0 + b_1\right]\frac{\partial f}{\partial \delta\hat{v}} + \delta\hat{v}\frac{\partial f}{\partial \delta\hat{x}} + \frac{1}{2}\sigma_g^2\frac{\partial^2 f}{\partial b_1^2} + \frac{1}{2}\sigma_w^2\frac{\partial^2 f}{\partial \delta\hat{v}^2} \tag{5.12}$$

for any $f \in C_0^2(\mathbb{R})$. (see Appendix A)

5.2.2. The Kolmogorov Forward Equation (KFE)

The Kolmogorov Forward Equation (described in sec. A.2) gives the law of evolution of the density of distribution with respect to time:

$$\frac{\partial p}{\partial t} = \frac{1}{\tau}\frac{\partial b_1 p}{\partial b_1} - \left[s_f s\left(t\right) + b_0 + b_1\right]\frac{\partial p}{\partial \delta\hat{v}} - \delta\hat{v}\frac{\partial p}{\partial \delta\hat{x}} + \frac{1}{2}\sigma_g^2\frac{\partial^2 p}{\partial b_1^2} + \frac{1}{2}\sigma_w^2\frac{\partial^2 p}{\partial \delta\hat{v}^2} \quad (5.13)$$

$$p\left(0, x\right) = f\left(x\right) \quad (5.14)$$

where f is the initial density.

5.2.3. Numerical Resolution of the KFE

In this section we propose a numerical resolution of the KFE.

This equation can be written in the form of 3 flux A, B and C towards each variables:

$$\frac{\partial p}{\partial t} = \frac{\partial A}{\partial b_1} + \frac{\partial B}{\partial \delta\hat{v}} + \frac{\partial C}{\partial \delta\hat{x}} \quad (5.15)$$

with

$$\begin{aligned} A &= \frac{1}{\tau}b_1 p + \frac{1}{2}\sigma_g^2\frac{\partial p}{\partial b_1} \\ B &= -\left[s_f s\left(t\right) + b_0 + b_1\right]p + \frac{1}{2}\sigma_w^2\frac{\partial p}{\partial \delta\hat{v}} \\ C &= -\delta\hat{v}p \end{aligned}$$

This form of the equation let us suggest to use an operator splitting method to solve the system.[ZMV98, PTVF07].

The numerical scheme we are going to adopt here is as suggested in [PTVF07] a Crank-Nicholson tridiagonal scheme. This method has shown a high level of stability as it uses an implicit scheme.

We discretize over all variables of p. Let $p_{i,j,k}^n$ the probability at discrete time n for the discrete value i of b_1, j of $\delta\hat{v}$ and k of $\delta\hat{x}$. The operator splitting method suggest to divide the time from n to $n+1$ in 3 equally spaced intervals: $\left[n, n+\frac{1}{3}\right] \cup \left[n+\frac{1}{3}, n+\frac{2}{3}\right] \cup \left[n+\frac{2}{3}, n+1\right]$.

For each interval we apply one of the splitting operator: This drives to:

$$\frac{p_{i,j,k}^{n+\frac{1}{3}} - p_{i,j,k}^{n}}{\Delta t} = \frac{A_{i+1,j,k}^{n+\frac{1}{3}} - A_{i-1,j,k}^{n+\frac{1}{3}}}{2\Delta b_1} \tag{5.16}$$

$$\frac{p_{i,j,k}^{n+\frac{2}{3}} - p_{i,j,k}^{n+\frac{1}{3}}}{\Delta t} = \frac{B_{i,j+1,k}^{n+\frac{2}{3}} - B_{i,j-1,k}^{n+\frac{2}{3}}}{2\Delta \hat{v}} \tag{5.17}$$

$$\frac{p_{i,j,k}^{n+1} - p_{i,j,k}^{n+\frac{2}{3}}}{\Delta t} = -\delta \hat{v}_j \frac{p_{i,j,k+1}^{n+1} - p_{i,j,k-1}^{n+1}}{2\Delta \hat{x}} \tag{5.18}$$

For which we set:

$$A_{i+1,j,k} = \frac{1}{\tau} b_{1_{i+1}} p_{i+1,j,k} + \frac{1}{2}\sigma_g^2 \frac{p_{i+1,j,k} - p_{i,j,k}}{\Delta b_1}$$

$$A_{i-1,j,k} = \frac{1}{\tau} b_{1_{i-1}} p_{i-1,j,k} + \frac{1}{2}\sigma_g^2 \frac{p_{i,j,k} - p_{i-1,j,k}}{\Delta b_1}$$

$$B_{i,j+1,k} = -\left[s_f s\left(t\right) + b_0 + b_{1_i}\right] p_{i,j+1,k} + \frac{1}{2}\sigma_w^2 \frac{p_{i,j+1,k} - p_{i,j,k}}{\Delta \delta \hat{v}}$$

$$B_{i,j-1,k} = -\left[s_f s\left(t\right) + b_0 + b_{1_i}\right] p_{i,j-1,k} + \frac{1}{2}\sigma_w^2 \frac{p_{i,j,k} - p_{i,j-1,k}}{\Delta \delta \hat{v}}$$

Let's rewrite the equation 5.16:

$$p_{i,j,k}^{n+\frac{1}{3}} - p_{i,j,k}^{n} = \frac{\Delta t}{2\tau \Delta b_1}\left(b_{1_{i+1}} p_{i+1,j,k}^{n+\frac{1}{3}} - b_{1_{i-1}} p_{i-1,j,k}^{n+\frac{1}{3}}\right) + \frac{\sigma_g^2 \Delta t}{4\Delta b_1^2}\left(p_{i+1,j,k}^{n+\frac{1}{3}} - 2p_{i,j,k}^{n+\frac{1}{3}} + p_{i-1,j,k}^{n+\frac{1}{3}}\right) \tag{5.19}$$

by putting all together the terms at $n+\frac{1}{3}$ and by defining $r_{A1} = \frac{\Delta t}{2\tau \Delta b_1}$ and $r_{A2} = \frac{\sigma_g^2 \Delta t}{4\Delta b_1^2}$ we obtain the tridiagonal scheme:

$$\left(r_{A1} b_{1_{i-1}} - r_{A2}\right) p_{i-1,j,k}^{n+\frac{1}{3}} + \left(1 + 2r_{A2}\right) p_{i,j,k}^{n+\frac{1}{3}} - \left(r_{A1} b_{1_{i+1}} + r_{A2}\right) p_{i+1,j,k}^{n+\frac{1}{3}} = p_{i,j,k}^{n} \tag{5.20}$$

by proceeding in the same way for equation 5.17, we obtain:

$$p_{i,j,k}^{n+\frac{2}{3}} - p_{i,j,k}^{n+\frac{1}{3}} = -\frac{\Delta t\left[s_f s\left(t\right) + b_0 + b_{1_i}\right]}{2\Delta\delta\hat{v}}\left(p_{i,j+1,k}^{n+\frac{2}{3}} - p_{i,j-1,k}^{n+\frac{2}{3}}\right) + \frac{\sigma_w^2\Delta t}{4\Delta\delta\hat{v}^2}\left(p_{i,j+1,k}^{n+\frac{2}{3}} - 2p_{i,j,k}^{n+\frac{2}{3}} + p_{i,j-1,k}^{n+\frac{2}{3}}\right) \tag{5.21}$$

by putting all together the terms at $n+\frac{2}{3}$ and by defining $r_{B1} = -\frac{\Delta t\left[s_f s(t)+b_0+b_{1_i}\right]}{2\Delta\delta\hat{v}}$ and $r_{B2} = \frac{\sigma_{b_w}^2\Delta t}{4\Delta\delta\hat{v}^2}$, we obtain the tridiagonal scheme:

$$\left(r_{B1} - r_{B2}\right)p_{i,j-1,k}^{n+\frac{2}{3}} + \left(1 + 2r_{B2}\right)p_{i,j,k}^{n+\frac{2}{3}} - \left(r_{B1} + r_{B2}\right)p_{i,j+1,k}^{n+\frac{2}{3}} = p_{i,j,k}^{n+\frac{1}{3}} \tag{5.22}$$

The "True" acceleration $s\left(t\right)$ can be considered as the a priori scenario for which we want to study the error propagation. In the following example, we simulate different scenarios.

Let's define $r_C = -\frac{\delta\hat{v}_j\Delta t}{2\Delta\hat{x}}$ the third discrete equation can be written as follows:

$$r_C p_{i,j,k-1}^{n+1} + p_{i,j,k}^{n+1} - r_C p_{i,j,k+1}^{n+1} = p_{i,j,k}^{n+\frac{2}{3}} \tag{5.23}$$

Finally from 5.20, 5.22 and 5.23 we build up the expression of the density function for each discrete point. In the following we represent the graphical representation of error propagation using a specific scenario.

5.2.4. Numerical results and analysis

We solve the numerical problem using the following parameters:

- $\sigma_{b_1} = 1.2$ milli-g
- $\sigma_w = 1$ milli-g
- $\tau = 5$ seconds
- $s_f = 0.1$
- $s\left(t\right) = 0$
- $\sigma_{b_1 0} = 0.15m/s^2$
- $\sigma_{\delta\hat{v}_0} = 0.05m/s$ this corresponds to a typical vertical velocity based on GBAS measurement
- $\sigma_{\delta\hat{x}_0} = 1.6m$ which corresponds to a conservative standard deviation of a GBAS vertical error

The propagation time considered is $T_f = 10$ seconds and the following state grid has been used:

- $b_1 \in [-20\sigma_{b1_0}, 20\sigma_{b1_0}]$ with a step of $40\sigma_{b1_0}/200$
- $\delta\hat{v} \in [-40\sigma_{\delta\hat{v}_0}, 40\sigma_{\delta\hat{v}_0}]$ with a step of $80\sigma_{\delta\hat{v}_0}/200$
- $\delta\hat{x} \in [-30\sigma_{\delta\hat{x}_0}, 30\sigma_{\delta\hat{x}_0}]$ with a step of $60\sigma_{\delta\hat{x}_0}/200$
- $t \in [0, T_f]$ with a step of $T_f/100$

The dimension of the grid has been chosen as a trade off between high resolution and computational memory. This is for the moment considered as a fixed grid that can be improved in a future work using an adaptive grid.

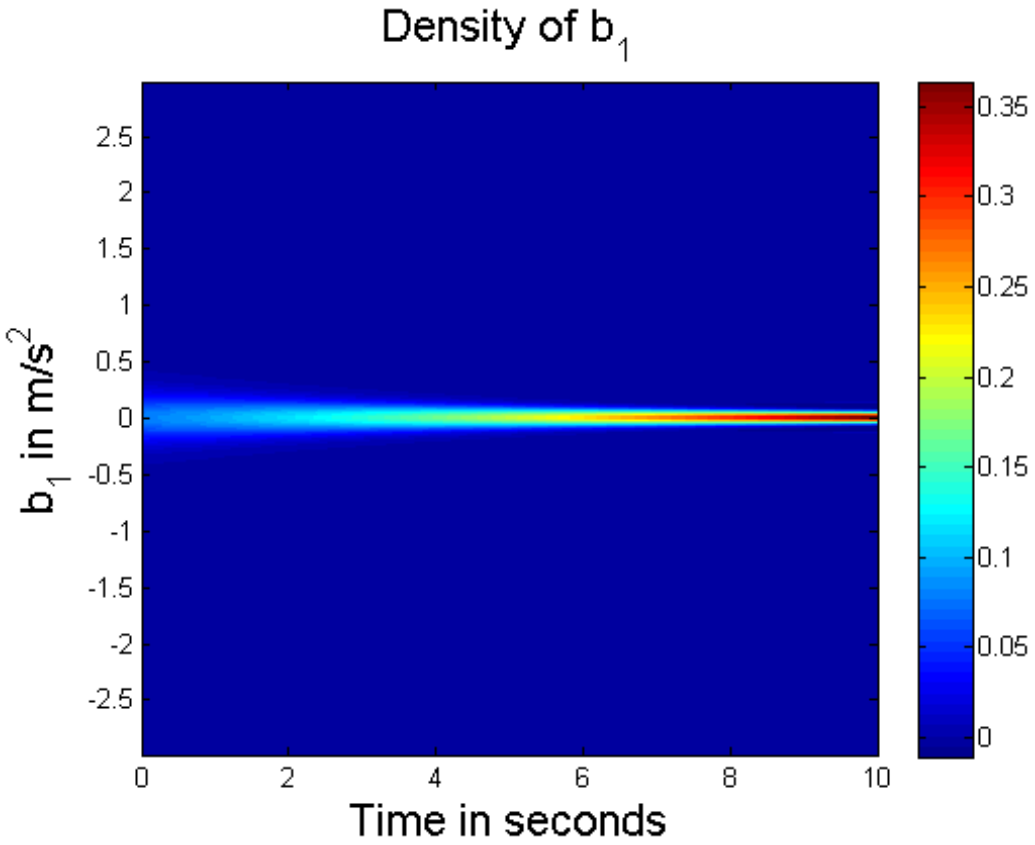

Figure 5.1.: Evolution of the density of the time varying bias of the accelerometer b_1 vs. t

Fig. 5.1 shows the solution of the Kolmogorov forward equation. The integration time is 10 seconds. The used parameters are $\tau = 100$ seconds and $\sigma_{b_1} = 1.2$ milli-g as proposed in [GE04]. We assumed an initial Gaussian distribution of b_1 to be centered with a standard deviation of $5 \times 10^{-2} m/s^2$.

To show the impact of imperfections in the accelerometer, let assume the true acceleration to be a sinusoidal function of time.Fig. 5.2 shows the distribution of the velocity error with respect to time.

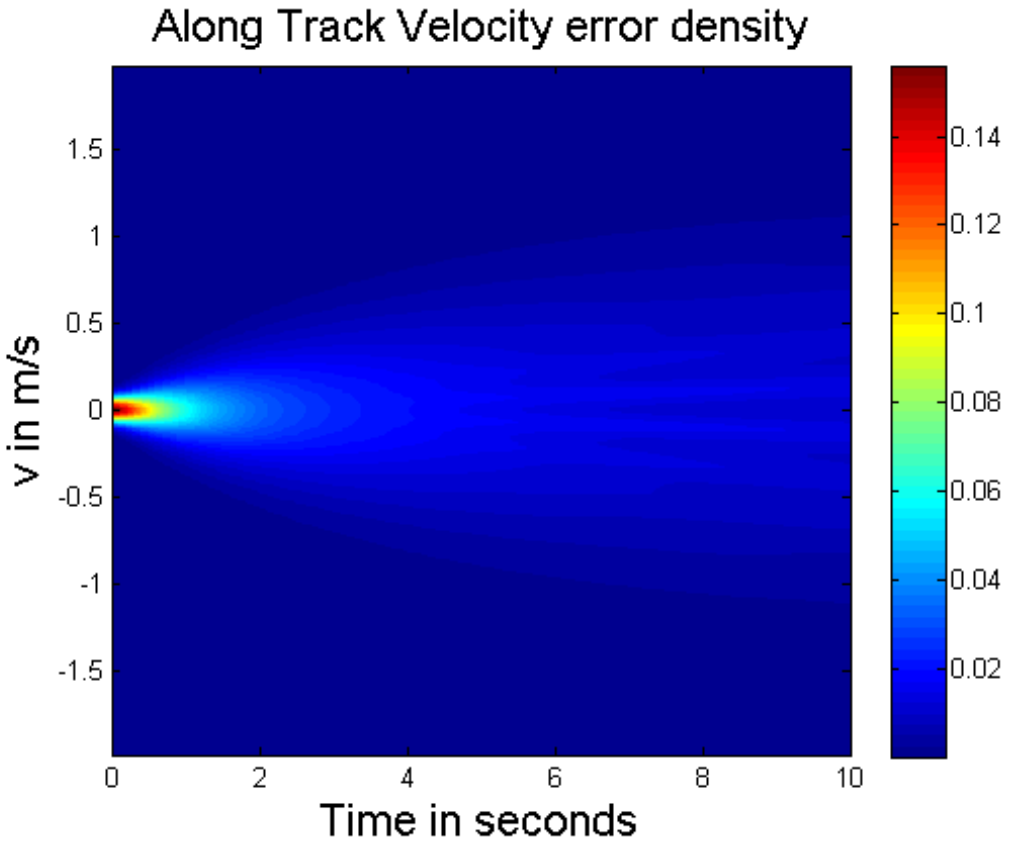

Figure 5.2.: Evolution of the density of velocity error vs. t

Fig. 5.3 shows the evolution of the altitude error. We assume that the initial distribution is the one provided by a GBAS (Ground Based Augmentation System) error distribution. The probability density function taken for GBAS is a very conservative one. Additionally to this plot, we plot the protection level envelope corresponding to an integrity risk of 0.5×10^{-7} (represented by the 2 curves). These protection envelopes are calculated for each time step by integrating from the bottom and from the top the probability density function at each time step until the required integrity risk has been reached. An equal allocation for the risk at both side of the PDF has been assumed.

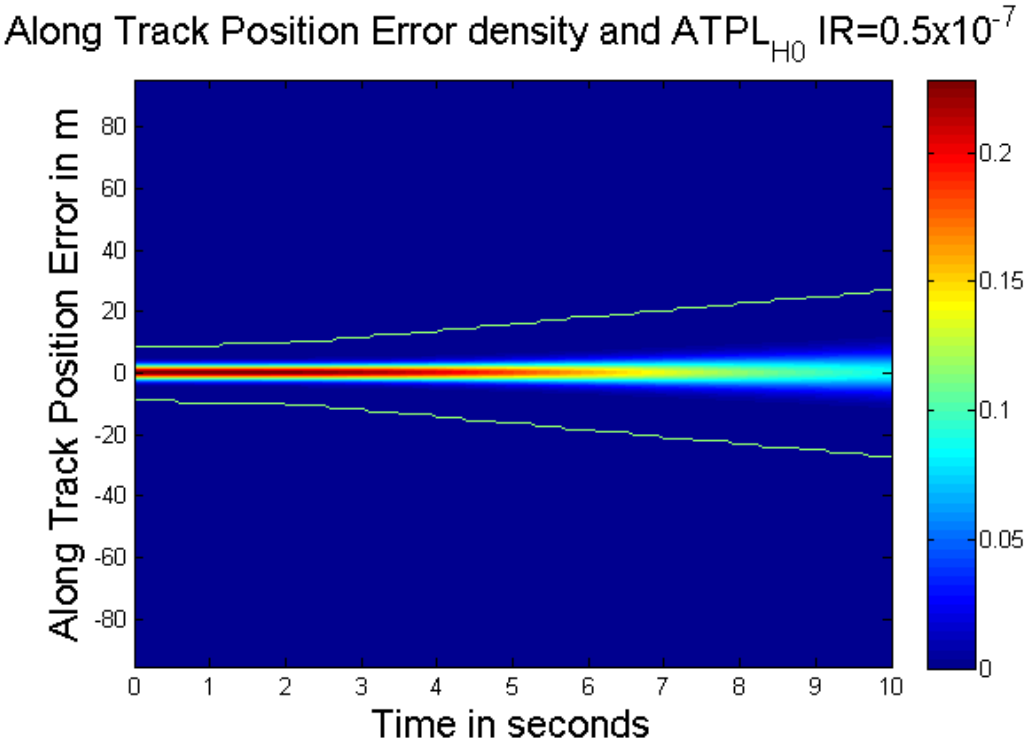

Figure 5.3.: Evolution of the density of altitude error vs. t using GBAS along track error over-bound coasted with inertial

A GBAS user receiver provides a 2Hz position solution to a user (usually an aircraft on approach) located in the vicinity of the GBAS station. In case of a GBAS outage, it is possible to use inertial sensors to coast the position. The maximum period of time allowed for coasting is the one that provides a protection level below the required alarm limit (The maximum tolerable error in the navigation system). As the inertial measurement unit is an integrator, the error are cumulative and the maximum level of error corresponds to the maximum coasting time (just before the next GBAS update).

For each time t, it is possible to find the Gaussian over-bound of the vertical error, take the maximum standard deviation of all these Gaussian over bounds in the considered period of time and multiply it with a coefficient to account for the

maximum allowed integrity risk. As the altitude error is a diffusion process with a diffusion coefficient greater than one, the maximum values are obtained at $t = T$ (at the end of the time period). We can see that the protection level is very sensitive to the integration time. We considered the initial distribution of b_1 to be centered which is not the reality. A non centrality term will automatically introduce a bias in the altitude error and should be taken into consideration in the protection level equation.

5.3. The Analytical Evolution of the Expectation and the Variance

The numerical resolution of the pdf evolution of the diffusion process was not necessary because the error process is a linear Ito diffusion and in that case we know that the state process is Gaussian distributed for each time t therefore it is sufficient to know the propagation of the first and second moment of the diffusion process. For that we can rewrite the Ito equation of the problem as an Ito integral:

$$dX_t = \beta_t(X_t)\,dt + \sigma dB_t \tag{5.24}$$

with $\beta_t(X_t) = \begin{pmatrix} -\frac{1}{\tau}b_{1t} & s_f s(t) + b_0 + b_{1t} & \delta\hat{v}_t \end{pmatrix}^T$, $\sigma = \begin{pmatrix} \sigma_g & 0 & 0 \\ 0 & \sigma_w & 0 \end{pmatrix}^T$ and $dB_t = \begin{pmatrix} dB_{gt} & dB_{wt} \end{pmatrix}^T$.

$$X_t = X_0 + \int_0^t \beta_u(X_u)\,du + \sigma B_t$$

If we consider the first component of the state vector, we have:

$$db_{1t} = -\frac{1}{\tau}b_{1t}dt + \sigma_g dB_{gt}$$

This is in fact an Ornstein-Uhlenbeck process (for continuous time) or an AR(1) (for discrete time) with equilibrium at 0.

We can show that the integrated process can be written as follows:

$$b_{1t} = b_{10}e^{-\frac{t}{\tau}} + \sigma_g \int_0^t e^{\frac{u-t}{\tau}} dB_{gu}$$

we have the mean and the variance (assuming b_0 being a normal distributed random variable):

$E[b_{1t}] = E[b_{10}]e^{-\frac{t}{\tau}}$ and $V[b_{1t}] = E\left[(b_{1t} - E[b_{1t}])^2\right] = \tau\frac{\sigma_g^2}{2}\left(1 - \exp\left(-\frac{2t}{\tau}\right)\right) + V[b_{10}]e^{-\frac{2t}{\tau}}$

The integrated form of the stochastic differential equation can be written as follows:

$$\begin{aligned} b_{1t} &= b_{10}e^{-\frac{t}{\tau}} + \sigma_g \int_0^t e^{\frac{u-t}{\tau}} dB_{gu} \\ \delta\hat{v}_t &= \delta\hat{v}_0 + \int_0^t (s_f s(u) + b_0 + b_{1u})\, du + \sigma_w B_{wt} \\ \delta\hat{x}_t &= \delta\hat{x}_0 + \int_0^t \delta\hat{v}_u du \end{aligned}$$

We propose to calculate the expectation and the variance of the process for each time step:

$$E[X_t] = E[X_0] + E\left[\int_0^t \beta_t(X_t)\, dt\right] + \sigma E[B_t]$$

$E[B_t] = 0$ and $E\left[\int_0^t \beta_t(X_t)\, dt\right] = \int_0^t E[\beta_t(X_t)]\, dt$

$$E[X_t] = E[X_0] + \int_0^t E[\beta_t(X_t)]\, dt$$

We recall that $X_t = (b_{1t} \quad \delta\hat{v}_t \quad \delta\hat{x}_t)^T$

$\int_0^t E[\beta_t(X_t)]\, dt = \int_0^t \left(-\frac{1}{\tau}E[b_{1t}] \quad s_f s(t) + b_0 + E[b_{1t}] \quad E[\delta\hat{v}_t]\right)^T dt$

Therefore we have:

$$\begin{aligned} E[b_{1t}] &= E[b_{10}]e^{-\frac{t}{\tau}} \\ E[\delta\hat{v}_t] &= E[\delta\hat{v}_0] + s_f\int_0^t s(u)\, du + b_0 t - \tau E[b_{10}]\left(e^{-\frac{t}{\tau}} - 1\right) \\ E[\delta\hat{x}_t] &= E[\delta\hat{x}_0] + E[\delta\hat{v}_0]\, t + s_f\int_0^t \left(\int_0^r s(u)\, du\right) dr + \frac{1}{2}b_0 t^2 + \tau^2 E[b_{10}]\left(e^{-\frac{t}{\tau}} + \frac{t}{\tau} - 1\right) \end{aligned}$$

The variance of the state process is: $V[X_t] = E\left[(X_t - E[X_t])(X_t - E[X_t])^T\right]$

We first express the vector $X_t - E[X_t] \equiv \widetilde{X_t}$ function of all parameters of the model:

$$\begin{aligned} \widetilde{b_{1t}} &= b_{10}e^{-\frac{t}{\tau}} - E[b_{10}]e^{-\frac{t}{\tau}} + \sigma_g\int_0^t e^{\frac{u-t}{\tau}} dB_{gu} \\ \widetilde{\delta\hat{v}_t} &= \delta\hat{v}_0 + \int_0^t (s_f s(u) + b_0 + b_{1u})\, du + \sigma_w B_{wt} - E[\delta\hat{v}_t] \\ \widetilde{\delta\hat{x}_t} &= \delta\hat{x}_0 + \int_0^t \delta\hat{v}_u du - E[\delta\hat{x}_t] \end{aligned}$$

$$\begin{array}{rcl}
\widetilde{b_{1t}} & = & \widetilde{b_{10}}e^{-\frac{t}{\tau}} + \sigma_g \int_0^t e^{\frac{u-t}{\tau}} dB_{gu} \\
\widetilde{\delta\hat{v}_t} & = & \delta\hat{v}_0 + s_f \int_0^t s\left(u\right) du + b_0 t + \int_0^t b_{1u} du + \sigma_w B_{wt} - E\left[\delta\hat{v}_t\right] \\
\widetilde{\delta\hat{x}_t} & = & \delta\hat{x}_0 + \int_0^t \delta\hat{v}_u du - E\left[\delta\hat{x}_t\right]
\end{array}$$

$$\begin{array}{rcl}
\widetilde{b_{1t}} & = & \widetilde{b_{10}}e^{-\frac{t}{\tau}} + \sigma_g \int_0^t e^{\frac{u-t}{\tau}} dB_{gu} \\
\widetilde{\delta\hat{v}_t} & = & \widetilde{\delta\hat{v}_0} - \tau\widetilde{b_{10}}\left(e^{-\frac{t}{\tau}} - 1\right) + \sigma_g \int_0^t \int_0^r e^{\frac{u-r}{\tau}} dB_{gu} dr + \sigma_w B_{wt} \\
\widetilde{\delta\hat{x}_t} & = & \widetilde{\delta\hat{x}_0} + \widetilde{\delta\hat{v}_0} t + \tau^2\widetilde{b_{10}}\left(e^{-\frac{t}{\tau}} + \frac{t}{\tau} - 1\right) + \sigma_g \int_0^t \int_0^r \int_0^q e^{\frac{u-q}{\tau}} dB_{gu} dq dr + \sigma_w \int_0^t B_{wu} du
\end{array}$$

$$\begin{array}{rcl}
\widetilde{b_{1t}} & = & \widetilde{b_{10}}e^{-\frac{t}{\tau}} + \sigma_g \int_0^t e^{\frac{u-t}{\tau}} dB_{gu} \\
\widetilde{\delta\hat{v}_t} & = & \widetilde{\delta\hat{v}_0} - \tau\widetilde{b_{10}}\left(e^{-\frac{t}{\tau}} - 1\right) + \sigma_g \eta_t\left(\tau\right) + \sigma_w B_{wt} \\
\widetilde{\delta\hat{x}_t} & = & \widetilde{\delta\hat{x}_0} + \widetilde{\delta\hat{v}_0} t + \tau^2\widetilde{b_{10}}\left(e^{-\frac{t}{\tau}} + \frac{t}{\tau} - 1\right) + \sigma_g \mu_t\left(\tau\right) + \sigma_w \gamma_t
\end{array}$$

with $\eta_t\left(\tau\right) = \int_0^t \int_0^r e^{\frac{u-r}{\tau}} dB_{gu} dr$, $\mu_t\left(\tau\right) = \int_0^t \int_0^r \int_0^q e^{\frac{u-q}{\tau}} dB_{gu} dq dr$ and $\gamma_t = \int_0^t B_{wu} du$

$V\left[X_t\right] = E\left[\widetilde{X_t}\widetilde{X_t}^T\right]_{ij} = c_{ij}$

$$c_{11} = V\left[b_{10}\right] e^{-\frac{2t}{\tau}} + \tau\frac{\sigma_g^2}{2}\left(1 - \exp\left(-\frac{2t}{\tau}\right)\right)$$

$$c_{22} = V\left[\delta\hat{v}_0\right] + \tau^2 V\left[b_{10}\right]\left(e^{-\frac{t}{\tau}} - 1\right)^2 + \sigma_g^2 V\left[\eta_t\left(\tau\right)\right] + \sigma_w^2 t$$

$$c_{33} = V\left[\delta\hat{x}_0\right] + V\left[\delta\hat{v}_0\right] t^2 + \tau^4 V\left[b_{10}\right]\left(e^{-\frac{t}{\tau}} + \frac{t}{\tau} - 1\right)^2 + \sigma_g^2 V\left[\mu_t\left(\tau\right)\right] + \sigma_w^2 V\left[\gamma_t\right]$$

$$c_{12} = -\tau V\left[b_{10}\right]\left(e^{-\frac{2t}{\tau}} - e^{-\frac{t}{\tau}}\right) + \sigma_g^2 E\left[\eta_t\left(\tau\right)\int_0^t e^{\frac{u-t}{\tau}} dB_{gu}\right]$$

$$c_{13} = \tau^2 V\left[b_{10}\right]\left(e^{-\frac{2t}{\tau}} + \frac{t}{\tau}e^{-\frac{t}{\tau}} - e^{-\frac{t}{\tau}}\right) + \sigma_g^2 E\left[\mu_t\left(\tau\right)\int_0^t e^{\frac{u-t}{\tau}} dB_{gu}\right]$$

$$c_{23} = V\left[\delta\hat{v}_0\right]t^2 - \tau^3 V\left[b_{10}\right]\left(e^{-\frac{t}{\tau}} - 1\right)\left(e^{-\frac{t}{\tau}} + \frac{t}{\tau} - 1\right) + \sigma_g^2 E\left[\eta_t\left(\tau\right)\mu_t\left(\tau\right)\right] + \sigma_w^2 E\left[B_{wt}\gamma_t\right]$$

These coefficients define entirely the covariance matrix $V\left[X_t\right]$.

We have assumed that $\widetilde{b_{10}}$, B_{gu}, $\widetilde{\delta\hat{v}_0}$, B_{wt}, $\widetilde{\delta\hat{x}_0}$ are 2 by 2 independent.

As $\eta_t\left(\tau\right)$, $\mu_t\left(\tau\right)$ are function of B_{gu} we kept the cross products as non necessarily zero terms.The same applies for B_{wt} and $\gamma_t\left(\tau\right)$. In fact $E\left[B_{wt}\gamma_t\right] = \frac{t^2}{2}$ (see Appendix D for more details).

We have also:

$$\begin{array}{c} E\left[\eta_t\left(\tau\right)\mu_t\left(\tau\right)\right] = \frac{t^2\tau^2}{2e^{\frac{t}{\tau}}} + t\tau^3 + 4\frac{t\tau^3}{e^{\frac{t}{\tau}}} - \tau^4 e^{\frac{t}{\tau}} \\ \frac{1}{8}t^4 - \frac{5}{2}\tau^4 + \frac{\tau^4}{2e^{2\frac{t}{\tau}}} + 3\frac{\tau^4}{e^{\frac{t}{\tau}}} - \frac{1}{6}t^3\tau + \frac{3}{2}t^2\tau^2 \end{array} \tag{5.25}$$

(See Appendix D for more details),

$E\left[\eta_t\left(\tau\right)\int_0^t e^{\frac{u-t}{\tau}}dB_{gu}\right] = \frac{1}{2}\tau^2 - \frac{\tau^2}{e^{\frac{t}{\tau}}} + \frac{\tau^2}{2e^{2\frac{t}{\tau}}}$, $E\left[\mu_t\left(\tau\right)\int_0^t e^{\frac{u-t}{\tau}}dB_{gu}\right] = -\frac{t\tau^2}{e^{\frac{t}{\tau}}} + \frac{1}{2}\tau^3 - \frac{\tau^3}{2e^{2\frac{t}{\tau}}}$.
We can also express the variance of the following expressions:

$V\left[\gamma_t\right] = \frac{t^3}{3}$

$V\left[\eta_t\left(\tau\right)\right] = t\tau^2 - \frac{3}{2}\tau^3 + 2\frac{\tau^3}{e^{\frac{t}{\tau}}} - \frac{\tau^3}{2e^{2\frac{t}{\tau}}}$

$V\left[\mu_t\left(\tau\right)\right] = \frac{1}{3}t^3\tau^2 - t^2\tau^3 + t\tau^4 - 2\frac{t\tau^4}{e^{\frac{t}{\tau}}} + \frac{1}{2}\tau^5 - \frac{\tau^5}{2e^{2\frac{t}{\tau}}}$

Finally we observe that the covariance matrix $V\left[X_t\right]$ is not diagonal in the general case.

We observe that when the random variables in the model of the sensor are all Gaussian distributed (including the initial point b_{10}, $\delta\hat{v}_0$ and $\delta\hat{x}_0$), the state vector is also Gaussian distributed. Therefore the propagation of the mean and the variance is sufficient if we want to characterize the whole distribution.

Given all these expressions, we can express the expectation and the variance of the state vector just function of time t, time constant τ and the parameters of the problem.

$$E\left[b_{1t}\right] = \frac{\mu_{b10}}{e^{\frac{t}{\tau}}}$$

$$E\left[\delta\hat{v}_t\right] = I_{st}s_f + b_0 t + \mu_{b10}\tau - \frac{\mu_{b10}\tau}{e^{\frac{t}{\tau}}} + \mu_{\delta v0}$$

$$E\left[\delta\hat{x}_t\right] = II_{st}s_f + \frac{1}{2}b_0t^2 + \mu_{b10}t\tau - \mu_{b10}\tau^2 + \frac{\mu_{b10}\tau^2}{e^{\frac{t}{\tau}}} + \mu_{\delta v0}t + \mu_{\delta x0}$$

$$V\left[b_{1t}\right] = \frac{1}{2}\sigma_g^2\tau - \frac{\sigma_g^2\tau}{2e^{2\frac{t}{\tau}}} + \frac{\sigma_{b10}^2}{e^{2\frac{t}{\tau}}}$$

$$V\left[\delta\hat{v}_t\right] = \sigma_g^2t\tau^2 - \frac{3}{2}\sigma_g^2\tau^3 + 2\frac{\sigma_g^2\tau^3}{e^{\frac{t}{\tau}}} - \frac{\sigma_g^2\tau^3}{2e^{2\frac{t}{\tau}}} + \sigma_{b10}^2\tau^2 - 2\frac{\sigma_{b10}^2\tau^2}{e^{\frac{t}{\tau}}} + \frac{\sigma_{b10}^2\tau^2}{e^{2\frac{t}{\tau}}} + \sigma_w^2t + -\frac{1}{2}\sigma_{\delta v0}^2$$

$$\begin{aligned} V\left[\delta\hat{x}_t\right] = \; & \tfrac{1}{3}\sigma_g^2t^3\tau^2 - \sigma_g^2t^2\tau^3 + \sigma_g^2t\tau^4 - 2\tfrac{\sigma_g^2t\tau^4}{e^{\frac{t}{\tau}}} + \tfrac{1}{2}\sigma_g^2\tau^5 \\ & -\tfrac{\sigma_g^2\tau^5}{2e^{2\frac{t}{\tau}}} + \sigma_{b10}^2t^2\tau^2 - 2\sigma_{b10}^2t\tau^3 + 2\tfrac{\sigma_{b10}^2t\tau^3}{e^{\frac{t}{\tau}}} + \sigma_{b10}^2\tau^4 \\ & -2\tfrac{\sigma_{b10}^2\tau^4}{e^{\frac{t}{\tau}}} + \tfrac{\sigma_{b10}^2\tau^4}{e^{2\frac{t}{\tau}}} + \tfrac{1}{3}\sigma_w^2t^3 + \sigma_{\delta v0}^2t^2 + \sigma_{\delta x0}^2 \end{aligned}$$

With the following notations:

μ_{b10} is the mean of the initial Gauss Markov drift

I_{st} is the integral with respect to time of the "true" acceleration s_t

s_f is the scaling factor for the sensor considered

b_0 is the sensor offset

$\mu_{\delta v0}$ is the mean of the initial velocity error

II_{st} is the double integral with respect to time of the "true" acceleration s_t

$\mu_{\delta x0}$ is the mean of the initial position error

σ_{b1} is the standard deviation of the Gauss Markov process

σ_g is the standard deviation of the noise in the Gauss Markov process

σ_w is the standard deviation of the noise added to the Gauss Markov process

$\sigma_{\delta x0}$ is the standard deviation of the initial position error

We define a protection bound with respect to an integrity risk as being the integrity risk quantile for the position error given by the following equation:

$$PB_{\text{kff},\delta\hat{x}_t} = \left|E\left[\delta\hat{x}_t\right]\right| + k_{\text{ff}}\sqrt{V\left[\delta\hat{x}_t\right]} \tag{5.26}$$

where k_{ff} is the multiplication coefficient corresponding to the considered integrity risk requirement.

For example $k_{\text{ff}} \approx 5.33$ for an integrity risk of 10^{-7}. This concept of protection bound assumes that the sign of the bias term (first term in equation 5.26) is unknown therefore a conservative approach will consider an upper bound for this first term and its absolute value. For a 2D problem, the protection bound is intuitively a closed smooth contour for which the bias term should be replaced by a norm and the second term should be defined as follows:

$$PB_{2D,\text{kff},\delta\hat{x}_t} = \left\| E\left[\delta\hat{x}_t\right] \right\|_{\mathbb{R}^2} + k_{\text{ff2D}} \sqrt{V\left[\delta\hat{x}_t\right]} \tag{5.27}$$

5.3.1. Sensitivity Analysis to Parameters of the Sensor Model

From the analytical form of the expectation and the variance of the process as defined above, we investigate the sensitivity of the integrity bounds to the parameters of the sensor model.

We are going to analyze the sensitivity of the protection bounds to each parameter of the model while fixing the others to their nominal values. The nominal values are taken as follows:

$\tau_{\text{nom}} = 100$ s

$\mu_{b10,\text{nom}} = 0$ milli-g. Assuming a null-shift of the drift (after calibration)

$s_{f,\text{nom}} = 0.1$

$b_{0,\text{nom}} = 0$ m/s^2

$\mu_{\delta v0,\text{nom}} = 0$ m/s

$II_{st,\text{nom}} = 0$ m

$\mu_{\delta x0,\text{nom}} = 0$ m

$\sigma_{b10,\text{nom}} = 1.2$ milli-g. This value corresponds to the standard deviation of the drift after the Gauss Markov Process is stabilized

$\sigma_{g,\text{nom}} = 1.2\sqrt{\frac{2}{\tau}}$ milli-g.

$\sigma_{w,\text{nom}} = 1$ milli-g

$\sigma_{\delta x0,\text{nom}} = 0.5$ meter

$k_{\text{ff,nom}} = 5.33$

5.3.2. 2D Accelerometer

In this part we assume to have two accelerometers in the along and cross track directions. We can take as an example the train application.

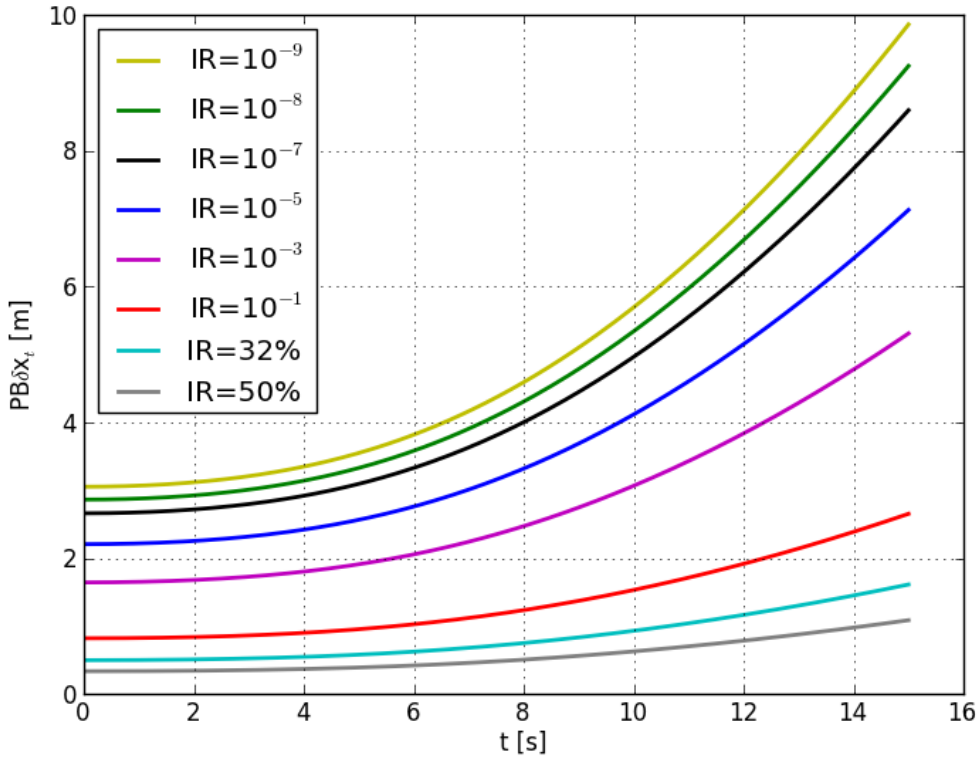

Figure 5.4.: sensitivity of the protection level to the integrity risk

We assume these accelerometers are independent. Which means that the principal axis of the error ellipses are the along and cross track axis.

In other words, if we call σ_{AT} and σ_{CT} the standard deviation of the error in the along and cross track direction respectively, the covariance matrix of the 2D error can be written as follows:

$$M = \begin{pmatrix} \sigma_{AT}^2 & 0 \\ 0 & \sigma_{CT}^2 \end{pmatrix}$$

The bi-variate probability density function can be written as follows:

$$f(u,v) = \frac{1}{2\pi} \frac{1}{\sqrt{\det M}} \exp\left\{ -\frac{1}{2} \begin{pmatrix} u & v \end{pmatrix} M^{-1} \begin{pmatrix} u \\ v \end{pmatrix} \right\}$$

The first problem we want to solve is: For a given integrity risk IR, we want to find the ellipse inside which the integral of the bi-variate probability density function

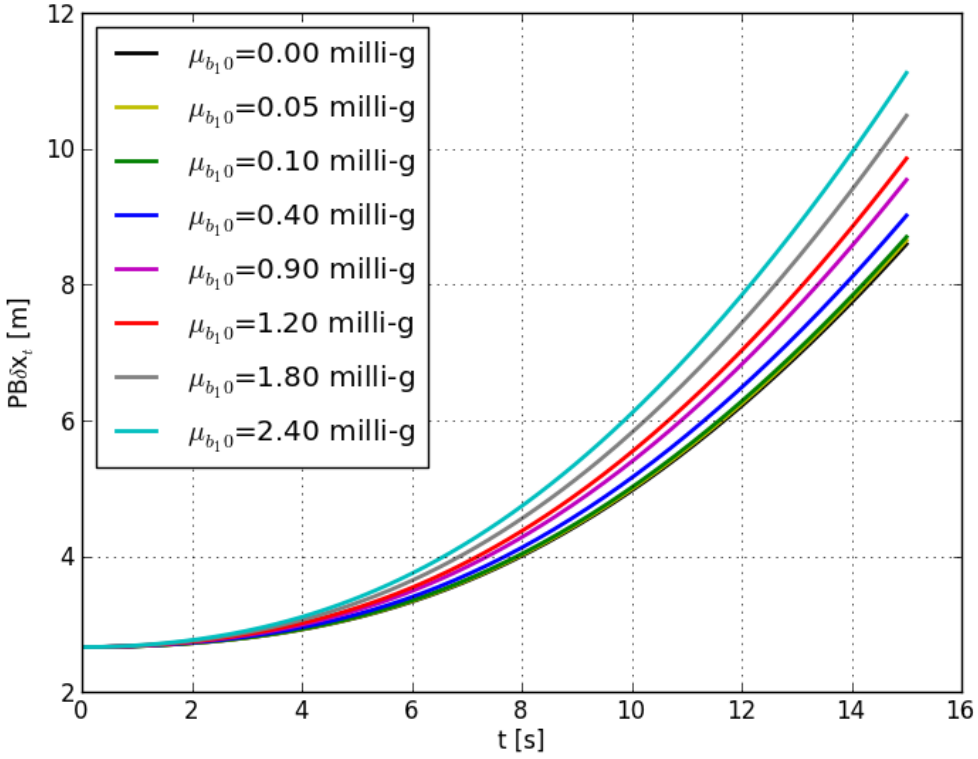

Figure 5.5.: sensitivity of the protection level to the initial drift bias

inside the surface of this ellipse is precisely $1 - IR$. Taking into account the form of the matrix M, f can be written as follows:

$$f(u,v) = \frac{1}{2\pi} \frac{1}{\sqrt{\sigma_{AT}^2 + \sigma_{CT}^2}} \exp\left\{-\frac{1}{2}\left(\frac{u^2}{\sigma_{AT}^2} + \frac{v^2}{\sigma_{CT}^2}\right)\right\}$$

Before calculating the integral it is suitable to change the variables: $X = \frac{u}{\sigma_{AT}}$ and $Y = \frac{v}{\sigma_{CT}}$.

$$f(X,Y) = \frac{1}{2\pi} \frac{1}{\sqrt{\sigma_{AT}^2 + \sigma_{CT}^2}} \exp\left\{-\frac{1}{2}\left(X^2 + Y^2\right)\right\}$$

We can observe that the iso-density lines are the lines for which $X^2 + Y^2 = cst$. This describes circles in the (X,Y)plan (ellipses in the (u,v) plan)

It is suitable to proceed to another variable change: from (X,Y) to (r,θ) with $X = r\cos\theta$ and $Y = r\sin\theta$

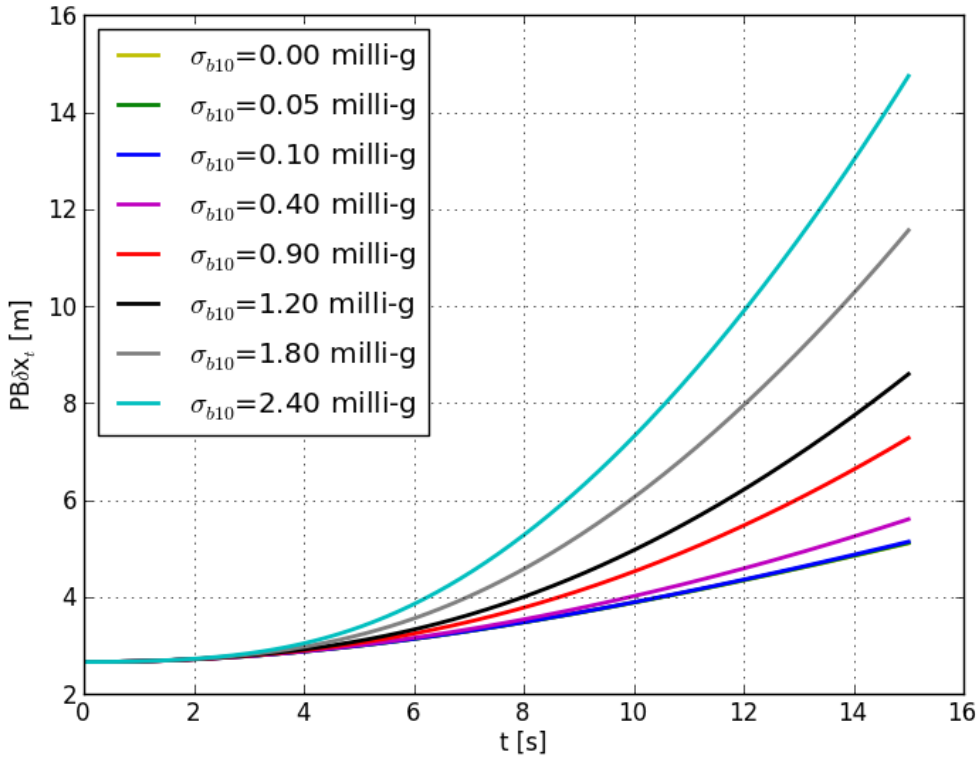

Figure 5.6.: sensitivity of the protection level to the standard deviation of the initial drift

$$f(r,\theta) = f(r) = \frac{1}{2\pi}\frac{1}{\sqrt{\sigma_{AT}^2 + \sigma_{CT}^2}}\exp\left\{-\frac{1}{2}r^2\right\}$$

We observe that f is only function of the radius r. To calculate the integral of f in the surface described by a circle centered at 0 and of radius $r = R$. We proceed simply by integrating f in concentric rings of thickness dr and of radius r and let r variate from 0 to R. We are looking for R for which the integral of f is exactly equal to $1 - IR$. In an equation form we have:

$$\int_0^R f(r)\,(2\pi r dr) = 1 - IR$$

$$\frac{1}{\sqrt{\sigma_{AT}^2 + \sigma_{CT}^2}}\int_0^R \exp\left\{-\frac{1}{2}r^2\right\} r dr = 1 - IR$$

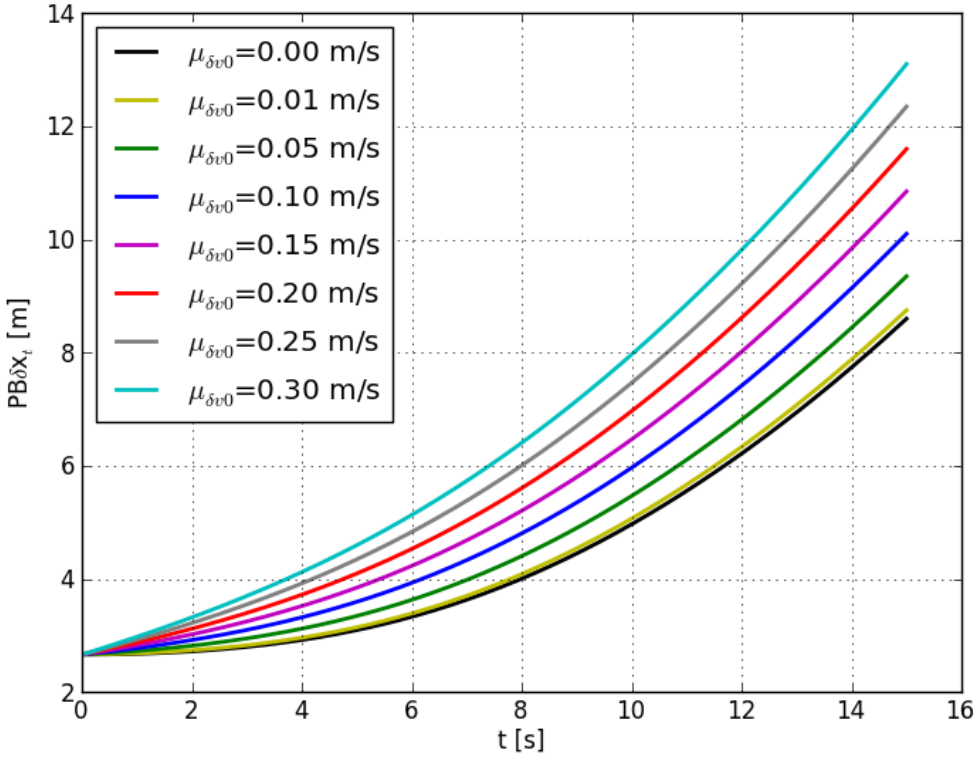

Figure 5.7.: sensitivity of the protection level to the initial velocity error bias

We observe that $\exp\left\{-\frac{1}{2}r^2\right\} rdr = d\left(-\exp\left\{-\frac{1}{2}r^2\right\}\right)$. The integral of the probability density function in the whole $\mathbb{R}^2$ plan is equal to 1 (property of a probability distribution) so we have to find the normalizing factor k such that $\frac{k}{\sqrt{\sigma_{AT}^2+\sigma_{CT}^2}} \int_0^\infty \exp\left\{-\frac{1}{2}r^2\right\} rdr = 1$. This gives $k = \sqrt{\sigma_{AT}^2 + \sigma_{CT}^2}$. Therefore we have the condition:

$$\left(1 - \exp\left\{-\frac{1}{2}R^2\right\}\right) = 1 - IR$$

$$\exp\left\{-\frac{1}{2}R^2\right\} = IR$$

$$R = \sqrt{-2\log\left(IR\right)}$$

The integral of the bi-variate density function over the surface delimited by the ellipse with semi axis ($R\sigma_{AT}$,$R\sigma_{CT}$) is equal to $1 - IR$.

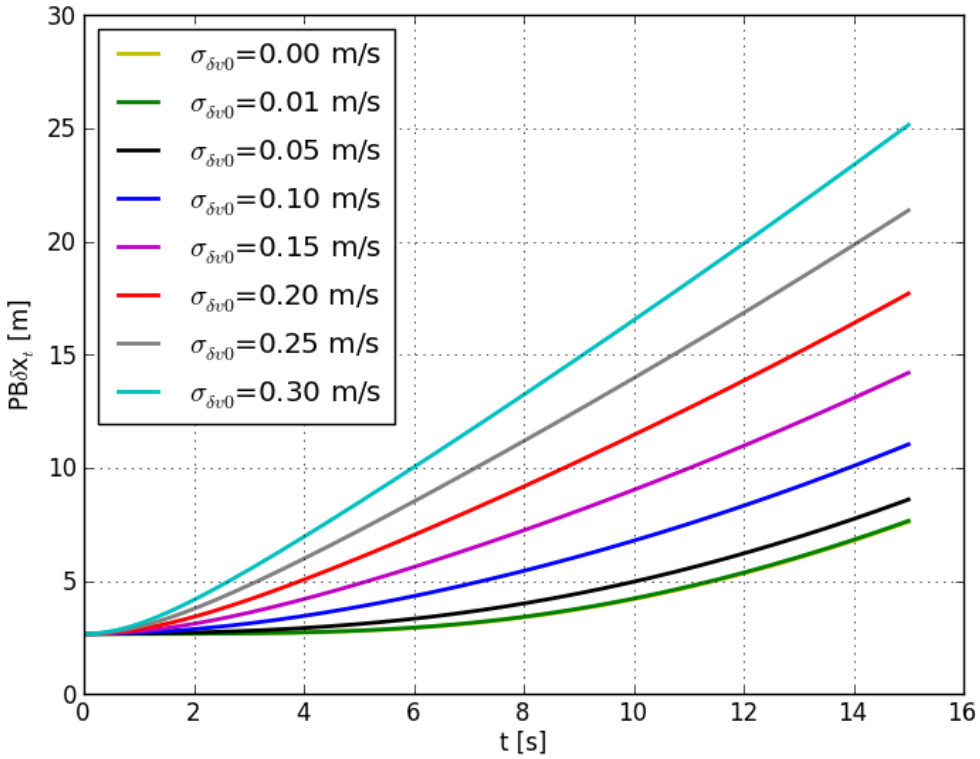

Figure 5.8.: sensitivity of the protection level to the standard deviation of the initial velocity error

In fact an infinite number of surfaces can provide the same integral. We choose the one that defines the smallest surface or the one corresponding to an iso-density.

In the following we take the example of a train moving in rectilinear tracks. We consider the same parameters as before for the acceleration error model except for the acceleration scaling factor that we now set to $s_f = 0.1$ and we considered an integrity risk of 10^{-7} which correspond to $k_{\text{ff2D}} = 5,68$.

We assume a velocity profile as described in Fig. 5.13.

5.3.3. 3D Accelerometer

Let's call AT, CT, ZT the 3 body frame axis (AT is the along track, CT is the cross track and ZT so that (AT, CT, ZT)forms a direct reference frame). In this case we have:

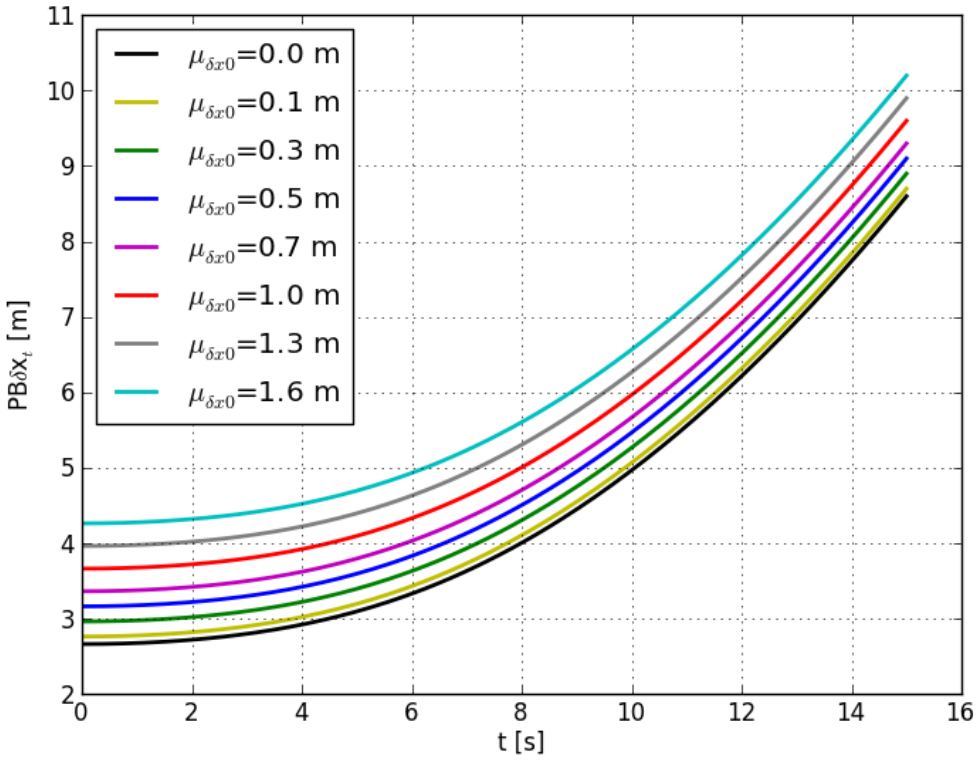

Figure 5.9.: sensitivity of the protection level to the initial position error bias

$$M = \begin{pmatrix} \sigma_{AT}^2 & 0 & 0 \\ 0 & \sigma_{CT}^2 & 0 \\ 0 & 0 & \sigma_{ZT}^2 \end{pmatrix}$$

The bi-variate probability density function can be written as follows:

$$f(u,v,w) = \frac{1}{2\pi}\frac{1}{\sqrt{\det M}} \exp\left\{ -\frac{1}{2} \begin{pmatrix} u & v & w \end{pmatrix} M^{-1} \begin{pmatrix} u \\ v \\ w \end{pmatrix} \right\}$$

The first problem we want to solve is: For a given integrity risk, we want to find the ellipse inside which the integral of the bi-variate probability density function in the surface of this ellipse is precisely $1 - IR$. Taking into account the form of the matrix M (diagonal), f can be written as follows:

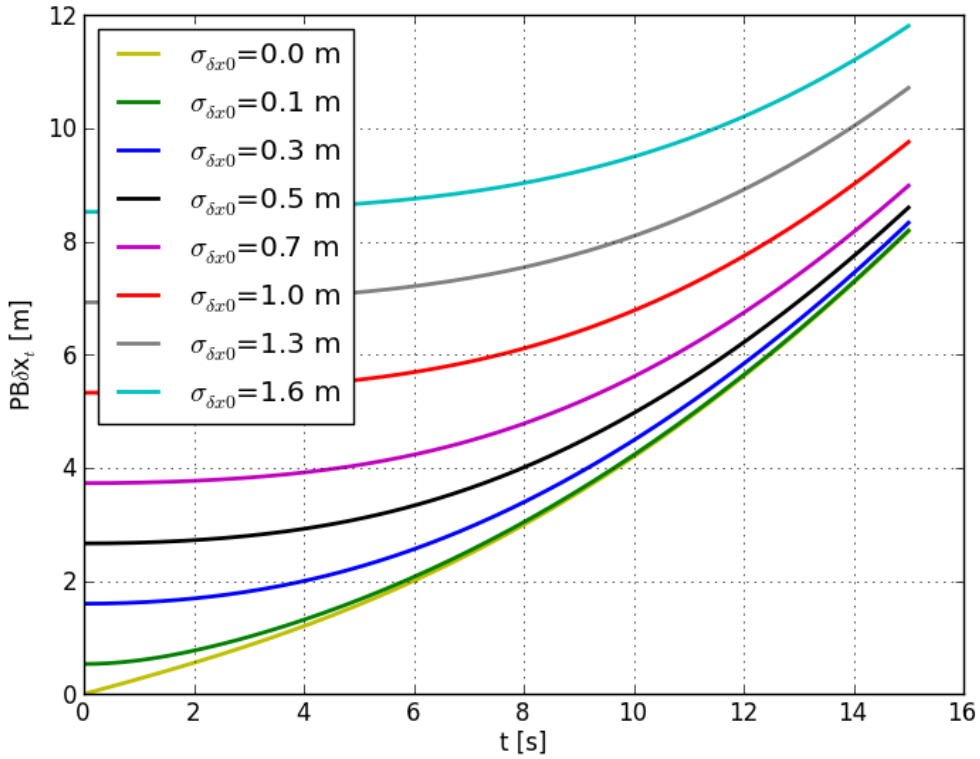

Figure 5.10.: sensitivity of the protection level to the standard deviation of the initial position error

$$f(u,v,w) = \frac{1}{2\pi}\frac{1}{\sqrt{\sigma_{AT}^2+\sigma_{CT}^2+\sigma_{ZT}^2}}\exp\left\{-\frac{1}{2}\left(\frac{u^2}{\sigma_{AT}^2}+\frac{v^2}{\sigma_{CT}^2}+\frac{w^2}{\sigma_{ZT}^2}\right)\right\}$$

Before calculating the integral it is suitable to change the variables: $X = \frac{u}{\sigma_{AT}}$,$Y = \frac{v}{\sigma_{CT}}$ and $Y = \frac{w}{\sigma_{ZT}}$.

$$f(X,Y,Z) = \frac{1}{2\pi}\frac{1}{\sqrt{\sigma_{AT}^2+\sigma_{CT}^2+\sigma_{ZT}^2}}\exp\left\{-\frac{1}{2}\left(X^2+Y^2+Z^2\right)\right\}$$

We can observe that the iso-density surfaces are the surfaces for which $X^2+Y^2+Z^2 = cst$. This describes spheres in the (X,Y,Z)plan (ellipsoids in the (u,v,w) plan)

It is suitable to proceed to an other variable change: from (X,Y,Z) to (r,θ,ϕ) with $X = r\cos\theta\cos\phi$, $Y = r\sin\theta\cos\phi$ and $Z = r\sin\phi$

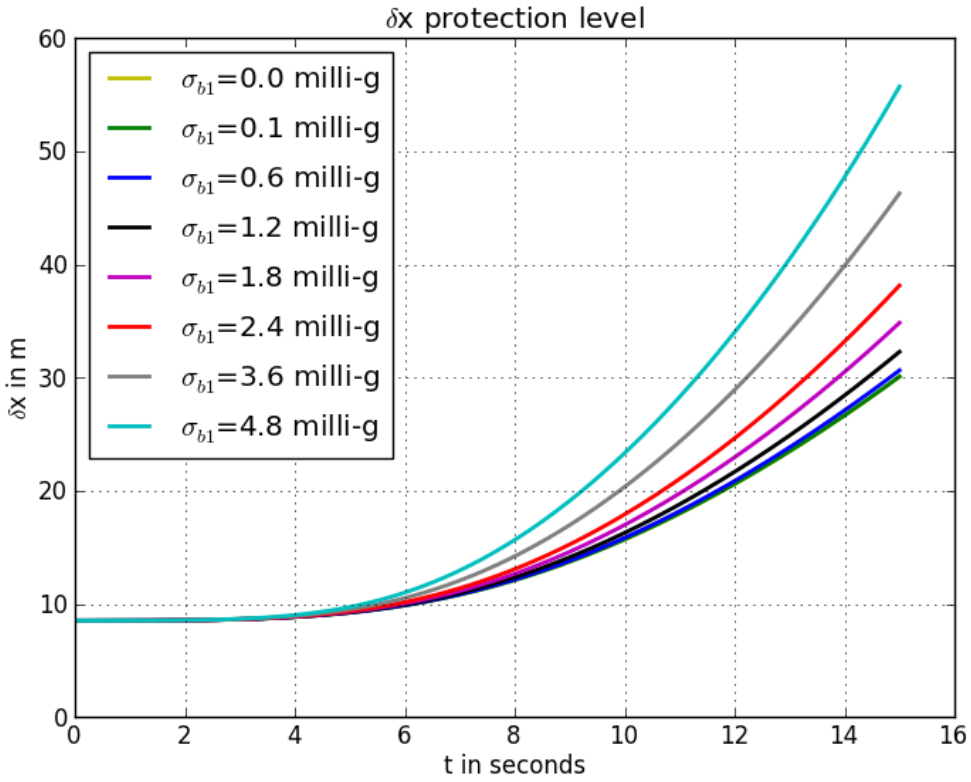

Figure 5.11.: sensitivity of the protection level to the standard deviation of the Gauss Markov noise

$$f(r,\theta,\phi) = f(r) = \frac{1}{2\pi}\frac{1}{\sqrt{\sigma_{AT}^2+\sigma_{CT}^2+\sigma_{ZT}^2}}\exp\left\{-\frac{1}{2}r^2\right\}$$

We observe that f is only function of the radius r. To calculate the integral of f in the surface described by a circle centered at 0 and of radius $r = R$. We proceed simply by integrating f in concentric spherical shells of thickness dr and of radius r and let r variate from 0 to R. We are looking for R for which the integral of f is exactly equal to $1 - IR$. The mathematical interpretation of this problem is presented as follows:

$$\int_0^R f(r)\left(4\pi r^2 dr\right) = 1 - IR$$

$$\frac{2}{\sqrt{\sigma_{AT}^2+\sigma_{CT}^2+\sigma_{ZT}^2}}\int_0^R \exp\left\{-\frac{1}{2}r^2\right\} r^2 dr = 1 - IR$$

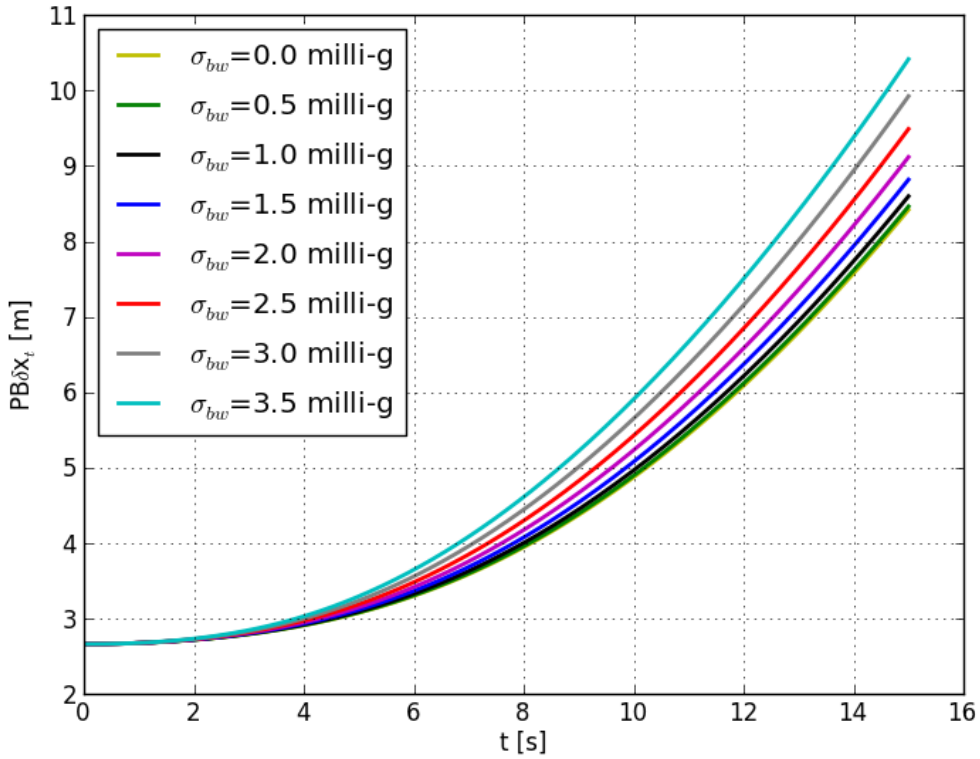

Figure 5.12.: sensitivity of the protection level to the standard deviation of the drift noise

We observe that $\exp\left\{-\frac{1}{2}r^2\right\} r^2 dr = rd\left(-\exp\left\{-\frac{1}{2}r^2\right\}\right)$.

$$\frac{2}{\sqrt{\sigma_{AT}^2 + \sigma_{CT}^2 + \sigma_{ZT}^2}} \int_0^R rd\left(-\exp\left\{-\frac{1}{2}r^2\right\}\right) = 1 - IR$$

$$\frac{2}{\sqrt{\sigma_{AT}^2 + \sigma_{CT}^2 + \sigma_{ZT}^2}} \left\{\left[-r\exp\left\{-\frac{1}{2}r^2\right\}\right]_0^R + \int_0^R \exp\left\{-\frac{1}{2}r^2\right\} dr\right\} = 1 - IR$$

$$\frac{2}{\sqrt{\sigma_{AT}^2 + \sigma_{CT}^2 + \sigma_{ZT}^2}} \left\{-R\exp\left\{-\frac{1}{2}R^2\right\} + \frac{\sqrt{\pi}}{2}\mathrm{erf}\left(R\right)\right\} = 1 - IR$$

where erf is the error function.

we define the normalizing factor k such that when R tends to ∞, the integral of the density should be equal to 1.

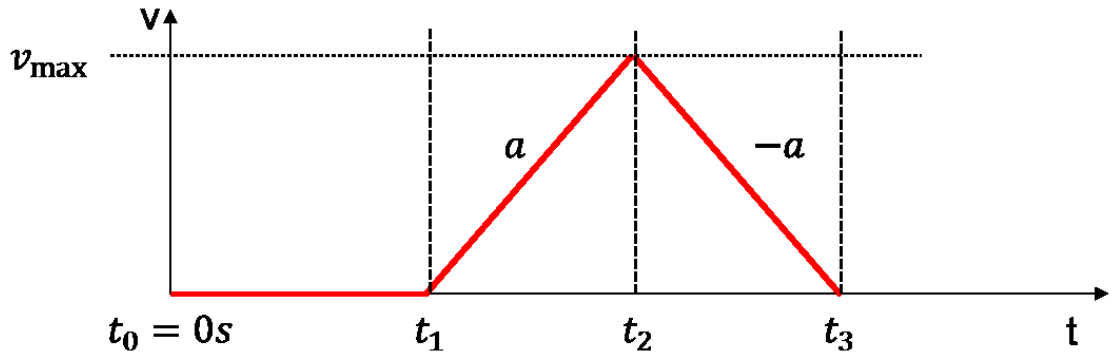

Figure 5.13.: Velocity scenario of a train moving on rectilinear tracks. The scenario starts at t_0, start accelerating at t_1 and decelarating at t_2 to stop again at t_3. We assume the same constant absolute acceleration and deceleration

$$\frac{2k}{\sqrt{\sigma_{AT}^2 + \sigma_{CT}^2 + \sigma_{ZT}^2}} \frac{\sqrt{\pi}}{2} = 1$$

We therefore have $k = \frac{\sqrt{\sigma_{AT}^2+\sigma_{CT}^2+\sigma_{ZT}^2}}{\sqrt{\pi}}$.

The radius corresponding to the the integrity risk IR is therefore solution of the algebraic equation:

$$\frac{2}{\sqrt{\pi}} \left\{ -R \exp\left\{ -\frac{1}{2} R^2 \right\} + \frac{\sqrt{\pi}}{2} \mathrm{erf}\,(R) \right\} = 1 - IR$$

$$\mathrm{erf}\,(R) - \frac{2R}{\sqrt{\pi}} \exp\left\{ -\frac{1}{2} R^2 \right\} = 1 - IR$$

The integral of the trivariate density function over the surface delimited by the ellipsoid with semi axis ($R\sigma_{AT}$,$R\sigma_{CT}$,$R\sigma_{ZT}$) is equal to $1 - IR$.

In fact an infinite number of surfaces of integration provides the same result. We choose the smallest one or the one corresponding to an iso-density. Fig. 5.16Fig. 5.17 show the 3 D protection bounds using the same integrity risk (10^{-7}) of an accelerating and decelerating train. the cross track and the radial track (CT and ZT) have no acceleration and no speed. All 3 accelerometers have the same characteristics. In the along track, we simulate an acceleration of 1.5 ms^{-2} during 40 seconds and in the second plot we simulate a break of -1.5 ms^{-2} and an initial speed such that after 40 seconds of constant brake, the train stops.

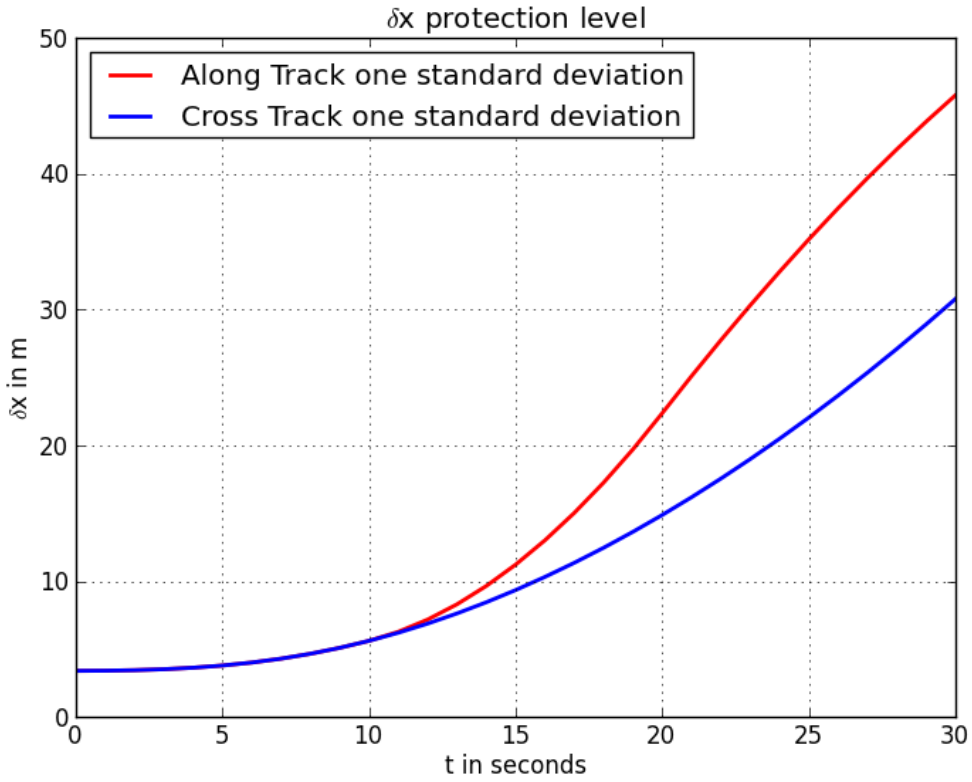

Figure 5.14.: Comparison of the along and cross track semi axis with respect to time using a scaling factor $s_f = 0.1$ (see 5.1) and an integrity risk of $IR = 10^{-7}$

5.4. Integrity assessment of a generalized non-linear filtering problem

5.4.1. General Filtering Equation

Let's assume that the signal process is described (in continuous form) using the following stochastic differential equation:

$$dX_t = b(X_t)dt + \sigma(X_t)dB_t \tag{5.28}$$

where X_t is the state vector of a continuous time stochastic process states (d-dimensional diffusion process). dB_t is a vector of continuous time elementary Brownian motions.
b and σ are deterministic functions of the state X_t and t in a very general case. The observation process is an m-dimensional diffusion process satisfying the following

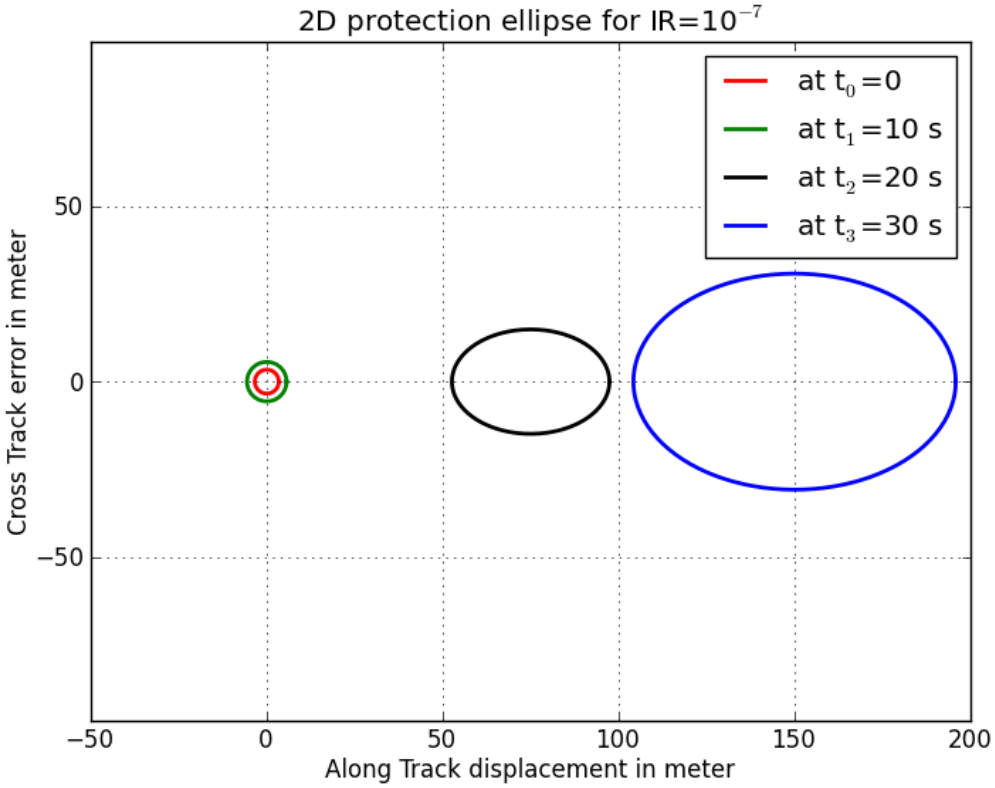

Figure 5.15.: Evolution of the 10^{-7}quantile with respect to time for a given dynamic scenario

stochastic differential equation:

$$dZ_t = h(X_t)dt + \eta(X_t)dW_t \tag{5.29}$$

This form is the incremental form of the observation equation. This representation is preferred for an easier mathematical resolution of the filtering problem, in that case the measurement equation is a stochastic differential equation for which we can use the usual formalism of Itō or Stratanovich calculus. Furthermore this form doesn't add or loose information with respect to its usual snapshot form. Solving the filtering problem is equivalent to find the best estimate X_t based on the measurements up to time t. The measurements or the information gathered up to time t generate a $\sigma-$algebra $\mathcal{G}_t = \sigma\left(Z_s, 0 \leq s \leq t\right)$. $\mathcal{G}_t$ is called a filtration and we have the following property: $\mathcal{G}_s \subseteq \mathcal{G}_t$ for any $0 \leq s \leq t$ (the quantity of information is increasing with the measurements).

Under bounding and Lipschitz conditions on the functions $\{b, h, \sigma, \eta\}$, the filtering problem has a unique solution (see for example [Xio08] in Chapter 6.4). This solution is the "best" estimate of the state given the available information up to time

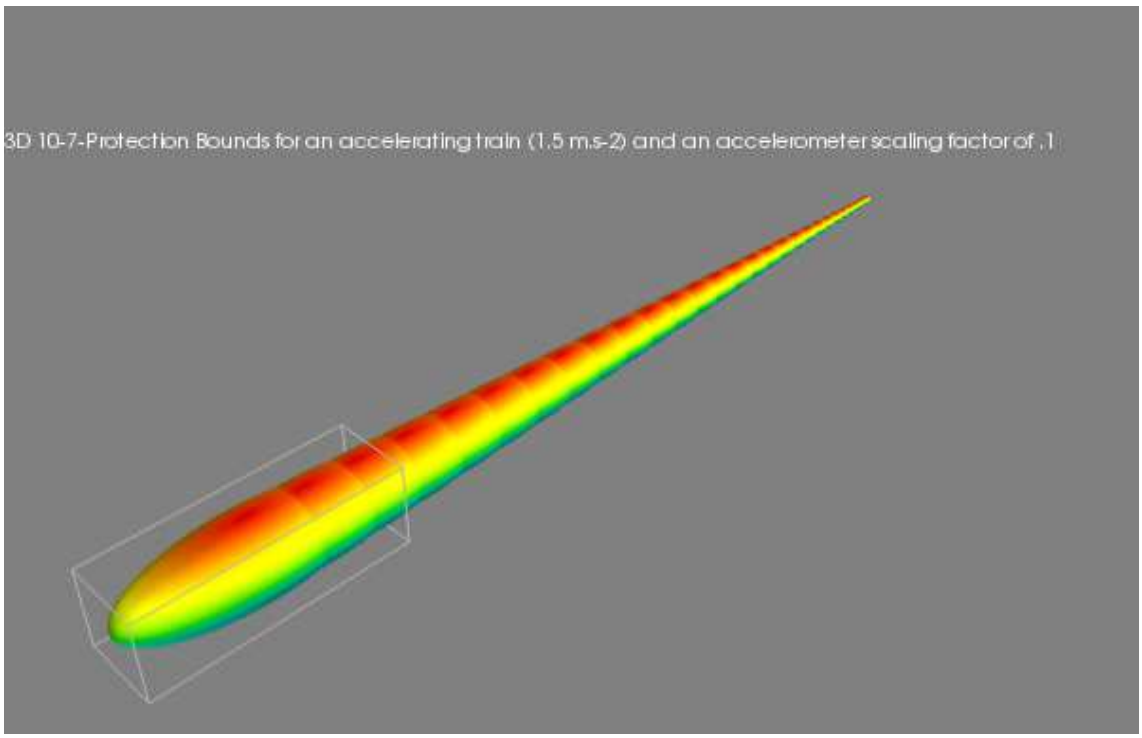

Figure 5.16.: Evolution of the 10^{-7}quantile with respect to time for an accelerating train

t. "Best" in the sense of minimizing the least square error. If $\hat{X}_t$ represents this solution, $\hat{X}_t$ is $\mathcal{G}_t-$measurable and among all $\mathcal{G}_t-$measurable random processes it is the one that minimize the least square error.
It is proven that the best estimate for X_t is $E[X_t|\mathcal{G}_t]$, which is the conditional expectation of X_t given the available information $\mathcal{G}_t$ see for example [Xio08] or [Oks07]. Let π_t being the conditional probability distribution of X_t given $\mathcal{G}_t$, we have $E[X_t|\mathcal{G}_t] = \langle \pi_t, 1 \rangle$, where $\langle \pi_t, 1 \rangle$ is the integral of X_t with respect to the probability measure π_t. If we are interested in the best estimate of a function of the random process $f(X_t)$ where f is a continuous bounded function. Depending on the properties of f, if we call $\hat{X}_t = E[X_t|\mathcal{G}_t]$, the relation $\widehat{f(X_t)} = f(\hat{X}_t)$ is only true if f is linear with respect to X_t.
The following relation gives the relation between the conditional probability measure (the distribution we want to estimate) and the expectation with respect to the probability measure of X_t.

$$E[f(X_t)|\mathcal{G}_t] = \langle \pi_t, f \rangle \tag{5.30}$$

The filtering problem consists of determining the conditional probability distribution π_t with respect to any function of the signal process X_t given the measurements up to t ($(Z_s)_{\{0 \leq s \leq t\}}$). After applying consecutively the Girsanov theorem (for change of probability measures), the Radon-Nickodym derivative and the pendant of the

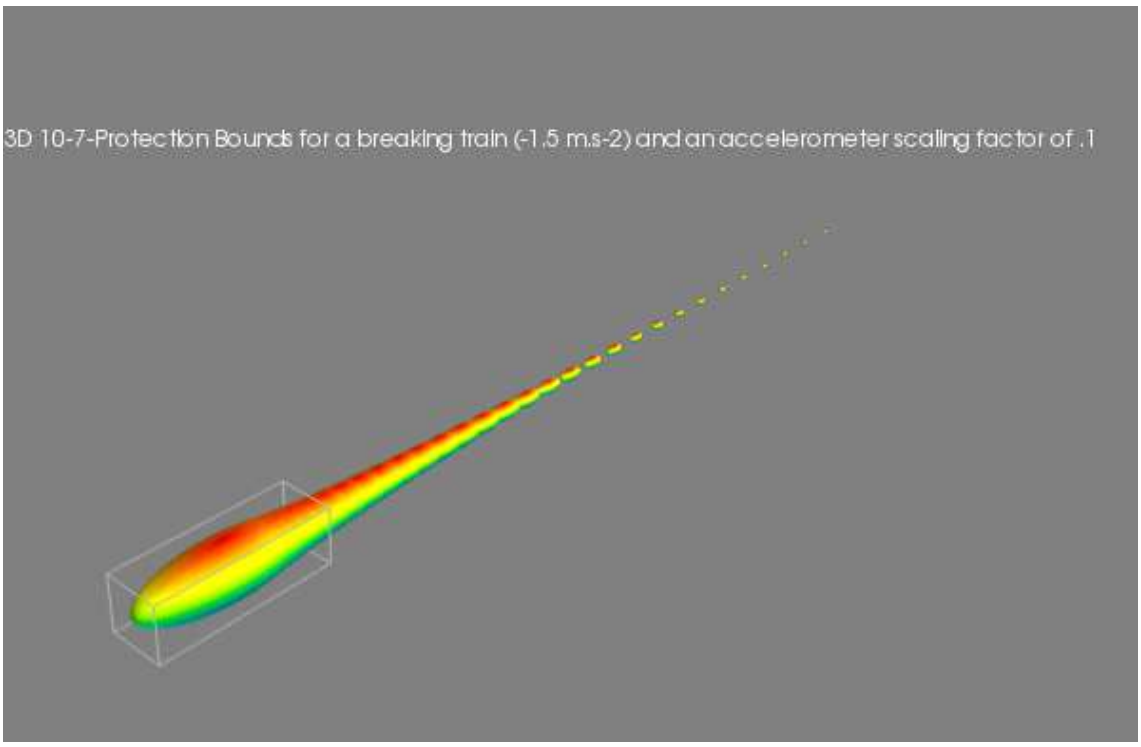

Figure 5.17.: Evolution of the 10^{-7}quantile with respect to time for a braking train

Bayesian formula in the filtering theory (the Kallianpur-Striebel formula), we end up with the normalized filter solution π solution of a stochastic partial differential equation (The Kushner equation). A detailed description of the approach can be found in Chapter 5 of [Xio08]. For simplification, we consider f being the identity function, σ and η independent from X_t and t.

$$d\pi = L\pi dt + \pi \left(h - E\left[h\right]\right)^T \left(\eta^T \eta\right)^{-1} \left(dz - E\left[h\right] dt\right) \tag{5.31}$$

In this equation we omitted (X_t) for simplification of the equation (we wrote h rather than $h\left(X_t\right)$ for example and π rather than $\pi(t,x)$). The L operator is the generator of the diffusion process solution of the state equation (not conditioned by the measurements). The expression of this diffusion process for any continuous bounded function π in the set $[0,t\ ) \times \mathbb{R}^d$ with d being the dimension of the state vector can be expressed as follows (keeping the same notations as in Equation (5.28) and (5.29))

$$L\pi\left(x\right) = \sum_i b_i\left(x\right) \frac{\partial \pi}{\partial x_i} + \frac{1}{2} \sum_{i,j} \left(\sigma\sigma^T\right)_{i,j}\left(x\right) \frac{\partial^2 \pi}{\partial x_i \partial x_j}$$

In this equation, we dropped the time as it is a partial differential equation with respect to state variables. In Equation (5.31), the term $dz - E\left[h\right] dt$ is the infinitesimal innovation process, which is the quantity of information gained from the new

measurements with respect to the prediction. If the measurement equation is perfectly modeled, the expectation of the innovation process is zero (no miss-modeling of the measurement equation). In the next section, we are considering a possible bias as a fault mode and we will see how the filter reacts in different miss-modeling cases.

5.4.2. Overbounding Concept of the Filtering Equation

For safety of life applications, it is important to bound the errors with an acceptable probability of hazardous misleading information (integrity risk). For fault free measurements whose error distribution can be bounded using a Gaussian distribution and considering the bias free models for both the state and the measurement equations describing the nominal case, the integrity risk quantile of the over-bounding distribution is the inflated Gaussian over-bounding state and measurement noise. In the filtering equation, it would correspond to the nominal equations with noise inflation for both the signal and the measurement models.
Additionally to the fault free mode and Gaussian over-bound, we also need to over-bound the non-linearity of both the state and the measurement equation using linear functions. The aim of this procedure is from the general measurement-conditioned probability density function solution of the Kushner equation (5.31), to find a family of over-bounding probability density functions solutions of a family of linear form of the Kushner equation (Kalman-Bucy filter equation). Each of these linearized filtering equations represent a fault mode equations, whose solution is the fault mode conditioned probability density functions. These fault modes comprises miss-modeling of the measurement equations and abnormal behavior of the sensors provided the measurements. For the state propagation equation, this fault modes corresponds to miss-modeling of the state equation including the level of state noise. In this section, we allow non linear and non Gaussian behavior of the true state and measurement equations, but we limit the over-bounding equations for both measurements and state to linear processes and to Gaussian over-bounding distributions for both measurement and state equations. This will allow us to apply a Kalman filter for each fault mode.
We assume that the fault modes considered are mutually independent.
The first principle adopted here is to define a fault mode as being a parameter of the deterministic part of the models kept at its maximum value keeping the other parameters to their nominal values.
The fault tree assumption considered here is that each fault mode is equiprobable to occur with an a-priori probability of being in any of these fault modes being 0.1% of the total risk. The a-priori probability of being in the fault free case is such that the sum of all fault free and fault modes probabilities is equal to one.
These figures can be updated taking into account a permanent monitoring of the probability of occurrence. This approach follows the integrity concept assumptions usually adopted in the satellite navigation.

5.4.3. Example of Train Localization

We assume here the problem of localizing a train in his tracks. We assume in a first approach that the tracks coordinates are known and that at a given epoch, the position of the train is perfectly known (for example when it is stopped at a reference point at a train station). In the following we assume all variables, parameters or equations being related to the over-bounded variables, parameters or equations.
Additionally we consider the discrete time approach of the over-bounding filtering equations.

We consider the following state vector:

- $x_k^{(0)}$ being the position of the train along the track (curvilinear abscissa),
- $x_k^{(1)}$ being the velocity of the train along the track (curvilinear velocity),
- $x_k^{(2)}$ being the along track acceleration,
- $x_k^{(3)}$ being the drift of the accelerometer modeled as a first order Gauss Markov process.

And we consider the following measurement vector:

- $z_k^{(0)}$ being the 2 dimensional position provided by a GNSS receiver and projected in the track,
- $z_k^{(1)}$ being the velocity provided by the same GNSS receiver and also projected in the direction of the train,
- $z_k^{(2)}$ being the along track acceleration provided by the along track accelerometer.

We assume in our study, that the train is moving in a perfectly horizontal plane with the gravity vector being normal to the plan of motion. We also assume that the miss-alinement errors are negligible. This could be considered covered by the over-bounding concept presented in the fault modes.
The state equation considers a constant along track acceleration with an additional noise process over-bounded by a centered white Gaussian noise. The speed and the position along the track does not assume any additional noise, except the integrated acceleration noise.

$$X_{k+1} = FX_k + \Sigma\epsilon_k \tag{5.32}$$

with

$$F = \begin{pmatrix} 1 & dt & \frac{dt^2}{2} & 0 \\ 0 & 1 & dt & 0 \\ 0 & 0 & 1 & 0 \\ 0 & 0 & 0 & 1 - \frac{dt}{\tau_3} \end{pmatrix}$$

$$\Sigma = \begin{pmatrix} \frac{dt^2}{2}\sigma_2 & 0 \\ dt\sigma_2 & 0 \\ \sigma_2 & 0 \\ 0 & \sigma_3 \end{pmatrix}$$

and

$$\epsilon_k = \begin{pmatrix} dB_{2,k} \\ dB_{3,k} \end{pmatrix}$$

We consider the driving noise of the Gauss Markov Process $dB_{3,k}$ being independent from the state noise $dW_{2,k}$. The measurement equation in time discrete form is as follows:

$$Z_k = HX_k + \eta\nu_k \tag{5.33}$$

with

$$H = \begin{pmatrix} 1 & 0 & 0 & 0 \\ 0 & 1 & 0 & 0 \\ 0 & 0 & 1+s_f & 1 \end{pmatrix}$$

In the sensor fault mode scenarios, we introduce an additive bias in the measurement equation:

$$Z_k = HX_k + B + \eta\nu_k \tag{5.34}$$

with

$$B = \begin{pmatrix} bx^{(0)} \\ bx^{(1)} \\ b_0 \end{pmatrix},$$

with $bx^{(0)}$, $bx^{(1)}$, b_0 being a bias in the measured position, a bias in the measured velocity and the null-shift of the along track accelerometer, respectively. The latter is considered as a bias in the measured along track accelerometer.

$$\eta = \begin{pmatrix} \sigma_{z0} & 0 & 0 \\ 0 & \sigma_{z1} & 0 \\ 0 & 0 & \sigma_{z2} \end{pmatrix}$$

and

$$\nu_k = \begin{pmatrix} dW_{0,k} \\ dW_{1,k} \\ dW_{2,k} \end{pmatrix}$$

In this model, b_0 corresponds to the null-shift of the along track accelerometer. If well calibrated, this null-shift should be kept to zero or to a value close to zero. $bx^{(0)}$ resp. $bx^{(1)}$ is a bias in the measurement of the GNSS position resp. velocity. These parameters are going to be considered in the fault mode conditions for the establishment of the along track protection levels. s_f corresponds to a scaling factor modeling a proportional error to the true acceleration.
The non-linearity of the measurements is implicitly present in the projection of the position and measurement in the track as described in Fig. 5.18 and Fig. 5.19.

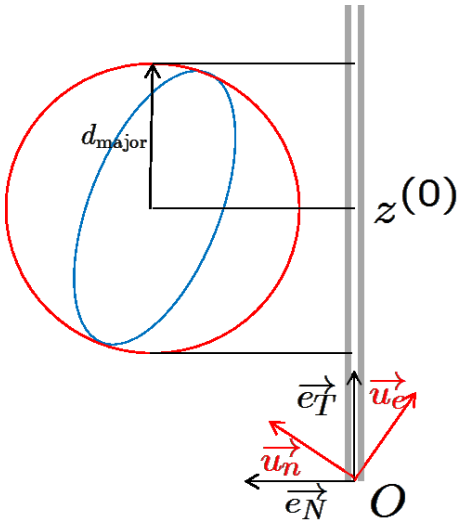

Figure 5.18.: Linear projection of a GNSS position along the track. The lines of projection are parallel. In this case the Gaussian property of the distribution is kept in the new support.

The non linear projection introduces in the along track direction under certain conditions an inflation of the area of uncertainty (see Fig. 5.19). But we can consider that the projection is locally linear depending on the curvature and the location of the error ellipsoid with respect to the track. Furthermore the linear approximation preserve the Gaussian distribution of the error along the track. This approximation is available if the radius of the track curvature is sufficiently large with respect to the distance separating the position distribution provided by GNSS and the track as illustrated in Fig. 5.20.

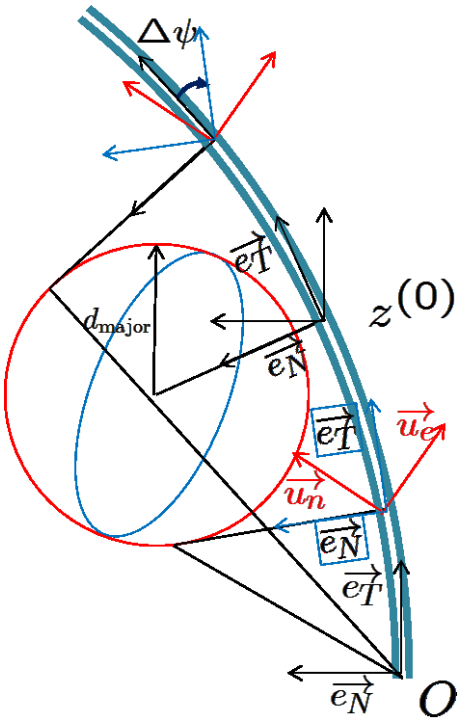

Figure 5.19.: Non Linear projection of a GNSS position distribution in the along the track direction. The protection level of the position error delimited by the red circle projects in curved tracks without preserving the Gaussian nature of the distribution. The distribution remains symmetric though

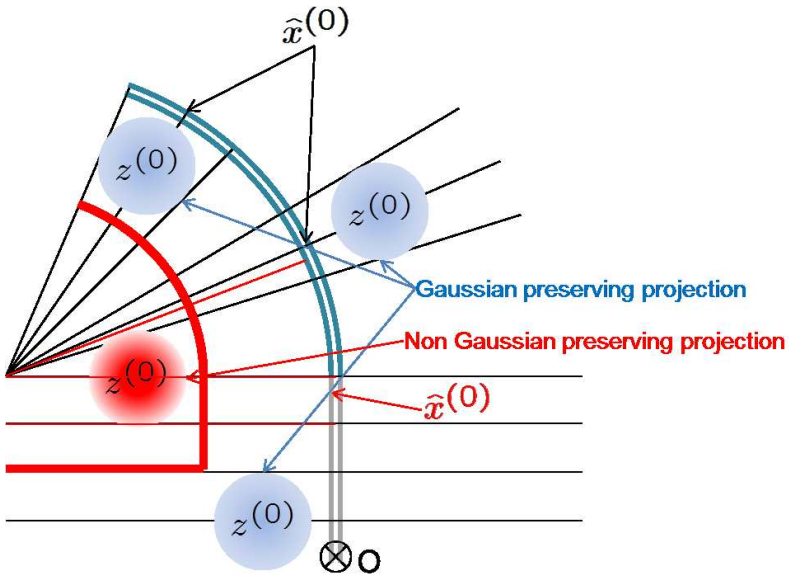

Figure 5.20.: Areas of linear and Gaussian preserving projection. The blue disks represents the areas for which the projections are considered as Gaussian preserving: $E\left[\mathcal{P}\left(Z^{(0)}\right)\right] = \mathcal{P}\left(E\left[Z^{(0)}\right]\right)$ and $V\left[\mathcal{P}\left(Z^{(0)}\right)\right] = \mathcal{P}\left(V\left[Z^{(0)}\right]\right)$. The red area is the area of non preserving Gaussian distribution. The projection of the position of a user in the along track direction when the measurement is inside the red area will be non Gaussian. Outside the red area, the projection in the along track direction will preserve the Gaussian nature of the distribution.

5.4.4. Estimation process of the state vector overbound

The overbounding process being solution of a linear filter with white Gaussian noise, the Kalman-Bucy theory applies and we can derive the usual iterative algorithm: The predicted state:

$$\hat{X}_{i+1|i} = F\hat{X}_{i|i} \tag{5.35}$$

The prediction estimate covariance is:

$$P_{i+1|i} = FP_{i|i}F^T + Q \tag{5.36}$$

Expression of the innovation:

$$\tilde{Y}_{i+1} = Z_{i+1} - H\hat{X}_{i+1|i} \tag{5.37}$$

and the innovation covariance:

$$S_{i+1} = HP_{i+1,i}H^T + R \tag{5.38}$$

The Kalman gain in the very classical form:

$$K_{i+1} = P_{i+1,i}H^T S_{i+1}^{-1} \tag{5.39}$$

Updated state estimate:

$$\hat{X}_{i+1|i+1} = \hat{X}_{i+1|i} + K_{i+1}\tilde{Y}_{i+1} \tag{5.40}$$

and the updated estimate covariance matrix:

$$P_{i+1|i+1} = (I - K_{i+1}H)\, P_{i+1|i} \tag{5.41}$$

5.4.5. Along Track Protection Levels

Let us describe each fault mode (FM) by a set of model parameters. We keep one parameter to the maximum and the others remain to their nominal values. Each fault mode has an a-priori probability of occurrence based on the fault tree allocation. If we call n the fault mode identification, we have a corresponding k_n inflation factor of the Gaussian overbound corresponding to the allocated probability of hazardous misleading information for the mode n. We call $\hat{X}_{i+1|i+1,n}$ the estimation of the state vector overbound given the measurements up to (and including) epoch $i+1$ and given the parameter set of the fault mode n. We define then the protection levels as follows:

$$\begin{aligned}\mathrm{XPL}_{i+1|i+1,n} =& E\left[\hat{X}_{i+1|i+1,n}\right] + \\ & k_n\sqrt{\det V\left[\hat{X}_{i+1|i+1,n}\right]}\end{aligned} \tag{5.42}$$

This equation is too general for our problem, because it is here assumed a protection level for the overall state vector and the k_n coefficient corresponds to the state vector quantile and not only the along track position quantile which is the case we want to focus on in this section. The along-track protection level (APL) is the $P_{\text{HMI},n}$ quantile of the along track position for the fault mode n.

$$\begin{aligned}\text{APL}_{i+1|i+1,n} =& E\left[\hat{x}^{(0)}_{i+1|i+1,n}\right] + \\ & k_n\sqrt{V\left[\hat{x}^{(0)}_{i+1|i+1,n}\right]}\end{aligned} \tag{5.43}$$

In these equations E, resp. V represent the expectation resp. the variance operator with respect to the probability measure along the track.
In the following we are going to express the iterative form of these expectation and variance. Let's start with the variance:
By definition and keeping the same notation as before,

$$\begin{aligned}V\left[\hat{X}_{i+1|i+1,n}\right] &= P_{i+1|i+1} \\ &= (I - K_{i+1}H)\,P_{i+1|i} \\ &= (I - K_{i+1}H)\left(FP_{i|i}F^T + Q\right) \\ &= (I - K_{i+1}H) \\ &\qquad \left(FV\left[\hat{X}_{i|i,n}\right]F^T + Q\right)\end{aligned} \tag{5.44}$$

The variance is expressed in an iterative way and depends on the parameter of the fault mode and on the initial covariance.
In the same way, we can express the expectation of the estimate over-bound:

$$E\left[\hat{X}_{i+1|i+1,n}\right] = E\left[\hat{X}_{i+1|i}\right] + K_{i+1}E\left[\tilde{Y}_{i+1}\right] \tag{5.45}$$

$$\begin{aligned}E\left[\hat{X}_{i+1|i+1,n}\right] =& (F - K_{i+1}HF)\,E\left[\hat{X}_{i|i,n}\right] + \\ & K_{i+1}E\left[Z_{i+1|n}\right]\end{aligned} \tag{5.46}$$

In the expectation and variance equations, all matrices are conditioned by the fault mode considered. For clarity reason, we did not mentioned the index n everywhere. In the expectation equation, the last term of the right member represent the eventual biases that the sensor may introduce.
In the measurement equation of the filter over-bound, we had introduced a vector B corresponding to the eventual bias in the measurement equation. Assuming that the user does not know that the measurement equation introduces a bias, this bias is not corrected by the filter and is just attenuated by the Kalman gain (if the Kalman gain is decreasing with time).

$$E\left[\hat{X}_{i+1|i+1,n}\right] = (F - K_{i+1}HF)\, E\left[\hat{X}_{i|i,n}\right] + K_{i+1}B \tag{5.47}$$

5.4.6. Results using a simulated scenario

In this section, we show the results of our system we described above. That is we introduce the applied simulation scenario and discuss the corresponding protection level envelop. Moreover, we propose our curvature change detection and monitoring scheme.

5.4.6.1. Scenario

We have set for each parameter a maximum (inflated) and nominal value. The Tab. 5.1 summarizes this setup.

	Scenario			**Mode**
Parameters	**FF Nom.**	**FF Inflated**	**FM Inflated**	**ID**
σ_2 [m/s^2]	$1.7 \cdot 10^{-3}$	$5 \cdot 10^{-3}$	$5 \cdot 10^{-3}$	0
σ_3 [m/s^2]	$1.7 \cdot 10^{-3}$	$5 \cdot 10^{-3}$	$5 \cdot 10^{-3}$	0
$\sigma_{z0}[m]$	2	10	10	0
σ_{z1} [m/s]	$5 \cdot 10^{-2}$	$1.5 \cdot 10^{-1}$	$1.5 \cdot 10^{-1}$	0
σ_{z2} [m/s^2]	$9.81 \cdot 10^{-3}$	$2.94 \cdot 10^{-2}$	$2.94 \cdot 10^{-2}$	0
$bx^{(0)}$ [m]	0	0	± 2	$1\pm$
$bx^{(1)}$ [m/s]	0	0	$\pm 5 \cdot 10^{-2}$	$2\pm$
b_0 [m/s^2]	0	0	$\pm 5 \cdot 10^{-3}$	$3\pm$
s_f	0	0	$\pm 10^{-2}$	$4\pm$

Table 5.1.: Fault free and faulty scenario parameter definition

The protection levels are calculated in the following way: The global integrity risk budget is 10^{-7}. We consider that the probability to be in the fault free mode is 0.991 and the a-priori probability to be in any of the other fault modes is 10^{-3} for the simulation period considered (in our case 100 seconds). Considering the fault modes mutually independent and neglecting the probability of multiple faults as a first assumption. The integrity budget associated to each fault mode is therefore $10^{-7}/P_{occ,i}$ with $P_{occ,i}$ being the probability of occurrence of the fault mode i with fault mode 0 being by convention the fault free mode. The protection level of the

along track position of the train is the maximum protection level among all modes. This maximum is calculated for each epoch.
The dynamic scenario chosen are as follows: The train has a constant speed of 40 m/s, starting at $x_0^{(0)} = 0$ except for the fault mode 4+ and 4- (corresponding to maximum scaling factor for the accelerometer as described in Tab. 5.1) for which we assume a deceleration of -1.2 m/s^2.

5.4.6.2. Protection Level Envelop

The protection levels are calculated as described earlier. Each mode provide a protection level (in fact two functions of time one representing an upper bound and the other the lower bound). The inflation factor is function of the integrity risk allocated to its mode. Assuming the modes independent from each others and assuming only one fault mode at a time, we can derive a global protection level based on the envelop of all these upper bounds.

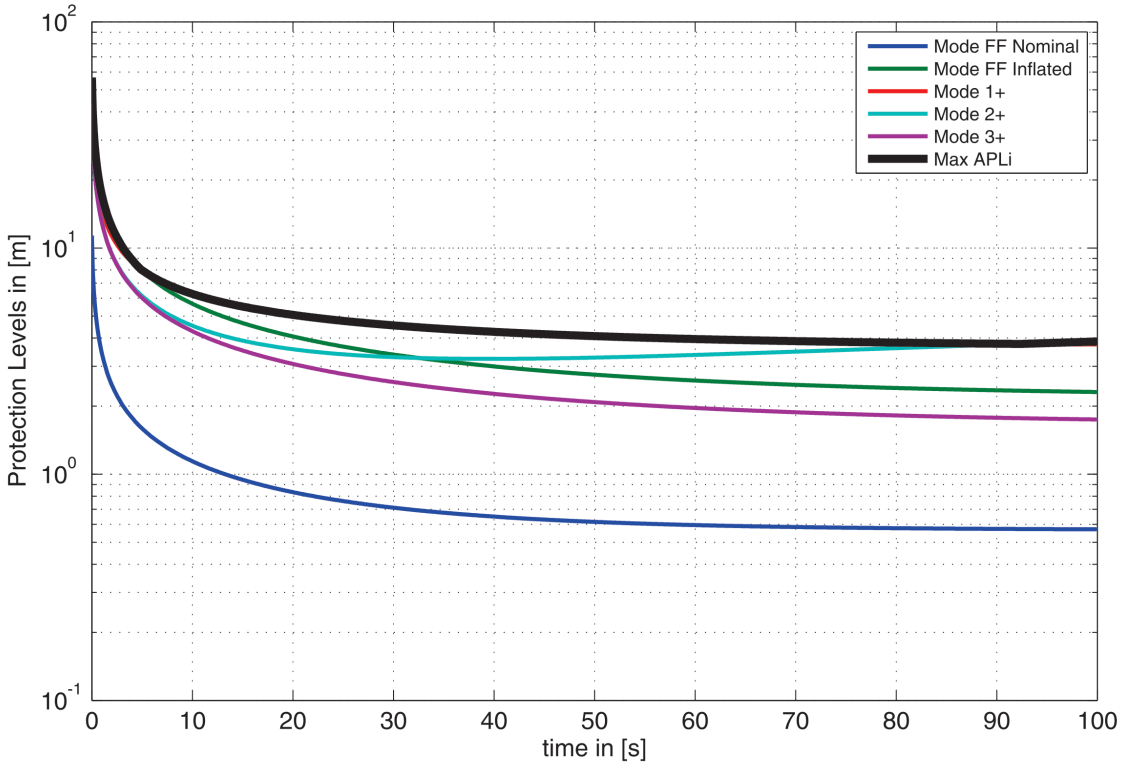

Figure 5.21.: Protection level for each failure mode including the fault free mode. The global protection level is the maximum between all individual protection levels for each time step. This is the upper envelop of all protection levels

In Fig. 5.21 we represented for selected fault modes the position protection level. The envelop of the protection levels is not driven by one mode but by different

modes depending on the time sequence considered. In this example, 3 phases have been observed. In the first part of the simulations, the protection level is driven by the fault free inflated mode (mode 0), the second time period is dominated by the bias mode in the position (mode 1+) and at the very end of the 100 seconds simulations, the bias in the velocity is dominant.
This analysis is based on the set of parameters chosen which may not reflected the general behavior of a filter.

5.4.6.3. Combination With a Curvature Change Detector

In the following section, the physical assessment of the track curvature is introduced and three different methods are outlined. As we already stated in [BGH+13a], we define the curvilinear abscissa $s(t)$ as a function of the length of the arc represented by the track from a reference position to a current point. The velocity vector of the train is $\mathbf{v} = \dot{s}\mathbf{e}_{AT}$ and the acceleration vector is:

$$\mathbf{a} = \frac{d\mathbf{v}}{dt} = \frac{d\left(\dot{s}\mathbf{e}_{AT}\right)}{dt} = \ddot{s}\mathbf{e}_{AT} + \dot{s}\dot{\mathbf{e}}_{AT} \tag{5.48}$$

$\mathbf{e}_{AT}$ and $\mathbf{e}_{CT}$ are the along track and cross track unit vectors. In this expression and in the rest of this chapter we drop the time t for simplification. The dot above variables always means the derivative of the given variable with respect to time. During dt, the point M moved from s to $s + ds$ and the unit along track vector has rotated with the angle $d\psi$. This drives to the following relation:

$$\dot{\mathbf{e}}_{AT} = \dot{\psi}\mathbf{e}_{CT}$$

Observing that the acceleration vector lies in the osculating plan defined by $(\mathbf{e}_{AT}, \mathbf{e}_{CT})$, we can decompose the acceleration into 2 components: and taking the same notation as for the unit vectors, we have:

$$\mathbf{a}(t) = a_{AT}\mathbf{e}_{AT} + a_{CT}\mathbf{e}_{CT},$$

with

$$\begin{aligned} a_{AT} &= \ddot{s}, \\ a_{CT} &= \dot{s}\dot{\psi}. \end{aligned}$$

We observe that $\dot{s} = r\dot{\psi}$, so we have the following expression:

$$a_{CT} = r\dot{\psi}^2, \tag{5.49}$$

with r being the local radius of the trajectory.

We observe that Equation (5.49) can be expressed in terms of $\dot{s}$ rather than $\dot{\psi}$ and observing that $\|\mathbf{v}\| = \dot{s}$, we have:

$$a_{CT} = \frac{\|\mathbf{v}\|^2}{r} \tag{5.50}$$

There is a relation between the speed of the train, the cross track acceleration and the heading rate for a given trajectory.

We have the following relations:

$$a_{CT} = r\dot{\psi}^2 = \frac{\|\mathbf{v}\|^2}{r} \tag{5.51}$$

In this equation, we can directly sense the cross track acceleration a_{CT}, the heading rate $\dot{\psi}$ and indirectly the velocity of the train $\mathbf{v}$ (integral of the along track acceleration). This is an important a-priori information that can be used in a test statistic to decide which direction the train has taken after a switch. By convention we will choose to work with the curvature rather than with r. Let $\kappa = 1/r$ the relation above can be written as follows:

$$a_{CT} = \frac{\dot{\psi}^2}{\kappa} = \kappa \|\mathbf{v}\|^2 \tag{5.52}$$

In this equation, κ can be obtained in three different ways:

$$\text{Method 1: } \kappa_1 = \frac{\dot{\psi}^2}{a_{CT}} \tag{5.53}$$

$$\text{Method 2: } \kappa_2 = \frac{\left|\dot{\psi}\right|}{\|\mathbf{v}\|} \tag{5.54}$$

$$\text{Method 3: } \kappa_3 = \frac{a_{CT}}{\|\mathbf{v}\|^2} \tag{5.55}$$

All three methods can also be used in a non-stationary scenario, i.e., while the train is moving. Otherwise the curvature determination might be not defined. That is if $a_{CT} = 0$, κ_1 is undefined and if $\|\mathbf{v}(t)\| = 0$, κ_2 and κ_3 are undefined.

We analyze the resulting test statistic based on the three curvature determination methods. To compute $\kappa_i, i = 1, \ldots, 3$, we need the heading rate, along-track and cross-track accelerations. These measurements are distorted by sensor errors. Using the Stochastic Differential Equations (SDE), we can access the error distribution of each measurement required to determine the curvature. However, the distribution of curvatures itself is not simple to derive since we have to obtain the distribution of a ratio of random variables. The resulting distribution might not be symmetric

and can be even heavy tailed. In the following, we discuss the expected behavior of the test statistics.

Naturally, if all measurements would be error-free, all three curvature computations would deliver the same result $\kappa_1 = \kappa_2 = \kappa_3$. But due to the randomness of the measurements of $a_{CT}(t)$, $\dot{\psi}(t)$ and $\mathbf{v}(t)$, the obtained curvatures are not equal (random realization) and not equal in distribution sense.

First test κ_1: The measurements of this test can be directly observed, so no integration of the measurements is required. However, we can see that if the curvature of the path is zero, i.e., the track is straight, the numerator will take positive random values following a χ^2 distribution and the denominator will take values centered at 0. This induces fat tails in the distribution of κ_1. Consequently, it might be not very promising to use this method for the hypothesis test when the curvature is very small.

Second test κ_2: Here, we observe a ratio between a normally distributed random variable and a folded normal distribution (the absolute value of a normally distributed random variable). In the case of a ratio between two independent, normally distributed random variables with zero mean, the distribution of the ratio follows a Cauchy distribution. In the case of non-centered distributions, it has been demonstrated [Hin69] that the probability density function can be written as follows:

$$\begin{aligned} p_{K_2^*}(\kappa_2^*) =& \frac{\alpha \exp\left\{\frac{1}{2}\frac{\alpha^2}{\gamma} - \frac{1}{2}\xi\right\}}{\gamma^3}\frac{1}{\psi} \times \left(2\Phi\frac{\alpha}{\gamma} - 1\right) + \\ &+ \frac{1}{\gamma\pi\psi}\exp\left\{-\frac{1}{2}\xi\right\}, \end{aligned} \tag{5.56}$$

where

$$\begin{aligned} \alpha &= \frac{E\left[\dot{\psi}\right]}{V\left[\dot{\psi}\right]}\kappa_2 + \frac{E[v]}{V[v]} \\ \gamma &= \frac{1}{V\left[\dot{\psi}\right]}\kappa_2^2 + \frac{1}{V[v]} \\ \xi &= \frac{E\left[\dot{\psi}\right]^2}{V\left[\dot{\psi}\right]} + \frac{E[v]^2}{V[v]} \\ \psi &= \sqrt{V\left[\dot{\psi}\right]V[v]} \end{aligned}$$

and $\kappa_2^* = \frac{\dot{\psi}(t)}{\mathbf{v}(t)}$, and $\Phi(u) = \int_{-\infty}^{u}\frac{1}{\sqrt{2\pi}}\exp\left\{-\frac{1}{2}z^2\right\}dz$. This expression is not representing the test statistic of interest κ_2 for which no closed form could be found.

Third test κ_3: Similar to κ_2, the nominator can be seen as normal distributed random variable. However, the denominator is not only linear dependent on a folded normal distributed random variable, but quadratically dependent. Also in this case no close solution can be found.

In the remaining section, we assess the distributions of $\kappa_i, i = 1, \ldots, 3$ via Monte-Carlo simulations. As derived before we can compute the probability distributions of $a_{CT}(t)$, $\dot{\psi}(t)$ and $\mathbf{v}(t)$ depending on the quality of the sensor and on the initialization performance parameters. It must be noted that the direct use of heavy tailed distributions can generate instabilities of the test statistics. In this case, the mean and variance may not exist especially in the case of high densities around zero for the test statistics denominators.

One possibility is to exclude the samples of $a_{CT}(t)$, $\|\mathbf{v}(t)\|$ and $\|\mathbf{v}(t)\|^2$ that are close to zero, or in an interval around zero. The area to exclude using a pretest should not be too large for one reason essentially: the exclusion reduces the availability of the test statistics (for each sample falling in the excluded area, the corresponding test statistics is set as unavailable). But the closer the exclusion bounds are to zero, the wider the distribution of the test statistics and therefore the smaller the minimum detectable curvature difference (MDCD).

To classify or identify a certain curvature, we compare our computed curvature with a threshold curvature. The latter, we have determined by a standard hypothesis test algorithm (the Neyman-Pearson test). We briefly describe this algorithm in the following.

First of all, a reliable knowledge of curvature determination error behavior is required. We denoted this curvature error probability density function as $p_K(\kappa)$. We assume that this pdf is centered at the true curvature. Then we can define the distributions for two different track curvature hypotheses that we want to test. For example, after a switch a train might have two possibilities to move on, i.e., track segment one with curvature κ_a or track segment two with curvature κ_b. In order to make a decision, we have to define a threshold T against which we compare our curvature measurements. If our measurement is below the obtained threshold, we decide for H_a and if it exceeds this threshold, we decide for H_b. To find this threshold we have to consider the probability of false alarm $P_{\text{fa}} = P_K(\kappa > T|H_a)$. This probability is a system reliability requirement and accounts for the case, where we decided for H_b (indicated segment two, while hypothesis H_a was correct). Consequently, the threshold is given by

$$T = \underset{T}{\arg}\left(P_{\text{fa}} = \int_T^\infty p_K(\kappa|H_a)d\kappa\right).$$

Similar considerations can now be done for hypothesis H_b as well. A probability of missed detection, i.e., we decided for segment one while the train took segment two,

is normally defined as

$$P_{\text{md}} = P_K(\kappa < T|H_b) = \int_{-\infty}^{T} p_K(\kappa|H_b)d\kappa.$$

P_{md} is also a system reliability requirement and normally predefined by the system. So for a given P_{md}, we can find a κ_m such that

$$\kappa_m = \arg_{\kappa_m} \left(\int_{-\infty}^{T} p_K(\kappa|H_m)d\kappa = P_{\text{md}} \right),$$

where H_m is the hypothesis that the train has taken a track with curvature κ_m. Thus, we can define a minimum detectable curvature difference MDCD $= \kappa_m - \kappa_a$ for the given system requirements of false alert and missed detection. Both probabilities, P_{md} and P_{fa} indicate that a wrong decision is made. Since we consider that the hypothesis H_a while on the track b and H_b while on the track a are equally "hazardous", we set $P_{\text{fa}} = P_{\text{md}} = P_{\text{wd}}$, where wd stands for wrong decision.

The MDCD is a function of the velocity of the train. Intuitively the larger the velocity of the train, the smaller the dispersion of the test statistic.

We investigate the MDCD for each test statistic as function of the train velocity at a switch and for different IMU qualities. In the following investigations, we set our curvature of hypothesis H_a to $\kappa_0 = 10^-4$ [m^{-1}].

In Fig. 5.22), we have plotted the corresponding MDCD vs. the velocity for each test statistic and for a tactical grade IMU. Similar results for different IMU grades can be seen in [BGH$^+$13a]. The black horizontal lines represent the standard curvatures of tracks observed in Germany. Each standard line starts at $v = 0$ [km/h] and stop at the maximal allowed velocity for the corresponding curvature. The larger the curvature, the smaller the maximal allowable speed. The initial and reference curvature to be almost zero (a curvature of exactly 0 lends to a singularity). We see that the lower the velocity, the higher the MDCD. As we can see a very effective κ_2 based test statistic. In fact the combination of high accurate velocity and high performance heading gyro provides a sharp distribution and therefore a clear signature when the train change its track. For this tactical grade IMU, κ_2 and κ_3 are not crossing in the velocity range $[0 - 200]$ [km/h].

Conclusion and major contributions

In this chapter we have introduced a notion of integrity related to general filters. Our integrity bounds are based on Gaussian overbounds of both process and measurement noise. Considering different fault modes, we have proposed a new protection level envelop based on dominating individual protection levels for each fault modes. This concept considers various system integrity requirements. That is first the overall maximum allowable integrity risk that should not be exceeded by large errors,

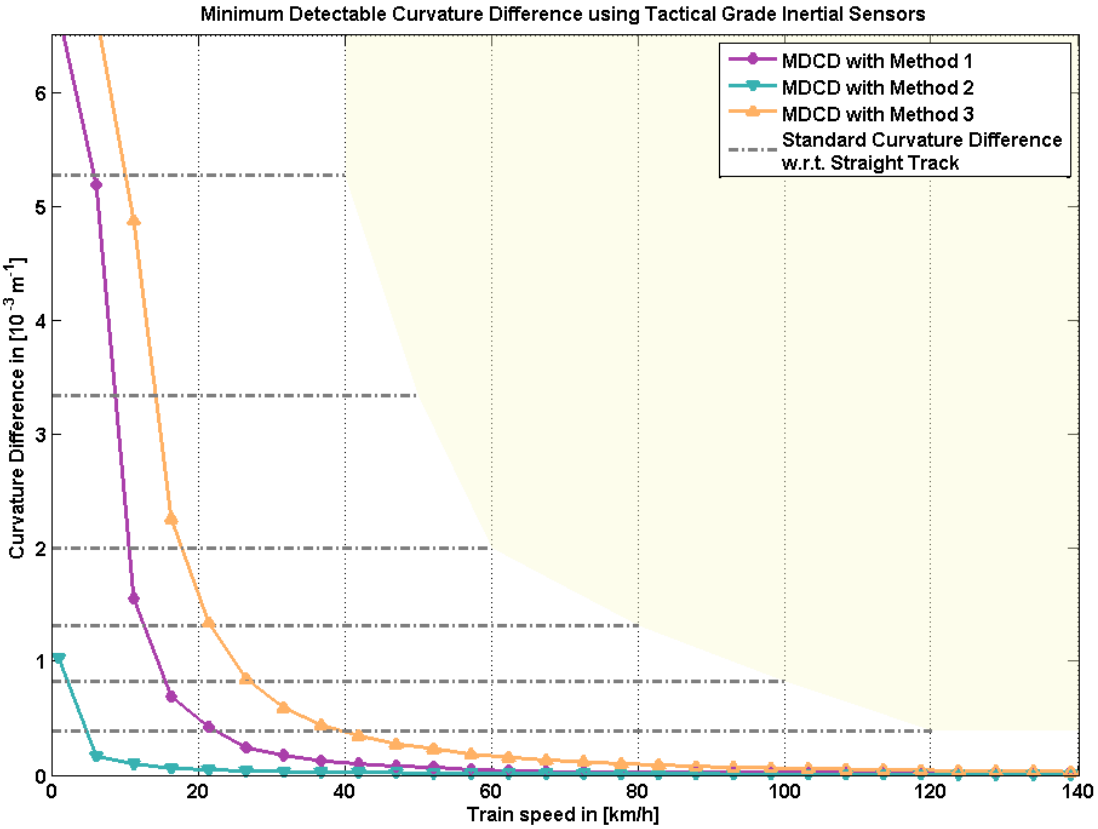

Figure 5.22.: Minimum detectable curvature difference with respect to $\kappa_0 = 10^{-4}$ $[\mathrm{m}^{-1}]$ obtained with the three different curvature determination methods κ_1, κ_2 and κ_3 vs. velocity are shown. For comparison, the standard German curvatures and their max. velocities are indicated by black lines. This plot is valid for a $P_{\mathrm{wd}} = 10^{-5}$ and using tactical grade sensors.

second the error modes to be considered and third the magnitude of each error parameter for the nominal as well as the maximum assumptions.
The fault free and the fault hypothesis are treated as independent and should build a partition of the possible events space. This allows us to apply the law of total probability and the breakdown of the total integrity risk into corresponding single fault modes risks.
The along track protection level combined with a curvature change detection and monitoring scheme completes the integrity concept for train navigation on the track network topology.
We assume dedicated sensors for the corresponding state variables and we consider the along track positioning problem and the track change detection at switch as two independent processes. In a future work, we will consider the two problems coupled in the same system of equation. Furthermore, the sensors redundancy (direct or indirect) will be considered and optimized in a global information space.

This work has been published in [GBM10, GB12, BGH$^+$13a, BGH$^+$13b, BG13, CGBR14]

6. Conclusion and Future Work

6.1. Conclusion

This thesis was addressing the complex problem of evaluating the performance of satellite navigation systems including augmentations in a broader range than just a rough estimation of an average position accuracy.

A characterization of the positioning error sources was made based on extensive analysis of measurements from different reference stations. Then, the impact of these errors in a stand alone GNSS position solution have been conducted considering single constellation single frequency scenarios and then dual frequency and dual constellation scenarios. Additionally to this study, the impact of a residual pseudo range error in the code carrier smoothing algorithm was analyzed. In this part closed forms for the smoothed error expectation and variance taking into account a band limited code and phase noise (modeled both as first order Gauss Markov processes) have been derived.

Taking into account the properties of the instantaneous pseudo range errors developed in the first part of this thesis, a tighter measure of integrity was proposed taking into account not only the magnitude of the pseudo range errors but also the spatial correlation of the errors between satellites in visibility of a receiver. This integrity assessment was derived from a stand alone GNSS position solution in the form of a generalized autonomous integrity monitoring algorithm. It appeared that the use of a generalized error model can provide smaller protection levels than a traditional RAIM algorithm for the same requirements in terms of integrity risk would do.

In a second part of the thesis, augmentations systems for GNSS were considered and their performances were analyzed. Especially the Ground Based Augmentation System was deeply investigated. For this system, not only the nominal performance were analyzed, also the ionosphere ground monitor which is responsible for detecting very rare but severe ionospheric gradients considered as threats for the integrity of the GBAS solution have been evaluated. For this special monitor, some innovative architectures have been suggested taking into account the particular form of the test statistic distribution.

In a third part of the thesis, the uncertainty propagation of an hybrid GNSS/INS was considered. For this system, a closed form for the propagation of the error expectation and variance have been developed and evaluated. A sensitivity analysis

was conducted to evaluate the impact of different parameters in the overall performances. Considering a given integrity risk, the corresponding protection surfaces are derived here again a closed form could be found under specific assumptions (translational movements only, no misalignment of accelerometers, neglected Coriolis effects...). An original approach for evaluating the inertial navigation integrity has been suggested and evaluated using typical inertial sensor performances. Based on this integrity assessment, a novel track change detector for train applications has been developed and evaluated based on simulations.

In this thesis, protection levels or their generalization form for higher dimensions called protection surfaces or protection bounds were considered as a measure of the fault free integrity. A method to evaluate these protection surfaces for different configurations including filtering has been developed.

Large errors due to the occurrence of an abnormal fault must be treated in a different way than using the protection level concepts, because their probability of occurrence does not follow a Gaussian law or may not be overbounded by a Gaussian distribution. For this type of fault, the system must provide a countermeasure in form of a fault detector. This concept have been developed in the case of large ionospheric gradients.

Integrity risks must be mitigated appropriately. In the fault free case, the aim is to reduce the volatility of the state variables without adding biases. In the faulty case when the fault is large (not covered by the fault free protection surfaces) and/or the onset probability of the fault is higher than the allocated probability for this type of fault, this fault must be detected and isolated with a probability of missed detection not larger than a specified threshold. The resulting protection surface is considered as the envelop of all individual protection surfaces. This approach was adopted to derive a faulty case protection bounds of a combined GNSS/INS solution.

6.2. Future Work

The Galileo constellation is under deployment and although the system architecture is similar to the GPS constellation, some differences exist: For example, the signal structure is different, the satellite clocks are of different nature, the satellite orbits are different and of course the monitoring and processing facilities is also different. For this new constellation, an intensive threat analysis need to be conducted and the necessary monitors need to be adapted for this specific case. Only then, this constellation will be accepted in the navigation solution of a safety critical applications. A threat analysis center should be developed in order to characterize the system and should be optimized to enable a fast characterization. Based on such a system, the integration of the new constellation in safety critical applications will be done faster and will enable receiver manufacturers to integrate it in their system.

The provision of multiple frequencies and the integration of new robust constellations in the satellite navigation world enable more efficient self consistency checks. Therefore new autonomous integrity monitoring algorithms have to be developed that take into account the variety of constellations and their threats characteristics. The methodology adopted in this thesis with that respect can serve as a systematic approach to decide when a constellation is ready for integration in a navigation system for critical applications.

Novel RAIM algorithms taking into account error characteristics in a satellite by satellite and constellation by constellation basis should be developed and considering the approach presented in this thesis is the case of GPS, should improve considerably the integrity of the navigation solution.

A multi-constellation and multi-frequency environment will enable also an increase of performance for SBAS and GBAS. The challenge will be to find an optimal processing strategy that limits the development and operational costs, that is compatible with legacy systems and enable a performance increase. A cost function that considers all these aspect has still to be developed.

The satellite navigation signals are very weak and very vulnerable to radio frequency interferences like jammers and spoofers. Parallel to the development of new GNSS/INS hybridization strategies, alternative positioning navigation and timing (APNT) systems are necessary. These non GNSS based navigation systems should be able to provide a robust navigation solution when GNSS signals are lost by the user during a critical operational phase. Again the methodology adopted in this thesis can serve as a guideline for the development of a robust APNT architecture, starting by a threat characterization of the new system, designing integrity monitors for the threats that cannot be covered by a fault free case and developing an integrity scheme that ensures that the system fulfills some required performances.

A. Properties of Stochastic Diffusion Equations[Oks07]

An Itō diffusion is a stochastic process X_t satisfying a stochastic differential equation of the form:

$$dX_t = b(X_t)\,dt + \sigma(X_t)\,dB_t \qquad t \geq 0\,;\ \text{with } X_0 = x \tag{A.1}$$

where B_t is an m-dimensional standard ($B_0 = 0_{[m\times 1]}$) Brownian motion, $b : \mathbb{R}^n \to \mathbb{R}^n$ and $\sigma : \mathbb{R}^n \to \mathbb{R}^{n\times m}$ satisfying the Lipschitz continuous condition (to guarantee existence and uniqueness of the solution). This solution is noted $X_t^{0,x}, t \geq 0$. The associated probability measure of X_t is denoted P^x. The upper index x means that the process starts at x.

A.1. Generator of a diffusion process

Let X_t be a time-homogeneous Itō diffusion process in $\mathbb{R}^n$, the infinitesimal generator A of X_t is defined as follows:

$$Af(x) = \lim_{t\downarrow 0} \frac{E^x[f(X_t)] - f(x)}{t};\ x \in \mathbb{R}^n \tag{A.2}$$

Where $t \downarrow 0$ means t approaching 0 from above. In this equation, E^x represents the expectation relative to the probability measure P^x.We can see that if a process X_t is solution of A.1 and if $f \in C_0^2(\mathbb{R}^n)$ (second spatial derivative of f is continuous in $\mathbb{R}^n$) then $f \in \mathcal{D}_A$ (set of f for which the generator exist for any $x \in \mathbb{R}^n$) and:

$$Af(x) = \sum_{i=1}^{n} b_i(x)\frac{\partial f}{\partial x_i} + \frac{1}{2}\sum_{i,j=1}^{n}\left(\sigma\sigma^T\right)_{i,j}(x)\frac{\partial^2 f}{\partial x_i \partial x_j} \tag{A.3}$$

In this equation, A is an operator acting on f, the second summation is a double summation on i and j. $\left(\sigma\sigma^T\right)_{i,j}(x)$ is the (i,j) element of the matrix $\sigma\sigma^T$ and can be function of x. b and σ are defined in Equation A.1. $\frac{\partial f}{\partial x_i}$ is the first order partial derivative of f with respect to the variable x_i and $\frac{\partial^2 f}{\partial x_i \partial x_j}$ is the second order derivative of f with respect to the variables x_i and x_j.

See [Oks07] Chapter 7 for the demonstration of this important result.

A.2. The Kolmogorov Forward Equation

The adjoint of the generator A is denoted A^* and is defined as follows:

$$A^* f(x) = -\sum_{i=1}^{n} b_i(x) \frac{\partial f}{\partial x_i} + \frac{1}{2} \sum_{i,j=1}^{n} \left(\sigma\sigma^T\right)_{i,j}(x) \frac{\partial^2 f}{\partial x_i \partial x_j} \tag{A.4}$$

then if we set $p(t,x)$ the density of (X_t) with the initial condition: $p(0,x) = p_0(x)$, p is solution of the partial differential equation:

$$\frac{\partial p}{\partial t} = A^* p \quad \text{and} \quad p(0,x) = p_0(x) \tag{A.5}$$

A.3. The Ornstein-Uhlenbeck (OU-) process

An important process encountered in the thesis is the solution of the following SDE and is named the Ornstein-Uhlenbeck (OU-) process:

$$dX_t = \theta(\mu - X_t)\, dt + \sigma dW_t \tag{A.6}$$

where θ, μ, and σ are the parameters of the process and W_t is the standard Brownian motion.

θ is also called the rate of mean reversion and σ the degree of volatility.

The process is stationary, Gaussian and Markovian.

The probability density function of this process satisfy the Fokker-Planck equation:

$$\frac{\partial f}{\partial t} = \theta \frac{\partial}{\partial x}\left[(x-\mu) f\right] + \frac{\sigma^2}{2} \frac{\partial^2 f}{\partial x^2} \tag{A.7}$$

The stationary solution of this equation is the limit when time tends to infinity of f and is a Gaussian density function with mean μ and variance $\sigma^2/(2\theta)$.

$$f_\infty(x) = \sqrt{\frac{\theta}{\pi\sigma^2}} \exp\left\{-\frac{\theta(x-\mu)^2}{\sigma^2}\right\} \tag{A.8}$$

B. Summary of Error Structures[Bou03]

If Y is a random variable. Let's define ΔY the error in Y. We define the following set of assumptions:

a1. $E[\Delta Y|Y]$ and $V[\Delta Y|Y]$ are known

a2. Errors are small ($\Delta Y \ll Y$) to allow the limitation of the Taylor expansion to the first order

a3. $E[\Delta Y|Y]$ and $V[\Delta Y|Y]$ are of the same order of magnitude[1]

Under given conditions on a function f, there is a possibility to derive the law of propagation of the error (restricted to the law of propagation of the bias and the variance). The starting point is the second order Taylor expansion.

$$\Delta(f(Y)) = f'(Y)\Delta Y + \frac{1}{2}f''(Y)(\Delta Y)^2 + \text{negligible terms} \tag{B.1}$$

Using the definition of the conditional variance, we have:

$$\begin{aligned} V[\Delta(f(Y))|Y] &= f'^2(Y)V[\Delta Y|Y] \\ E[\Delta(f(Y))|Y] &= f'(Y)E[\Delta Y|Y] + \tfrac{1}{2}f''(Y)V[\Delta Y|Y] \end{aligned} \tag{B.2}$$

An error structure $\mathcal{S}$ is defined as follows:

$$\mathcal{S} = (\Omega, \mathcal{A}, \mathbb{P}, \mathbb{D}, \Gamma, \mathcal{D}_A, A) \tag{B.3}$$

Where $(\Omega, \mathcal{A}, \mathbb{P})$ is a probability space, $\mathbb{D}$ is a dense sub-vector space of $L^2(\mathbb{P})$[2], Γ is a positive, symmetric bilinear application from $\mathbb{D} \times \mathbb{D}$ into $L^1(\Omega, \mathcal{A}, \mathbb{P})$[3] satisfying the following property:

[1] This is indeed the bias and the variance that are meant and not the bias and the standard deviation. See [Bou03] for a detailed justification of this assumption.

[2] The space $L^2(\mathbb{P})$is the space of squared Lebesgue integrable functions with respect to the probability measure $\mathbb{P}$

[3] This is space of functions for which their absolute value is Lebesgue Integrable

$\forall u \in \mathbb{D}^m$, $\forall v \in \mathbb{D}^n$, $\forall F : \mathbb{R}^m \to \mathbb{R}$, $\forall G : \mathbb{R}^n \to \mathbb{R}$ with F and G being of class $\mathcal{C}^1$ (continuous derivative) and Lipschitzian (the norm of its derivative is bounded in $\mathbb{R}$), we have:

$$\Gamma\left[F\left(u\right), G\left(v\right)\right] = \sum_{i,j} \frac{\partial F}{\partial x_i}\left(u\right) \frac{\partial G}{\partial x_j}\left(v\right) \Gamma\left[u_i, v_j\right] \qquad \mathbb{P}\text{-a.s.} \tag{B.4}$$

$\mathbb{P}$-a.s. means that it is verified with probability $\mathbb{P}$ equal to one (a.s. stand for almost surely).

$\Gamma$is such that the bilinear form $\mathcal{E}\left[u, v\right] := \frac{1}{2} E\left[\Gamma\left[u, v\right]\right]$ is closed (by convention we set $\mathcal{E}\left[u, u\right] = \mathcal{E}\left[u\right]$ and $\Gamma\left[u, u\right] = \Gamma\left[u\right]$), which means that the space $\mathbb{D}$ equipped with the norm

$$\left\|u\right\|_{\mathbb{D}} = \left(\left\|u\right\|^2_{L^2(\mathbb{P})} + \mathcal{E}\left[u\right]\right)^{\frac{1}{2}} \tag{B.5}$$

is complete.

The error structures used in this thesis are Markovian (which is equivalent to write that the constant function 1 belongs to $\mathbb{D}$).

Associated to this operator, and under weak additional assumptions described in [Bou03], the strongly-continuous contraction semigroup $(P_t)_{t\geq 0}$ possesses a generator A that satisfies:

$$A\left[F\left(u\right)\right] = \sum_{i} \frac{\partial F}{\partial x_i}\left(u\right) A\left[u_i\right] + \frac{1}{2} \sum_{i,j} \frac{\partial^2 F}{\partial x_i \partial x_j}\left(u\right) \Gamma\left[u_i, u_j\right] \qquad \mathbb{P}\text{-a.s.} \tag{B.6}$$

$\forall F : \mathbb{R}^m \to \mathbb{R}$ of class $\mathcal{C}^2$, Lipschitzian and for which, $\forall u \in \mathbb{R}^m$ $A\left[F\left(u\right)\right]$ exists. The set of functions for which the generator exists for every u is denoted $\mathcal{D}_A$. In Equation B.6 $A\left[u_i\right]$ should be interpreted as the expectation of the error in u_i (actually a bias in u_i).

The error structure as defined above provides a method to propagate errors under the assumptions defined above.

It provides the law to propagate the variance (which depends on a first order functional derivative) and the bias (which includes a second order functional derivative terms multiplied by the error variance).

A very rich formalism especially applied in Financial Engineering has been developed since the publication of [Bou03].

C. Variance of the Hatch filter

C.1. Variance of D_t

with $D_t = \int_0^t e^{\frac{s-t}{\tau_\mathcal{E}}} V_s ds - \frac{e^{\frac{-t}{\tau_h}}}{\tau_h} \int_0^t e^{\frac{-s}{\tau_\mathcal{E}^\star}} \int_0^s e^{\frac{u}{\tau_\mathcal{E}}} V_u du ds$

$$V[D_t] = \underbrace{E\left[\left(\int_0^t e^{\frac{s-t}{\tau_\mathcal{E}}} V_s ds\right)^2\right]}_{VD1_t} + \frac{e^{\frac{-2t}{\tau_h}}}{\tau_h^2} \underbrace{E\left[\left(\int_0^t e^{\frac{-s}{\tau_\mathcal{E}^\star}} \int_0^s e^{\frac{u}{\tau_\mathcal{E}}} V_u du ds\right)^2\right]}_{VD2_t} - \\ - 2\frac{e^{\frac{-t}{\tau_h}}}{\tau_h} \underbrace{E\left[\int_0^t e^{\frac{s-t}{\tau_\mathcal{E}}} V_s ds \int_0^t e^{\frac{-s}{\tau_\mathcal{E}^\star}} \int_0^s e^{\frac{u}{\tau_\mathcal{E}}} V_u du ds\right]}_{VD12_t} \quad \text{(C.1)}$$

$$\begin{aligned}
VD1_t &= E\left[\int_0^t e^{\frac{s-t}{\tau_\mathcal{E}}} V_s ds \int_0^t e^{\frac{s'-t}{\tau_\mathcal{E}}} V_{s'} ds'\right] \\
&= E\left[\int_0^t \int_0^t e^{\frac{s+s'-2t}{\tau_\mathcal{E}}} V_s V_{s'} ds' ds\right] \\
&= \int_0^t \int_0^t e^{\frac{s+s'-2t}{\tau_\mathcal{E}}} E[V_s V_{s'}] ds' ds \\
&= \int_0^t \int_0^t e^{\frac{s+s'-2t}{\tau_\mathcal{E}}} (s \wedge s') ds' ds \\
&= \int_0^t \left[\int_0^s e^{\frac{s+s'-2t}{\tau_\mathcal{E}}} (s \wedge s') ds' + \int_s^t e^{\frac{s+s'-2t}{\tau_\mathcal{E}}} (s \wedge s') ds'\right] ds \\
&= \int_0^t \left[\int_0^s s' e^{\frac{s+s'-2t}{\tau_\mathcal{E}}} ds' + \int_s^t s e^{\frac{s+s'-2t}{\tau_\mathcal{E}}} ds'\right] ds \\
&= \int_0^t \int_0^s s' e^{\frac{s+s'-2t}{\tau_\mathcal{E}}} ds' ds + \int_0^t \int_s^t s e^{\frac{s+s'-2t}{\tau_\mathcal{E}}} ds' ds \qquad \text{(C.2)}
\end{aligned}$$

We solve this integral using the symbolic package sympy of python and we obtain:

$$VD1_t = t\tau_\epsilon^2 - \frac{3\tau_\epsilon^3}{2} + 2\tau_\epsilon^3 e^{-\frac{t}{\tau_\epsilon}} - \frac{\tau_\epsilon^3}{2} e^{-\frac{2t}{\tau_\epsilon}} \quad \text{(C.3)}$$

$$
\begin{aligned}
VD2_t &= E\left[\int_0^t e^{\frac{-s}{\tau_\mathcal{E}^\star}}\int_0^s e^{\frac{u}{\tau_\mathcal{E}}}V_u du ds \int_0^t e^{\frac{-s'}{\tau_\mathcal{E}^\star}}\int_0^{s'} e^{\frac{u'}{\tau_\mathcal{E}}}V_{u'}du'ds'\right] \\
&= E\left[\int_0^t\int_0^s e^{\frac{-s}{\tau_\mathcal{E}^\star}}e^{\frac{u}{\tau_\mathcal{E}}}V_u du ds \int_0^t\int_0^{s'} e^{\frac{-s'}{\tau_\mathcal{E}^\star}}e^{\frac{u'}{\tau_\mathcal{E}}}V_{u'}du'ds'\right] \\
&= E\left[\int_0^t\int_0^s\int_0^t\int_0^{s'} e^{\frac{-s}{\tau_\mathcal{E}^\star}}e^{\frac{u}{\tau_\mathcal{E}}}e^{\frac{-s'}{\tau_\mathcal{E}^\star}}e^{\frac{u'}{\tau_\mathcal{E}}}V_uV_{u'}du'ds'duds\right] \\
&= \int_0^t\int_0^s\int_0^t\int_0^{s'} \underbrace{e^{\frac{u+u'}{\tau_\mathcal{E}}-\frac{s+s'}{\tau_\mathcal{E}^\star}}}_{f}(u\wedge u')\,du'ds'duds \\
&= \int_0^t\int_0^s\left[\int_0^u\int_0^{s'} u'f du'ds' + \int_u^t\left[\int_0^u u'f du' + \int_u^{s'} uf du'\right]ds'\right]duds
\end{aligned}
\tag{C.4}
$$

As before we solve this integral using sympy for python:

$$
\begin{aligned}
VD2_t = &-\frac{t\tau_\epsilon^5\tau_h^2e^{\frac{2t}{\tau_h}}}{-\tau_\epsilon^3+\tau_\epsilon^2\tau_h+\tau_\epsilon\tau_h^2-\tau_h^3} + \frac{t\tau_\epsilon^4\tau_h^3e^{\frac{2t}{\tau_h}}}{-\tau_\epsilon^3+\tau_\epsilon^2\tau_h+\tau_\epsilon\tau_h^2-\tau_h^3} + \\
&+\frac{t\tau_\epsilon^3\tau_h^4e^{\frac{2t}{\tau_h}}}{-\tau_\epsilon^3+\tau_\epsilon^2\tau_h+\tau_\epsilon\tau_h^2-\tau_h^3} - \frac{t\tau_\epsilon^2\tau_h^5e^{\frac{2t}{\tau_h}}}{-\tau_\epsilon^3+\tau_\epsilon^2\tau_h+\tau_\epsilon\tau_h^2-\tau_h^3} - \\
&-\frac{2\tau_\epsilon^6\tau_h^2e^{-\frac{t}{\tau_\epsilon}}e^{\frac{2t}{\tau_h}}}{-\tau_\epsilon^3+\tau_\epsilon^2\tau_h+\tau_\epsilon\tau_h^2-\tau_h^3} + \frac{3\tau_\epsilon^6\tau_h^2e^{\frac{2t}{\tau_h}}}{-2\tau_\epsilon^3+2\tau_\epsilon^2\tau_h+2\tau_\epsilon\tau_h^2-2\tau_h^3} + \\
&+\frac{\tau_\epsilon^6\tau_h^2e^{-\frac{2t}{\tau_\epsilon}}e^{\frac{2t}{\tau_h}}}{-2\tau_\epsilon^3+2\tau_\epsilon^2\tau_h+2\tau_\epsilon\tau_h^2-2\tau_h^3} - \frac{\tau_\epsilon^5\tau_h^3e^{\frac{2t}{\tau_h}}}{-2\tau_\epsilon^3+2\tau_\epsilon^2\tau_h+2\tau_\epsilon\tau_h^2-2\tau_h^3} + \\
&+\frac{\tau_\epsilon^5\tau_h^3e^{-\frac{2t}{\tau_\epsilon}}e^{\frac{2t}{\tau_h}}}{-2\tau_\epsilon^3+2\tau_\epsilon^2\tau_h+2\tau_\epsilon\tau_h^2-2\tau_h^3} - \frac{2\tau_\epsilon^4\tau_h^4e^{\frac{2t}{\tau_h}}}{-\tau_\epsilon^3+\tau_\epsilon^2\tau_h+\tau_\epsilon\tau_h^2-\tau_h^3} + \\
&+\frac{2\tau_\epsilon^4\tau_h^4e^{\frac{t}{\tau_h}}}{-\tau_\epsilon^3+\tau_\epsilon^2\tau_h+\tau_\epsilon\tau_h^2-\tau_h^3} + \frac{2\tau_\epsilon^4\tau_h^4e^{-\frac{t}{\tau_\epsilon}}e^{\frac{2t}{\tau_h}}}{-\tau_\epsilon^3+\tau_\epsilon^2\tau_h+\tau_\epsilon\tau_h^2-\tau_h^3} - \\
&-\frac{2\tau_\epsilon^4\tau_h^4e^{-\frac{t}{\tau_\epsilon}}e^{\frac{t}{\tau_h}}}{-\tau_\epsilon^3+\tau_\epsilon^2\tau_h+\tau_\epsilon\tau_h^2-\tau_h^3} - \frac{\tau_\epsilon^3\tau_h^5e^{\frac{2t}{\tau_h}}}{-2\tau_\epsilon^3+2\tau_\epsilon^2\tau_h+2\tau_\epsilon\tau_h^2-2\tau_h^3} + \\
&+\frac{\tau_\epsilon^3\tau_h^5}{-2\tau_\epsilon^3+2\tau_\epsilon^2\tau_h+2\tau_\epsilon\tau_h^2-2\tau_h^3} - \frac{2\tau_\epsilon^2\tau_h^6e^{\frac{t}{\tau_h}}}{-\tau_\epsilon^3+\tau_\epsilon^2\tau_h+\tau_\epsilon\tau_h^2-\tau_h^3} + \\
&+\frac{3\tau_\epsilon^2\tau_h^6e^{\frac{2t}{\tau_h}}}{-2\tau_\epsilon^3+2\tau_\epsilon^2\tau_h+2\tau_\epsilon\tau_h^2-2\tau_h^3} + \frac{\tau_\epsilon^2\tau_h^6}{-2\tau_\epsilon^3+2\tau_\epsilon^2\tau_h+2\tau_\epsilon\tau_h^2-2\tau_h^3}
\end{aligned}
\tag{C.5}
$$

We are going to solve $VD12_t$

$$
\begin{aligned}
VD12_t &= E\left[\int_0^t e^{\frac{s-t}{\tau_\mathcal{E}}} V_s ds \int_0^t e^{\frac{-s'}{\tau_\mathcal{E}^\star}} \int_0^{s'} e^{\frac{u'}{\tau_\mathcal{E}}} V_{u'} du' ds'\right] \\
&= E\left[\int_0^t \int_0^t \int_0^{s'} e^{\frac{s-t}{\tau_\mathcal{E}}} e^{\frac{-s'}{\tau_\mathcal{E}^\star}} e^{\frac{u'}{\tau_\mathcal{E}}} V_s V_{u'} du' ds' ds\right] \\
&= \int_0^t \int_0^t \int_0^{s'} e^{\frac{s-t}{\tau_\mathcal{E}}} e^{\frac{-s'}{\tau_\mathcal{E}^\star}} e^{\frac{u'}{\tau_\mathcal{E}}} E\left[V_s V_{u'}\right] du' ds' ds \\
&= \int_0^t \int_0^t \int_0^{s'} \underbrace{e^{\frac{s-t+u'}{\tau_\mathcal{E}} - \frac{s'}{\tau_\mathcal{E}^\star}}}_{g} (s \wedge u')\, du' ds' ds \\
&= \int_0^t \left[\int_0^s \int_0^{s'} u' g du' ds' + \int_s^t \left[\int_0^s u' g du' + \int_s^{s'} s g du'\right] ds'\right] ds \qquad \text{(C.6)}
\end{aligned}
$$

finally we get:

$$
\begin{aligned}
VD12_t = {} & t\tau_\epsilon^2 \tau_h e^{\frac{t}{\tau_h}} - \frac{\tau_\epsilon^4 \tau_h^2 e^{\frac{t}{\tau_h}}}{-\tau_\epsilon^2 + \tau_h^2} + \frac{\tau_\epsilon^4 \tau_h^2 e^{-\frac{t}{\tau_\epsilon}}}{-\tau_\epsilon^2 + \tau_h^2} + \frac{\tau_\epsilon^4 \tau_h}{-\tau_\epsilon + \tau_h} - \\
& - \frac{\tau_\epsilon^4 \tau_h e^{-\frac{t}{\tau_\epsilon}} e^{\frac{t}{\tau_h}}}{-\tau_\epsilon + \tau_h} - \frac{\tau_\epsilon^4 \tau_h e^{-\frac{t}{\tau_\epsilon}}}{-\tau_\epsilon + \tau_h} + \frac{\tau_\epsilon^4 \tau_h e^{\frac{t}{\tau_h}}}{-2\tau_\epsilon + 2\tau_h} + \frac{\tau_\epsilon^4 \tau_h e^{-\frac{2t}{\tau_\epsilon}} e^{\frac{t}{\tau_h}}}{-2\tau_\epsilon + 2\tau_h} - \\
& - \frac{\tau_\epsilon^3 \tau_h^2 e^{\frac{t}{\tau_h}}}{\tau_\epsilon + \tau_h} + \frac{\tau_\epsilon^3 \tau_h^2 e^{-\frac{t}{\tau_\epsilon}}}{\tau_\epsilon + \tau_h} - \tau_\epsilon^3 \tau_h e^{\frac{t}{\tau_h}} + \tau_\epsilon^3 \tau_h + \tau_\epsilon^3 \tau_h e^{-\frac{t}{\tau_\epsilon}} e^{\frac{t}{\tau_h}} - \\
& - \tau_\epsilon^3 \tau_h e^{-\frac{t}{\tau_\epsilon}} - \frac{\tau_\epsilon^2 \tau_h^3 e^{\frac{t}{\tau_h}}}{\tau_\epsilon + \tau_h} + \frac{\tau_\epsilon^2 \tau_h^3 e^{-\frac{t}{\tau_\epsilon}}}{\tau_\epsilon + \tau_h} + \tau_\epsilon^2 \tau_h^2 - \tau_\epsilon^2 \tau_h^2 e^{-\frac{t}{\tau_\epsilon}} \qquad \text{(C.7)}
\end{aligned}
$$

C.2. Variance of P_t

with $P_t = W_t - \int_0^t \left[\frac{1}{\tau_\eta} e^{\frac{s-t}{\tau_\eta}} + \frac{1}{\tau_h} e^{\frac{s-t}{\tau_h}} e^{\frac{-s}{\tau_\eta}}\right] W_s ds + \frac{1}{\tau_\eta \tau_h} \int_0^t \int_0^s e^{\frac{u-s}{\tau_\eta} + \frac{s-t}{\tau_h}} W_u du ds$

$$V[P_t] = \underbrace{E\left[W_t^2\right]}_{VP1_t} + \underbrace{E\left[\left(\int_0^t \left(\frac{1}{\tau_\eta}e^{\frac{s-t}{\tau_\eta}} + \frac{1}{\tau_h}e^{\frac{s-t}{\tau_h}}e^{\frac{-s}{\tau_\eta}}\right)W_s ds\right)^2\right]}_{VP2_t} +$$
$$\frac{1}{\tau_h^2\tau_\eta^2}\underbrace{E\left[\left(\int_0^t\int_0^s e^{\frac{u-s}{\tau_\eta}+\frac{s-t}{\tau_h}}W_u du ds\right)^2\right]}_{VP3_t} - 2\underbrace{E\left[\int_0^t\left(\frac{1}{\tau_\eta}e^{\frac{s-t}{\tau_\eta}} + \frac{1}{\tau_h}e^{\frac{s-t}{\tau_h}}e^{\frac{-s}{\tau_\eta}}\right)W_t W_s ds\right]}_{VP4_t} +$$
$$+\frac{2}{\tau_h\tau_\eta}\underbrace{E\left[\int_0^t\int_0^s e^{\frac{u-s}{\tau_\eta}+\frac{s-t}{\tau_h}}W_t W_u du ds\right]}_{VP5_t} -$$
$$-\frac{2}{\tau_h\tau_\eta}\underbrace{E\left[\int_0^t\left(\frac{1}{\tau_\eta}e^{\frac{s-t}{\tau_\eta}} + \frac{1}{\tau_h}e^{\frac{s-t}{\tau_h}}e^{\frac{-s}{\tau_\eta}}\right)W_s ds\int_0^t\int_0^s e^{\frac{u-s}{\tau_\eta}+\frac{s-t}{\tau_h}}W_u du ds\right]}_{VP6_t} \quad \text{(C.8)}$$

$$VP1_t = t \quad \text{(C.9)}$$

$$VP2_t = E\left[\int_0^t\left(\frac{1}{\tau_\eta}e^{\frac{s-t}{\tau_\eta}} + \frac{1}{\tau_h}e^{\frac{s-t}{\tau_h}}e^{\frac{-s}{\tau_\eta}}\right)W_s ds\int_0^t\left(\frac{1}{\tau_\eta}e^{\frac{s'-t}{\tau_\eta}} + \frac{1}{\tau_h}e^{\frac{s'-t}{\tau_h}}e^{\frac{-s'}{\tau_\eta}}\right)W_{s'} ds'\right] \quad \text{(C.10)}$$

Let's define $h(s) = \frac{1}{\tau_\eta}e^{\frac{s-t}{\tau_\eta}} + \frac{1}{\tau_h}e^{\frac{s-t}{\tau_h}}e^{\frac{-s}{\tau_\eta}}$

$$\begin{aligned}
VP2_t &= \mathcal{E}\left[\int_0^t\int_0^t h(s)h(s')W_s W_{s'} ds ds'\right] \\
&= \int_0^t\int_0^t h(s)h(s')(s'\wedge s)\, ds ds' \\
&= \int_0^t\left[\int_0^{s'} h(s)h(s')(s'\wedge s)\, ds + \int_{s'}^t h(s)h(s')(s'\wedge s)\, ds\right]ds' \\
&= \int_0^t\left[\int_0^{s'} sh(s)h(s')\, ds + \int_{s'}^t s'h(s)h(s')\, ds\right]ds' \quad \text{(C.11)}
\end{aligned}$$

we have

$$\begin{aligned}
h(s)h(s') &= \left(\frac{1}{\tau_\eta}e^{\frac{s-t}{\tau_\eta}} + \frac{1}{\tau_h}e^{\frac{s-t}{\tau_h}}e^{\frac{-s}{\tau_\eta}}\right)\left(\frac{1}{\tau_\eta}e^{\frac{s'-t}{\tau_\eta}} + \frac{1}{\tau_h}e^{\frac{s'-t}{\tau_h}}e^{\frac{-s'}{\tau_\eta}}\right) \\
&= \underbrace{\frac{1}{\tau_\eta^2}e^{\frac{s+s'-2t}{\tau_\eta}}}_{hh1} + \underbrace{\frac{1}{\tau_h\tau_\eta}e^{\frac{s-t}{\tau_\eta}+\frac{s'-t}{\tau_h}-\frac{s'}{\tau_\eta}}}_{hh2} + \underbrace{\frac{1}{\tau_h\tau_\eta}e^{\frac{s'-t}{\tau_\eta}-\frac{s}{\tau_\eta}+\frac{s-t}{\tau_h}}}_{hh3} + \underbrace{\frac{1}{\tau_h^2}e^{\frac{s+s'-2t}{\tau_h}-\frac{s+s'}{\tau_\eta}}}_{hh4}
\end{aligned} \quad \text{(C.12)}$$

Finally we have:

$$
\begin{aligned}
VP2_t = &-\frac{t\tau_\eta^3 e^{-\frac{2t}{\tau_\eta}}}{-\tau_\eta^3+3\tau_\eta^2\tau_h-3\tau_\eta\tau_h^2+\tau_h^3}+\frac{t\tau_\eta^2\tau_h e^{-\frac{2t}{\tau_\eta}}}{-\tau_\eta^3+3\tau_\eta^2\tau_h-3\tau_\eta\tau_h^2+\tau_h^3}+\\
&+\frac{2t\tau_\eta^2 e^{-\frac{t}{\tau_\eta}}}{\tau_\eta^2-2\tau_\eta\tau_h+\tau_h^2}-\frac{2t\tau_\eta\tau_h e^{-\frac{t}{\tau_\eta}}}{\tau_\eta^2-2\tau_\eta\tau_h+\tau_h^2}+t-\frac{2\tau_\eta^3\tau_h e^{-\frac{t}{\tau_\eta}}e^{-\frac{t}{\tau_h}}}{-\tau_\eta^3+3\tau_\eta^2\tau_h-3\tau_\eta\tau_h^2+\tau_h^3}+\\
&+\frac{\tau_\eta^3\tau_h e^{-\frac{2t}{\tau_h}}}{-2\tau_\eta^3+6\tau_\eta^2\tau_h-6\tau_\eta\tau_h^2+2\tau_h^3}+\frac{3\tau_\eta^3\tau_h e^{-\frac{2t}{\tau_\eta}}}{-2\tau_\eta^3+6\tau_\eta^2\tau_h-6\tau_\eta\tau_h^2+2\tau_h^3}-\\
&-\frac{\tau_\eta^3 e^{-\frac{t}{\tau_\eta}}}{\tau_\eta^2-2\tau_\eta\tau_h+\tau_h^2}+\frac{\tau_\eta^3 e^{-\frac{2t}{\tau_\eta}}}{\tau_\eta^2-2\tau_\eta\tau_h+\tau_h^2}+\frac{2\tau_\eta^2\tau_h e^{-\frac{t}{\tau_h}}}{\tau_\eta^2-2\tau_\eta\tau_h+\tau_h^2}-\\
&-\frac{\tau_\eta^2\tau_h e^{-\frac{t}{\tau_\eta}}e^{-\frac{t}{\tau_h}}}{\tau_\eta^2-2\tau_\eta\tau_h+\tau_h^2}-\frac{\tau_\eta^2\tau_h e^{-\frac{2t}{\tau_\eta}}}{\tau_\eta^2-2\tau_\eta\tau_h+\tau_h^2}+\frac{\tau_\eta^2 e^{-\frac{t}{\tau_\eta}}e^{-\frac{t}{\tau_h}}}{-\tau_\eta+\tau_h}-\\
&-\frac{\tau_\eta^2 e^{-\frac{2t}{\tau_\eta}}}{-\tau_\eta+\tau_h}-\frac{\tau_\eta\tau_h^2 e^{-\frac{t}{\tau_\eta}}}{\tau_\eta^2-2\tau_\eta\tau_h+\tau_h^2}+\frac{\tau_\eta\tau_h^2 e^{-\frac{t}{\tau_\eta}}e^{-\frac{t}{\tau_h}}}{\tau_\eta^2-2\tau_\eta\tau_h+\tau_h^2}-\\
&-\frac{3\tau_\eta}{2}+\tau_\eta e^{-\frac{t}{\tau_\eta}}+\tau_\eta e^{-\frac{t}{\tau_\eta}}e^{-\frac{t}{\tau_h}}-\frac{\tau_\eta}{2}e^{-\frac{2t}{\tau_\eta}}
\end{aligned}
\tag{C.13}
$$

$$
\begin{aligned}
VP3_t &= E\left[\left(\int_0^t\int_0^s e^{\frac{u-s}{\tau_\eta}+\frac{s-t}{\tau_h}}W_u du ds\right)^2\right]\\
&= E\left[\left(\int_0^t\int_0^s e^{\frac{u-s}{\tau_\eta}+\frac{s-t}{\tau_h}}W_u du ds\right)\left(\int_0^t\int_0^{s'} e^{\frac{u'-s'}{\tau_\eta}+\frac{s'-t}{\tau_h}}W_{u'} du' ds'\right)\right]\\
&= E\left[\int_0^t\int_0^s\int_0^t\int_0^{s'} e^{\frac{u+u'-s-s'}{\tau_\eta}+\frac{s+s'-2t}{\tau_h}}W_u W_{u'} du' ds' du ds\right]\\
&= \int_0^t\int_0^s\int_0^t\int_0^{s'} \underbrace{\underbrace{e^{\frac{u+u'-s-s'}{\tau_\eta}+\frac{s+s'-2t}{\tau_h}}}_{f}(u'\wedge u)}_{g} du' ds' du ds\\
&= \int_0^t\int_0^s\left[\int_0^u\int_0^{s'} g du' ds' + \int_u^t\int_0^{s'} g du' ds'\right] du ds\\
&= \int_0^t\left[\int_0^s\left[\int_0^u\int_0^{s'} g du' ds' + \int_u^t\left[\int_0^u g du' + \int_u^{s'} g du'\right]\right] ds'\right] du ds\\
&= \int_0^t\left[\int_0^s\left[\int_0^u\int_0^{s'} u' f du' ds' + \int_u^t\left[\int_0^u u' f du' + \int_u^{s'} u f du'\right]\right] ds'\right] du ds
\end{aligned}
\tag{C.14}
$$

We use symbolic package of Python (sympy) to find a closed form solution of the above defined integral and we obtain:

$$
\begin{aligned}
VP3_t = & \frac{\tau_\eta^6 \tau_h^2 \left(e^{\frac{t}{\tau_h}+\frac{t}{\tau_\eta}} - 1\right) e^{-\frac{t}{\tau_h}-\frac{t}{\tau_\eta}}}{(2\tau_\eta + 2\tau_h)\left(-\tau_\eta^2 + \tau_h^2\right)} + \frac{\tau_\eta^6 \tau_h^2 \left(e^{\frac{t}{\tau_h}-\frac{t}{\tau_\eta}} - 1\right) e^{-\frac{t}{\tau_h}}}{(-\tau_\eta + \tau_h)\left(-\tau_\eta^2 + \tau_h^2\right)} - \\
& - \frac{\tau_\eta^6 \tau_h^2 \left(e^{\frac{t}{\tau_h}-\frac{t}{\tau_\eta}} - 1\right) e^{-\frac{t}{\tau_h}-\frac{t}{\tau_\eta}}}{(-\tau_\eta + \tau_h)\left(-2\tau_\eta^2 + 2\tau_h^2\right)} + \frac{\tau_\eta^5 \tau_h^3 \left(e^{\frac{t}{\tau_h}+\frac{t}{\tau_\eta}} - 1\right) e^{-\frac{t}{\tau_h}-\frac{t}{\tau_\eta}}}{(2\tau_\eta + 2\tau_h)\left(-\tau_\eta^2 + \tau_h^2\right)} - \\
& - \frac{\tau_\eta^5 \tau_h^3 \left(e^{\frac{t}{\tau_h}-\frac{t}{\tau_\eta}} - 1\right) e^{-\frac{t}{\tau_h}-\frac{t}{\tau_\eta}}}{(-\tau_\eta + \tau_h)\left(-2\tau_\eta^2 + 2\tau_h^2\right)} - \frac{\tau_\eta^5 \tau_h^2 e^{-\frac{t}{\tau_h}-\frac{t}{\tau_\eta}}}{-\tau_\eta^2 + \tau_h^2}\left(e^{\frac{t}{\tau_h}} - 1\right) + \\
& + \frac{\tau_\eta^5 \tau_h^2 \left(e^{\frac{t}{\tau_h}} - 1\right) e^{-\frac{t}{\tau_h}}}{-\tau_\eta^2 + \tau_h^2} - \frac{\tau_\eta^4 \tau_h^4 \left(e^{\frac{t}{\tau_h}-\frac{t}{\tau_\eta}} - 1\right) e^{-\frac{t}{\tau_h}}}{(-\tau_\eta + \tau_h)\left(-\tau_\eta^2 + \tau_h^2\right)} + \\
& + \frac{\tau_\eta^4 \tau_h^4 \left(e^{\frac{t}{\tau_h}-\frac{t}{\tau_\eta}} - 1\right) e^{-\frac{2t}{\tau_h}}}{(-\tau_\eta + \tau_h)\left(-\tau_\eta^2 + \tau_h^2\right)} - \frac{\tau_\eta^4 \tau_h^3 e^{-\frac{t}{\tau_h}-\frac{t}{\tau_\eta}}}{-\tau_\eta^2 + \tau_h^2}\left(e^{\frac{t}{\tau_h}} - 1\right) - \\
& - \frac{\tau_\eta^4 \tau_h e^{-\frac{t}{\tau_h}}}{-\tau_\eta^2 + \tau_h^2}\left(\tau_h^2 + \tau_h\left(t - \tau_h\right) e^{\frac{t}{\tau_h}}\right) - \frac{\tau_\eta^3 \tau_h^4 \left(e^{\frac{t}{\tau_h}} - 1\right) e^{-\frac{t}{\tau_h}}}{-\tau_\eta^2 + \tau_h^2} + \\
& + \frac{\tau_\eta^3 \tau_h^4 \left(e^{\frac{t}{\tau_h}} - 1\right) e^{-\frac{2t}{\tau_h}}}{-\tau_\eta^2 + \tau_h^2} + \frac{\tau_\eta^2 \tau_h^5 \left(e^{\frac{t}{\tau_h}} - 1\right) e^{-\frac{2t}{\tau_h}}}{-\tau_\eta^2 + \tau_h^2} - \\
& - \frac{\tau_\eta^2 \tau_h^5 \left(e^{\frac{2t}{\tau_h}} - 1\right) e^{-\frac{2t}{\tau_h}}}{-2\tau_\eta^2 + 2\tau_h^2} + \frac{\tau_\eta^2 \tau_h^3 e^{-\frac{t}{\tau_h}}}{-\tau_\eta^2 + \tau_h^2}\left(\tau_h^2 + \tau_h\left(t - \tau_h\right) e^{\frac{t}{\tau_h}}\right)
\end{aligned} \tag{C.15}
$$

Expression of $VP4_t$

$$
\begin{aligned}
VP4_t &= E\left[\int_0^t h\left(s\right) W_t W_s ds\right] \\
&= \int_0^t h\left(s\right)\left(t \wedge s\right) ds \\
&= \int_0^t s h\left(s\right) ds
\end{aligned} \tag{C.16}
$$

Finally we have:

$$VP4_t = t + \frac{\tau_\eta^2 \tau_h e^{-\frac{t}{\tau_h}}}{(-\tau_\eta + \tau_h)^2} + \tau_\eta \left(-1 + e^{-\frac{t}{\tau_\eta}}\right) - \\ - \frac{\tau_\eta e^{-\frac{t}{\tau_\eta}}}{(-\tau_\eta + \tau_h)^2} (-t\tau_\eta + t\tau_h + \tau_\eta \tau_h) \quad \text{(C.17)}$$

Epression of $VP5_t$

$$VP5_t = E\left[\int_0^t \int_0^s e^{\frac{u-s}{\tau_\eta} + \frac{s-t}{\tau_h}} W_t W_u du ds\right] \\ = \int_0^t \int_0^s u e^{\frac{u-s}{\tau_\eta} + \frac{s-t}{\tau_h}} du ds \quad \text{(C.18)}$$

Finally we have:

$$VP5_t = t\tau_\eta \tau_h + \frac{\tau_\eta^3 \tau_h e^{-\frac{t}{\tau_h}}}{-\tau_\eta + \tau_h} - \frac{\tau_\eta^3 \tau_h e^{-\frac{t}{\tau_\eta}}}{-\tau_\eta + \tau_h} - \tau_\eta^2 \tau_h + \\ + \tau_\eta^2 \tau_h e^{-\frac{t}{\tau_h}} - \tau_\eta \tau_h^2 + \tau_\eta \tau_h^2 e^{-\frac{t}{\tau_h}} \quad \text{(C.19)}$$

Calculation of $VP6_t$

$$VP6_t = \mathcal{E}\left[\int_0^t \left(\frac{1}{\tau_\eta} e^{\frac{s-t}{\tau_\eta}} + \frac{1}{\tau_h} e^{\frac{s-t}{\tau_h}} e^{\frac{-s}{\tau_\eta}}\right) W_s ds \int_0^t \int_0^{s'} e^{\frac{u'-s'}{\tau_\eta} + \frac{s'-t}{\tau_h}} W_{u'} du' ds'\right] \\ = \mathcal{E}\left[\int_0^t \int_0^t \int_0^{s'} \underbrace{\left(\frac{1}{\tau_\eta} e^{\frac{s-t}{\tau_\eta}} + \frac{1}{\tau_h} e^{\frac{s-t}{\tau_h}} e^{\frac{-s}{\tau_\eta}}\right) e^{\frac{u'-s'}{\tau_\eta} + \frac{s'-t}{\tau_h}}}_{k(s,s',u')} W_{u'} W_s du' ds' ds\right] \\ = \int_0^t \int_0^t \int_0^{s'} k(s,s',u')(u' \wedge s) du' ds' ds \\ = \int_0^t \int_0^t \left[\int_0^s k(s,s',u')(u' \wedge s) du' + \int_s^{s'} k(s,s',u')(u' \wedge s) du'\right] ds' ds \\ = \int_0^t \int_0^t \left[\int_0^s u' k(s,s',u') du' + \int_s^{s'} s k(s,s',u') du'\right] ds' ds \quad \text{(C.20)}$$

After solving this integral using the symbolic math toolbox of Matlab we obtain:

$$VP6t = \frac{t\tau_\eta^3\tau_h e^{-\frac{t}{\tau_\eta}}}{\tau_\eta^2 - 2\tau_\eta\tau_h + \tau_h^2} - \frac{t\tau_\eta^3\tau_h e^{-\frac{t}{\tau_\eta}} e^{-\frac{t}{\tau_h}}}{\tau_\eta^2 - 2\tau_\eta\tau_h + \tau_h^2} - \frac{t\tau_\eta^2\tau_h^2 e^{-\frac{t}{\tau_\eta}}}{\tau_\eta^2 - 2\tau_\eta\tau_h + \tau_h^2} +$$
$$+ \frac{t\tau_\eta^2\tau_h^2 e^{-\frac{t}{\tau_\eta}} e^{-\frac{t}{\tau_h}}}{\tau_\eta^2 - 2\tau_\eta\tau_h + \tau_h^2} - \frac{t\tau_\eta^2\tau_h}{-\tau_\eta + \tau_h} + \frac{t\tau_\eta^2\tau_h e^{-\frac{t}{\tau_h}}}{-\tau_\eta + \tau_h} + \frac{t\tau_\eta\tau_h^2}{-\tau_\eta + \tau_h} -$$
$$- \frac{t\tau_\eta\tau_h^2 e^{-\frac{t}{\tau_h}}}{-\tau_\eta + \tau_h} + \frac{\tau_\eta^4\tau_h e^{-\frac{t}{\tau_h}}}{\tau_\eta^2 - 2\tau_\eta\tau_h + \tau_h^2} - \frac{\tau_\eta^4\tau_h e^{-\frac{t}{\tau_\eta}}}{\tau_\eta^2 - 2\tau_\eta\tau_h + \tau_h^2} -$$
$$- \frac{\tau_\eta^4\tau_h e^{-\frac{t}{\tau_\eta}} e^{-\frac{t}{\tau_h}}}{\tau_\eta^2 - 2\tau_\eta\tau_h + \tau_h^2} + \frac{\tau_\eta^4\tau_h e^{-\frac{2t}{\tau_\eta}}}{\tau_\eta^2 - 2\tau_\eta\tau_h + \tau_h^2} - \frac{2\tau_\eta^3\tau_h e^{-\frac{t}{\tau_\eta}}}{-\tau_\eta + \tau_h} -$$
$$- \frac{\tau_\eta^3\tau_h e^{\frac{t}{\tau_\eta}} e^{-\frac{t}{\tau_h}}}{-2\tau_\eta + 2\tau_h} + \frac{3\tau_\eta^3\tau_h}{-2\tau_\eta + 2\tau_h} + \frac{\tau_\eta^3\tau_h e^{-\frac{t}{\tau_\eta}} e^{-\frac{t}{\tau_h}}}{-2\tau_\eta + 2\tau_h} + \frac{\tau_\eta^3\tau_h e^{-\frac{2t}{\tau_\eta}}}{-2\tau_\eta + 2\tau_h} -$$
$$- \frac{\tau_\eta^2\tau_h^2}{-\tau_\eta + \tau_h} + \frac{\tau_\eta^2\tau_h^2 e^{-\frac{t}{\tau_h}}}{-\tau_\eta + \tau_h} + \frac{\tau_\eta^2\tau_h^2 e^{-\frac{t}{\tau_\eta}}}{-\tau_\eta + \tau_h} - \frac{\tau_\eta^2\tau_h^2 e^{-\frac{t}{\tau_\eta}} e^{-\frac{t}{\tau_h}}}{-\tau_\eta + \tau_h} \quad \text{(C.21)}$$

C.3. Variance of $\tilde{\rho}_u^{(k)}(t)$

Expression of the variance of the code carrier smoothing solution:

$$
\begin{aligned}
V\left[\widetilde{\rho}_u^{(k)}(t)\right] &= \frac{2t\tau_{\mathcal{E}}^4 V[\mathcal{E}_0]}{\tau_{\mathcal{E}}^3\tau_h^2-\tau_{\mathcal{E}}^2\tau_h^3-\tau_{\mathcal{E}}\tau_h^4+\tau_h^5}+\frac{2t\tau_{\mathcal{E}}^3 V[\mathcal{E}_0]}{-\tau_{\mathcal{E}}^3\tau_h+\tau_{\mathcal{E}}^2\tau_h^2+\tau_{\mathcal{E}}\tau_h^3-\tau_h^4}+\\
&+\frac{2t\tau_{\mathcal{E}}^2 V[\mathcal{E}_0]}{-\tau_{\mathcal{E}}^3+\tau_{\mathcal{E}}^2\tau_h+\tau_{\mathcal{E}}\tau_h^2-\tau_h^3}-\frac{2t\tau_{\mathcal{E}}\tau_h V[\mathcal{E}_0]}{-\tau_{\mathcal{E}}^3+\tau_{\mathcal{E}}^2\tau_h+\tau_{\mathcal{E}}\tau_h^2-\tau_h^3}-\\
&-\frac{2t}{\tau_h^2}\tau_{\mathcal{E}}V[\mathcal{E}_0]-\frac{2t\tau_\eta^2 V[\eta_0]\,e^{-\frac{2t}{\tau_\eta}}}{-\tau_\eta^3+3\tau_\eta^2\tau_h-3\tau_\eta\tau_h^2+\tau_h^3}+\\
&+\frac{2t\tau_\eta\tau_h V[\eta_0]\,e^{-\frac{2t}{\tau_\eta}}}{-\tau_\eta^3+3\tau_\eta^2\tau_h-3\tau_\eta\tau_h^2+\tau_h^3}-\frac{4t\tau_\eta V[\eta_0]\,e^{-\frac{t}{\tau_\eta}}}{\tau_\eta^2-2\tau_\eta\tau_h+\tau_h^2}+\\
&+\frac{4t\tau_\eta V[\eta_0]\,e^{-\frac{t}{\tau_\eta}}e^{-\frac{t}{\tau_h}}}{\tau_\eta^2-2\tau_\eta\tau_h+\tau_h^2}-\frac{2t\tau_\eta V[\eta_0]}{-\tau_\eta^2+\tau_h^2}+\frac{2t\tau_h^2 V[\eta_0]}{-\tau_\eta^3+\tau_\eta\tau_h^2}+\\
&+\frac{4t\tau_h V[\eta_0]\,e^{-\frac{t}{\tau_\eta}}}{\tau_\eta^2-2\tau_\eta\tau_h+\tau_h^2}-\frac{4t\tau_h V[\eta_0]\,e^{-\frac{t}{\tau_\eta}}e^{-\frac{t}{\tau_h}}}{\tau_\eta^2-2\tau_\eta\tau_h+\tau_h^2}-\frac{4t\tau_h V[\eta_0]}{-\tau_\eta^2+\tau_\eta\tau_h}+\\
&+\frac{4t\tau_h V[\eta_0]\,e^{-\frac{t}{\tau_h}}}{-\tau_\eta^2+\tau_\eta\tau_h}+\frac{4tV[\eta_0]}{-\tau_\eta+\tau_h}-\frac{4tV[\eta_0]\,e^{-\frac{t}{\tau_h}}}{-\tau_\eta+\tau_h}+\frac{4t}{\tau_\eta}V[\eta_0]-\\
&-\frac{3\tau_{\mathcal{E}}^5 V[\mathcal{E}_0]}{\tau_{\mathcal{E}}^3\tau_h^2-\tau_{\mathcal{E}}^2\tau_h^3-\tau_{\mathcal{E}}\tau_h^4+\tau_h^5}+\frac{4\tau_{\mathcal{E}}^5 V[\mathcal{E}_0]\,e^{-\frac{t}{\tau_{\mathcal{E}}}}}{\tau_{\mathcal{E}}^3\tau_h^2-\tau_{\mathcal{E}}^2\tau_h^3-\tau_{\mathcal{E}}\tau_h^4+\tau_h^5}-\\
&-\frac{\tau_{\mathcal{E}}^5 V[\mathcal{E}_0]\,e^{-\frac{2t}{\tau_{\mathcal{E}}}}}{\tau_{\mathcal{E}}^3\tau_h^2-\tau_{\mathcal{E}}^2\tau_h^3-\tau_{\mathcal{E}}\tau_h^4+\tau_h^5}-\frac{\tau_{\mathcal{E}}^4 V[\mathcal{E}_0]}{-\tau_{\mathcal{E}}^3\tau_h+\tau_{\mathcal{E}}^2\tau_h^2+\tau_{\mathcal{E}}\tau_h^3-\tau_h^4}+\\
&+\frac{\tau_{\mathcal{E}}^4 V[\mathcal{E}_0]\,e^{-\frac{2t}{\tau_{\mathcal{E}}}}}{-\tau_{\mathcal{E}}^3\tau_h+\tau_{\mathcal{E}}^2\tau_h^2+\tau_{\mathcal{E}}\tau_h^3-\tau_h^4}-\frac{4\tau_{\mathcal{E}}^3 V[\mathcal{E}_0]}{-\tau_{\mathcal{E}}^3+\tau_{\mathcal{E}}^2\tau_h+\tau_{\mathcal{E}}\tau_h^2-\tau_h^3}+\\
&+\frac{4\tau_{\mathcal{E}}^3 V[\mathcal{E}_0]\,e^{-\frac{t}{\tau_h}}}{-\tau_{\mathcal{E}}^3+\tau_{\mathcal{E}}^2\tau_h+\tau_{\mathcal{E}}\tau_h^2-\tau_h^3}+\frac{4\tau_{\mathcal{E}}^3 V[\mathcal{E}_0]\,e^{-\frac{t}{\tau_{\mathcal{E}}}}}{-\tau_{\mathcal{E}}^3+\tau_{\mathcal{E}}^2\tau_h+\tau_{\mathcal{E}}\tau_h^2-\tau_h^3}-\\
&-\frac{4\tau_{\mathcal{E}}^3 V[\mathcal{E}_0]\,e^{-\frac{t}{\tau_{\mathcal{E}}}}e^{-\frac{t}{\tau_h}}}{-\tau_{\mathcal{E}}^3+\tau_{\mathcal{E}}^2\tau_h+\tau_{\mathcal{E}}\tau_h^2-\tau_h^3}-\frac{4\tau_{\mathcal{E}}^3 V[\mathcal{E}_0]}{\tau_{\mathcal{E}}^2\tau_h-\tau_h^3}+\frac{4\tau_{\mathcal{E}}^3 V[\mathcal{E}_0]\,e^{-\frac{t}{\tau_{\mathcal{E}}}}e^{-\frac{t}{\tau_h}}}{\tau_{\mathcal{E}}^2\tau_h-\tau_h^3}+\\
&+\frac{2\tau_{\mathcal{E}}^3 V[\mathcal{E}_0]}{\tau_{\mathcal{E}}\tau_h^2-\tau_h^3}+\frac{4\tau_{\mathcal{E}}^3 V[\mathcal{E}_0]\,e^{-\frac{t}{\tau_h}}}{\tau_{\mathcal{E}}\tau_h^2-\tau_h^3}-\frac{4\tau_{\mathcal{E}}^3 V[\mathcal{E}_0]\,e^{-\frac{t}{\tau_{\mathcal{E}}}}}{\tau_{\mathcal{E}}\tau_h^2-\tau_h^3}-\frac{4\tau_{\mathcal{E}}^3 V[\mathcal{E}_0]\,e^{-\frac{t}{\tau_{\mathcal{E}}}}e^{-\frac{t}{\tau_h}}}{\tau_{\mathcal{E}}\tau_h^2-\tau_h^3}+\\
&+\frac{2\tau_{\mathcal{E}}^3 V[\mathcal{E}_0]\,e^{-\frac{2t}{\tau_{\mathcal{E}}}}}{\tau_{\mathcal{E}}\tau_h^2-\tau_h^3}-\frac{\tau_{\mathcal{E}}^2\tau_h V[\mathcal{E}_0]}{-\tau_{\mathcal{E}}^3+\tau_{\mathcal{E}}^2\tau_h+\tau_{\mathcal{E}}\tau_h^2-\tau_h^3}+\frac{\tau_{\mathcal{E}}^2\tau_h V[\mathcal{E}_0]\,e^{-\frac{2t}{\tau_h}}}{-\tau_{\mathcal{E}}^3+\tau_{\mathcal{E}}^2\tau_h+\tau_{\mathcal{E}}\tau_h^2-\tau_h^3}+\\
&+\frac{\tau_{\mathcal{E}}^2 V[\mathcal{E}_0]\,e^{-\frac{2t}{\tau_h}}}{\tau_{\mathcal{E}}^2-2\tau_{\mathcal{E}}\tau_h+\tau_h^2}-\frac{2\tau_{\mathcal{E}}^2 V[\mathcal{E}_0]\,e^{-\frac{t}{\tau_{\mathcal{E}}}}e^{-\frac{t}{\tau_h}}}{\tau_{\mathcal{E}}^2-2\tau_{\mathcal{E}}\tau_h+\tau_h^2}+\frac{\tau_{\mathcal{E}}^2 V[\mathcal{E}_0]\,e^{-\frac{2t}{\tau_{\mathcal{E}}}}}{\tau_{\mathcal{E}}^2-2\tau_{\mathcal{E}}\tau_h+\tau_h^2}+\frac{4\tau_{\mathcal{E}}^2 V[\mathcal{E}_0]}{\tau_{\mathcal{E}}\tau_h+\tau_h^2}-\\
&-\frac{4\tau_{\mathcal{E}}^2 V[\mathcal{E}_0]\,e^{-\frac{t}{\tau_{\mathcal{E}}}}e^{-\frac{t}{\tau_h}}}{\tau_{\mathcal{E}}\tau_h+\tau_h^2}+\frac{\tau_{\mathcal{E}}^2 V[\mathcal{E}_0]}{\tau_h^2}-\frac{4V[\mathcal{E}_0]}{\tau_h^2}\tau_{\mathcal{E}}^2 e^{-\frac{t}{\tau_h}}+\frac{4V[\mathcal{E}_0]}{\tau_h^2}\tau_{\mathcal{E}}^2 e^{-\frac{t}{\tau_{\mathcal{E}}}}e^{-\frac{t}{\tau_h}}-\\
&-\frac{\tau_{\mathcal{E}}^2 V[\mathcal{E}_0]}{\tau_h^2}e^{-\frac{2t}{\tau_{\mathcal{E}}}}+\frac{3\tau_{\mathcal{E}}\tau_h^2 V[\mathcal{E}_0]}{-\tau_{\mathcal{E}}^3+\tau_{\mathcal{E}}^2\tau_h+\tau_{\mathcal{E}}\tau_h^2-\tau_h^3}-\frac{4\tau_{\mathcal{E}}\tau_h^2 V[\mathcal{E}_0]\,e^{-\frac{t}{\tau_h}}}{-\tau_{\mathcal{E}}^3+\tau_{\mathcal{E}}^2\tau_h+\tau_{\mathcal{E}}\tau_h^2-\tau_h^3}+
\end{aligned}
$$

$$+\frac{\tau_{\mathcal{E}}\tau_h^2 V\left[\mathcal{E}_0\right]e^{-\frac{2t}{\tau_h}}}{-\tau_{\mathcal{E}}^3+\tau_{\mathcal{E}}^2\tau_h+\tau_{\mathcal{E}}\tau_h^2-\tau_h^3}+\frac{4\tau_{\mathcal{E}}V\left[\mathcal{E}_0\right]}{\tau_{\mathcal{E}}+\tau_h}-\frac{4\tau_{\mathcal{E}}V\left[\mathcal{E}_0\right]e^{-\frac{t}{\tau_{\mathcal{E}}}}}{\tau_{\mathcal{E}}+\tau_h}e^{-\frac{t}{\tau_h}}-$$
$$-\frac{4\tau_{\mathcal{E}}}{\tau_h}V\left[\mathcal{E}_0\right]e^{-\frac{t}{\tau_h}}+\frac{4\tau_{\mathcal{E}}}{\tau_h}V\left[\mathcal{E}_0\right]e^{-\frac{t}{\tau_{\mathcal{E}}}}e^{-\frac{t}{\tau_h}}-\frac{\tau_\eta^3 V\left[\eta_0\right]}{\tau_\eta^3+\tau_\eta^2\tau_h-\tau_\eta\tau_h^2-\tau_h^3}+$$
$$+\frac{\tau_\eta^3 V\left[\eta_0\right]e^{-\frac{t}{\tau_\eta}}e^{-\frac{t}{\tau_h}}}{\tau_\eta^3+\tau_\eta^2\tau_h-\tau_\eta\tau_h^2-\tau_h^3}+\frac{2\tau_\eta^3 V\left[\eta_0\right]e^{-\frac{t}{\tau_h}}}{-\tau_\eta^3+\tau_\eta^2\tau_h+\tau_\eta\tau_h^2-\tau_h^3}-$$
$$-\frac{2\tau_\eta^3 V\left[\eta_0\right]e^{-\frac{t}{\tau_\eta}}}{-\tau_\eta^3+\tau_\eta^2\tau_h+\tau_\eta\tau_h^2-\tau_h^3}-\frac{\tau_\eta^3 V\left[\eta_0\right]e^{-\frac{t}{\tau_\eta}}e^{-\frac{t}{\tau_h}}}{-\tau_\eta^3+\tau_\eta^2\tau_h+\tau_\eta\tau_h^2-\tau_h^3}+$$
$$+\frac{\tau_\eta^3 V\left[\eta_0\right]e^{-\frac{2t}{\tau_\eta}}}{-\tau_\eta^3+\tau_\eta^2\tau_h+\tau_\eta\tau_h^2-\tau_h^3}-\frac{\tau_\eta^2\tau_h V\left[\eta_0\right]}{\tau_\eta^3+\tau_\eta^2\tau_h-\tau_\eta\tau_h^2-\tau_h^3}+$$
$$+\frac{\tau_\eta^2\tau_h V\left[\eta_0\right]e^{-\frac{t}{\tau_\eta}}e^{-\frac{t}{\tau_h}}}{\tau_\eta^3+\tau_\eta^2\tau_h-\tau_\eta\tau_h^2-\tau_h^3}+\frac{\tau_\eta^2\tau_h V\left[\eta_0\right]e^{-\frac{2t}{\tau_h}}}{-\tau_\eta^3+3\tau_\eta^2\tau_h-3\tau_\eta\tau_h^2+\tau_h^3}-$$
$$-\frac{4\tau_\eta^2\tau_h V\left[\eta_0\right]e^{-\frac{t}{\tau_\eta}}e^{-\frac{t}{\tau_h}}}{-\tau_\eta^3+3\tau_\eta^2\tau_h-3\tau_\eta\tau_h^2+\tau_h^3}+\frac{3\tau_\eta^2\tau_h V\left[\eta_0\right]e^{-\frac{2t}{\tau_\eta}}}{-\tau_\eta^3+3\tau_\eta^2\tau_h-3\tau_\eta\tau_h^2+\tau_h^3}-$$
$$-\frac{\tau_\eta^2\tau_h V\left[\eta_0\right]e^{-\frac{t}{\tau_\eta}}e^{-\frac{t}{\tau_h}}}{-\tau_\eta^3+\tau_\eta^2\tau_h+\tau_\eta\tau_h^2-\tau_h^3}+\frac{\tau_\eta^2\tau_h V\left[\eta_0\right]e^{-\frac{2t}{\tau_\eta}}}{-\tau_\eta^3+\tau_\eta^2\tau_h+\tau_\eta\tau_h^2-\tau_h^3}-$$
$$-\frac{4\tau_\eta^2 V\left[\eta_0\right]e^{-\frac{t}{\tau_h}}}{\tau_\eta^2-2\tau_\eta\tau_h+\tau_h^2}+\frac{2\tau_\eta^2 V\left[\eta_0\right]e^{-\frac{t}{\tau_\eta}}}{\tau_\eta^2-2\tau_\eta\tau_h+\tau_h^2}+\frac{4\tau_\eta^2 V\left[\eta_0\right]e^{-\frac{t}{\tau_\eta}}e^{-\frac{t}{\tau_h}}}{\tau_\eta^2-2\tau_\eta\tau_h+\tau_h^2}-$$
$$-\frac{2\tau_\eta^2 V\left[\eta_0\right]e^{-\frac{2t}{\tau_\eta}}}{\tau_\eta^2-2\tau_\eta\tau_h+\tau_h^2}+\frac{2\tau_\eta^2 V\left[\eta_0\right]}{-\tau_\eta^2+\tau_h^2}-\frac{2\tau_\eta^2 V\left[\eta_0\right]e^{-\frac{t}{\tau_h}}}{-\tau_\eta^2+\tau_h^2}-\frac{2\tau_\eta^2 V\left[\eta_0\right]e^{-\frac{t}{\tau_\eta}}}{-\tau_\eta^2+\tau_h^2}+$$
$$+\frac{2\tau_\eta^2 V\left[\eta_0\right]e^{-\frac{t}{\tau_\eta}}e^{-\frac{t}{\tau_h}}}{-\tau_\eta^2+\tau_h^2}-\frac{2\tau_\eta\tau_h^2 V\left[\eta_0\right]e^{-\frac{t}{\tau_h}}}{-\tau_\eta^3+\tau_\eta^2\tau_h+\tau_\eta\tau_h^2-\tau_h^3}+$$
$$+\frac{2\tau_\eta\tau_h^2 V\left[\eta_0\right]e^{-\frac{2t}{\tau_h}}}{-\tau_\eta^3+\tau_\eta^2\tau_h+\tau_\eta\tau_h^2-\tau_h^3}+\frac{2\tau_\eta\tau_h^2 V\left[\eta_0\right]e^{-\frac{t}{\tau_\eta}}}{-\tau_\eta^3+\tau_\eta^2\tau_h+\tau_\eta\tau_h^2-\tau_h^3}-$$
$$-\frac{2\tau_\eta\tau_h^2 V\left[\eta_0\right]e^{-\frac{t}{\tau_\eta}}e^{-\frac{t}{\tau_h}}}{-\tau_\eta^3+\tau_\eta^2\tau_h+\tau_\eta\tau_h^2-\tau_h^3}+\frac{4\tau_\eta\tau_h V\left[\eta_0\right]e^{-\frac{t}{\tau_\eta}}}{\tau_\eta^2-2\tau_\eta\tau_h+\tau_h^2}-$$
$$-\frac{2\tau_\eta\tau_h V\left[\eta_0\right]e^{-\frac{t}{\tau_\eta}}e^{-\frac{t}{\tau_h}}}{\tau_\eta^2-2\tau_\eta\tau_h+\tau_h^2}-\frac{2\tau_\eta\tau_h V\left[\eta_0\right]e^{-\frac{2t}{\tau_\eta}}}{\tau_\eta^2-2\tau_\eta\tau_h+\tau_h^2}+\frac{2\tau_\eta\tau_h V\left[\eta_0\right]}{-\tau_\eta^2+\tau_h^2}-$$
$$-\frac{2\tau_\eta\tau_h V\left[\eta_0\right]e^{-\frac{t}{\tau_h}}}{-\tau_\eta^2+\tau_h^2}-\frac{2\tau_\eta\tau_h V\left[\eta_0\right]e^{-\frac{t}{\tau_\eta}}}{-\tau_\eta^2+\tau_h^2}+\frac{2\tau_\eta\tau_h V\left[\eta_0\right]e^{-\frac{t}{\tau_\eta}}e^{-\frac{t}{\tau_h}}}{-\tau_\eta^2+\tau_h^2}+$$
$$+\frac{2\tau_\eta V\left[\eta_0\right]e^{\frac{t}{\tau_\eta}}e^{-\frac{t}{\tau_h}}}{-\tau_\eta+\tau_h}-\frac{6\tau_\eta V\left[\eta_0\right]}{-\tau_\eta+\tau_h}+\frac{4\tau_\eta V\left[\eta_0\right]e^{-\frac{t}{\tau_h}}}{-\tau_\eta+\tau_h}+$$

$$
\begin{aligned}
&+\frac{4\tau_\eta V[\eta_0]\,e^{-\frac{t}{\tau_\eta}}}{-\tau_\eta+\tau_h}-\frac{4\tau_\eta V[\eta_0]\,e^{-\frac{2t}{\tau_\eta}}}{-\tau_\eta+\tau_h}-\frac{3\tau_h^3 V[\eta_0]}{-\tau_\eta^3+\tau_\eta\tau_h^2}+\\
&+\frac{4\tau_h^3 V[\eta_0]\,e^{-\frac{t}{\tau_h}}}{-\tau_\eta^3+\tau_\eta\tau_h^2}-\frac{\tau_h^3 V[\eta_0]\,e^{-\frac{2t}{\tau_h}}}{-\tau_\eta^3+\tau_\eta\tau_h^2}+\frac{\tau_h^2 V[\eta_0]\,e^{-\frac{2t}{\tau_h}}}{\tau_\eta^2-2\tau_\eta\tau_h+\tau_h^2}-\\
&-\frac{2\tau_h^2 V[\eta_0]\,e^{-\frac{t}{\tau_\eta}}}{\tau_\eta^2-2\tau_\eta\tau_h+\tau_h^2}+\frac{\tau_h^2 V[\eta_0]\,e^{-\frac{2t}{\tau_\eta}}}{\tau_\eta^2-2\tau_\eta\tau_h+\tau_h^2}-\frac{2\tau_h^2 V[\eta_0]}{-\tau_\eta^2+\tau_h^2}+\\
&+\frac{4\tau_h^2 V[\eta_0]\,e^{-\frac{t}{\tau_h}}}{-\tau_\eta^2+\tau_h^2}-\frac{2\tau_h^2 V[\eta_0]\,e^{-\frac{2t}{\tau_h}}}{-\tau_\eta^2+\tau_h^2}+\frac{4\tau_h V[\eta_0]}{-\tau_\eta+\tau_h}-\\
&-\frac{4\tau_h V[\eta_0]\,e^{-\frac{t}{\tau_h}}}{-\tau_\eta+\tau_h}-\frac{4\tau_h V[\eta_0]\,e^{-\frac{t}{\tau_\eta}}}{-\tau_\eta+\tau_h}+\frac{4\tau_h V[\eta_0]\,e^{-\frac{t}{\tau_\eta}}e^{-\frac{t}{\tau_h}}}{-\tau_\eta+\tau_h}-\\
&-3V[\eta_0]+4V[\eta_0]\,e^{-\frac{t}{\tau_h}}-2V[\eta_0]\,e^{-\frac{t}{\tau_\eta}}+2V[\eta_0]\,e^{-\frac{t}{\tau_\eta}}e^{-\frac{t}{\tau_h}}-\\
&\qquad-V[\eta_0]\,e^{-\frac{2t}{\tau_\eta}}+V\left[\widetilde{\rho}_u^{(k)}(0)\right]e^{-\frac{2t}{\tau_h}}-\frac{4\tau_h}{\tau_\eta}V[\eta_0]+\frac{4\tau_h}{\tau_\eta}V[\eta_0]\,e^{-\frac{t}{\tau_h}}
\end{aligned}
\tag{C.22}
$$

D. Expectation of Various Integrals of Brownian Motions

D.1. Expectation of $X_t = B_t \int_0^t B_s ds$

$$E[X_t] = E\left[B_t \int_0^t B_s ds\right] \tag{D.1}$$

We define $\Delta t = t/n$ and $t_k = k\Delta t$. The Riemann sum approximation of $X_t$is:

$$X_{t_n} = B_{t_n} \sum_{k=0}^{n-1} B_{t_k} \Delta t \tag{D.2}$$

$$E[X_{t_n}] = E\left[B_{t_n} \sum_{k=0}^{n-1} B_{t_k} \Delta t\right] \tag{D.3}$$

$$E[X_{t_n}] = \Delta t \sum_{k=0}^{n-1} E[B_{t_n} B_{t_k}] \tag{D.4}$$

$$E[X_{t_n}] = \Delta t \sum_{k=0}^{n-1} (t_n \wedge t_k) \tag{D.5}$$

where $t_n \wedge t_k = \min(t_n, t_k)$

$$E[X_{t_n}] = \Delta t \sum_{k=0}^{n-1} t_k \tag{D.6}$$

$$E[X_{t_n}] = \Delta t^2 \sum_{k=0}^{n-1} k \tag{D.7}$$

$$E\left[X_{t_n}\right] = \Delta t^2 \frac{n\left(n-1\right)}{2} \tag{D.8}$$

$$E\left[X_{t_n}\right] = \frac{t^2}{n^2} \frac{n\left(n-1\right)}{2} \tag{D.9}$$

By continuity we have $E\left[X_{t_n}\right] \to E\left[X_t\right]$ when $n \to \infty$ and

$$E\left[X_t\right] = \frac{t^2}{2} \tag{D.10}$$

D.2. Expectation of $X_t = \eta_t\left(\tau\right)\mu_t\left(\tau\right)$

with $\eta_t\left(\tau\right) = \int_0^t \int_0^r e^{\frac{u-r}{\tau}} dB_u dr$ and $\mu_t\left(\tau\right) = \int_0^t \int_0^r \int_0^q e^{\frac{u-q}{\tau}} dB_u dq dr = \int_0^t \eta_r\left(\tau\right) dr$ we rewrite $\eta_t\left(\tau\right)$ and $\mu_t\left(\tau\right)$ using successive integration by parts formula. Let's start with $\eta_t\left(\tau\right)$

$$\eta_t\left(\tau\right) = \int_0^t e^{\frac{-r}{\tau}} \int_0^r e^{\frac{u}{\tau}} dB_u dr$$

$$\int_0^r e^{\frac{u}{\tau}} dB_u = \left[e^{\frac{u}{\tau}} B_u\right]_0^r - \frac{1}{\tau}\int_0^r e^{\frac{u}{\tau}} B_u du$$

$$\int_0^r e^{\frac{u}{\tau}} dB_u = e^{\frac{r}{\tau}} B_r - \frac{1}{\tau}\int_0^r e^{\frac{u}{\tau}} B_u du$$

$$\eta_t\left(\tau\right) = \int_0^t e^{\frac{-r}{\tau}} \left(e^{\frac{r}{\tau}} B_r - \frac{1}{\tau}\int_0^r e^{\frac{u}{\tau}} B_u du\right) dr$$

$$\eta_t\left(\tau\right) = \int_0^t B_r dr - \frac{1}{\tau}\int_0^t \int_0^r e^{\frac{u-r}{\tau}} B_u du dr$$

With $\mu_t\left(\tau\right) = \int_0^t \eta_r\left(\tau\right) dr$, we have:

$$\mu_t(\tau) = \int_0^t \int_0^r B_u du dr - \frac{1}{\tau}\int_0^t \int_0^r \int_0^q e^{\frac{u-q}{\tau}} B_u du dq dr$$

$$X_t = \begin{array}{c} \int_0^t B_r dr \int_0^t \int_0^r B_u du dr - \frac{1}{\tau}\int_0^t \int_0^r e^{\frac{u-r}{\tau}} B_u du dr \int_0^t \int_0^r B_u du dr \\ -\frac{1}{\tau}\int_0^t B_r dr \int_0^t \int_0^r \int_0^q e^{\frac{u-q}{\tau}} B_u du dq dr + \frac{1}{\tau^2}\int_0^t \int_0^r e^{\frac{u-r}{\tau}} B_u du dr \int_0^t \int_0^r \int_0^q e^{\frac{u-q}{\tau}} B_u du dq dr \end{array} \tag{D.11}$$

$$E[X_t] = \begin{array}{c} E\left[\int_0^t B_r dr \int_0^t \int_0^r B_u du dr\right] - \frac{1}{\tau}E\left[\int_0^t \int_0^r e^{\frac{u-r}{\tau}} B_u du dr \int_0^t \int_0^r B_u du dr\right] \\ -\frac{1}{\tau}E\left[\int_0^t B_r dr \int_0^t \int_0^r \int_0^q e^{\frac{u-q}{\tau}} B_u du dq dr\right] + \frac{1}{\tau^2}E\left[\int_0^t \int_0^r e^{\frac{u-r}{\tau}} B_u du dr \int_0^t \int_0^r \int_0^q e^{\frac{u-q}{\tau}} B_u du dq dr\right] \end{array} \tag{D.12}$$

We define $\Delta t = t/n$ and $t_k = k\Delta t$. X_t can be approximated using the Riemann sum approximation:

$$X_{t_n} = \begin{array}{c} X_{1t_n} + X_{2t_n} \\ +X_{3t_n} + X_{4t_n} \end{array} \tag{D.13}$$

$$X_{1t_n} = \left(\sum_{i=0}^{n-1} B_{t_i}\Delta t\right)\left(\sum_{j=0}^{n-1}\sum_{k=0}^{j} B_{t_k}\Delta t^2\right) \tag{D.14}$$

$$X_{1t_n} = \Delta t^3 \sum_{i,j=0}^{n-1}\left(B_{t_i}\sum_{k=0}^{j} B_{t_k}\right) \tag{D.15}$$

$$X_{1t_n} = \Delta t^3 \sum_{i,j=0}^{n-1}\sum_{k=0}^{j}\left(B_{t_i}B_{t_k}\right) \tag{D.16}$$

$$E[X_{1t_n}] = \Delta t^3 \sum_{i,j=0}^{n-1}\sum_{k=0}^{j}\left(t_i \wedge t_k\right) \tag{D.17}$$

$$E\left[X_{1t_n}\right] = \Delta t^4 \sum_{i,j=0}^{n-1} \sum_{k=0}^{j} (i \wedge k) \tag{D.18}$$

$$E\left[X_{1t_n}\right] = \frac{t^4}{n^4} \sum_{i,j=0}^{n-1} \sum_{k=0}^{j} (i \wedge k) \tag{D.19}$$

$$\frac{n^4}{t^4} E\left[X_{1t_n}\right] = \sum_{i,j=0}^{n-1} \sum_{k=0}^{j} (i \wedge k) \tag{D.20}$$

$$\frac{n^4}{t^4} E\left[X_{1t_n}\right] = \sum_{i=0}^{n-1} \sum_{j=0}^{n-1} \sum_{k=0}^{j} (i \wedge k)$$

$$\frac{n^4}{t^4} E\left[X_{1t_n}\right] = \sum_{i=0}^{n-1} \left(\sum_{j=0}^{i-1} \sum_{k=0}^{j} (i \wedge k) + \sum_{j=i}^{n-1} \sum_{k=0}^{j} (i \wedge k) \right)$$

in the first term of the right side of the equation, $(i \wedge k) = k$ because $k \leqslant i$.

$$\frac{n^4}{t^4} E\left[X_{1t_n}\right] = \sum_{i=0}^{n-1} \left(\sum_{j=0}^{i-1} \sum_{k=0}^{j} k + \sum_{j=i}^{n-1} \left(\sum_{k=0}^{i-1} (i \wedge k) + \sum_{k=i}^{j} (i \wedge k) \right) \right)$$

$$\frac{n^4}{t^4} E\left[X_{1t_n}\right] = \sum_{i=0}^{n-1} \left(\sum_{j=0}^{i-1} \sum_{k=0}^{j} k + \sum_{j=i}^{n-1} \left(\sum_{k=0}^{i-1} k + \sum_{k=i}^{j} i \right) \right)$$

We use Python (sympy package) to do the calculations. After expressing $E\left[X_{1t_n}\right]$ we take the limit when $n \to \infty$ to finally find:

$$E\left[X_{1t}\right] = \frac{1}{8} t^4$$

We now express $E\left[X_{2t}\right]$ given that:

$$X_{2t} = -\frac{1}{\tau}\int_0^t \int_0^r e^{\frac{u-r}{\tau}} B_u du dr \int_0^t \int_0^r B_u du dr$$

$$X_{2t_n} = -\frac{1}{\tau}\left(\sum_{i=0}^{n-1}\sum_{k=0}^{i} e^{\frac{t_k - t_i}{\tau}} B_{t_k}\Delta t^2\right)\left(\sum_{j=0}^{n-1}\sum_{l=0}^{j} B_{t_l}\Delta t^2\right) \tag{D.21}$$

In order to avoid any confusion, we choose different summation indexes.

$$X_{2t_n} = -\frac{\Delta t^4}{\tau}\left(\sum_{i,j=0}^{n-1}\sum_{k,l=0}^{i,j} e^{\frac{t_l - t_i}{\tau}} B_{t_l} B_{t_k}\right) \tag{D.22}$$

$$E\left[X_{2t_n}\right] = -\frac{\Delta t^4}{\tau}\left(\sum_{i,j=0}^{n-1}\sum_{k,l=0}^{i,j} e^{\frac{t_l - t_i}{\tau}} (t_l \wedge t_k)\right) \tag{D.23}$$

$$E\left[X_{2t_n}\right] = -\frac{t^5}{\tau n^5}\left(\sum_{i,j=0}^{n-1}\sum_{k,l=0}^{i,j} e^{\frac{t_l - t_i}{\tau}} (l \wedge k)\right) \tag{D.24}$$

$$E\left[X_{2t_n}\right] = -\frac{t^5}{\tau n^5}\sum_{i,j=0}^{n-1}\sum_{k,l=0}^{i,j} e^{\frac{t_l - t_i}{\tau}} (l \wedge k) \tag{D.25}$$

We define $r = e^{\frac{\Delta t}{\tau}} = e^{\frac{t}{\tau n}}$

$$\frac{n^5}{t^5} E\left[X_{2t_n}\right] = \sum_{i=0}^{n-1}\left[\sum_{j=0}^{i-1}\sum_{k,l=0}^{i,j} r^{l-i}(l \wedge k) + \sum_{j=i}^{n-1}\sum_{k,l=0}^{i,j} r^{l-i}(l \wedge k)\right] \tag{D.26}$$

We are going to omit the terms $r^{l-i}(l \wedge k)$ as we are concentrating our efforts in partitioning the summations in order that in each partition, we can order l and k and therefore simplify$l \wedge k$.

$$\sum_{i=0}^{n-1}\left[\sum_{j=0}^{i-1}\sum_{k,l=0}^{i,j} + \sum_{j=i}^{n-1}\sum_{k,l=0}^{i,j}\right]$$

$$= \sum_{i=0}^{n-1}\left[\sum_{j=0}^{i-1}\sum_{l=0}^{j}\sum_{k=0}^{i} + \sum_{j=i}^{n-1}\sum_{l=0}^{j}\sum_{k=0}^{i}\right]$$

$$= \sum_{i=0}^{n-1} \left[\sum_{j=0}^{i-1} \sum_{l=0}^{j} \left[\sum_{k=0}^{l-1} + \sum_{k=l}^{i} \right] + \sum_{j=i}^{n-1} \left[\sum_{l=0}^{i-1} + \sum_{l=i}^{j} \right] \sum_{k=0}^{i} \right]$$

$$= \sum_{i=0}^{n-1} \left[\sum_{j=0}^{i-1} \sum_{l=0}^{j} \left[\sum_{k=0}^{l-1} \{1\} + \sum_{k=l}^{i} \{2\} \right] + \sum_{j=i}^{n-1} \left[\sum_{l=0}^{i-1} \left[\sum_{k=0}^{l-1} \{3\} + \sum_{k=l}^{i} \{4\} \right] + \sum_{l=i}^{j} \sum_{k=0}^{i} \{5\} \right] \right]$$

in $\{1\}$ we have $l \wedge k = k$

in $\{2\}$ we have $l \wedge k = l$

in $\{3\}$ we have $l \wedge k = k$

in $\{4\}$ we have $l \wedge k = l$

in $\{5\}$ we have $l \wedge k = k$

We use Python (sympy package) to do the calculations. After expressing $E\left[X_{2t_n}\right]$ we take the limit when $n \to \infty$ to finally find:

$$E\left[X_{2t}\right] = t^2\tau^2 + \frac{t^2\tau^2}{e^{\frac{t}{\tau}}} + 2t\tau^3 + 4\frac{t\tau^3}{e^{\frac{t}{\tau}}} - \tau^4 e^{\frac{t}{\tau}} - 4\tau^4 + 5\frac{\tau^4}{e^{\frac{t}{\tau}}}$$

we calculate now the expectation of X_{3t}

$$E\left[X_{3t}\right] = -\frac{1}{\tau} E\left[\int_0^t B_r dr \int_0^t \int_0^r \int_0^q e^{\frac{u-q}{\tau}} B_u du dq dr \right]$$

$$E\left[X_{3t}\right] = -\frac{1}{\tau} E\left[\sum_{i=0}^{n-1} B_{t_i} \Delta t \sum_{j=0}^{n-1} \sum_{k=0}^{j} \sum_{l=0}^{k} e^{\frac{t_l - t_k}{\tau}} B_{t_l} \Delta t^3 \right]$$

$$E\left[X_{3t}\right] = -\frac{\Delta t^4}{\tau} E\left[\sum_{i=0}^{n-1} \sum_{j=0}^{n-1} \sum_{k=0}^{j} \sum_{l=0}^{k} e^{\frac{t_l - t_k}{\tau}} B_{t_i} B_{t_l} \right]$$

As in the previous development, we define $r = e^{\frac{\Delta t}{\tau}} = e^{\frac{t}{\tau n}}$:

$$E\left[X_{3t}\right] = -\frac{t^4}{\tau n^4} \sum_{i=0}^{n-1} \sum_{j=0}^{n-1} \sum_{k=0}^{j} \sum_{l=0}^{k} r^{l-k} E\left[B_{t_i} B_{t_l}\right]$$

$$E\left[X_{3t}\right] = -\frac{t^5}{\tau n^5} \sum_{i=0}^{n-1} \sum_{j=0}^{n-1} \sum_{k=0}^{j} \sum_{l=0}^{k} r^{l-k} \left(i \wedge l\right)$$

In the same way as before, we partition the sums in order to have an explicit form of $i \wedge l$.

$$\sum_{i=0}^{n-1}\sum_{j=0}^{n-1}\sum_{k=0}^{j}\sum_{l=0}^{k}$$

$$= \sum_{i=0}^{n-1}\left[\sum_{j=0}^{i-1}\sum_{k=0}^{j}\sum_{l=0}^{k} + \sum_{j=i}^{n-1}\sum_{k=0}^{j}\sum_{l=0}^{k}\right]$$

$$= \sum_{i=0}^{n-1}\left[\sum_{j=0}^{i-1}\sum_{k=0}^{j}\sum_{l=0}^{k} + \sum_{j=i}^{n-1}\left[\sum_{k=0}^{i-1}\sum_{l=0}^{k} + \sum_{k=i}^{j}\sum_{l=0}^{k}\right]\right]$$

$$= \sum_{i=0}^{n-1}\left[\sum_{j=0}^{i-1}\sum_{k=0}^{j}\sum_{l=0}^{k} + \sum_{j=i}^{n-1}\left[\sum_{k=0}^{i-1}\sum_{l=0}^{k} + \sum_{k=i}^{j}\left[\sum_{l=0}^{i-1} + \sum_{l=i}^{k}\right]\right]\right]$$

$$E[X_{3t}] = -\frac{t^5}{\tau n^5}\sum_{i=0}^{n-1}\left[\sum_{j=0}^{i-1}\sum_{k=0}^{j}\sum_{l=0}^{k}\{1\} + \sum_{j=i}^{n-1}\left[\sum_{k=0}^{i-1}\sum_{l=0}^{k}\{2\} + \sum_{k=i}^{j}\left[\sum_{l=0}^{i-1}\{3\} + \sum_{l=i}^{k}\{4\}\right]\right]\right]$$

in $\{1\}$ we have $l \wedge i = l$

in $\{2\}$ we have $l \wedge i = l$

in $\{3\}$ we have $l \wedge i = l$

in $\{4\}$ we have $l \wedge i = i$

We use Python (sympy package) to do the calculations. After expressing $E[X_{3t_n}]$ we take the limit when $n \to \infty$ to finally find:

$$E[X_{3t}] = -\frac{1}{8}t^4 + \frac{1}{3}t^3\tau - \frac{1}{2}t^2\tau^2 - \frac{t\tau^3}{e^{\frac{t}{\tau}}} + \tau^4 - \frac{\tau^4}{e^{\frac{t}{\tau}}}$$

we calculate now the expectation of X_{4t}

$$E[X_{4t}] = \frac{1}{\tau^2}E\left[\int_0^t\int_0^r e^{\frac{u-r}{\tau}}B_u du dr \int_0^t\int_0^r\int_0^q e^{\frac{u-q}{\tau}}B_u du dq dr\right]$$

$$E[X_{4t}] = \frac{1}{\tau^2}E\left[\sum_{i=0}^{n-1}\sum_{m=0}^{i} e^{\frac{t_m-t_i}{\tau}}B_{t_m}\Delta t^2 \sum_{j=0}^{n-1}\sum_{k=0}^{j}\sum_{l=0}^{k} e^{\frac{t_l-t_k}{\tau}}B_{t_l}\Delta t^3\right]$$

$$E[X_{4t}] = \frac{\Delta t^5}{\tau^2}E\left[\sum_{i=0}^{n-1}\sum_{m=0}^{i}\sum_{j=0}^{n-1}\sum_{k=0}^{j}\sum_{l=0}^{k} e^{\frac{t_m-t_i}{\tau}}e^{\frac{t_l-t_k}{\tau}}B_{t_m}B_{t_l}\right]$$

As in the previous development, we define $r = e^{\frac{\Delta t}{\tau}} = e^{\frac{t}{\tau n}}$:

$$E\left[X_{4t}\right] = \frac{\Delta t^5}{\tau^2} \sum_{i=0}^{n-1} \sum_{m=0}^{i} \sum_{j=0}^{n-1} \sum_{k=0}^{j} \sum_{l=0}^{k} r^{m-i+l-k} E\left[B_{t_m} B_{t_l}\right]$$

$$E\left[X_{4t}\right] = \frac{t^6}{\tau^2 n^6} \sum_{i=0}^{n-1} \sum_{m=0}^{i} \sum_{j=0}^{n-1} \sum_{k=0}^{j} \sum_{l=0}^{k} r^{m-i+l-k} \left(m \wedge l\right)$$

In the same way as before, we partition the sums in order to have an explicit form of $m \wedge l$.

$$\sum_{i=0}^{n-1} \sum_{m=0}^{i} \sum_{j=0}^{n-1} \sum_{k=0}^{j} \sum_{l=0}^{k}$$

$$= \sum_{i=0}^{n-1} \sum_{m=0}^{i} \left[\sum_{j=0}^{m-1} \sum_{k=0}^{j} \sum_{l=0}^{k} + \sum_{j=m}^{n-1} \left[\sum_{k=0}^{m-1} \sum_{l=0}^{k} + \sum_{k=m}^{j} \sum_{l=0}^{k} \right] \right]$$

$$= \sum_{i=0}^{n-1} \sum_{m=0}^{i} \left[\sum_{j=0}^{m-1} \sum_{k=0}^{j} \sum_{l=0}^{k} + \sum_{j=m}^{n-1} \left[\begin{array}{c} \sum_{k=0}^{m-1} \sum_{l=0}^{k} + \\ \sum_{k=m}^{j} \sum_{l=0}^{m-1} + \\ \sum_{k=m}^{j} \sum_{l=m}^{k} \end{array} \right] \right]$$

$$E\left[X_{4t}\right] = \frac{t^6}{\tau^2 n^6} \sum_{i=0}^{n-1} \sum_{m=0}^{i} \left[\sum_{j=0}^{m-1} \sum_{k=0}^{j} \sum_{l=0}^{k} \{1\} + \sum_{j=m}^{n-1} \left[\begin{array}{c} \sum_{k=0}^{m-1} \sum_{l=0}^{k} \{2\} \\ + \sum_{k=m}^{j} \sum_{l=0}^{m-1} \{3\} \\ + \sum_{k=m}^{j} \sum_{l=m}^{k} \{4\} \end{array} \right] \right]$$

in $\{1\}$ we have $l \wedge m = l$

in $\{2\}$ we have $l \wedge m = l$

in $\{3\}$ we have $l \wedge m = l$

in $\{4\}$ we have $l \wedge m = m$

We use Python (sympy package) to do the calculations. After expressing $E\left[X_{4t_n}\right]$ we take the limit when $n \to \infty$ to finally find:

$$E\left[X_{4t}\right] = \frac{1}{8}t^4 - \frac{1}{2}t^3\tau + t^2\tau^2 - \frac{t^2\tau^2}{2e^{\frac{t}{\tau}}} - t\tau^3 + \frac{t\tau^3}{e^{\frac{t}{\tau}}} + \frac{1}{2}\tau^4 - \frac{\tau^4}{e^{\frac{t}{\tau}}} + \frac{\tau^4}{2e^{2\frac{t}{\tau}}}$$

The expectation of X_t is the sum of the four expectation previously defined.

$$E[X_t] = E[X_{1t}] + E[X_{2t}] + E[X_{3t}] + E[X_{4t}] \tag{D.27}$$

$$\begin{aligned} E[X_t] = {} & \tfrac{1}{8}t^4 + t^2\tau^2 + \tfrac{t^2\tau^2}{e^{\frac{t}{\tau}}} + 2t\tau^3 + 4\tfrac{t\tau^3}{e^{\frac{t}{\tau}}} - \tau^4 e^{\frac{t}{\tau}} - 4\tau^4 \\ & + 5\tfrac{\tau^4}{e^{\frac{t}{\tau}}} - \tfrac{1}{8}t^4 + \tfrac{1}{3}t^3\tau - \tfrac{1}{2}t^2\tau^2 - \tfrac{t\tau^3}{e^{\frac{t}{\tau}}} + \tau^4 - \tfrac{\tau^4}{e^{\frac{t}{\tau}}} \\ & \tfrac{1}{8}t^4 - \tfrac{1}{2}t^3\tau + t^2\tau^2 - \tfrac{t^2\tau^2}{2e^{\frac{t}{\tau}}} - t\tau^3 + \tfrac{t\tau^3}{e^{\frac{t}{\tau}}} + \tfrac{1}{2}\tau^4 - \tfrac{\tau^4}{e^{\frac{t}{\tau}}} + \tfrac{\tau^4}{2e^{2\frac{t}{\tau}}} \end{aligned} \tag{D.28}$$

$$\begin{aligned} E[X_t] = {} & \tfrac{t^2\tau^2}{2e^{\frac{t}{\tau}}} + t\tau^3 + 4\tfrac{t\tau^3}{e^{\frac{t}{\tau}}} - \tau^4 e^{\frac{t}{\tau}} \\ & + 3\tfrac{\tau^4}{e^{\frac{t}{\tau}}} - \tfrac{1}{6}t^3\tau + \tfrac{3}{2}t^2\tau^2 \\ & \tfrac{1}{8}t^4 - \tfrac{5}{2}\tau^4 + \tfrac{\tau^4}{2e^{2\frac{t}{\tau}}} \end{aligned} \tag{D.29}$$

D.3. Expectation of $X_t = \mu_t(\tau)\int_0^t e^{\frac{u-t}{\tau}} dB_{b_1 u}$

With $\mu_t(\tau) = \int_0^t \int_0^r B_u du dr - \frac{1}{\tau}\int_0^t \int_0^r \int_0^q e^{\frac{u-q}{\tau}} B_u du dq dr$
We use an integration par part to express $\int_0^t e^{\frac{u-t}{\tau}} dB_{b_1 u}$

$$\int_0^t e^{\frac{u-t}{\tau}} dB_{b_1 u} = e^{\frac{-t}{\tau}} \int_0^t e^{\frac{u}{\tau}} dB_{b_1 u}$$

$$\int_0^t e^{\frac{u-t}{\tau}} dB_{b_1 u} = e^{\frac{-t}{\tau}} \left[e^{\frac{t}{\tau}} B_{b_1 t} - \frac{1}{\tau}\int_0^t e^{\frac{u}{\tau}} B_{b_1 u} du \right]$$

$$\int_0^t e^{\frac{u-t}{\tau}} dB_{b_1 u} = B_{b_1 t} - \frac{1}{\tau}\int_0^t e^{\frac{u-t}{\tau}} B_{b_1 u} du$$

Therefore we have (We omit the $b_1$index in the Brownian motion):

$$X_t = \begin{array}{c} \int_0^t \int_0^r B_t B_u du dr - \frac{1}{\tau}\int_0^t \int_0^r \int_0^q e^{\frac{u-q}{\tau}} B_t B_u du dq dr \\ -\frac{1}{\tau}\int_0^t e^{\frac{r-t}{\tau}} B_r dr \int_0^t \int_0^r B_u du dr + \frac{1}{\tau^2}\int_0^t e^{\frac{r-t}{\tau}} B_r dr \int_0^t \int_0^r \int_0^q e^{\frac{u-q}{\tau}} B_u du dq dr \end{array}$$

The expectation of X_t is simply:

$$E[X_t] = \begin{array}{c} \int_0^t \int_0^r u du dr - \frac{1}{\tau}\int_0^t \int_0^r \int_0^q e^{\frac{u-q}{\tau}} u du dq dr \\ -\frac{1}{\tau}\int_0^t \int_0^t \int_0^r e^{\frac{r'-t}{\tau}} (r' \wedge u)\, du dr dr' + \frac{1}{\tau^2}\int_0^t \int_0^t \int_0^r \int_0^q e^{\frac{r'-t+u-q}{\tau}} (r' \wedge u)\, du dq dr dr' \end{array}$$

We use the same procedure as before by considering this time the continuous time case. The two first terms can be solved directly. For the two other terms it is again necessary to partition the integrals in order to have an explicit form for $r' \wedge u$. This time we won't detail the procedure as it is similar to the procedure in the discrete case. Finally by using symbolic calculus we end up with:

$$E\left[X_t\right] = -\frac{t\tau^2}{e^{\frac{t}{\tau}}} + \frac{1}{2}\tau^3 - \frac{\tau^3}{2e^{2\frac{t}{\tau}}}$$

D.4. Expectation of $X_t = \eta_t\left(\tau\right)\int_0^t e^{\frac{u-t}{\tau}} dB_{b_1 u}$

With$\eta_t\left(\tau\right) = \int_0^t B_r dr - \frac{1}{\tau}\int_0^t \int_0^r e^{\frac{u-r}{\tau}} B_u du dr$ and $\int_0^t e^{\frac{u-t}{\tau}} dB_{b_1 u} = B_{b_1 t} - \frac{1}{\tau}\int_0^t e^{\frac{u-t}{\tau}} B_{b_1 u} du$

$$X_t = \begin{array}{c} \int_0^t B_t B_r dr - \frac{1}{\tau}\int_0^t \int_0^r e^{\frac{u-r}{\tau}} B_t B_u du dr \\ -\frac{1}{\tau}\int_0^t e^{\frac{r-t}{\tau}} B_r dr \int_0^t B_r dr + \frac{1}{\tau^2}\int_0^t e^{\frac{r-t}{\tau}} B_r dr \int_0^t \int_0^r e^{\frac{u-r}{\tau}} B_u du dr \end{array}$$

$$E\left[X_t\right] = \begin{array}{c} \int_0^t r dr - \frac{1}{\tau}\int_0^t \int_0^r u e^{\frac{u-r}{\tau}} du dr \\ -\frac{1}{\tau}\int_0^t \int_0^t e^{\frac{r'-t}{\tau}} \left(r' \wedge r\right) dr dr' + \frac{1}{\tau^2}\int_0^t \int_0^t \int_0^r e^{\frac{r'-t+u-r}{\tau}} \left(r' \wedge u\right) du dr dr' \end{array}$$

In the same way as before, we have:

$$E\left[X_t\right] = \frac{1}{2}\tau^2 - \frac{\tau^2}{e^{\frac{t}{\tau}}} + \frac{\tau^2}{2e^{2\frac{t}{\tau}}}$$

D.5. Variance of $\gamma_t\left(\tau\right)$

We recall that $\gamma_t\left(\tau\right) = \int_0^t B_{b_w u} du$.

The expectation of $\gamma_t\left(\tau\right)$ is equal to zero. Therefore the variance is simply $E\left[\left(\int_0^t B_{b_w u} du\right)^2\right] = \frac{t^3}{3}$

D.6. Variance of $\eta_t\left(\tau\right)$

We recall that $\eta_t\left(\tau\right) = \int_0^t B_r dr - \frac{1}{\tau}\int_0^t \int_0^r e^{\frac{u-r}{\tau}} B_u du dr$

The expectation of $\gamma_t\left(\tau\right)$ is equal to zero. Therefore the variance is:

$$V[\eta_t(\tau)] = E\left[\eta_t(\tau)^2\right]$$

$$V[\eta_t(\tau)] = \begin{array}{c} \frac{t^3}{3} + E\left[-\frac{2}{\tau}\int_0^t B_r dr \int_0^t \int_0^r e^{\frac{u-r}{\tau}} B_u du dr\right] \\ +E\left[\frac{1}{\tau^2}\int_0^t \int_0^r e^{\frac{u-r}{\tau}} B_u du dr \int_0^t \int_0^r e^{\frac{u-r}{\tau}} B_u du dr\right] \end{array}$$

$$V[\eta_t(\tau)] = \begin{array}{c} \frac{t^3}{3} - \frac{2}{\tau}\int_0^t \int_0^t \int_0^r e^{\frac{u-r}{\tau}} (r' \wedge u)\, du dr dr' \\ +\frac{1}{\tau^2}\int_0^t \int_0^{r'} \int_0^t \int_0^r e^{\frac{u'-r'+u-r}{\tau}} (u' \wedge u)\, du dr du' dr' \end{array}$$

$$V[\eta_t(\tau)] = t\tau^2 - \frac{3}{2}\tau^3 + 2\frac{\tau^3}{e^{\frac{t}{\tau}}} - \frac{\tau^3}{2e^{2\frac{t}{\tau}}}$$

D.7. Variance of $\mu_t(\tau)$

We recall that $\mu_t(\tau) = \int_0^t \int_0^r B_u du dr - \frac{1}{\tau}\int_0^t \int_0^r \int_0^q e^{\frac{u-q}{\tau}} B_u du dq dr$
The expectation of $\mu_t(\tau)$ is equal to zero. Therefore the variance is:

$$V[\mu_t(\tau)] = E\left[\mu_t(\tau)^2\right]$$

$$V[\mu_t(\tau)] = \begin{array}{c} E\left[\left(\int_0^t \int_0^r B_u du dr\right)^2\right] + E\left[-\frac{2}{\tau}\int_0^t \int_0^r B_u du dr \int_0^t \int_0^r \int_0^q e^{\frac{u-q}{\tau}} B_u du dq dr\right] \\ +E\left[\frac{1}{\tau^2}\left(\int_0^t \int_0^r \int_0^q e^{\frac{u-q}{\tau}} B_u du dq dr\right)^2\right] \end{array}$$

$$V[\mu_t(\tau)] = \begin{array}{c} \int_0^t \int_0^{r'} \int_0^t \int_0^r (u' \wedge u)\, du dr du' dr' \\ -\frac{2}{\tau}\int_0^t \int_0^{r'} \int_0^t \int_0^r \int_0^q e^{\frac{u-q}{\tau}} (u' \wedge u)\, du dq dr du' dr' \\ +\frac{1}{\tau^2}\int_0^t \int_0^{r'} \int_0^{q'} \int_0^t \int_0^r \int_0^q e^{\frac{u'-q'+u-q}{\tau}} (u' \wedge u)\, du dq dr du' dq' dr' \end{array}$$

$$V[\mu_t(\tau)] = \frac{1}{3}t^3\tau^2 - t^2\tau^3 + t\tau^4 - 2\frac{t\tau^4}{e^{\frac{t}{\tau}}} + \frac{1}{2}\tau^5 - \frac{\tau^5}{2e^{2\frac{t}{\tau}}}$$

Bibliography

[AIR01] AIRBUS. Getting to grips with CAT II/CAT III operations. Technical report, AIRBUS Flight Operations Support and Line Assistance, 2001.

[ARI00] ARINC. ICD-GPS-200C-004, space segment / navigation user interfaces. Technical report, Navstar GPS, 2000.

[BC98] R. G. Brown and Y. G. Chin. Gps raim: Calculation of threshold and protection radius using chi-square methods-a geometric approach. *Navigation*, V:155–178, 1998.

[BDF+10] Boubeker Belabbas, Thomas Dautermann, Michael Felux, Markus Rippl, Stefan Schlüter, Volker Wilken, Achim Hornbostel, and Michael Meurer. A GBAS Testbed to Support New Monitoring Algorithms Development for CAT III Precision Approach. In *ENC GNSS 2010*, 2010.

[BDLK10a] B. Belabbas, T. Dautermann, G. Looye, and J. Kladetzke. GBAS Based Autoland System: A Bottom Up Approach for GAST-D Requirements. In *ION-IEEE PLANS*, 2010.

[BDLK10b] Boubeker Belabbas, Thomas Dautermann, Gertjan Looye, and Jan Kladetzke. GBAS Based Autoland System: A Bottom Up Approach for GAST-D Requirements. In *Position, Location and Navigation Symposium*, pages 566 –574. IEEE, Mai 2010.

[BG02] J. W. Betz and D. B. Goldstein. Candidate designs for an additional civil signal in gps spectral bands. Technical report, MITRE, 2002.

[BG05] Boubeker Belabbas and Frédéric Gass. RAIM Algorithms Analysis for a Combined GPS/GALILEO Constellation. In *ION GNSS 2005*, September 2005.

[BG13] B. Belabbas and A. Grosch. Novel integrity monitoring for train navigation using a gnss-imu bayesian position estimator and a curvature change detector. In *ION GNSS+ 2013*, 2013.

[BGH+13a] Boubeker Belabbas, Anja Grosch, Oliver Heirich, Andreas Lehner, and Thomas Strang. Curvature change detection for trains using GNSS coasted with 3DoF IMU. In *ENC*, Vienna, Austria, 2013.

[BGH+13b] Boubeker Belabbas, Anja Grosch, Oliver Heirich, Andreas Lehner, and Thomas Strang. Curvature classification for trains using along-track and cross-track accelerometer and a heading rate gyroscope. In *ENC GNSS 2013*, 2013.

[BGN06] Boubeker Belabbas, Sebastian Graf, and Thoralf Noack. EGNOS Performance Monitoring using the DLR's Experimental Verification Network. In *IEEE ION PLANS 2006*, April 2006.

[BHS05a] B. Belabbas, A. Hornbostel, and M. Z. Sadeque. Error Analysis of Single Frequency GPS Measurements and Impact on Timing and Positioning Accuracy. In *WPNC'05 & UET'05*, 2005.

[BHS05b] Boubeker Belabbas, Achim Hornbostel, and Mohammed Zafer Sadeque. Accuracy Study of a Single Frequency Receiver Using a Combined GPS/GALILEO Constellation. In *ION GNSS 2005*, September 2005.

[BM12] Boubeker Belabbas and Michael Meurer. Carrier Phase and Code Based Absolute Slant Ionosphere Gradient Monitor for GBAS. In *Proceedings of the Institute of Navigation*, 2012.

[BMJ+08] B. Belabbas, C. Mayer, N. Jakowski, T. Pannowitsch, and M. Meurer. Integrity analysis of ionosphere gradient monitoring for precision approaches using GBAS. In *Proc. International Symposium on Precision Approach and Performance Based Navigation (ISPA 2008)*, Oktober 2008.

[Bou98] Ch. Bourga. UERE BUDGET. Technical report, 1998.

[Bou03] Nicolas Bouleau. *Error Calculus for Finance and Physics: The language of Dirichlet Forms*. de Gruyter Expositions in Mathematics 37, 2003.

[BPH05a] B. Belabbas, F. Petitprez, and A. Hornbostel. UERE analysis for static single frequency positioning using data of IGS stations. In *proceedings of the ION National Technical Meeting*, San Diego USA, January 2005.

[BPH05b] B. Belabbas, F. Petitprez, and A. Hornbostel. UERE Analysis for Static Single Frequency Positioning Using Data of IGS Stations. In *ION-National Technical Meeting, San Diego- USA, January 24-26, 2005*, volume Session A4, 2005.

[BRM08a] B. Belabbas, P. Rémi, and M. Meurer. Future GBAS architecture for precision approach and landing using GPS and Galileo. In *Proc. International Symposium on Precision Approach and Performance Based Navigation (ISPA 2008)*, Oktober 2008.

[BRM08b] Boubeker Belabbas, Patrick Rémi, and Michael Meurer. Galileo Performance Assessment for CAT III GBAS. In *ENC GNSS 2008*, 2008.

[BRMP11] Boubeker Belabbas, Patrick Rémi, Michael Meurer, and Sam Pullen. Absolute Slant Ionosphere Gradient Monitor for GAST-D: Issues and Opportunities. In *ION GNSS 2011*, September 2011.

[Bro92] R. Grover Brown. A Baseline RAIM Scheme and a Note on the Equivalence of Three RAIM Methods. *Navigation*, 39(3):301–316, 1992.

[BRWM08] B. Belabbas, P. Rémi, P. Worracharoen, and M. Meurer. Multi-frequency GBAS for precision approach and landing using GPS and Galileo. In *4th ESA Workshop on Satellite Navigation and User Equipment Technologies (NAVITEC 2008)*, Dezember 2008.

[BS05] B. Belabbas and S. Schlueter. Impact of NeQuick Correction Model to 3D position accuracy using Instantaneous Pseudo Range Error of Single Frequency Absolute Positioning Receivers. In *The European Navigation Conference GNSS 2005, Munich- Germany, 19-22 July 2005*, 2005.

[BSS05] Boubeker Belabbas, Stefan Schlueter, and Mohammed Zafer Sadeque. Impact of NeQuick Correction Model to Positioning and Timing Accuracy using the Instantaneous Pseudo Range Error of Single Frequency Absolute Positioning Receivers. In *ION GNSS 2005*, September 2005.

[CCH+06] Rob Conley, Ronald Cosentino, Christopher J. Hegarty, Elliot D. Kaplan, Joseph L. Leva, Maartin Uijt de Haag, and Karen Van Dyke. *Understanding GPS, Principles and Applications*, chapter Performance of Stand-Alone GPS, pages 301–378. Artech House Publishers, 2006.

[CGBR14] Omar Garcia Crespillo, Anja Grosch, Boubeker Belabbas, and Markus Rippl. Gnss-aided ins integrity concept. In *ION GNSS+ 2014*, 2014.

[CZ02] C. Cornacchini and A. Zappavigna. Link budget file. Technical report, Galileo Industries, 2002.

[DB04] S. Datta-Barua. Ionospheric threats to space-based augmentation system development. In *Proceedings of the ION GNSS*, 2004.

[DBM09] Thomas Dautermann, Boubeker Belabbas, and Michael Meurer. Error Propagation Concepts Including Flight Dynamics for Total System Performance Analysis During GBAS based Initial CAT-III Approach and Landing. In *ION GNSS 2009*, September 2009.

[DBR09a] Thomas Dautermann, Boubeker Belabbas, and Patrick Rémi. A Novel Integrity Concept for GBAS Precision Approaches Induced by Error Propagation with Non-Gaussian Distributions. In *European Navigation Conference - Global Navigation Satellite Systems 2009*, Proceedings of the ENC-GNSS 2009. EUGIN, Mai 2009.

[DBR09b] Thomas Dautermann, Boubeker Belabbas, and Patrick Rémi. A Novel Integrity Concept for GBAS Precision Approaches Induced by Error Propagation with Non-Gaussian Distributions. *13th International Symposium on Application of Laser Techniques to Fluid Mechanics*, 190:187–192, Dezember 2009.

[DBRP10] Thomas Dautermann, Boubeker Belabbas, Patrick Remi, and Sam Pullen. GBAS Ionospheric Threat Analysis using DLR's Hardware Signal Simulator. In *ESA Navitec 2010*, Dezember 2010.

[DMA+10] Thomas Dautermann, Christoph Mayer, Felix Antreich, Andriy Konovaltsev, Boubeker Belabbas, and Kälberer Ulrich. Non-Gaussian Error Modeling for GBAS Integrity Assessment. *IEEE TRANS. AEROSP. ELECTRON. SYST*, Dezember 2010. Contact Author for Preprint.

[EM99] L. H. Estey and C. M. Meertens. Teqc: The multi-purpose toolkit for gps/glonass data. *GPS Solutions*, 3(1):42–49, 1999.

[EWP+96] Per Enge, Todd Walter, Sam Pullen, Changdon Kee, Yi-Chung Chao, and Yeou-JYH Tsai. Wide Area Augmentation of the Global Positioning System. In *Proceedings of the IEEE*, volume 84, pages 1063–1088, August 1996.

[Fen05] Y. Feng. Future gnss performance: predictions using gps with a virtual galileo constellation. *GPS World*, 2005.

[FES+00] J. Furthner, E. Engler, A. Steingass, M. Angermann, J. Hahn, A. Hornbostel, R. Kraemer, H. P. Mueller, T. Noack, P. Robertson, S. Schlueter, and J. Selva. Realisation of an End-to-End Software Simulator for Navigation Systems. *International Journal of Satellite Communications*, 18, Number 4 & 5:371–389, 2000.

[Fuh01] S. Fuhrmann. Simulation des einflusses der empfangsantenne auf satellitennavigationssignale. Master's thesis, Hochschule Zittau/GÃ¶rlitz (FH), 2001.

[Gas05] FrÃ©dÃ©ric Gass. Study of RAIM algorithms for combined GPS/Galileo receivers. Master's thesis, Supaero, 2005.

[GB12] Anja Grosch and Boubeker Belabbas. Parameter Study of Loosely Coupled INS/GNSS Integrity Performance. In *Proceedings of IEEE/ION PLANS*, Myrtle Beach, SC, USA, 24-26 Apr 2012 2012.

[GBM10] Anja Grosch, Boubeker Belabbas, and Michael Meurer. Redundant Inertial-Aided GBAS for Civil Aviation. In *Navitec 2010*, Oktober 2010.

[GE04] Demoz Gebre-Egziabher. *DESIGN AND PERFORMANCE ANALYSIS OF A LOW-COST AIDED DEAD RECKONING NAVIGATOR.* PhD thesis, Stanford University, 2004.

[Hat82] R. R. Hatch. Synergism of gps code and carrier measurements. In *Proceedings of the Third International Geodetic Symposium on Satellite Doppler Positioning*, 1982.

[HGI+02] G. W. Hein, J. Godet, J.-L. Issler, J.-C. Martin, P. Erhard, R. Lucas-Rodriguez, and T. Pratt. Status of galileo frequency and signal design. In *proceedings of the ION*, 2002.

[Hin69] D. V. Hinkley. On the ratio of two correlated normal random variables. *Biometrika*, Vol. 56, No. 3:635–639, 1969.

[HM07] M. Harris and T. Murphy. Geometry Screening for GBAS to Meet CAT III Integrity and Continuity Requirements. In *Proceedings of the 2007 National Technical Meeting of The Institute of Navigation*, pages 1221 – 1233, San Diego, CA, Jan 2007.

[HM09] Matt Harris and Tim Murphy. Putting the Standardized GBAS Ionospheric Anomaly Monitors to the Test. In *Proceedings of the ION GNSS 2009*, Savannah, GA, Sep 2009.

[HSB+10] A. Hornbostel, S. Schlüter, B. Belabbas, V. Wilken, and M. Meurer. GBAS Performance Analysis by Hardware Simulations. In *ENC-GNSS 2010*, Oktober 2010.

[ICA06] ICAO. Annex 10 to the convention on international civil aviation: Aeronautical telecommunications, volume i: Radio navigation aids, July 2006.

[JAA03] JAA. Certification Specifications for All Weather Operations – CS-AWO. Technical report, European Aviation Safety Agency, October 17 2003. DECISION NO. 2003/6/RM.

[KLMP06] Elliot D. Kaplan, Joseph L. Leva, Dennis Milbert, and Mike S. Pavloff. *Understanding GPS: Principles and Applications*, chapter Fondamentals of Satellite Navigation, pages 21–65. Artech House, 2006.

[Klo85] J. A. Klobuchar. Ionospheric time delay effects on earth space propagation. In A. S. Jursa, editor, *Handbook of Geophysics and the space evironment*, chapter 10.8, pages 1084–1088. U.S. Air Force, ashingto, D.C., 1985.

[Klo96] J. A. Klobuchar. *Global Positioning System: Theory and Applications*, volume 164, chapter Ionospheric Effects on GPS, pages 485–515. AIAA Progress in Aeronautics and Astronautics, 1996.

[Kov00] Karl Kovach. New User Equivalent Range Error (UERE) Budget for the Modernized Navstar Global Positioning System (GPS). In *ION NTM*, 2000.

[KPRE06] Hiroyuki Konno, Sam Pullen, Jason Rife, and Per Enge. Evaluation of Two Types of Dual-Frequency Differential GPS Techniques under Anomalous Ionosphere Conditions. In *Proceedings of the ION National Technical Meeting*, 2006.

[KYP+10] Samer Khanafseh, Fan Yang, Boris Pervan, Sam Pullen, and John Warburton. Carrier Phase Ionospheric Gradient Ground Monitor for GBAS with Experimental Validation. In *Proceedings of the ION GNSS*, 2010.

[LLP+06] Jiyun Lee, Ming Luo, Sam Pullen, Young Shin Park, Per Enge, and Mats Brenner. Position-domain geometry screening to maximize laas availability in the presence of ionosphere anomalies. In *Proceedings of the ION GNSS*, 2006.

[LPD+03] Ming Luo, Sam Pullen, Jed Dennis, Hiroyuki Konno, Gang Xie, Todd Walter, Per Enge, Seebany Datta-Barua, and Tom Dehel. Laas ionosphere spatial gradient threat model and impact of lgf and airborne monitoring. In *Proceedings of the ION GPS*, 2003.

[LPE+04] Ming Luo, Sam Pullen, Alexandru Ene, Di Qiu, Todd Walter, and Per Enge. Ionosphere threat to laas: Updated model, user impact, and mitigations. In *Proceedings of the ION GNSS*, 2004.

[LPWE04] Ming Luo, Sam Pullen, Todd Walter, and Per Enge. Ionosphere spatial gradient threat for laas: Mitigation and tolerable threat space. In *Proceedings of the ION NTM*, 2004.

[LWG05] A. W. Lyon, J. Westbrook, and U. Guida. Operating EGNOS. In *ION GNSS*, pages 419–423, 2005.

[MBD09] Christoph Mayer, Boubeker Belabbas, and Winfried Dunkel. Ionospheric Threat Model Assessment. In *ICAO NSP Meeting*, 2009.

[MBJ+09] Christoph Mayer, Boubeker Belabbas, Norbert Jakowski, Michael Meurer, and Winfried Dunkel. Ionosphere Threat Space Model Assessment for GBAS. In *ION GNSS 2009*, Oktober 2009.

[ME06] Pratap Misra and Per Enge. *Global Positioning System, Signals, Measurements, and Performance*. Ganga-Jamuna Press, 2nd edition edition, 2006.

[MJB08a] Christoph Mayer, Norbert Jakowski, and Boubeker Belabbas. Towards an European GBAS CAT-III Iononspheric Threat Model. In *LATO Meeting*, 2008.

[MJB+08b] Christoph Mayer, Norbert Jakowski, Claudia Borries, Thomas Pannowitsch, and Boubeker Belabbas. Extreme ionospheric conditions over Europe observed during the last solar cycle. In *4th ESA Workshop on Satellite Navigation User Equipment Technologies*, 2008.

[NBHP07] Igor Nikiforov, Boubeker Belabbas, Patrick Henkel, and Hadrien Palcoux. GBAS with RAIM Based on the Constrained GLRT for Precision Landing Using Galileo and GPS. In Institute of Navigation, editor, *ION 2007 (National Technical Meeting)*, Januar 2007.

[Nie96] A. E. Niell. Global mapping functions of the atmosphere delay at radio wavelengths. *Journal of Geophysical Research*, 101 No. B2:3227–3246, 1996.

[NSKH04] T. Noack, I. Steinbach, D. Klähn, and R. Hartmann. Experimentation and verification network a new platform for the distribution of gnss data via internet -overview and fields of applications. In *ETC 2004*, Garmisch-Partenkirchen, Germany, May 2004.

[NSP10] ICAO NSP. GBAS CAT II/III Development Baseline SARPs. Technical report, International Civil Aviation Organization, May 2010.

[Oks07] Bernt Oksendal. *Stochastic Differential Equations Sixth Edition*. Number ISBN 978-3-540-04758-2. Springer, 6 edition, 2007.

[PAE00] R. Eric Phelts, Dennis M. Akos, and Per Enge. Robust Signal Quality Monitoring and Detection of Evil Waveforms. In *ION*, 2000.

[Phe01] Robert Eric Phelts. *MULTICORRELATOR TECHNIQUES FOR ROBUST MITIGATION OF THREATS TO GPS SIGNAL QUALITY*. PhD thesis, Stanford University, 2001.

[PMP+01] R. Eric Phelts, Alexander Mitelman, Sam Pullen, Dennis Akos, and Per Enge. Transient Performance Analysis of a Multicorrelator Signal Quality Monitor. In *ION*, 2001.

[PSJ96] B.W. Parkinson and J. J. Spilker Jr. *Global Positioning System: Theory and Applications Volume I*. American Institute of Aeronautics and Astronautics, 1996.

[PTVF07] William H. Press, Saul A. Teukolsky, William T. Vetterling, and Brian P. Flannery. *Numerical Recipes in C, Third Edition*. Cambridge University Press, 2007.

[RBDM09] Patrick Rémi, Boubeker Belabbas, Thomas Dautermann, and Michael Meurer. Performance Assessment of Dual FrequencyGBAS Protection Level Algorithms using a Dual Constellation and Non-Gaussian Error Distributions. In *ION GNSS 2009*, Proceedings of the ION GNSS 2009. Institute of Navigation, September 2009.

[RTC04] RTCA/DO-245A. Minimum Aviation System Performance Standards for the Local Area Augmentation System (LAAS). Technical Report 245A, Radio Technical Commission for Aeronautics, 2004.

[RTC06] RTCA/SC-159. RTCA/DO-229D Semi-Final: MINIMUM OPERATIONAL PERFORMANCE STANDARDS FOR GLOBAL POSITIONING SYSTEM/WIDE AREA AUGMENTATION SYSTEM AIRBORNE EQUIPMENT. Technical report, RTCA, 2006.

[RTC08] RTCA DO-253C. Minimum Operational Performance Standards for GPS Local Area Augmentation System Airborne Equipment. Technical Report 253C, Radio Technical Commission for Aeronautics, 2008.

[SC101] RTCA SC159. DO-229C, minimum operational performance standards for global positioning system/wide area augmentation system airborne equipment. Technical report, RTCA, 2001.

[SK12] John Warburton Samer Khanafseh, Sam Pullen. Carrier Phase Ionospheric Gradient Ground Monitor for GBAS with Experimental Validation. *Journal of Navigation*, 59:51–60, 2012.

[WBH06] Phillip Ward, John W. Betz, and Christopher J. Hegarty. *Understanding GPS: Principles and Applications*, chapter Satellite Signal Acquisi-

tion, Tracking and Data Demodulation, pages 153–240. Artech House, 2006.

[WE95] Todd Walter and Per Enge. Weighted RAIM for Precision Approach. In *Proceedins of the ION GPS*, pages 1995 – 2004. Institute of Navigation, 1995.

[WR03] David L.M. Warren and John F. Raquet. Broadcast vs. precise gps ephemerides: a historical perspective. In *GPS Solutions*, pages 151–156, 2003.

[Xio08] Jie Xiong. *An Introduction to Stochastic Filtering Theory*. Oxford University Press, 2008.

[You01] A. Younes. *Sequential Theory Applied to GNSS Integrity Monitoring and to GNSS/INS Hybridization*. PhD thesis, ENAC, 2001.

[Zap02] A. Zappavigna. Uere budget results. Technical Report GB2C/SE/TNO/0001, Space Engineering S.p.A., 2002.

[ZMV98] M.P. Zorzano, H. Mais, and L. Vazquez. Numerical solution for fokker-planck equations in accelerometers. *IEEE*, pages 1825–1827, 1998.

Nomenclature

ACR	Along track, Cross track, Radial
AOR-E	Atlantic Ocean Region East
ASIGMA	Absolute Slant Ionospheric Gradient Monitor Architecture
BOC	Binary Offset Carrier
BPSK	Binary Phase Shift Keying
CDF	Cumulative Density Function
CDMA	Code Division Multiple Access
CPCF	Central Processing and Control Facility
CS-AWO	Certifications Specifications – All Weather Operations
DLL	Delay Lock Loop
DME	Distance Measuring Equipment
DOP	Dilution of Precision
ECAC	European Civil Aviation Conference
ECEF	Earth Centered Earth Fixed
EGNOS	European Geostationary Navigation Overlay Service
ENU	East North Up
EVnet	Experimental and Verification network
GAST-C	GBAS Approach Service Type C
GAST-D	GBAS Approach Service Type D
GBAS	Ground Based Augmentation System
GDOP	Geometric Dilution of Precision

GGTO	GPS Galileo Time Offset
GNSS	Global Navigation Satellite System
GPS	Global Positioning System
HDOP	Horizontal Dilution of Precision
ICD	Interface Control Document
IGS	International GNSS Service
ILS	Instrument Landing System
INS	Inertial Navigation System
IPP	Ionosphere Pierce Point
IPRE	Instantaneous Pseudo Range Error
IPRED	Instantaneous Pseudo Range Error Database
ISM	Integrity Support Message
KFE	Kolmogorov Forward Equation
KFE	Kolmogorov Forward Equation
MDCD	Minimum Detectable Curvature Difference
NDB	Non Directional Beacon
NIMP	Network Integrity Monitoring Platform
ODTS	Orbit Determination and Time Synchronization
PCCGO	Phase Center Center of Gravity Offset
PCCGO	Phase Center Center of Gravity Offset
PDOP	Position Dilution of Precision
PLL	Phase Lock Loop
PRN	Pseudo Random Noise
RAC	Radial, Along track, Cross track
RAIM	Receiver Autonomous Integrity Monitoring

RCMPRE	Regional Covariance Matrix of Pseudo Range Error
SA	Selective Availability
SBAS	Space Based Augmentation System
SDE	Stochastic Differential Equation
SISRE	Signal In Space Range Error
TDOP	Time Dilution of Precision
TEC	Total Electron Content
UERE	User Equivalent Range Error
VDB	VHF Data Broadcast
VDOP	Vertical Dilution of Precision
VGC	Virtual Galileo Constellation
VNSE	Vertical Navigation System Error
VOR	VHF Omnidirectional Range
WAAS	Wide Area Augmentation System
wd	wrong decision
WGS84	World Geodetic System 1984